Ignasi Carrio
Pablo Ros
Editors

PET/MRI

Methodology and Clinical Applications

Springer

PET/MRI

Ignasi Carrio • Pablo Ros
Editors

PET/MRI

Methodology and Clinical Applications

Springer

Editors
Ignasi Carrio
Department Medicina Nuclear
Autonomous University of Barcelona
Hospital Sant Pau
Barcelona
Spain

Pablo Ros
Department of Radiology
University Hospitals Case
Medical Center
Cleveland, OH
USA

ISBN 978-3-642-40691-1 ISBN 978-3-642-40692-8 (eBook)
DOI 10.1007/978-3-642-40692-8
Springer Heidelberg New York Dordrecht London

Library of Congress Control Number: 2013956349

Printed on acid-free paper

Springer is part of Springer Science+Business Media (www.springer.com)

Contents

PET/MR System Design

1

Gaspar Delso and Sibylle Ziegler

Contents

Abstract

The combination of clinical MR and PET scanners has received increasing attention in recent years. In contrast to currently used PET/CT machines, PET/MR offers not only improved soft-tissue contrast and reduced ionizing radiation but also a wealth of available MR variations such as functional, spectroscopic, and diffusion tensor imaging. This combination, however, has proven to be very challenging, due to the detrimental effect of the scanners on each other's performance. Significant progress has been made in the last 10 years to solve the various technical issues, culminating with the recent release of clinical whole-body hybrid scanners.

In this chapter, we review the technological challenges of PET/MR design, briefly describing the different available architectures for hybrid clinical scanners, their capabilities, and limitations.

1.1 Introduction

Despite the extensive research effort dedicated to software coregistration in the 1990s, the introduction of combined scanners capable of acquiring positron emission tomography (PET) and computed tomography (CT) data sequentially [2] was met with enthusiasm by the medical community. Nine out of every ten PET scanners purchased nowadays are combined machines. The key to this

G. Delso (✉) • S. Ziegler
Nuklearmedizinische Klinik und Poliklinik, Klinikum rechts der Isar der Technischen Universität München, Ismaninger Str. 22, 81675 Munich, Germany
e-mail: gaspar.delso@tum.de; sibylle.ziegler@tum.de

I. Carrio, P. Ros (eds.), *PET/MRI*,
DOI 10.1007/978-3-642-40692-8_1,

success was not just the straightforward solution to the coregistration problem in most applications but also the significant improvement in workflow derived from both scanning the patient just once and not needing to perform a transmission scan for generating attenuation correction data.

PET/CT is currently fully integrated in clinical routine, but, though its advantages are many, CT still provides limited soft-tissue contrast and, when used for whole-body diagnosis, exposes the patients to high radiation doses (over 10 mSv) [15]. An alternative source of anatomical information would be magnetic resonance imaging (MR) [74].

The combination of MR and positron emission tomography scanners, however, has proven to be very challenging due to the potentially detrimental impact of the scanners on each other's performance. The intense static magnetic field, quickly changing gradient fields, and radiofrequency (RF) signals from the MR scanner affect the light yield of scintillator materials [9], prevent the normal operation of photomultiplier tubes, and induce interference in the front-end electronics of PET detectors. Conversely, the presence of the PET detector causes inhomogeneities in the magnetic field, degrades the performance of the coils, and can induce interference in the MR acquisition path.

However, in the last years, progress has been made in identifying scintillators with adequate magnetic properties [71], developing suitable PET detectors which either use optical fibers to guide the scintillation light away from the MR magnetic fields [6, 32, 36, 50, 57, 58] or replace the photomultipliers by magnetic-field-insensitive solid-state detectors [5, 21, 41, 44, 45, 60, 68], and designing shielded PET electronics to avoid electromagnetic interference [28].

To this day, several research groups have successfully developed small PET/MR prototypes for animal studies [5, 35, 45, 49, 57, 58, 68], and each of the three main manufacturers (General Electric, Philips, and Siemens) has recently released their own proposal of whole-body hybrid. However, these systems present radically different architectures, and it has to be shown which is the best configuration for clinical practice.

In this chapter, we briefly describe the main issues and choices involved in PET/MR system design. We discuss the advantages and limitations of the available architectures, giving the reader an overview of the different setups investigated by the various groups having reported on working PET/MR prototypes.

1.2 Compatibility Issues

1.2.1 Static Magnetic Field

At the heart of magnetic resonance imaging is the *static field*, a powerful magnetic field used to align the magnetic moments of atomic nuclei. In clinical practice, field intensities of 1.5 and 3 T are currently used. More advanced medical applications are being investigated with field intensities of up to 9.4 T.

The magnetic moments of nuclei in a magnetic field can be oriented *parallel* or *antiparallel* to the field. Due to the interaction between the nuclear magnetic moment and the external magnetic field, these two states have slightly different energy levels. The moments will therefore be in an equilibrium state governed by Maxwell-Boltzmann statistics. When an electromagnetic excitation is applied with a frequency that matches the energy difference between the two states, a resonant absorption is generated.

As the resonance frequency of the magnetic moments is proportional to the strength of the static field, the homogeneity of this field is of critical importance to ensure the desired distribution of excitation over the sample. This is achieved by a careful consideration of the geometry of the system and the susceptibility of the materials (Sect. 1.2.2), as well as by the use of passive and active *shimming*.

The excited nuclei will gradually return to an equilibrium state by releasing energy at the resonant frequency. To be able to discern the origin of these emissions, a set of spatially variant *gradient fields* are superimposed with the static field, leading to local variations in the frequency and phase of the emitted signal. The resulting information can be processed by a *reconstruction* algorithm to create two- or three-dimensional images of the resonance signal.

Consequently, inhomogeneities of the static magnetic field can alter the spatial encoding of the sample, leading to artifacts in the reconstructed images, such as geometrical distortions in the readout direction.

Another important effect of the static magnetic field is the generation of *Lorentz forces* on charged particles moving through it. This can have a positive effect, like an improvement in PET resolution due to the reduction of the average distance traveled by positrons prior to annihilation [23]. However, it has a severely detrimental effect in the performance of the photomultiplier tubes generally used in PET detectors [22].

1.2.2 Magnetic Susceptibility

Closely related to the issue of static field homogeneity is that of magnetic susceptibility. *Volume magnetic susceptibility* is a proportionality constant indicating the degree of magnetization (the magnetic dipole moment per unit volume) of a material in response to an applied magnetic field. In other words, materials placed in the static field will become magnetized, altering the overall magnetic field in their vicinity.

As a reference, an object with a susceptibility of 10^{-6} (1 ppm) produces a maximum perturbation of about ±1 ppm in the surrounding field and, consequently, in the resonant frequency. If the susceptibility is 10 ppm, the effect is ten times as large, etc... [33, 53].

Since MR image quality is strongly dependent on the uniformity of the static field, materials with high susceptibility (in absolute value) should be either avoided or placed as far from the field of view as possible.

1.2.3 Eddy Currents

Faraday's law of induction states that a time-varying magnetic flux through a closed circuit will generate an electromotive force proportional to its rate of change. The consequence of this is that the radiofrequency excitation field, as well as the switching of the gradient fields used for spatial encoding (e.g., 200 T/m/s), will induce currents in any conductive structures present in the scanner.

These local current loops, known as *eddy currents* or *Foucault currents*, will in turn create magnetic fields, degrading the homogeneity of the static field. If the eddy currents decay before the signal readout, the result will be a spatially variant phase change of the resonance signal. However, if the eddy current still persists during readout, the associated magnetic field will alter the spatial encoding of the signal, leading to a distortion of the reconstructed images [3, 51]. Eddy currents during slice selection may cause imperfect refocussing of the spins, leading to signal loss.

For conventional imaging with a rectilinear raster of the k-space, the effect of eddy currents is mainly visible in the phase image. However, for sequences with more complex raster patterns (such as echo planar imaging), the k-space shifting and phase accumulation can lead to ghosting, compression, shearing, or image displacement. Particularly strong artifacts can arise in sequences that require accurate phase images (such as phase-contrast imaging) or that combine multiple images (such as diffusion-weighted imaging). In the case of spectroscopy studies, eddy currents lead to time-varying shifts in the resonance frequency, degrading the resolution of the acquired spectrum [30].

Other undesired side effects of eddy currents are coil loading, heating, mechanical vibration, and interference, which are discussed in the following sections.

1.2.4 Coil Loading

The magnetic field generated by an eddy current always opposes the change of the field that created the eddy current in the first place (Lenz's law). The energy lost due to the generation of eddy currents has the effect of altering the *load* on the gradient and radiofrequency coils. As the load deviates from the ideal value for which the coils have been designed, their performance degrades: The resonance frequency of the coil shifts and its quality factor is reduced.

In the case of radiofrequency coils, this leads to a reduction of the signal-to-noise ratio of the images. In the case of gradient coils, it limits the rate of change of the gradient fields (or *slew rate*) and alters spatial encoding.

1.2.5 Temperature

As with any electric current circulating through a nonideal conductor, eddy currents will cause Joule heating. This effect can cause discomfort or, in extreme cases, burns when patients are in contact with metallic objects [14, 39].

More importantly for the purpose of system design, the performance of some electronic components can be sensitive to temperature [10, 16, 61]. This is of particular relevance when using solid-state photodetector technology (Sect. 1.3.1), where an increase of temperature will reduce the gain of the electron avalanche due to increased collisions with the semiconductor lattice [8]. Indeed, temperature variations have been shown to cause significant drifts (3.5 % per Kelvin) in the gain of avalanche photodiodes. In the case of silicon photomultipliers, temperature changes alter the breakdown voltage, leading to variations in photodetection efficiency, dark counts, and gain. These effects degrade the energy resolution of PET detectors, cause sensitivity variations, and, ultimately, result in reconstruction artifacts and quantification errors [10, 16, 61].

The temperature issue is aggravated by the preamplification required by solid-state photodetectors. Power consumption in the preamplifier is a constant source of intense heat in close proximity to the sensitive photodetector. Although preamplifier heating can have a severely detrimental effect on the performance of the PET system, it can be effectively managed by an adequate cooling system (Sect. 1.3.5) and accounted for in the system calibration. This is not always true for the localized, time-varying warming caused by the intense eddy currents induced by the more demanding MR sequences, another reason to design the system in such a way that minimizes eddy current load.

1.2.6 Mechanical Vibration

Due to the interaction of the static magnetic field with the time-varying currents used to generate the magnetic field gradients, the gradient coils are subject to Lorenz forces causing vibrations in the acoustic range. The vibration amplitude will increase with the magnetic flux density, the intensity of the current, and the coil radius. Lighter coils will generally present larger amplitudes. The length of the coil and the elastic properties of the coil materials will determine the frequency of the vibration modes, whereas the viscosity of the materials will affect how the vibrations decay [66]. It is worth mentioning that in scanners using actively shielded gradient coils, these vibrations are reduced by mechanically coupling them with the shielding coils. This is due to the different polarity of the currents that make the coils vibrate in opposed phase.

The airborne transport of these vibrations is the cause of the well-known acoustic noise in MR scanners, which can be of the order of 115 dB(A) in 3 T scanners. However, the mechanical vibration can also be directly transmitted through the different support structures in the system [52]. Despite the use of passive and active dampeners, some of these vibrations will reach other subsystems in the scanner.

It is a known fact that MR scanners are sensitive to mechanical vibration, especially at low frequencies (<100 Hz). External vibrations are more detrimental than those introduced by the scanner itself, which are often in phase with the experiment. But self-induced resonance effects can still cause artifacts in the reconstructed images [19]. We are not aware of any published studies on the effect of mechanical vibrations on PET detectors. However, two issues should be considered: Firstly, measures should be taken to prevent a degradation of the PET detector assembly due to the exposure to frequent, irregular mechanical vibrations; secondly, the geometry and mechanical properties of the materials used in the construction of the PET detector should be carefully selected, preventing resonance effects leading to vibrational modes potentially deleterious for the MR acquisition.

Mechanical vibrations can also be transmitted by eddy currents caused by the switching of the gradient fields. The interaction of these currents with the static field will in turn cause Lorenz forces on the conducting structure. This can give rise to significant mechanical vibration in structures with large metallic elements, such as the radiofrequency shielding of the PET detector.

1.2.7 Interference

Electronic cross talk between the scanner subsystems is another potential source of image artifacts and general performance degradation. Assuming that the MR and PET subsystems are electronically independent and all potential paths of conducted interference have been accounted for, the issue of electromagnetic interference must be addressed.

Radiated interference in PET/MR scanners is a two-sided problem:

On the one hand, the signals induced in the PET electronics by the switching field gradients and radiofrequency excitation signal must be considered. The gradient fields will induce currents with relatively low frequencies, in the order of 10^2–10^3 Hz, which will have to be filtered. The radiofrequency signal will induce currents in a narrow band around the Larmor frequency (42.58 MHz/T) and subsequent harmonics, usually in short (e.g., 1 ms) bursts repeated with a frequency in the order of 10^2 Hz. In this case, the interference can overlap the upper operating band of some PET front-end electronics. Filtering out such interference leads to a trade-off with the achievable sharpness of the scintillation signal rise time (and therefore the temporal resolution of the system). Appropriate radiofrequency shielding and/or temporal multiplexing of PET and MR acquisition is often employed.

On the other hand, the emissions due to the operation of the PET detectors can be picked up by the sensitive MR acquisition path. The desired resonance signal is extremely weak, in the order of 10^{-9} T, yielding below −23 dBm in the coils. High preamplification factors are therefore required (>30 dB) as well as high dynamic ranges (>160 dB), making the system extremely sensitive to interference in its operating band. This is the reason why MR systems must operate in a *Faraday cage*, preferably with in- and outbound signals transmitted optically and only (filtered) DC lines entering the cage. Interference sources inside the cage should be avoided at all costs. Fortunately, the receiver acquires a relatively narrow frequency band, ranging from 10 kHz to 1 MHz depending on the field gradient strength.

1.2.8 Gamma Attenuation

An important factor affecting the quality of PET images is the signal that is lost due to interactions with the different elements in the field of view. Indeed, the number of *counts* (pairs of detected gamma rays assumed to originate in the same positron annihilation event) in a *line of response* (line joining two detector elements) will decrease exponentially with the thickness and attenuation factor (at 511 keV) of the structures that it intersects.

Most of these losses are due to *Compton interactions* of the gamma rays with the electron shell of the materials along their path. In these cases, the gammas are *scattered* away from their original trajectory and, in most cases, lost. However, depending on the geometry of the system, a fraction of the scattered gammas will still reach a detector, causing the event to be registered in an erroneous line of response. These counts due to scattered gammas can be seen as a contribution to the noise level of the measurement and require specific correction algorithms to be applied after the acquisition.

1.3 Design Options

1.3.1 Photodetectors

There are several available technologies to detect the gamma radiation that constitutes the PET signal (this topic is extensively covered in a different chapter). In standard clinical scanners, passive *scintillator* crystals [38] are used to convert the

incoming gammas into lower wavelength photons (400–500 nm). Photomultiplier tubes (PMTs) are then used to convert these photons into electrical signals.

Unfortunately, photomultiplier tubes are extremely sensitive to external magnetic fields [22, 65]. This is due to photoelectrons and secondary electrons deviating from their normal trajectories due to Lorentz forces. As a reference, a clinical scanner can experience variations of performance along its detector ring due to the different orientation of the photomultipliers with respect to the Earth's magnetic field. To prevent this effect, mu-metal sheets or grids can be used to individually shield the photomultipliers [13]. Also, generic photomultiplier tubes are not well suited to operate under mechanical vibration and have metallic structures susceptible to magnetic induction.

Nevertheless, it is possible to use photomultiplier-based detectors to acquire PET data inside the bore of an MR scanner. Simon Cherry's group [57, 58] was the first to develop MR-compatible PET detectors, using optical fibers to guide the light from the scintillator crystals to photomultipliers situated where the magnetic field dropped below 10 mT. This kind of design, however, leads to limitations in the PET scanner performance due, among other factors, to the signal loss in the light guides [36].

Solid-state photodetector devices have been proposed as a magnetically insensitive alternative to photomultiplier tubes. Two such technologies are currently in use: avalanche photodiodes (APDs) and silicon photomultipliers (SiPM).

Avalanche photodiodes were first used to avoid having to guide the scintillation light outside the magnetic field [45, 46]. A similar concept using position-sensitive APDs was presented in Wu et al. [69]. APDs are compact, have higher quantum efficiency than PMTs, require a lower supply voltage, and, above all, are capable of operating in high magnetic fields. On the other hand, they are noisier than PMTs, which has a detrimental impact on energy and time resolution, and have worse gain, meaning that more powerful preamplifier electronics must be used and the subsequent temperature issues dealt with [61]. The main drawback of APD technology in current PET/MR systems is arguably the limited time resolution.

Silicon photomultipliers offer a possible solution to the temporal resolution issue [41, 60]. These devices are basically a tightly packed array of APDs (>1,000 per square millimeter) on a common silicon substrate. Each cell operates in Geiger mode, which means that their response to excitation is binary. The SiPM output is the combination of all the individual cell responses, achieving a dynamic detection range from a single photon to the available number of cells. They are compact, offer quantum efficiency, and gain similar to traditional photomultipliers and temporal resolutions of less than a nanosecond [20]. This last property would render SiPM-based systems capable of time-of-flight measurement.

1.3.2 Radiofrequency Shielding

Electromagnetic interference shielding refers to the use of certain structures to reflect and/or absorb electromagnetic radiation. In the case of PET/MR, shielding is required to prevent the strong time-varying fields of the MR, such as switching gradients and emitted RF field, from interfering with the PET detector. Both the front-end electronics and the data transmission lines must be shielded. Conversely, shielding might be required to prevent high-frequency signals from the PET electronics, such as clock signals, from interfering with MR reception.

The s*hielding effectiveness* (in dB) of a structure indicates the losses undergone by a signal going through it. These losses are primarily due to reflection and absorption, but other effects such as multiple reflections can also be exploited by certain shield structures. The reflection loss is proportional to the electrical conductivity of the material and inversely proportional to its magnetic permeability. The absorption loss is proportional to both conductivity and permeability, as well as to the thickness of the shield. Copper and aluminum make excellent reflection shields due to their high conductivity, whereas mu-metal is excellent for absorption, due to its high magnetic permeability [7].

A useful parameter when designing electromagnetic shielding is the *skin depth* of the

material. It is defined as the depth at which the field drops to e^{-1} of the incident value. The skin depth of a material is inversely proportional to the square root of the electrical conductivity, of the magnetic permeability, and of the signal frequency. As a reference, the skin depth of a copper plate is 5.9 μm at 127 MHz (Larmor frequency at 3 T). It should be noted that the skin depth is an approximation that considers a planar wave interacting with an infinite surface. A shielding effectiveness beyond that indicated by the skin depth can be achieved, depending on the shield geometry [17]. As a side note, the skin depth of a conductor can be affected by temperature.

There are several constraints to be considered when designing electromagnetic shielding for PET/MR scanners. Firstly, the susceptibility of shield materials (e.g., $-1.0 \cdot 10^{-5}$ for copper and $2.2 \cdot 10^{-5}$ for aluminum) will dictate how they degrade the homogeneity of the static field. Also, their gamma attenuation properties must be considered, if the shield is in the PET field of view (e.g., ~0.73 cm^{-1} for copper and ~0.23 cm^{-1} for aluminum). Both arguments advocate for a minimization of the amount of material used in the shields. This can be achieved by the use of conductor mesh layers, as well as by employing multiple layers of thin conductor materials. The latter also enables a finer control of the spectral properties of the shield by studying the transmission/reflection interactions between the different layers [67].

More importantly, the conductive nature of radiofrequency shields makes them susceptible to eddy current induction, with the subsequent heating, vibration, secondary fields, and coil performance degradation. The use of segmented structures limiting the conductive paths along the shield surface can alleviate this problem [26, 43].

1.3.3 Data Transmission

The relative positioning of the PET front-end and post-processing systems with respect to the MR has profound implications in the performance and capabilities of the hybrid scanner. A corollary of this is the importance of how the measured data is transmitted between those systems.

As previously discussed, the first prototypes of PET/MR scanner were basically arrays of scintillator crystals coupled to long optical fiber bundles that led the scintillation light to a sufficiently distant photodetector and processing unit [57, 58]. Despite its conceptual simplicity, this setup has serious drawbacks: Coupling and transmission losses lead to a degradation of the scintillation signal that limits the energy and time resolution of the system [36]. Furthermore, the bulk and rigidity of the optical fibers limit the scalability of such designs. New, flexible optical fibers have been recently proposed to overcome this limitations [70].

With the adoption of solid-state photodetectors came the opportunity to introduce both the scintillator crystals and the photodetectors in the MR bore, leaving the post-processing unit outside. Several setups have been proposed, using short optical fibers [5] or direct coupling [27] between the scintillators and the photodetectors. A vulnerable spot of these systems is the transmission of the (preamplified) analog signal obtained from the photodetectors to the remote unit, which will then multiplex, digitize, and perform the coincidence sorting. The long (usually coaxial) cables used for this purpose are prone to signal degradation. Shielding is possible but leads in turn to eddy current problems. A variation of this method proposes using low-capacitance, high-impedance cables to directly transmit the charge signal from SiPM detectors to shielded preamplifiers placed outside the scanner [29].

In order to render the PET detectors more robust to the interference of the MR system, there is an ongoing research effort to minimize the amount of analog processing. An important step in this direction has been the development of *digital silicon photomultipliers*, which include integrated photon counting logic and yield a digital output signal [18]. Application-specific integrated circuits are also being designed to be included next to the photodetectors in order to extract the timing and energy information from the detected light pulses. Being able to transmit the information in such a digital form has the advantage of reducing the bulk of transmission lines required to communicate with the

post-processing unit. This can be combined with the integration of laser-emitting diodes in the front-end boards to enable optical transmission of the PET signal [40].

1.3.4 Gamma Shielding

A common problem in PET acquisition is the influence of gamma rays originating outside the field of view of the scanner. Indeed, regions of high activity, such as the brain or the bladder—in the case of 18F-FDG scans—are often present during the scan of other organs. Not being covered by any direct line of response, the pairs of back-to-back gammas created in these regions shouldn't be detected. However, it is possible that, due to Compton scattering, some of these gamma pairs are detected. Furthermore, even single gammas can degrade the performance of the system, increasing the dead time of the detectors and increasing the fraction of *random coincidences* (i.e., being paired up with gammas from other annihilation events) [62].

The standard solution to this problem in standalone PET scanners is the inclusion of *end shields* [25]. These are annular structures made of some material with high gamma attenuation, such as lead or tungsten. As a reference, 1 cm of lead attenuates approximately 83 % of the incoming radiation (assuming 511 keV) and 1 cm of tungsten 93 %. They are placed at one or both ends of the scanner bore in order to stop out-of-field radiation from reaching the scintillator ring.

Large, massive rings of metal are far from a desirable complement to an MR scanner. They can lead to serious susceptibility artifacts (the susceptibility of lead is approximately −15.8 ppm and that of tungsten 77.2 ppm). They are also susceptible to the induction of eddy currents (the conductivity of lead is approximately $4.8 \cdot 10^6$ S/m and that of tungsten $18.2 \cdot 10^6$ S/m) with the subsequent field inhomogeneities and coil performance degradation.

Several materials and configurations have been studied to overcome this problem [63], but in all cases there is a trade-off between magnetic compatibility, conductivity, and cost. Tungsten carbide has good magnetic properties but is too conductive. Lead is still an option, particularly so if combined with a layer of paramagnetic material to optimize the total susceptibility of the shield. Measures must be taken to limit the conduction paths on the shield. Dividing the shield into multiple segments is possible, similarly to what is done for radiofrequency shielding. But in this case, due to the thickness of the structure, the gaps have to be significantly larger to prevent capacitive effects. This in turn compromises the homogeneity of the shielding, unless some sort of shifted multilayer structure is used.

Composite materials of attenuating metals suspended in an insulating medium, like epoxy resin, have also been studied. However, they seem to lose their insulating properties before acceptable attenuation properties can be obtained. Further research on this topic may show otherwise. Heavy-element-based insulating materials, such as some scintillator materials or heavy-metal oxides, show promising shielding and magnetic compatibility properties but are at the moment too expensive for practical use.

Finally, the feasibility of gamma shielding is limited in some architectures (Sects. 1.4.2 and 1.4.3) by the space restrictions associated with the integration of the PET detectors in the MR bore.

1.3.5 Cooling

Perhaps a little surprisingly, one of the most important tasks to ensure a good performance of the PET system is keeping the temperature in check. As we have seen, this is particularly important in integrated systems relying on solid-state photodetector technology.

The main choice in this case is between air-based cooling (such as that used in the first hybrid system for human imaging, the Siemens BrainPET insert) and liquid cooling (such as implemented in its immediate successor, the Biograph mMR). Other more sophisticated approaches have been reported, such as the combination of water-cooled plates and a nitrogen atmosphere used in the ClearPEM system [1].

The main goal of such sophisticated cooling approaches is keeping the photodetector temperature stable, providing a sink for the heat generated by the preamplifier circuit. This is critical for APD-based systems, like the ones mentioned above, due to their relatively low intrinsic gain and therefore strong amplification needs. In the case of SiPM technology, where less amplification is needed, and in particular with digital silicon photomultipliers which do not require external ASICs, air cooling may prove to be sufficient.

A further improvement is using thermoelectric heat pumps (Peltier devices) to individually regulate the temperature of the detectors, thus ensuring the stability of the PET subsystem even in the presence of time-varying induction heating. Such an approach can be combined with a temperature-dependent gain control system for optimal stability [72].

1.3.6 Hardware Attenuation

The attenuation due to the patient tissue is accounted for during the reconstruction process. The different algorithms available for this purpose and their implications for the design of the system are covered in a different chapter.

Two issues remain to be considered: the attenuation of fixed hardware structures, such as the patient bed and the radiofrequency coil in integrated scanners, and the attenuation of movable elements, such as local coils, positioning aids, and medical probes.

It stands to reason that the attenuation of elements within the field of view of the PET scanner should be minimized in all cases. This said, the presence of fixed MR hardware directly in front of the PET detector ring is considerably less disruptive than that of removable elements. In general, the attenuation introduced by fixed hardware can be accounted for in the normalization factors computed during the scanner's daily calibration. And, the closer a structure is to the PET detectors, the smaller the (transaxial) errors introduced by scattered gammas. Notice that, on the other hand, scattering near the detectors can introduce a significant amount of axial blurring that is not considered in standard scatter correction algorithms.

The attenuation due to moving structures is a more delicate issue [12, 34, 64]. Models of this attenuation can be obtained by measurement or computer design and stored in the system. There is, however, an intrinsic relation between the resolution that can be used for this model and the accuracy with which the position of the coils in the field of view can be estimated. The sharper the edges in an attenuation model, the stronger the artifacts due to an incorrect positioning will be.

The design of all hardware elements that will be present in the PET field of view should be reconsidered, minimizing the presence of dense structures. As a general rule, large flat surfaces of moderately attenuating materials (often found in the casing) lead to more visible image artifacts than small, highly attenuating elements (such as certain electronic components). This is due to two factors: On the one hand, count losses are dependent on the attenuation properties of a given structure times the length of the line-of-response segment intersecting it. In other words, lines of response aligned with flat sections of a coil casing will experience greater losses than lines of response intersecting an inductor or a piece of copper cabling. On the other hand, the losses experienced by a source in a given location are the sum of the losses experienced by all the lines of response intersecting that location. Thus, small high-attenuation elements will lead to localized artifacts, whereas less attenuating structures subtending a large solid angle will cause quantitative errors in wide areas of the image. Furthermore, in clinical practice, PET images are inspected by parsing one or more Cartesian planes. In this representation, artifacts due to flat surfaces aligned with one of the scanner's axes are far more obvious than those due to localized high-attenuation elements.

In general, hardware elements with rounded contours should be preferred, avoiding sharp edges and large surfaces aligned with the transaxial plane. Replacing glass-reinforced plastic casing with lower attenuation materials, like aramid fiber compounds,

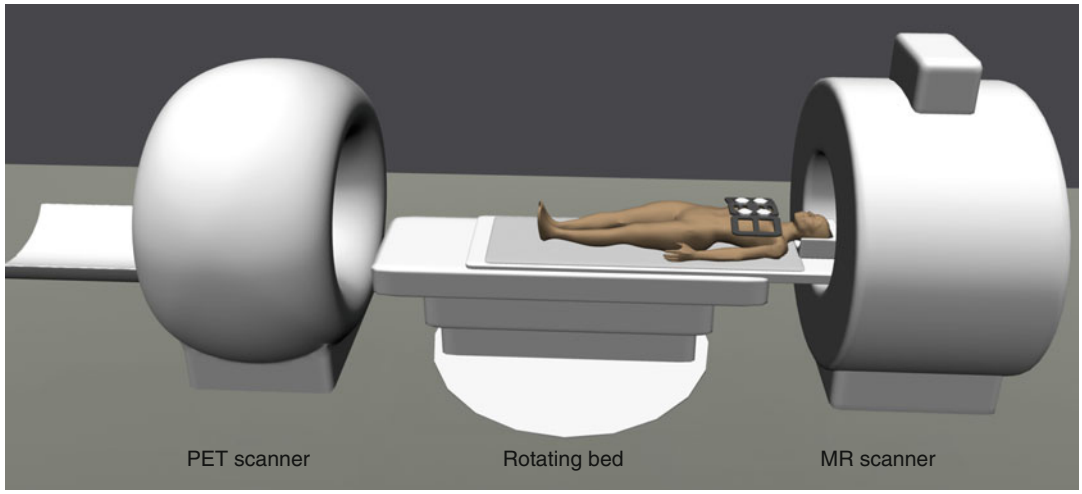

Fig. 1.1 Example of sequential system architecture

can contribute to alleviate the problem. Notice however that the choice of construction materials is restricted by the rigidity constraints required to prevent vibration during the MR acquisition.

1.4 PET/MR System Designs

The vast majority of PET/MR systems published to this date can be classified as belonging to one of three categories: *Sequential* systems combine both modalities in the same manner as PET/CT systems do, placing them in a tandem configuration, often physically separated. A second approach relies on a removable PET *insert* which is placed within the bore of the MR scanner. Finally, i*ntegrated* systems include the PET detectors inside the MR scanner.

In the following sections, we discuss the main advantages and drawbacks of each architecture.

1.4.1 Sequential Architecture

The most straightforward way to create a combined PET/MR scanner is to adapt existing PET and MR machines to work in a tandem configuration. This is the design used in clinical PET/CT scanners. In this approach, the patient is placed on a mechanical bed that slides in sequence through both scanners (Fig. 1.1). After reconstruction, the sensor-coded bed position information is used to perform the registration and fusion of the acquired data. An advantage of this configuration is that it minimizes the adjustments in the individual components required to create the hybrid scanner.

The PET scanner either can be located in a separate space [75] or can be inside the radiofrequency cage of the MR. An example of the former option is General Electric's Discovery PET/CT+MR combo. The latter option has been adopted by Philips in their Ingenuity TF system [73].

In the case of placing both scanners in the MR cage, mutual interference and the presence of the static field have to be accounted for, either using magnetic-field-insensitive photodetectors or providing adequate separation and shielding of the photomultipliers. In the particular case of the Ingenuity TF, the centers of the scanners are 4.2 m apart, the PET detector ring is surrounded by a laminated steel shield, and each photomultiplier is inserted in a mu-metal case. As a side note, increased physical separation has been advertised as a way to improve patient comfort and reduce claustrophobia.

From the software point of view, this approach requires minimal modifications of the existing packages, needing little more than the introduction of a tool to define the scan sequence, manage the bed displacement, and display the fused results.

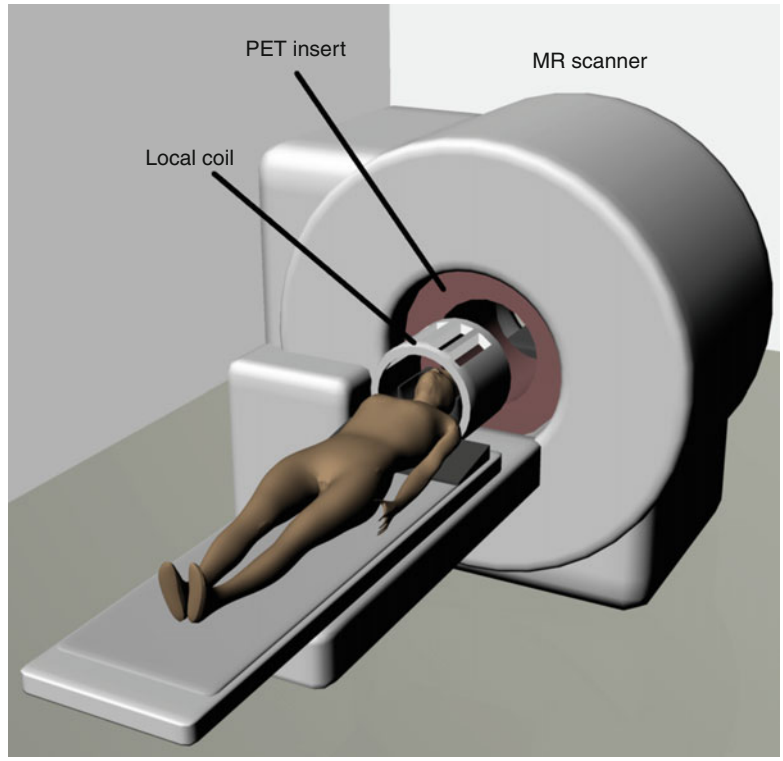

Fig. 1.2 Example of insert system architecture

A feature that can have a significant impact is whether the PET subsystem is also capable of acquiring CT data. This is of particular importance for the creation of attenuation maps, as MR-based attenuation correction is one of the major ongoing issues in hybrid imaging.

On the downside, the inability to perform real simultaneous acquisition of both modalities is the main limitation of this architecture. Both PET and MR being usually long exams, adding up the acquisition times is a major disadvantage for clinical centers. This is less so in systems where the PET scanner is outside the radiofrequency cage, in which case two patients could, in theory, be scanned at the same time. Furthermore, registration errors due to physiologic activity and patient motion during the scan transition can be extremely challenging to correct.

Last but not least, tandem system configurations come at a cost in room size, which might be a limitation for centers planning to update existing equipment.

1.4.2 Insert Architecture

Insert architecture was the approach used in the first research attempts to improve PET spatial resolution by exploiting the potential reduction of positron range inside a magnetic field. The idea is to build a removable insert containing a PET detector ring capable of working within the bore of a conventional MR scanner (Fig. 1.2).

The main technical challenge of this approach is the introduction of electronic circuits in the scanner bore, where the static field is most intense. The devices used for the scintillation light readout and signal amplification must therefore be either insensitive to the magnetic field or placed in a shielded enclosure outside the fringe field region.

Furthermore, the magnetic susceptibility of all elements placed in the scanner bore must be such that the disturbance to the magnetic field is minimized. Passive shimming structures might be necessary to ensure MR image quality.

Finally, electronic components in the insert must be shielded to prevent electromagnetic interference.

This is particularly important in insert architectures because the PET detectors are in the field of view of the MR transmit coils. It is common to avoid this problem by designing custom transmit/receive coils to be fitted inside the PET insert.

A limitation of this architecture is the narrowing of the scanner bore due to the presence of the insert, restricting these systems to small animal studies and either neurological or limb explorations on humans.

The same size restrictions have consequences in the performance of the PET system: Limiting the radial extent of the insert means limiting the length of the scintillator crystals and thus the detector sensitivity; narrowing the detector ring leads to an increase of sensitivity but also of scatter fraction; heat management is complicated due to the compact design.

Despite the mentioned technical challenges, insert systems allow the simultaneous acquisition of both modalities, a feature that constitutes their main advantage with respect to sequential architectures. This leads to a reduction of the total acquisition time (estimated in the order of 40 %), ensures an excellent spatial and temporal coregistration of the data, and opens the way to a range of novel applications, such as simultaneous fMRI/PET, dual-tracer studies, and MR-based motion and partial volume correction.

The possibility of simultaneous scanning, low cost, and modular nature has made this architecture the first choice for research groups (with access to an MR scanner) that want to investigate PET/MR. Several working prototypes for animal studies can be found in the literature:

The first MR-compatible PET detector [57, 58] was based on the use of 4 m long optical fibers guiding the light from the scintillator crystals to position-sensitive PMTs situated where the magnetic field dropped below 10 mT. Based on this technology, the first simultaneous PET/MR phantom images were obtained using a 38 mm diameter LSO ring within a 0.2 T scanner [57, 58]. Artifact-free simultaneous PET and MRI could be demonstrated with a similar prototype and various MR scanning protocols [59]. The acquisition of simultaneous PET and MR imaging as well as MR spectroscopy for small animals was first reported in Carson et al. [4] using optical fibers to couple the scintillators to an external detection module (Fig. 1.3a). A similar system with two opposed detector heads instead of a full detector ring was also presented in Raylman et al. [49].

Avalanche photodiodes have been used instead of PMTs to avoid having to guide the scintillation light outside the magnetic field:

A nonmagnetic version of the APD-based RatCAP tomograph was described in Schlyer et al. [56] (Fig. 1.3b). The main characteristic of this design is the fact that the PET detector ring is mounted on the animal head and not to the MR scanner. The same technology has been recently adapted to create a hybrid breast scanner [48].

Also based on APD technology, a collaboration between the University of California Davis and the University of Tubingen developed two different insert prototypes fully contained in the MR bore, one relying on short optical fiber bundles [5] (Fig. 1.3c) and the other on direct coupling to the scintillators [27] (Fig. 1.3d).

An APD-based system for clinical neurology applications, the Siemens prototype BrainPET insert, was demonstrated in the Society of Nuclear Medicine's 2007 annual meeting [54], proving the feasibility of performing hybrid imaging in humans [55].

Such a system would offer clinical centers already equipped with an MR scanner a cost-effective access to PET/MR without major modifications of the existing facilities, other than the unavoidable certification to work with radioactive materials in the MR room. Certainly, the possibility of removing the insert to perform conventional MR acquisitions provides great flexibility to centers which cannot afford a dedicated PET/MR system. One can imagine, however, that it would take a very careful restructuration of the clinical workflow to make such a setup cost-effective, something that would no doubt limit the commercial penetration of the system.

1.4.3 Integrated Architecture

Although the above-mentioned architectures may offer some advantages, there is a strong interest in an approach enabling full-body scanning while

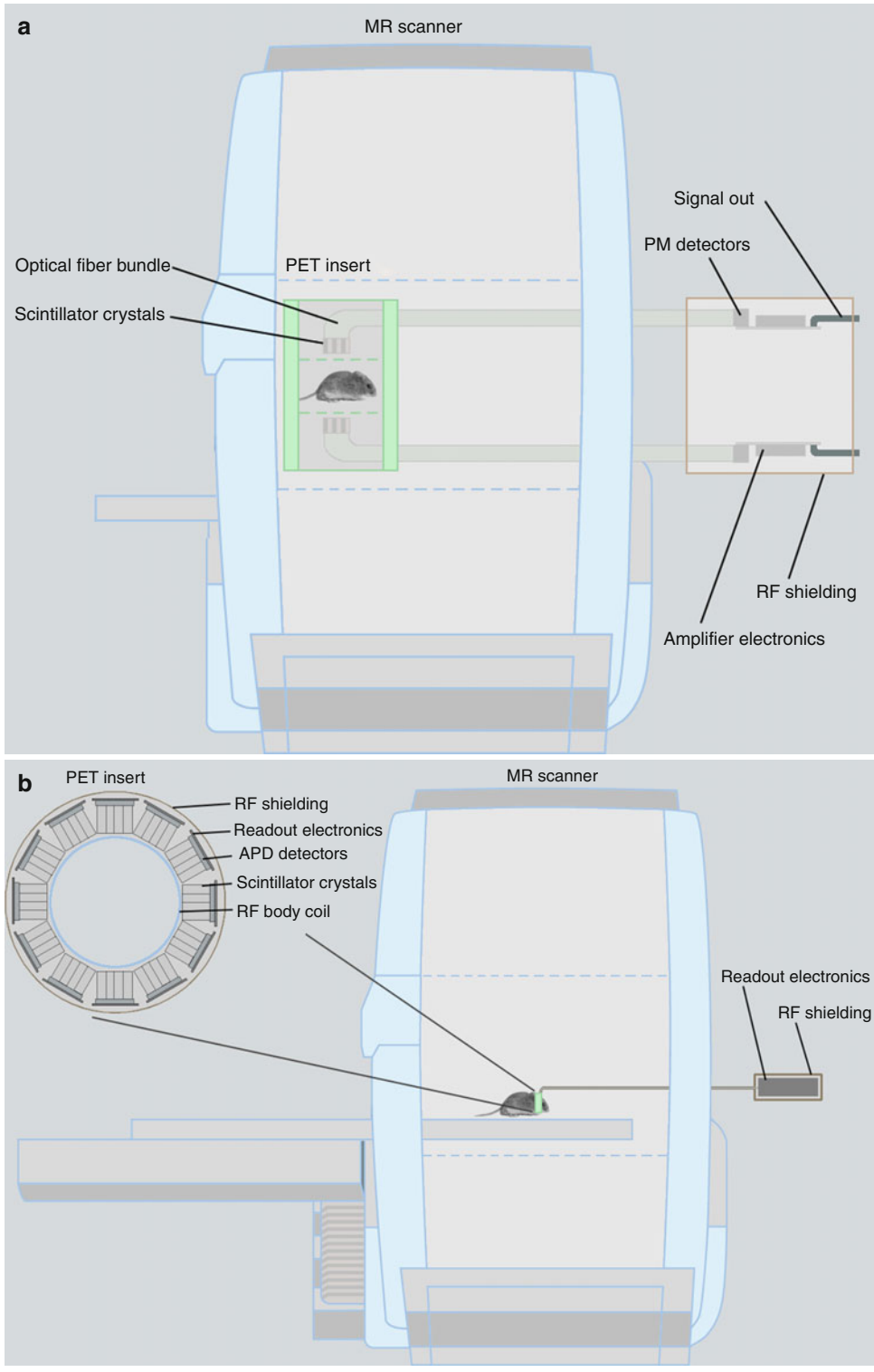

Fig. 1.3 Insert system architectures for small animal imaging. (**a**) Based on photomultiplier detectors linked by optic fibers to the scintillator array. (**b**) Based on a non-magnetic version of the RatCAP tomograph. (**c**) Based on avalanche photodiode detectors linked by optical fibers to the scintillator array. (**d**) Based on avalanche photodiode detectors directly coupled to the scintillator array

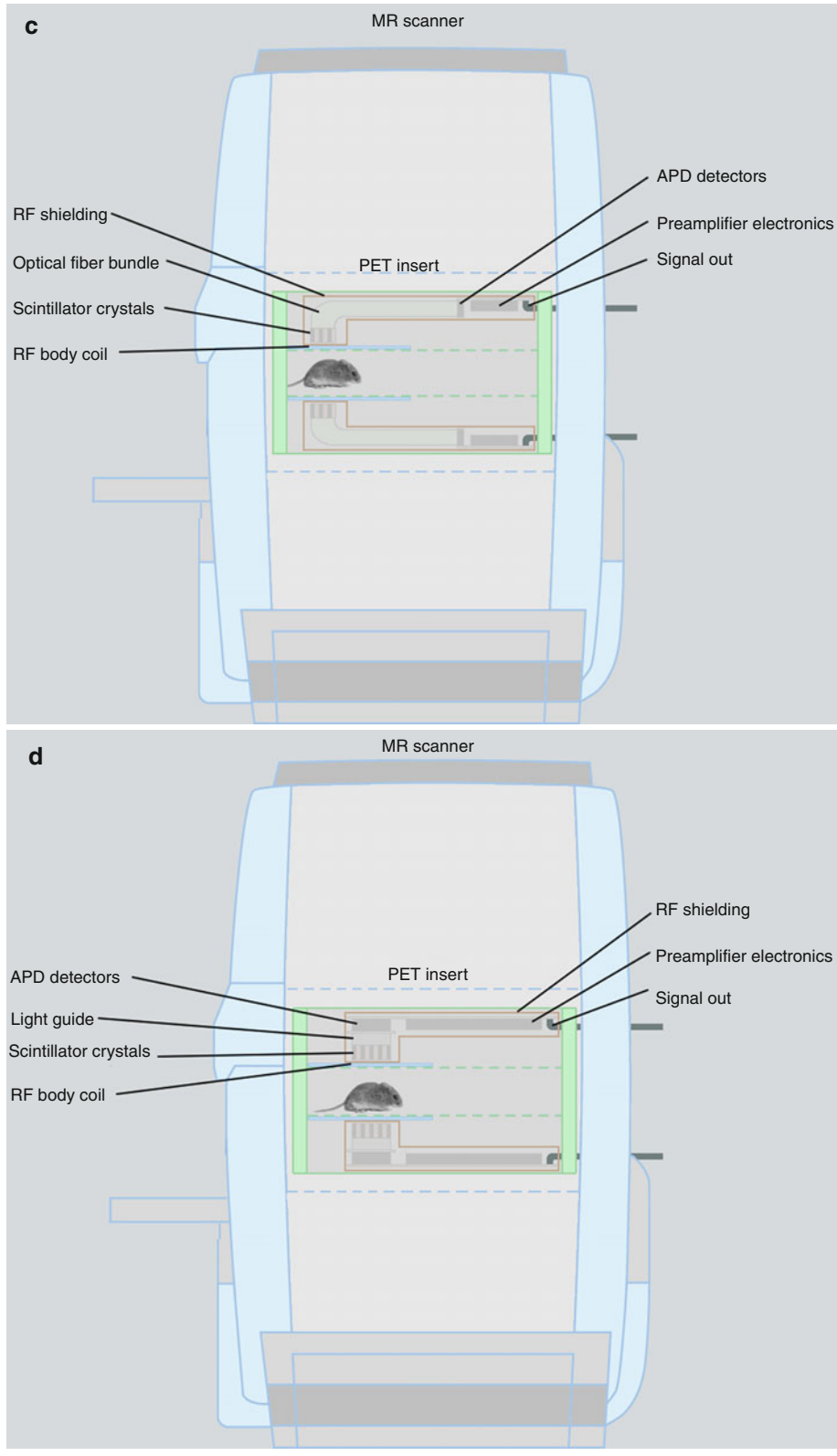

Fig. 1.3 (continued)

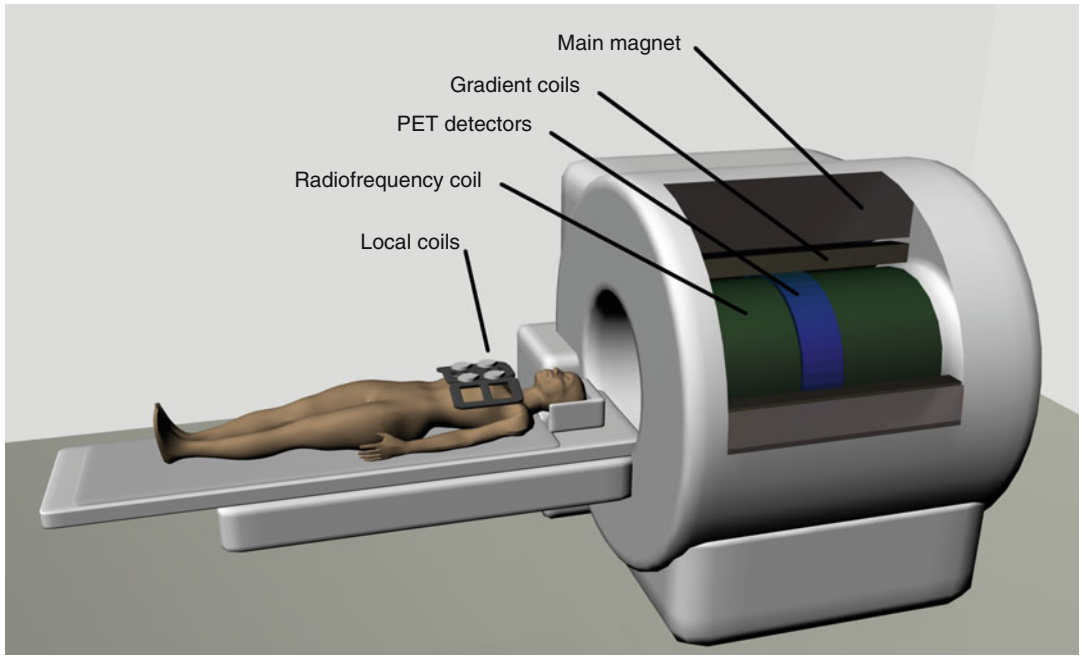

Fig. 1.4 Example of integrated system architecture

retaining the possibility of simultaneous acquisition. The way to achieve this is the complete integration of the PET detector and electronics within the MR scanner (Fig. 1.4).

From a technical point of view, this is the most challenging approach, requiring significant changes to both subsystems. However, the inherent potential for new diagnostic and research applications is an undeniable advantage of this architecture.

The integrated designs published so far rely either on the use of a split superconducting magnet, on the use of field-cycled MR, or on the insertion of the PET detector ring behind the radiofrequency coil of the MR scanner.

In the first case, the MR superconducting coil is built in two separate elements, leaving between them an axial space of several centimeters in which a PET scintillator ring can be accommodated. The scintillation light is guided by radially distributed fiber optic bundles to PMTs situated outside the 1 mT fringe field. Such a system was tested for preclinical imaging at the neuroscience department of the University of Cambridge [32]. This design requires a low-field magnet (~1 T) and specialized gradient set, which likely restricts this approach to small animal imaging.

In the case of field-cycled acquisition, two separate and dynamically controllable magnets are used for polarization and readout. This enables interleaving in the acquisition of MR data certain temporal frames free of magnetic field, in which the PET acquisition can take place. This design, like the previous one, is for the moment restricted to preclinical imaging [24].

In the last case, both the scintillator crystals and the associated photodetectors are located behind the radiofrequency coil of the MR scanner. This can be achieved either by reducing the radius of the radiofrequency coil to provide space for the PET detector [47] or by using a split gradient coil [42]. The former is the approach adopted in the Siemens Biograph mMR, currently the only commercially available integrated clinical PET/MR system. The latter is the approach announced by Philips for their integrated system, presently still being developed under the EU SUBLIMA project (Sub nanosecond Leverage in PET/MR Imaging, 01.09.2010–31.08.2014, http://www.sublima-pet-mr.eu/). Another relevant difference

between these systems is that the mMR uses APD technology, whereas Philips is aiming at time-of-flight capability by using SiPM detectors.

Fitting the detector ring between the radiofrequency and gradient coils entails problems similar to those of insert architectures: The smaller ring diameter compared to standard geometries results in better sensitivity but increases random and scattered count rates [37]. However, these effects can be made to cancel each other, to a certain extent, by reducing the energy acceptance window of the detectors [11].

Using a split gradient coil would considerably simplify some of the previous issues while allowing for a larger portion of the processing electronics to be directly coupled to the detectors, making the output signals more robust to interference. Of course, this might come at a yet undetermined cost in gradient field performance, e.g., due to the misalignments introduced over time by the system vibrations on the gradient sub-coils.

In both cases, integrating the PET detectors behind the radiofrequency coil has the advantage of reducing the interference due to the MR excitation pulses. On the other hand, the environment temperature in that space is higher than ambient and can undergo fluctuations of tens of degrees. Also, the scatter and attenuation due to the radiofrequency coil and any other hardware in the field of view of the PET will have to be accounted for.

1.5 Discussion

The technological challenges of building combined PET/MR scanners are manifold, but the performance results of the Ingenuity TF Zaidi et al. [73] and the mMR [11] prove the suitability of these systems for clinical applications.

While sequential scanning in a tandem design resembles the current PET/CT practice, it results in potentially long scan times and doesn't allow simultaneous acquisition. With the three major manufacturers being involved in the development of integrated whole-body systems, it seems that this architecture is going to be the main focus of research for the upcoming years.

Indeed, the possibilities of using MR data to perform motion correction of the PET scan and of monitoring dynamic processes are likely to lead to valuable new applications once combined scanners are widely spread. The study of tumors with dual-labeled contrast agents [31] or simultaneous PET and fMRI monitoring of brain activity would be just two examples of what might come.

To conclude, we can expect technical advancements in the near future to further trigger the development of correction algorithms on both the PET side, for attenuation and scatter compensation and for truncation recovery, and MR, shimming and eddy current compensation. New detector technology will lead to hybrid systems with time-of-flight and depth-of-interaction capabilities. Light sensors which require less sophisticated and less sensitive electronics, in combination with matching scintillation crystals, may offer new opportunities. On the clinical side, extensive work will be necessary to define new protocols, optimized for hybrid scanning. Also, the need to provide diagnostic images for all regions (e.g., lungs and bones) will drive the development of new MR sequences.

Ultimately, only the use in preclinical and clinical settings will prove which design will be advantageous for which application.

Acknowledgments This work was supported by a research grant from Siemens AG to the Klinikum rechts der Isar der Technischen Universität München. The PET/MR system used for this study was funded through the Deutsche Forschungsgemeinschaft (DFG) Grossgeräteinitiative 2010.

References

1. Albuquerque E, Almeida FG, Almeida P, et al. An overview of the clear-PEM breast imaging scanner. IEEE Nuclear Science Symposium Conference Record, 2008; p. 5616–8. doi:10.1109/NSSMIC.2008.4774518.
2. Beyer T, Townsend DW, Brun T, et al. A combined PET/CT scanner for clinical oncology. J Nucl Med. 2000;41(8):1369–79.
3. Camacho CR, Plewes DB, Henkelman RM. Nonsusceptibility artifacts due to metallic objects in MR imaging. J Magn Reson Imaging. 1995;5(1):75–88.
4. Carson R, Herscovitch P, Daube-Witherspoon M, editors. Quantitative functional brain imaging with

positron emission tomography. Waltham, MA: Academic Press; 1998.
5. Catana C, Wu Y, Judenhofer MS, et al. Simultaneous acquisition of multislice PET and MR images: initial results with a MR-compatible PET scanner. J Nucl Med. 2006;47(12):1968–76.
6. Christensen NL, Hammer BE, Heil BG, et al. Positron emission tomography within a magnetic field using photomultiplier tubes and lightguides. Phys Med Biol. 1995;40(4):691–7.
7. Chung D. Materials for electromagnetic interference shielding. J Mater Eng Perform. 2000;9(3):350–4.
8. Conradi J. Temperature effects in silicon avalanche diodes. Solid State Electron. 1974;17(1):99–106.
9. Cumalat JP, Cheung HWK, Hassed J, et al. Effects of magnetic fields on the light yield of scintillators. Nucl Instrum Methods Phys Res A. 1990;293(3):606–14.
10. Del Guerra A, Belcari N, Giuseppina Bisogni M, et al. Advantages and pitfalls of the silicon photomultiplier (SiPM) as photodetector for the next generation of PET scanners. Nucl Instrum Methods Phys Res A. 2010;617(1–3):223–6.
11. Delso G, Fürst S, Jakoby B, et al. Performance measurements of the Siemens mMR integrated whole-body PET/MR scanner. J Nucl Med. 2011; 52(12):1914–22.
12. Delso G, Martinez-Moller A, Bundschuh RA, et al. Evaluation of the attenuation properties of MR equipment for its use in a whole-body PET/MR scanner. Phys Med Biol. 2010;55(15):4361–74.
13. De Meester GD, Morich MA, McMahon KC et al. . Magnetic shielding for a PET detector system. U. P. Application. Eindhoven: US, Koninklijke Philips Electronics N.V.; 2009. 20090195249.
14. Dempsey MF, Condon B. Thermal injuries associated with MRI. Clin Radiol. 2001;56(6):457–65.
15. European Commission. Referral guidelines for imaging, Radiation protection, vol. 118. Luxembourg: European Commission; 2001.
16. España S, Fraile LM, Herraiz JL, et al. Performance evaluation of SiPM photodetectors for PET imaging in the presence of magnetic fields. Nucl Instrum Methods Phys Res A. 2010;613(2):308–16.
17. Fahy S, Kittel C, Louie SG. Electromagnetic screening by metals, AAPT. Am J Phys. 1988;56:989. doi:10.1119/1.15353
18. Frach T, Prescher G, Degenhardt C, et al. The digital silicon photomultiplier – Principle of operation and intrinsic detector performance. In: IEEE nuclear science symposium conference record, Orlando, USA. 2009.
19. Gallichan D, Scholz J, Bartsch A, et al. Addressing a systematic vibration artifact in diffusion-weighted MRI. Hum Brain Mapp. 2010;31(2):193–202.
20. Golovin V, Saveliev V. Novel type of avalanche photodetector with Geiger mode operation. Nucl Instrum Methods Phys Res A. 2004;518(1–2):560–4.
21. Grazioso R, Zhanga N, Corbeila J, et al. APD-based PET detector for simultaneous PET/MR imaging. Nucl Instrum Methods Phys Res A. 2006;569(2): |301–5.
22. Hamamatsu. Photomultiplier tubes – Basics and applications. Hamamatsu, Shizuoka, Japan: Hamamatsu photonics K.K. Electron Tube Division; 2006.
23. Hammer BE, Christensen NL, Heil BG. Use of a magnetic field to increase the spatial resolution of positron emission tomography. Med Phys. 1994; 21(12):1917–20.
24. Handler W, Chronik B, Scholl T, et al. Combining field-cycled magnetic resonance imaging with positron emission tomography. J Nucl Med Meet Abstr. 2007;48:89.
25. Hasegawa T, Michei C, Kawashima K, et al. A study of external end-shields for PET. IEEE Trans Nucl Sci. 2000;47(3):1099–103.
26. Jihoon K, Yong C, Key Jo H, et al. Characterization of cross-compatibility of small animal. insertable PET and MRI. IEEE Nuclear Science Symposium Conference Record (NSS/MIC). 2009; p. 3816–21. doi:10.1109/NSSMIC.2009.5401902
27. Judenhofer MS, Wehrl HF, Newport DF, et al. Simultaneous PET-MRI: a new approach for functional and morphological imaging. Nat Med. 2008; 14(4):459–65.
28. Junnarkar SS, Fried J, O'Connor P, et al. MRI compatible G-link and PCI based data acquisition hardware for the RatCAP scanner. In: IEEE nuclear science symposium conference record, San Diego, USA. 2006; p. 380–3.
29. Kang J, Choi Y, Hong KJ, et al. A feasibility study of photosensor charge signal transmission to preamplifier using long cable for development of hybrid PET-MRI, AAPM. Med Phys. 2010;37(11):5655–64.
30. Klose U. In vivo proton spectroscopy in presence of eddy currents. Magn Reson Med. 1990;14(1): 26–30.
31. Lee H-Y, Li Z, Chen K, et al. PET/MRI dual-modality tumor imaging using arginine-glycine-aspartic (RGD)–conjugated radiolabeled iron oxide nanoparticles. J Nucl Med. 2008;49(8):1371–9.
32. Lucas AJ, Hawkes RC, Ansorge RE, et al. Development of a combined microPET-MR system. Technol Cancer Res Treat. 2006;5(4):337–41.
33. Lüdeke KM, Röschmann P, Tischler R. Susceptibility artefacts in NMR imaging. Magn Reson Imaging. 1985;3(4):329–43.
34. MacDonald LR, Kohlmyer S, Liu C, et al. Effects of MR surface coils on PET quantification. Med Phys. 2011;38(6):2948–56.
35. Mackewn JE, Strul D, Hallett WA, et al. Design and development of an MR-compatible PET scanner for imaging small animals. IEEE Trans Nucl Sci. 2005;52(5):1376–80.
36. Marsden PK, Strul D, Keevil SF, et al. Simultaneous PET and NMR. Br J Radiol. 2002;75:S53–9.
37. Martinez MJ, Torres I, Ladebeck R, et al. Whole-body MR-PET: characterization of PET performance by Monte Carlo simulations. J Nucl Med. 2007; 48 Suppl 2:46P.
38. Melcher CL. Scintillation crystals for PET. J Nucl Med. 2000;41(6):1051–5.

39. Nyenhuis JA, Sung-Min P, Kamondetdacha R, et al. MRI and implanted medical devices: basic interactions with an emphasis on heating. IEEE Trans Device Mater Reliability. 2005;5(3):467–80.
40. Olcott PD, Peng H, Levin CS. Novel electro-optical coupling technique for magnetic resonance-compatible positron emission tomography detectors. Mol Imaging. 2009;8(2):74–86.
41. Otte AN, Barral J, Dolgoshein B, et al. A test of silicon photomultipliers as readout for PET. Nucl Instrum Methods Phys Res A. 2005;545:705–15.
42. Overweg JA, Schulz V, Solf T, et al. Split gradient coil and PET/MTI hybrid system using the same. U. P. T. Office. Eindhoven, NL: Koninklijke Philips Electronics N.V. 2010.
43. Peng BJ, et al. Studies of the interactions of an MRI system with the shielding in a combined PET/MRI scanner. Phys Med Biol. 2010;55(1):265.
44. Pichler B, Lorenz E, Mirzoyan R, et al. Performance test of a LSO-APD PET module in a 9.4 Tesla magnet. In: IEEE nuclear science symposium conference record, Albuquerque, USA. 1997.
45. Pichler BJ, Judenhofer MS, Catana C, et al. Performance test of an LSO-APD detector in a 7-T MRI scanner for simultaneous PET/MRI. J Nucl Med. 2006;47(4):639–47.
46. Pichler BJ, Swann BK, Rochelle J, et al. Lutetium oxyorthosilicate block detector readout by avalanche photodiode arrays for high resolution animal PET. Phys Med Biol. 2004;49(18):4305–19.
47. Quick HH, Ladebeck R, Georgi J-C. Whole-body MR/PET hybrid imaging: technical considerations, clinical workflow and initial results. Magnetom Flash. 2011;46(1):88–100.
48. Ravindranath B, Maramraju SH, Junnarkar SS, et al. A simultaneous PET/MRI breast scanner based on the RatCAP. In: IEEE nuclear science symposium conference record, Dresden, DE. 2008.
49. Raylman RR, Majewski S, Lemieux SK, et al. Simultaneous MRI and PET imaging of a rat brain. Phys Med Biol. 2006;51(24):6371–9.
50. Raylman RR, Majewski S, Velan SS, et al. Simultaneous acquisition of magnetic resonance spectroscopy (MRS) data and positron emission tomography (PET) images with a prototype MR-compatible, small animal PET imager. J Magn Reson. 2007;186(2):305–10.
51. Reese TG, Heid O, Weisskoff RM, et al. Reduction of eddy-current-induced distortion in diffusion MRI using a twice-refocused spin echo. Magn Reson Med. 2003;49(1):177–82.
52. Roozen NB, Koevoets AH, den Hamer AJ. Active vibration control of gradient coils to reduce acoustic noise of MRI systems. IEEE/ASME Trans Mechatron. 2008;13(3):325–34.
53. Schenck JF. The role of magnetic susceptibility in magnetic resonance imaging: MRI magnetic compatibility of the first and second kinds, AAPM. Med Phys. 1996;23(6):815–50.
54. Schlemmer H-P, Pichler B, Wienhard K, Schmand M, Nahmias C, Townsend D, Heiss W-D, Claussen C. Simultaneous MR/PET for brain imaging: first patient scans. J Nucl Med Meet Abstr. 2007;48 Suppl 2:45P.
55. Schlemmer H-PW, Pichler BJ, Schmand M, et al. Simultaneous MR/PET imaging of the human brain: feasibility study. Radiology. 2008;248(3):1028–35.
56. Schlyer D, Vaska P, Tomasi D, et al. A simultaneous PET/MRI scanner based on RatCAP in small animals. In: IEEE nuclear science symposium conference record, Hawaii, USA. 2007.
57. Shao Y, Cherry SR, Farahani K, et al. Simultaneous PET and MR imaging. Phys Med Biol. 1997;42(10):1965–70.
58. Shao Y, Cherry SR, Farahani K, et al. Development of a PET detector system compatible with MRI/NMR systems. IEEE Trans Nucl Sci. 1997;44(3):1167–71.
59. Slates RB, Farahani K, Shao Y, et al. A study of artefacts in simultaneous PET and MR imaging using a prototype MR compatible PET scanner. Phys Med Biol. 1999;44(8):2015–27.
60. Spanoudaki VC, Mann AB, Otte AN, et al. Use of single photon counting detector arrays in combined PET/MR: Characterization of LYSO-SiPM detector modules and comparison with a LSO-APD detector. J Instrum. 2007;2:P12002.
61. Spanoudaki VC, McElroy DP, Torres-Espallardo I, et al. Effect of temperature on the performance of proportional APD-based modules for gamma ray detection in positron emission tomography. IEEE Trans Nucl Sci. 2008;55(1):469–80.
62. Spinks TJ, Miller MP, Bailey DL, et al. The effect of activity outside the direct field of view in a 3D-only whole-body positron tomograph. Phys Med Biol. 1998;43(4):895.
63. Strul D, Cash D, Keevil SF, et al. Gamma shielding materials for MR-compatible PET. IEEE Trans Nucl Sci. 2003;50(1):60–9.
64. Tellmann L, Quick HH, Bockisch A, et al. The effect of MR surface coils on PET quantification in whole-body PET/MR: results from a pseudo-PET/MR phantom study. Med Phys. 2011;38(5):2795–805.
65. Thompson CJ, Paus T, Clancy R. Magnetic shielding requirements for PET detectors during transcranial magnetic stimulation. IEEE Trans Nucl Sci. 1998;45(3):1303–7.
66. Tomasi D, Ernst T. A simple theory for vibration of MRI gradient coils. Braz J Phys. 2006;36:34–9.
67. Truhn D, Kiessling F, Schulz V. Optimized RF shielding techniques for simultaneous PET/MR. Med Phys. 2011;38(7):3995–4000.
68. Woody C, Schlyer D, Vaska P, et al. Preliminary studies of a simultaneous PET/MRI scanner based on the RatCAP small animal tomograph. Nucl Instrum Methods Phys Res A. 2007;571(1):102–5.
69. Wu Y, Catana C, Farrell R, et al. PET performance evaluation of an MR-compatible PET insert. IEEE Trans Nucl Sci. 2009;56(3):574–80.
70. Yamamoto S, Aoki M, Sugiyama E, et al. A flexible optical fiber based LGSO DOI block detector for a

high resolution integrated PET/MRI system: iPET/MRI-II. J Nucl Med Meet Abstr. 2010;51 Suppl 2:1402.
71. Yamamoto S, Kuroda K, Senda M. Scintillator selection for MR-compatible gamma detectors. IEEE Trans Nucl Sci. 2003;50(5):1683–5.
72. Yamamoto S, Satomi J, Watabe T, et al. A temperature-dependent gain control system for improving the stability of Si-PM-based PET systems. Phys Med Biol. 2011;56(9):2873.
73. Zaidi H, et al. Design and performance evaluation of a whole-body Ingenuity TF PET–MRI system. Phys Med Biol. 2011;56(10):3091.
74. Zaidi H, Mawlawi O, Orton CG. Point/counterpoint. Simultaneous PET/MR will replace PET/CT as the molecular multimodality imaging platform of choice. Med Phys. 2007;34(5):1525–8.
75. Zang-Hee Cho, Son Y-D, Hang-Keun Kim, Kyoung-Nam Kim, Se-Hong Oh, Jae-Yong Han, In-Ki Hong, Young-Bo Kim. A hybrid PET-MRI: an integrated molecular-genetic imaging system with HRRT-PET and 7.0-T MRI. Int J Imaging Syst Technol. 2007;17(4):252–65.

Image Distortions in Clinical PET/MR Imaging

2

S.H. Keller, A.E. Hansen, S. Holm, and T. Beyer

Contents

Abstract

Whole-body PET/MR imaging has the potential to supplement or even replace combined PET/CT imaging in selected clinical indications. In view of the lack of separate standard transmission sources in combined PET/MR imaging systems, attenuation correction (AC) of the PET data is performed using the available MR images. Given the novelty of MR-based AC (MR-AC), related image distortions and subsequent methodological pitfalls need to be recognized. Here, we review the most common artifacts observed in routine PET/MR imaging following MR-AC in either sequential or fully integrated system designs.

2.1 Introduction

State-of-the-art imaging is essential for efficient and cost-effective patient management. Recently, imaging was termed "the GPS of medicine" (H Hricak, RSNA 2010). With this analogy in mind, imaging-based diagnosis can be supported effectively only in the absence of any roadblocks, that is, image artifacts.

Today, most imaging techniques employed in early patient management are noninvasive by nature. These imaging modalities include traditional planar and tomographic imaging, such as X-ray and computed tomography (CT), respectively. Both provide anatomical image information of high spatial resolution that is essential for localizing disease and structural interpretation. Most

S.H. Keller • A.E. Hansen • S. Holm
Department of Clinical Physiology, Nuclear Medicine and PET, Rigshospitalet, Copenhagen, Denmark

T. Beyer, PhD (✉)
Medical University Vienna, Center for Medical Physics and Biomedical Engineering, General Hospital Vienna, 4L Waehringer Guertel 18-20, A-1090 Vienna, Austria
e-mail: thomas.beyer@meduniwien.ac.at

I. Carrio, P. Ros (eds.), *PET/MRI*,
DOI 10.1007/978-3-642-40692-8_2,

severe diseases, such as cancer, however, may not lead to changes of the anatomy but present early in the course of a disease through abnormal alterations of metabolic and signaling pathways. These changes can be visualized by nuclear medicine imaging techniques, such as single photon emission computed tomography (SPECT) [1] and positron emission tomography (PET) [2]. Nuclear medicine imaging techniques, and PET in particular, further benefit from the intrinsic ability to quantify metabolite concentrations noninvasively [3].

Early attempts of combining anatomical and metabolic image information have led to the development of integrated SPECT/CT and PET/CT systems [4]. A PET/CT prototype system was first introduced in 1998 [5] and followed by the commercial introduction of PET/CT systems in 2001. All PET/CT systems combine a spiral CT with up to 128 simultaneously acquired image planes and a whole-body PET detector system based on a scintillator-photomultiplier tube detector arrangement [6].

Combined PET/CT imaging has been shown to increase the diagnostic accuracy over PET and CT only in many oncology indications by at least 10–15 % [7]. PET/CT imaging has reduced overall imaging times to about a third of that of PET and CT imaging [8], which is partly contributed to the use of the CT images for attenuation correction (AC) of the PET emission data.

CT-based attenuation correction (CT-AC) is performed by separating the tissues into two classes above and below a threshold CT density (Hounsfield unit, HU) [9]. Tissue below the limit is considered a mixture of air and soft tissue, while the tissue above represents a mix of soft tissue and compact bone. A bi-linear function is constructed using the known attenuation coefficients at 511 keV for these three tissue classes (air, soft tissue, bone). This function effectively maps the CT-attenuation values (Hounsfield units at an effective CT energy of 80–90 keV) to the required values for PET (Fig. 2.1). CT-AC is accepted in clinical practice and, in view of almost all PET systems today being combined with CT, also considered gold standard [4].

Recently, a new combination of PET and magnetic resonance imaging (MRI or MR), PET/MRI or PET/MR, was introduced commercially. Today, two companies offer combined whole-body PET/MR systems [10, 11]: in one case, a 3 T MR and a whole-body PET are joint by a rotating patient handling system (Fig. 2.2a) [12], in the other case a whole-body PET system is integrated inside the coil system of a 3 T MR (Fig. 2.2c) [13].

Neither design concept of a combined PET/MR system (Fig. 2.2a, c) entails a CT-type transmission source for reasons of limited space in the combined gantry and crosstalk effects of the CT or other (moveable) transmission source and the magnetic field of the MR components. Therefore, CT-based AC is not an immediate option in PET/MR imaging, and thus, PET attenuation coefficients must be derived from the available MR information [14–16].

In the co-planar (sequential) PET/MR system, PET attenuation coefficients are estimated from T1-weighted MR images (*atMR*) acquired specifically for the purpose of attenuation correction [12, 15]. Using a combination of region-growing techniques and body surface recognition, the MR images are automatically segmented into three classes of voxels: air, lungs, and soft tissue (Fig. 2.2b). The non-attenuation-corrected (NAC) PET data can be used to estimate the contour of the patient as part of a truncation artifact correction [12]. Total acquisition time for *atMR* covering a 120 cm axial field-of-view (FOV) is on the order of 3–4 min. The *atMR* images do not hold the promise of being diagnostically useful, and separate dedicated MR sequences are acquired depending on the clinical indication.

In the fully integrated PET/MR system, MR-AC is performed similarly except that a 4-class segmentation is applied to MR images acquired with a 2-point (in- and opposed-phase) Dixon sequence. The Dixon sequence provides separate images of the water and fat constituents of the imaged patient (Fig. 2.2d). Both image sets are used to automatically delineate air and lungs as well [14]. The acquisition time of the Dixon-Water-Fat segmentation sequence (DWFS) is 19 s per bed position, preferably obtained in one breath-hold for the thorax/abdomen and covering an axial FOV of 120 cm in 2–3 min (attenuation data acquisition time only, PET data is acquired simultaneously). Similar to the 3-class

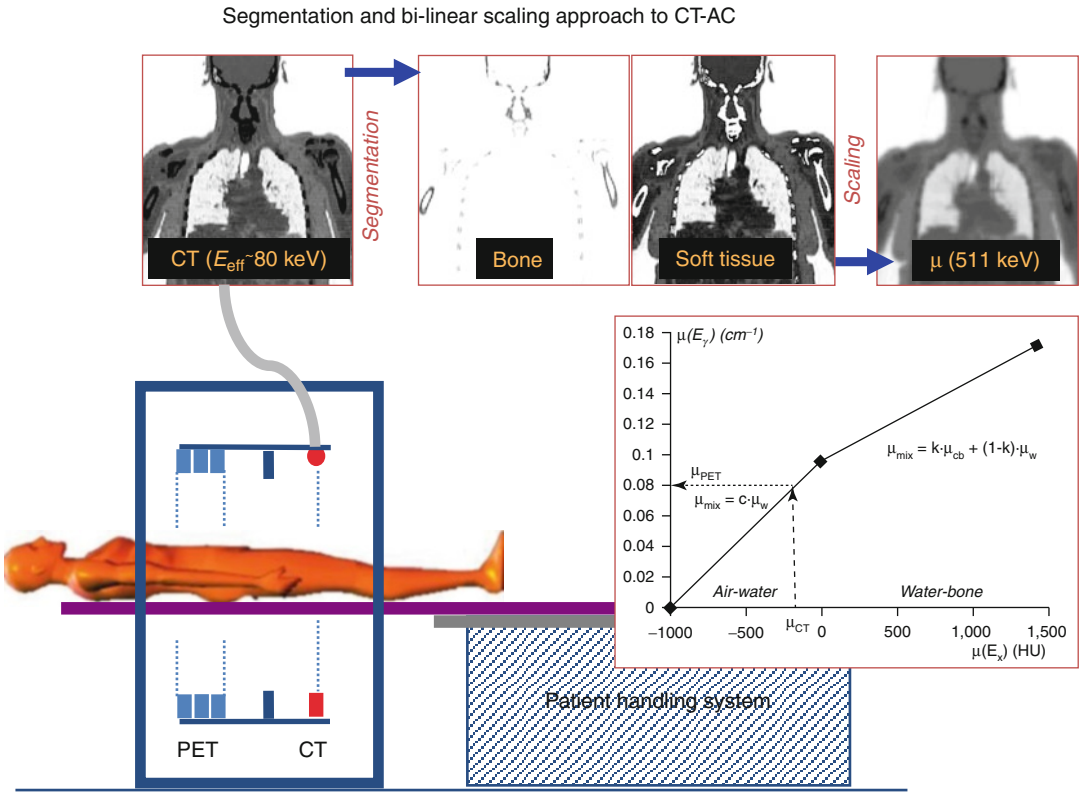

Fig. 2.1 Combined PET/CT imaging and CT-based attenuation correction. Linear attenuation values for PET are obtained by pixel mapping of the CT-values using a bilinear function (inserted plot). The two linear parts correspond to the parts of the image dominated by soft tissue or bone, as illustrated by a segmentation performed at the threshold value

segmentation method above, the DWFS is not intended for diagnostic purposes even though some users argue that the quality is sufficient to localize PET-positive lesions similar to using a low-dose CT in PET/CT [17]. However, this argument should be considered with caution as numerous studies have shown the clinical value of higher-quality CT in the context of whole-body PET/CT. Similar benefits can be expected from high-quality MR images in the context of combined PET/MRI.

Rigorous testing during the development and production of combined imaging systems ensures acceptable and reproducible performance. Nonetheless, the resulting images can be prone to distortions, that is to artifacts or a bias, or both [18, 19]. Distortions of hybrid images are not uncommon and may originate from a number of reasons. An artifact clearly noticed by most PET/CT users, for example, in the early days of this technology was the photopenic uptake area above the diaphragm in coronal PET images following CT-AC [9] arising from a mismatch of the anatomical extension of the thorax during the acquisition of the CT and emission data, as a result of the markedly different examination times of the CT and PET scans [20]. Table 2.1 summarizes the most common sources of image distortions in hybrid imaging, including more general causes such as system malfunction and incorrect patient referral and reporting. Naturally, the more complex an imaging system, the more sources of image distortions exist. This is particularly true for combined imaging systems. This chapter reviews the most common artifacts in co-planar (sequential) and fully integrated PET/MR and provides some references to potential corrections and improvements of the image quality.

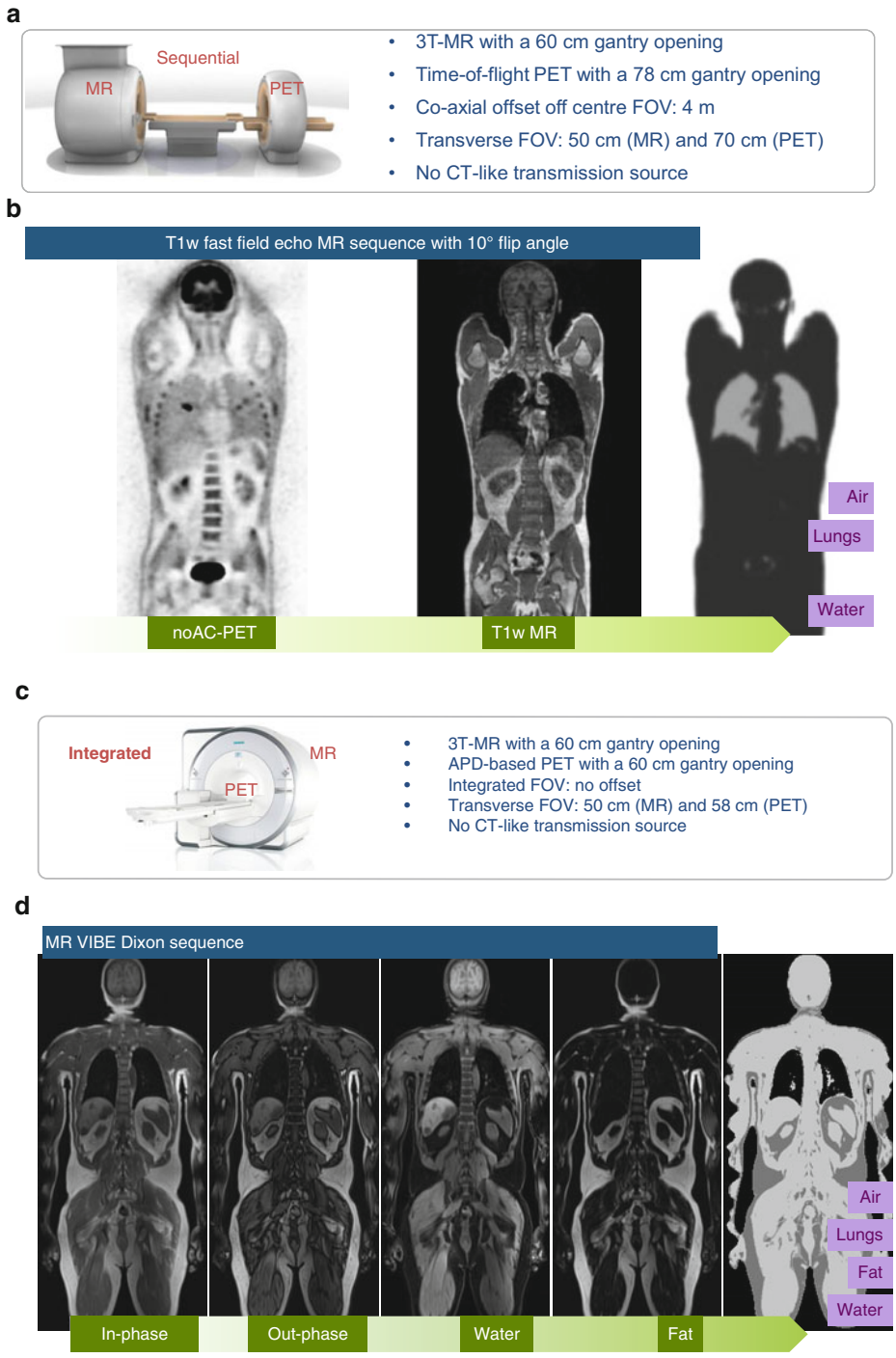

Fig. 2.2 (**a**) Sequential PET/MR system by Philips Healthcare. (**b**) MR-based AC uses 3-class segmentation of T1w-MR images. Additional truncation artifact correction can be performed when also employing the NAC-PET images. (**c**) Fully integrated PET/MR system by Siemens Healthcare. (**d**) MR-AC uses a 4-class segmentation model of Dixon T1w-MR images (With kind contributions to (**a** and **b**) by Antonis Kalemis, PhD and Frank DiLalla, PhD (Philips Healthcare))

Table 2.1 Source of image distortions and image bias in combined PET/CT and PET/MR

Source of artifacts	Observation	Solution
Hardware and design	Limited gantry opening and transverse FOV cause truncation artifacts in large patients	Position patients with arms up (if possible) Apply extended FOV reconstruction where available
Malfunctioning imaging system	Temporary or continuous system hardware and software failure causing noticeable image distortions and/or bias of image	Can be picked up by periodic (daily, weekly, monthly, etc.) quality control tests Trouble shooting and/or call vendor service
Indication and patient referral	Patients may be referred incorrectly or without proper preparation to a specific imaging examination (e.g., non-dieting patient sent for FDG PET or patient with MR contraindication sent for PET/MR)	Need to review local referral strategies Need to adopt and adhere to national imaging guidelines
Motion	PET and CT and PET and MR examination times are markedly different, thus rendering breath-hold hybrid examinations a challenge. Involuntary patient motion may cause noticeable local (or global) misalignment of PET/CT and PET/MR	Optimized patient preparation and instructions Retrospective image alignment and AC reprocessing Consider gating or motion correction using external marker/tracking system
Data processing	CT- and MR-based corrections causing image distortions and bias in AC-PET	Apply retrospective corrections, optimized imaging protocols
Reporting	Reporting doctor may misinterpret the examination, miss artifacts, etc	Ensure sufficient training of staff Increase level of staff experience

2.2 Image Artifacts in PET-Based Hybrid Imaging

Image artifacts, much like image-based diagnosis, are picked up through pattern recognition in the eye of the observer. Therefore, a good understanding of the methodology of a given imaging modality as well as experience with a wider range of applications of this imaging modality will help recognize and interpret artifacts more easily. Figure 2.3 illustrates the recognition of a typical image distortion in PET images following CT-AC. Due to the comparatively long examination time of the whole-body emission acquisition (30 min) performed in the caudo-cranial direction, the muscles of the neck did relax between the initial CT scan, and the multi-bed PET scan causing an inter-scan local shift of the head and neck region, which was pronounced by the lack of an effective head fixation [21]. When using the misaligned CT information for the purpose of CT-AC, the emission activity distribution is distorted, yielding an incorrect asymmetrical representation of the tracer uptake in the attenuation-corrected PET image.

Distortions of hybrid images can be observed in either of the two merged modalities; however, when being observed in the anatomical image volume that is used for the purpose of attenuation correction, then frequently a corresponding artifact can be recognized in the complementary attenuation-corrected PET image as well. In case no such image artifact is recognized in AC-PET images, misalignment effects may still cause a bias of the quantitative value in the AC-PET images. It is, therefore, imperative to also inspect the attenuation maps (μ-maps) and the uncorrected emission images (NAC-PET) during the clinical review in order to ensure correct interpretation of the AC-PET images.

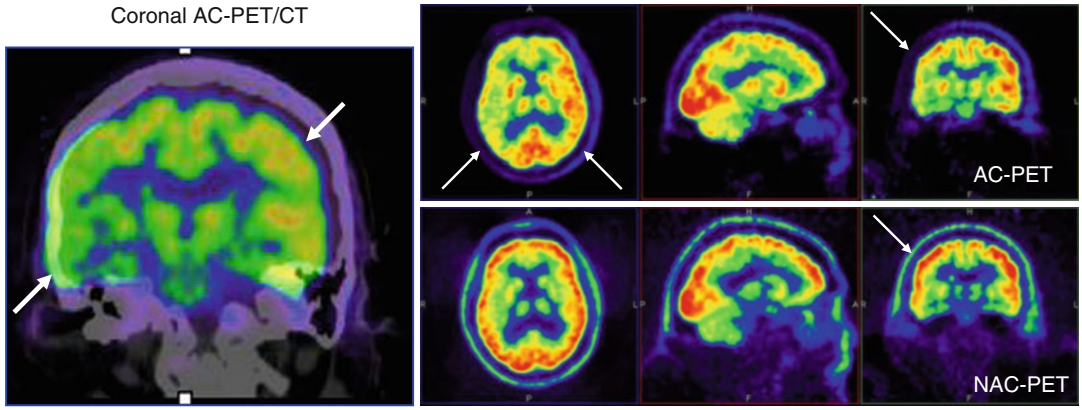

Fig. 2.3 Motion-induced misalignment in the area of the neck (from muscle relaxation) can cause significant distortions in the AC-PET activity distribution pattern (Data courtesy of MJ Ribeiro, CEA/SHFJ in Orsay, France)

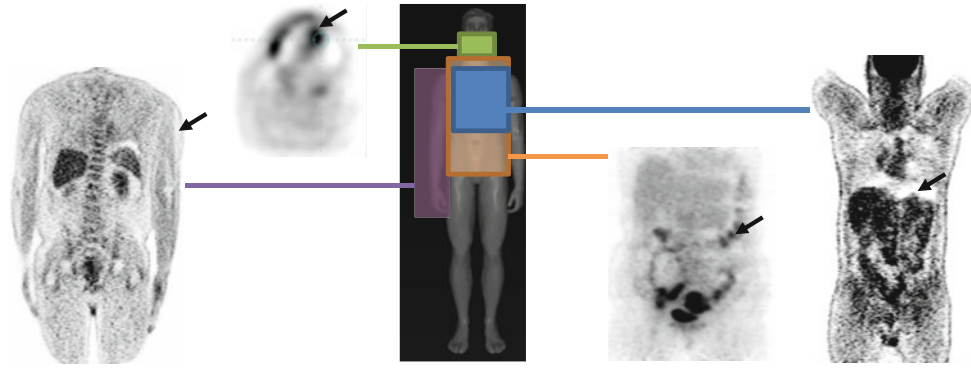

Fig. 2.4 Distortions most commonly observed in PET/CT relate to the presence of beam-hardening effects from dental implants (*green*) that are further enhanced by involuntary intra-scan motion of the patient, the presence of high-density CT contrast agents (*orange*), respiration mismatch (*blue*), and truncation effects in large patients (*purple*). Arrows indicate affected regions and its point to the regional image distortions

Many of the artifacts observed in PET images from PET/MR are similar in appearance and nature to the artifacts observed in PET/CT imaging following CT-AC. Figure 2.4 summarizes typical image distortions seen in PET/CT of which most arise from methodological issues with the CT (e.g., beam hardening) as well as from several aspects of data processing, namely, CT-AC performed with contrast-enhanced CT images. Intra-scan patient motion and truncation effects from mismatches of the measured transverse FOV of the CT and PET also may cause artifacts and bias in the AC-PET images [21].

Intra-scan patient motion and truncation effects are not specific to PET/CT and can be observed in PET/MRI as well. Metallic and other dense implants may cause beam-hardening artifacts on CT and subsequently on AC-PET/CT, while the same objects cause signal voids on MR images that may translate into artifacts on the MR-based attenuation maps and AC-PET/MR images. In PET/MR, AC-PET image distortions may further originate from the inability of the MR-based attenuation correction to recognize and handle all objects and tissues in the field of view appropriately.

2.3 PET/MR Artifacts

According to Table 2.1 PET/MR images may be affected by distortions from system design limitations, methodological aspects, and steps in the data processing. Here we review possible and

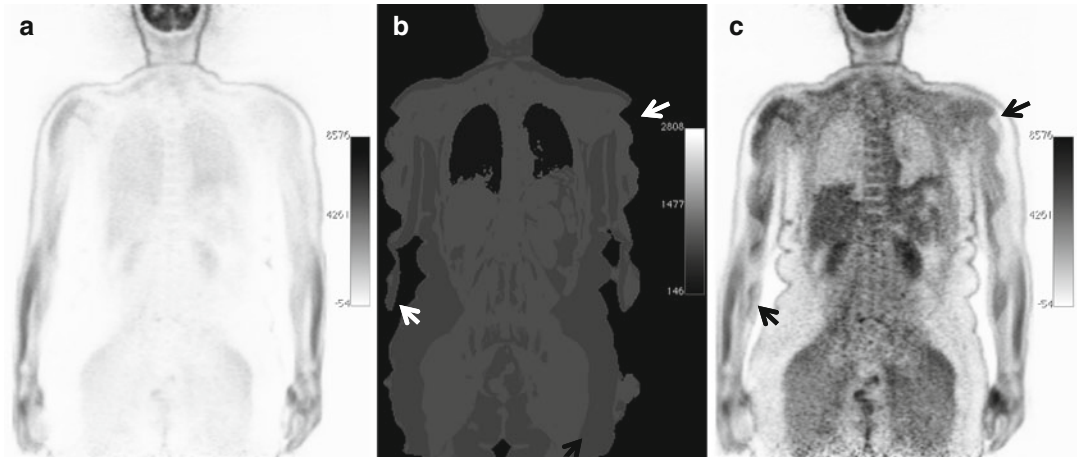

Fig. 2.5 Whole-body [^{18}F]-FDG PET/MRI study (Fig. 2.2b) with truncation artifacts. Patient was positioned with the arms down and along the body causing truncation of the attenuation-corrected PET data beyond the 50-cm measured transverse field of view of the MR. (**a**) PET emission image before AC, showing intense muscle uptake along the lower arms, (**b**) MR-based 4-class attenuation map illustrating truncation along the arms, and (**c**) AC-PET image (applying (**b**) to (**a**) demonstrating reduced tracer distribution along the arms corresponding to the area of truncation in (**b**) (*arrows* in (**a**,**b**))

common image distortions in PET from PET/MR systems.

2.3.1 Hardware and Design: Truncation

2.3.1.1 Description

In state-of-the-art PET/MR systems, the measured transverse field of view of the MR is smaller compared to that of the PET (Fig. 2.2). Given the comparatively longer imaging times and smaller bore diameter in MR (versus PET), oncology patients are typically positioned with their arms down, thus almost always leading to truncation effects along the arms.

2.3.1.2 Typical Findings

Any map of attenuation coefficients derived from MR information covering a FOV smaller than that covered by PET will lead to a "masking effect," thereby underestimating PET image information beyond the measured MR information. This can be appreciated from the reduced image contrast in the AC-PET along the arms (Fig. 2.5). The resulting underestimation of the AC-PET activity is largest in the area of truncation but can be in the order of 10–20 % in uniform reference regions further away from the truncated arm region.

In a patient study simulating truncation in whole-body PET/MR imaging, Delso and colleagues demonstrate an average bias of up to 15 % and local biases of up to 50 % when PET data were reconstructed with incomplete attenuation information [22]. This underestimation may have implications for lesion localization in melanoma patients. So far (March 2013), PET/MR users have not reported lesions to be missed on AC-PET versus NAC-PET owing to MR truncation artifacts.

2.3.1.3 Solutions

Delso et al. further show that completing the truncated attenuation map with data extracted from non-attenuation-corrected (NAC) PET data globally reduced these biases to below 10 % [22]. The idea of using NAC-PET images to improve low-quality attenuation maps was already considered before the introduction of combined PET/CT systems and is based on the concurrent reconstruction of both, the PET emission activity distribution and the attenuation map [23]. The improvements from using extended field-of-view attenuation maps [23, 24] in PET/MR are illustrated in Fig. 2.6.

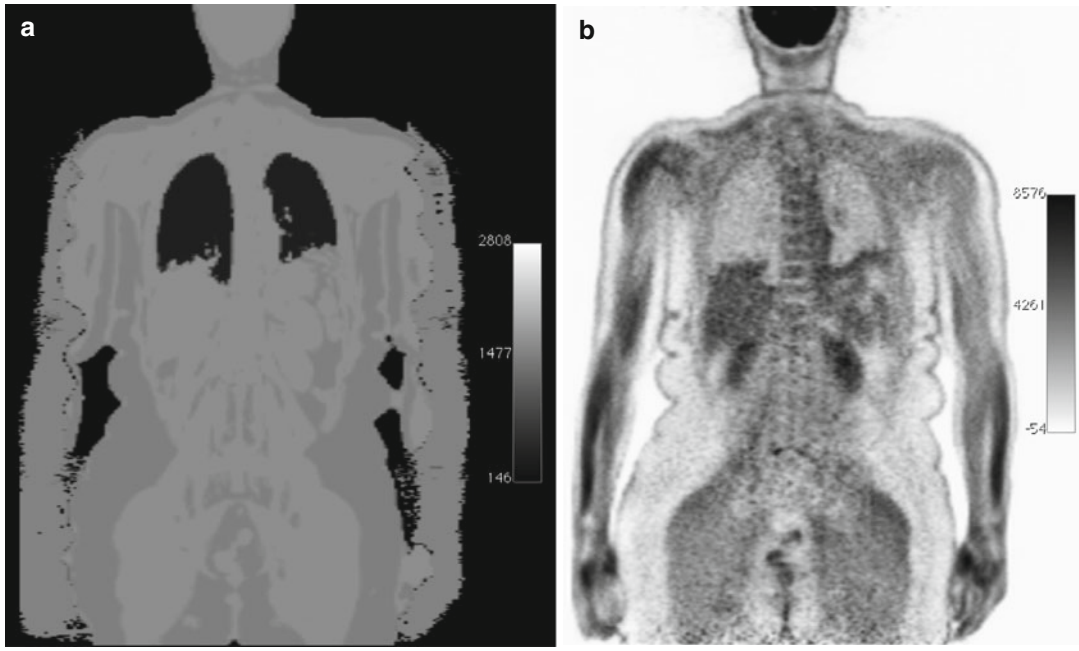

Fig. 2.6 Truncation artifacts can be corrected for by using a special reconstruction algorithm aimed at recovering both the tracer (activity) distribution and the attenuation map: Maximum Likelihood simultaneous Activity and Attenuation reconstruction, MLAA [24]. (**a**) MLAA-extended 4-class attenuation map and (**b**) AC-PET image using the attenuation map in (**a**) in a normal PET reconstruction (MLAA PET image discarded). Note the residual flaws of the attenuation data (**a**) but the marked improvement of PET activity recovery outside the transverse FOV of the MR (**b**) compared to Fig. 2.5 (same patient). This method is currently implemented on the fully integrated PET/MR (Fig. 2.2c)

2.3.2 Hardware and Design: Non-uniformities

2.3.2.1 Description

In addition to truncation effects (Fig. 2.5), non-uniformities can be observed at the edge of the transverse field of view of the MR images. These well-known image distortions originate from the limited homogeneity of the main magnetic field (B_0) and the linearity of field gradients used for spatial encoding [25], both of which are difficult to maintain homogeneous across an extended transverse and axial FOV.

2.3.2.2 Typical Findings

Field inhomogeneities are represented by sinusoidal edge enhancement in reformatted coronal views of the whole-body MR images (Fig. 2.7). In that regard these image distortions are similar to general truncation artifacts (Fig. 2.5), and both are observed together.

The non-uniformity artifacts in the PET images appear as alternating high- and low-activity concentrations along the arms (Fig. 2.7). These alterations in PET activity cause a reduced detectability of lesions in these regions and are most likely to be noticed in skin melanoma patients.

2.3.2.3 Solutions

Patients should be positioned within the maximum transverse FOV of the MR, if possible. In any case, users are advised to review the emission images without attenuation correction in addition to the AC-PET images. New, ongoing MR sequence developments that aim at maintaining homogenous fields in an extended FOV [26] may help reduce subsequent image distortion from nonuniformity effects in combined PET/MRI.

2.3.3 Methodological Pitfalls: Involuntary Patient Motion

2.3.3.1 Description

Involuntary patient motion, typically caused by respiration or relaxation of muscles, is a known

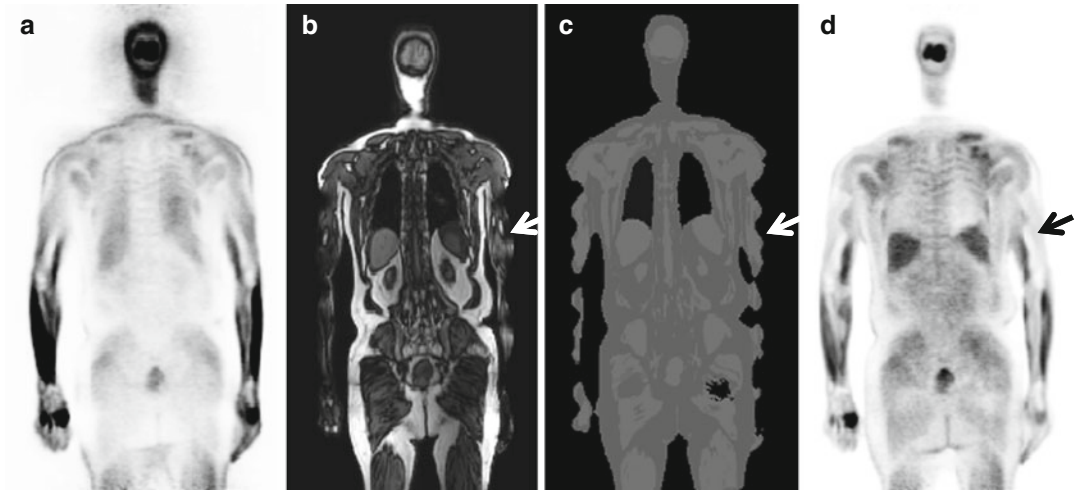

Fig. 2.7 Whole-body [^{18}F]-FDG PET/MRI study of a patient with arms down. (**a**) NAC-PET, (**b**) opposed phase of Dixon T1w-MR, (**c**) MR-based 4-class attenuation map, and (**d**) AC-PET following MR-AC of (**a**) using (**c**). The nonuniformity artifacts along the arms at the edge of the transverse FOV of the MR propagate through MR-AC and distort the AC-PET images (**d**). The *arrows* in (**b**)–(**d**) highlight the typical effect of this artifact

source of artifacts in PET/CT (Fig. 2.3). Likewise, patient motion can cause local or global misalignment and blurring of images in PET/MR.

2.3.3.2 Typical Findings

MR and PET emission acquisition times per bed position of a PET/MR study are generally too long for the patient to hold their breath. This holds true for some patients even for the 19 s Dixon sequence used for MR-AC in the fully integrated PET/MR system (Fig. 2.2b). Therefore, respiration causes the data to be blurred. In selected cases respiratory motion may cause local misalignment of PET and MR data due to the difference in the duration of the two examinations, also when acquiring the two data sets simultaneously. Figure 2.8 shows an example of respiratory motion leading to different caudo-cranial extension of the thorax during the MR and PET examination, thus affecting the PET tracer distribution in the upper abdomen.

2.3.3.3 Solutions

Breath-hold sequences can be performed as part of PET/MR acquisition protocols [27], thus supporting improved alignment in the thorax. Alternatively patients should be instructed to breathe quietly throughout the entire examination, or gating techniques can be used as for PET in PET/CT [28].

Lately, new algorithms have been proposed to adopt MR-based navigator tracking to estimate inter-scan motion of the head [29, 30] and abdomen [31] for systems recording PET and MR data simultaneously. Through data processing these motion vectors can be used to correct the complementary PET emission data for motion. This approach, however, is work in progress and not yet available for routine use.

2.3.4 Transformation of Attenuation Coefficients: Ignoring Bone

2.3.4.1 Description

The MR signal decays very rapidly in bone as compared to soft tissue or water. Therefore, with conventional MRI, little or no signal is detectable from bone, which appears dark [32]. In practice, the standard methods used for MR-based AC will classify most bone as soft tissue, and 3-class [16] and 4-class segmentation [14] do not account for the presence of bone tissue in MR-based attenuation maps.

In addition, the MR-based segmentation algorithms may assign large air-filled regions in anatomical regions of high complexity, such as the nasal cavities and the base of the skull. This MR artifact, which translates through MR-based AC, originates from difficulties in maintaining

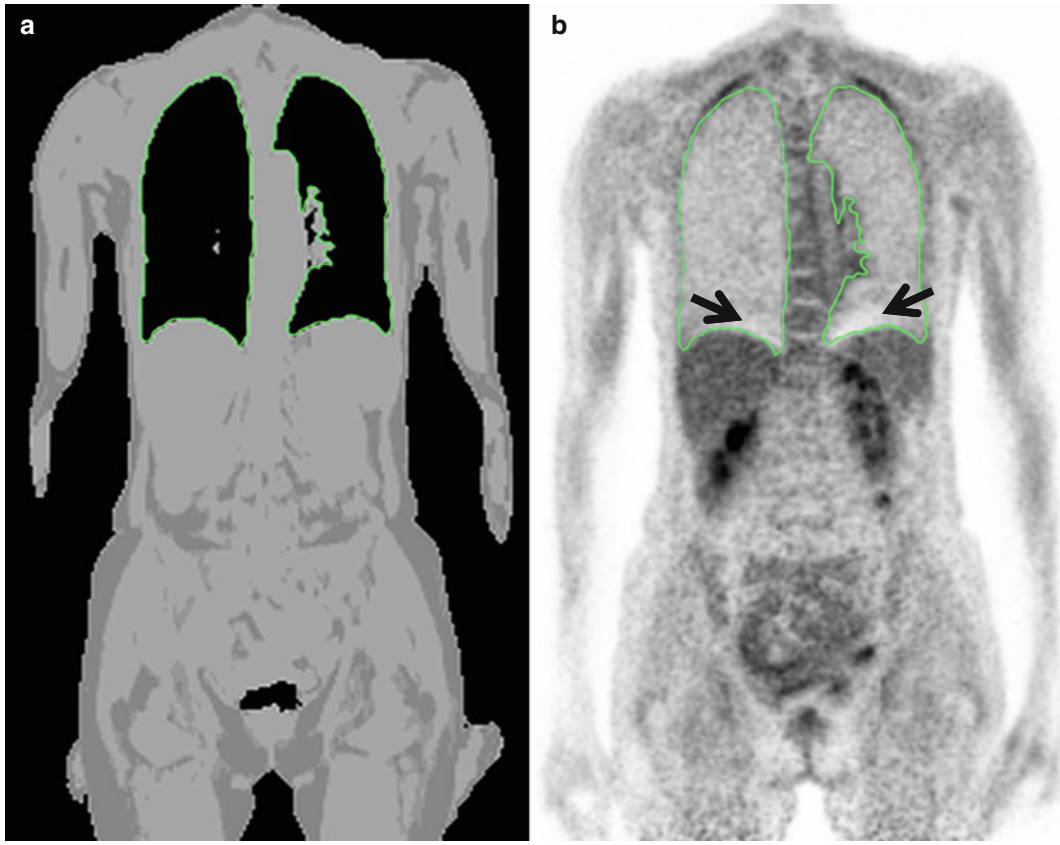

Fig. 2.8 Whole-body [^{18}F]-FDG PET/MR study. The patient was instructed to hold her breath in expiration during the 19 s acquisition of MR attenuation data in thorax and abdomen bed positions and breathe quietly during the remaining PET data acquisition: (**a**) MR-based 4-class attenuation map with the lungs segmented and (**b**) corresponding attenuation-corrected PET image with the segmentation from (**a**) overlaid. As indicated by the *arrows* in (**b**), breathing artifacts were present in spite of the effort to avoid them by careful patient instruction

magnetic field homogeneity across interfaces of materials with different magnetic susceptibilities (e.g., bone and air).

2.3.4.2 Typical Findings – Brain

Figure 2.9 shows a common artifact, whereby air cavities appear at the base of the skull, thus assigning air attenuation coefficients to areas that are actually made of bone or soft tissue layers. This causes an underestimation of the attenuation and subsequently of the PET activity in these regions.

Andersen et al. [33] and Hitz et al. [34] report a quantitative and visual effect of ignoring bone in MR-AC on the tracer distribution of brain PET studies. Figure 2.10 shows the relative difference of PET images corrected with CT-AC and MR-AC, demonstrating a gradually increasing underestimation of the MR AC-PET data from the center of the brain toward the skull [33].

2.3.4.3 Solutions – Brain

Partial bone tissue representation can be obtained directly from MR imaging using ultrashort echo time (UTE) sequences [35–38]. However, UTE imaging is technically demanding and suffers from general MR artifacts in complex anatomical regions (e.g., base of the skull) and has not yet been implemented for routine clinical use. An alternative solution may be the co-registration of a low-dose CT image for the purpose of attenuation correction. This procedure, however, entails separate imaging and exposure of the patient and counteracts the purpose of using PET/MR instead of PET/CT (or PET/CT and MR) for a given patient group.

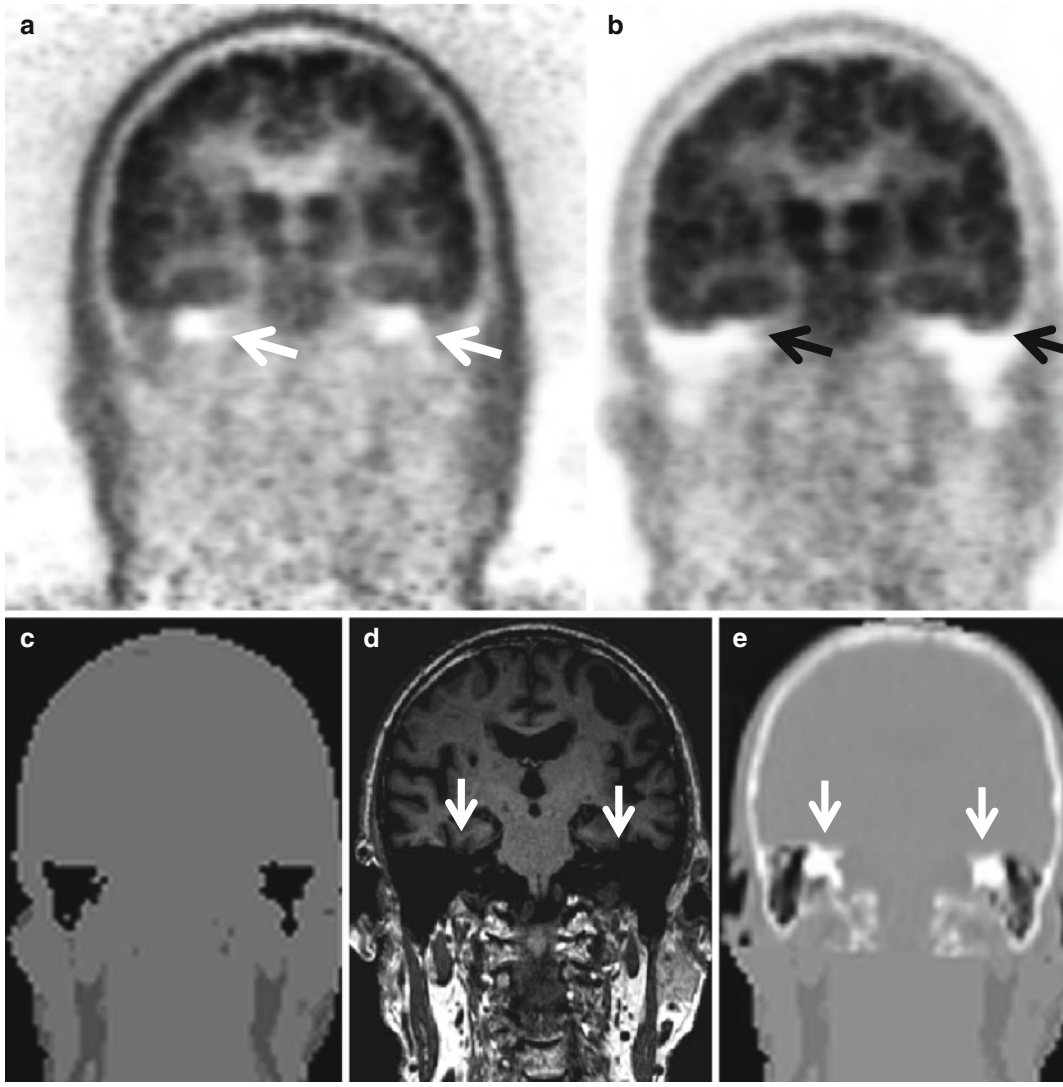

Fig. 2.9 Coronal [^{18}F]-FDG PET/MR images of a dementia patient: (**a**) NAC-PET, (**b**) AC-PET following MR-AC demonstrating enlarged photopenic areas at the base of the skull (*arrows*), (**c**) MR-based 4-class segmented attenuation map with air-filled regions near the base of the skull, (**d**) T1w-MR demonstrating corresponding signal voids in cortical bone structures (*arrows*) seen clearly on (**e**) the CT, which is co-registered to the MR for accurate attenuation correction (the lower part of the image is merged data from (**c**) as the CT FOV is shorter)

Alternatively, atlas and pattern recognition methods have been suggested that derive attenuation maps, including bone information, from a database of co-registered intra-subject CT and MR image sets and a patient-specific, independently acquired CT image volume [39]. Atlas methods were shown to yield promising results but are challenged by abnormal anatomy that is typically not matched in the database of aligned CT and MR data sets.

2.3.4.4 Typical Findings – Whole Body

Ignoring bone attenuation may have an effect outside the brain as well. Martinez-Möller et al. [14] reported in a simulation study employing PET/CT data a maximum bias of 14 % of PET uptake values in the region of the bone if bone is not accounted for during AC. Recently, Samarin and co-workers reported that substitution of bone attenuation by soft tissue attenuation values in AC maps resulted in an underestimation of

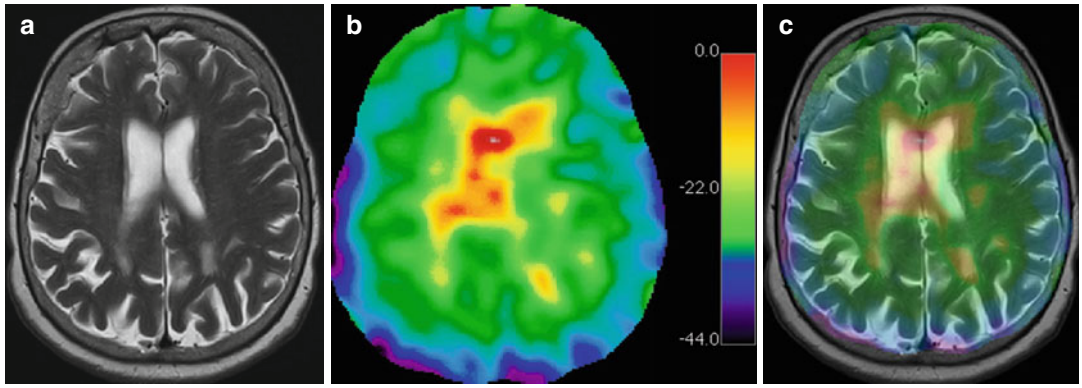

Fig. 2.10 Gradient effect in PET/MR imaging of the brain: (**a**) axial T2w-MR, (**b**) relative difference of AC-PET following 4-class MR-AC (ignoring bone) and AC-PET following CT-AC showing a gradually decreasing PET activity in PET/MR compared to PET/CT when moving from the center of the brain toward the skull bone and (**c**) fusion of (**a**) with (**b**) (Courtesy of Flemming L Andersen, Copenhagen University Hospital, Rigshospitalet)

tracer uptake of 3 % (range 0–4 %) and 11 % (range 2–31 %) in soft tissue lesions adjacent to bone and in osseous lesions, respectively [40]. Further analysis of the spine and pelvic osseous lesions revealed a substantial dependence of the error on the lesion composition, which may have implications for therapy monitoring. Figure 2.11 illustrates the relative regional effects when modifying bone attenuation values in whole-body PET studies and confirms the findings in literature [14, 40].

2.3.4.5 Solutions – Whole Body

For accurate quantification of bone lesions, atlas-based methods could be used as in the brain (as investigated, e.g., in [39]), while MLAA and UTE methods need to be further tested in whole-body studies. In the future, MLAA-based algorithms could further benefit from the incorporation of time-of-flight (TOF) information, which has been shown in a pilot study to result in much improved image quality and suppressed image distortions in AC-PET images [41].

2.3.5 Transformation of Attenuation Coefficients: Metallic Implants

2.3.5.1 Description

Given the significantly different magnetic susceptibilities of metal and human tissues, magnetic field variations will cause signal voids around the implants on MR images. In CT and AC-PET metallic implants give rise to beam hardening.

2.3.5.2 Typical Findings

In PET/MR the signal voids seen in the MR images are segmented as air-filled gaps in the MR-based attenuation map, leading to a loss of signal in the attenuation-corrected PET image. The problem is appreciated clearly in patients with hip endoprostheses (Fig. 2.12a) or knee replacements (Fig. 2.13) but more commonly with dental fillings leading to image distortions in the head/neck region (Fig. 2.14).

Artifacts arising from metallic or other dense implants can be observed occasionally in other regions of the body of patients undergoing whole-body PET/MR imaging. Figure 2.15 summarizes further artifacts, induced by metal and other high-density materials relevant particularly to oncology patients, such as from chemotherapy ports, tissue expanders, or, in the worst case, endoscopy devices.

2.3.5.3 Solutions

Ladefoged et al. investigated the use of semi-automated inpainting to correct for signal voids in MR and subsequent air-filled artifacts in MR-based attenuation maps in patients with endoprostheses

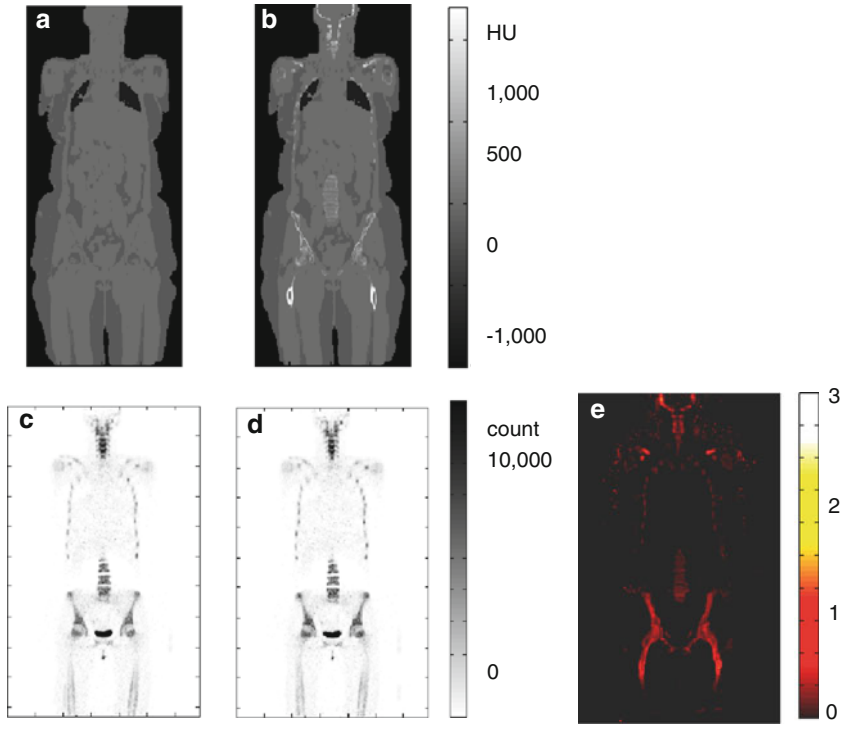

Fig. 2.11 Coronal images of a whole-body [^{18}F]-FDG PET/MR examination: (**a**) standard 4-class MR-based attenuation map, (**b**) as (**a**) with bone values segmented and inserted from a co-registered CT, (**c**) AC-PET following MR-AC using (**a**), and (**d**) AC-PET following AC using (**b**). Panel (**e**) represents the relative difference image [(**d**)–(**c**)]/(**c**) and illustrates the effect of ignoring bone during MR-AC; the bias is most prominent in the bone region and less noticeable in regions distant from bone (Data analysis courtesy of Rachida Sersar and Julie Hjorth Saabye, Technical University Copenhagen and Rigshospitalet, Denmark)

[42]. The authors showed that PET activity distribution can be recovered to a great extent in the area of the implant when the signal voids on the MR images used for MR-AC are replaced by soft tissue through "inpainting." The additional co-registration of the original CT attenuation values of the actual implant showed only marginal improvements.

The method can be ported to the dental region (Fig. 2.14), but given the more complex anatomy (mixed soft tissue, bone, and air) and the higher sensitivity to quantification errors in the brain, more complex inpainting techniques are needed. Similar signal-void artifacts arise from other dense implants (Fig. 2.15) that warrant retrospective corrections as proposed in [42], which, however, are not yet validated in clinical routine.

2.3.6 Transformation of Attenuation Coefficients: Tissue Inversion

2.3.6.1 Description

Standard MR-AC methods are based on the segmentation of three or four tissue classes (air, lung, and water or air, lung, fat, and water) from MR images that are acquired with dedicated sequences. However, segmentation may fail in routine application and cause inverted tissue classification.

2.3.6.2 Typical Findings

Figure 2.16 shows a patient study where the tissue classes air and lung tissue (4-class segmentation) were inverted for a limited coaxial imaging range of the lower thorax, leading to incorrect attenuation correction of the PET activity in the thorax.

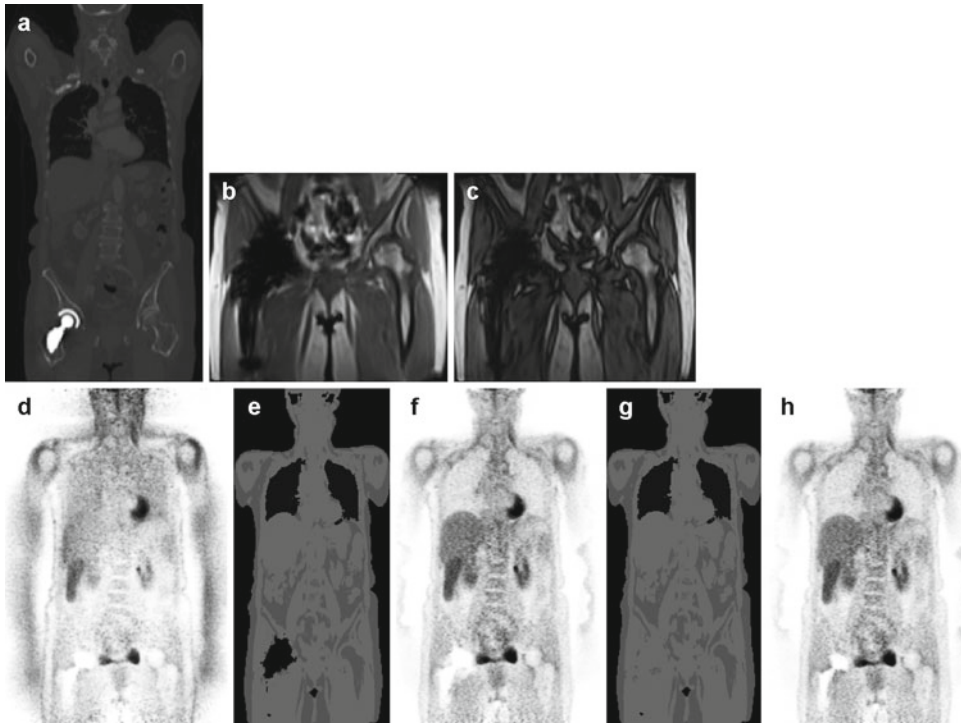

Fig. 2.12 Coronal views of a whole-body [^{18}F]-FDG PET/MR of a patient with a metal hip endoprosthesis: (**a**) CT image in bone window shows the right-sided implant. (**b**) opposed-phase MR and (**c**) in-phase MR, both with signal void around the implant. (**d**) NAC-PET, (**e**)standard MR-based 4-class attenuation map with an air pocket assigned in and around the implant, and (**f**) AC-PET image following MR-AC demonstrating a photopenic area extending beyond the implant region. The air-gap artifact in (**e**) can be removed using a retrospective inpainting technique [42] resulting in improved AC-PET quality. The improved μ-map is shown in (**g**) and the resulting AC-PET in (**h**)

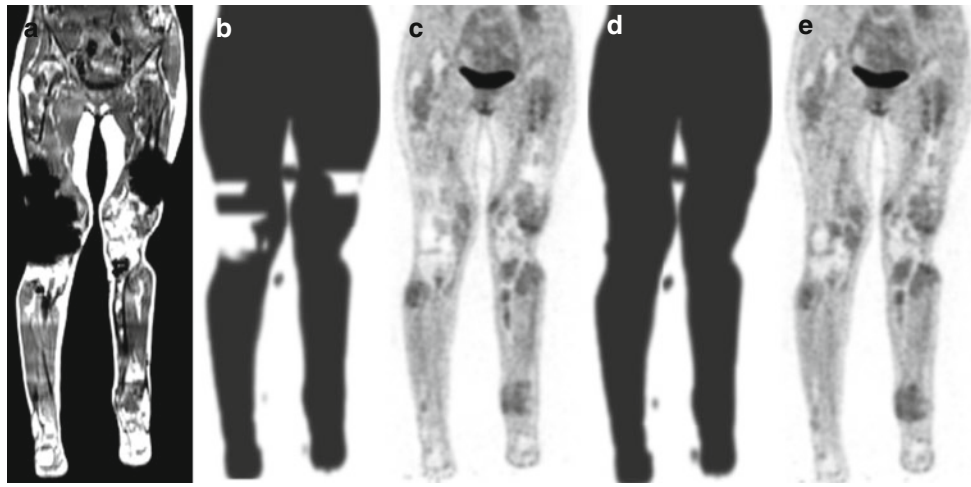

Fig. 2.13 Coronal views of a whole-body [^{18}F]-FDG PET/MR of a patient with a knee replacement: (**a**) *atMR* image for MR-AC, (**b**) 3-class MR-based attenuation map showing extensive air gaps in the area of the knee replacement, and (**c**) AC-PET image following MR-AC using (**a**) showing biased tracer uptake in the regions of the right knee and the lower thighs. The air gaps caused by signal voids on the MR (**a**) were corrected manually using a non-licensed tool that permits filling in the voids with signal intensities from soft tissue as shown in (**d**). The resulting AC-PET image (**e**) shows markedly improved tracer distribution in the regions corrected in the attenuation map (**d**) (Courtesy of Hopital Cantonal de Genéve, Switzerland)

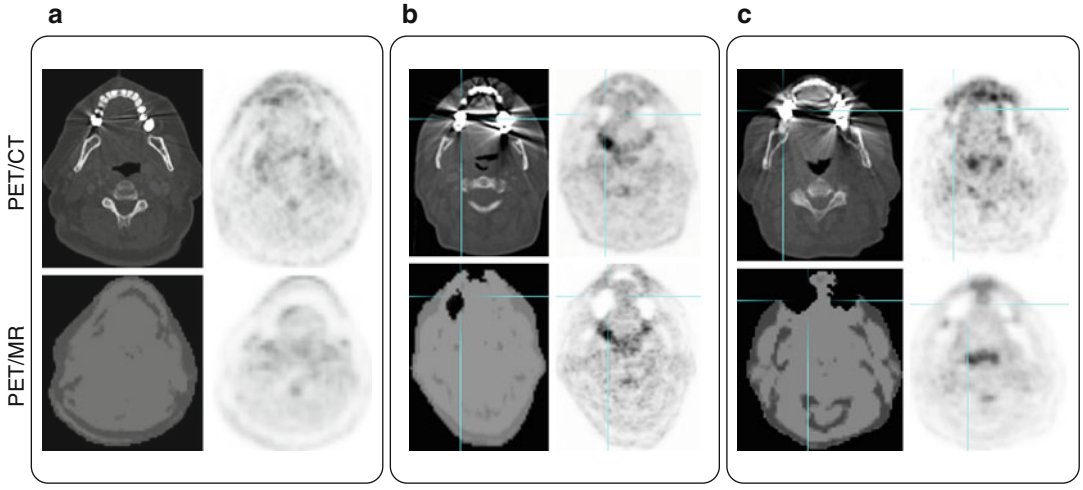

Fig. 2.14 Three patients (**a**–**c**) with dental restoration work. Dental implants cause beam-hardening effects in CT images that may translate into distortions of AC-PET images following CT-AC (*top row*). In PET/MRI (*bottom row*) the same dental work may cause artifacts that are seen as air gaps in the MR-based attenuation maps causing extended photopenia in the AC-PET images as seen in patients (**b**) and (**c**). The extent of these artifacts in PET/MR depends on the composition of the implant materials and their orientations with respect to the gradient field

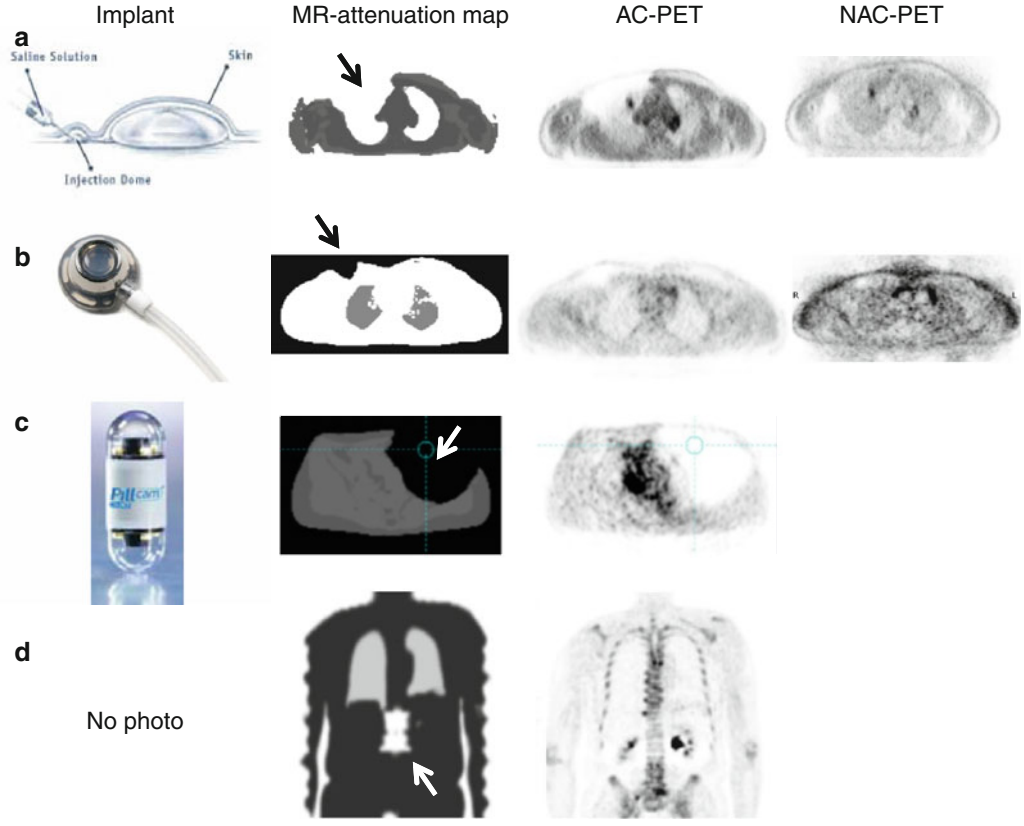

Fig. 2.15 High-density objects causing artifacts in PET/MRI following standard MR-AC: (**a**) tissue expander, (**b**) port-a-cath, (**c**) endoscopy unit, and (**d**) orthopedic spine brace. The *arrows* in MR-AC maps (a, b, c) indicate the affected regions and its point to image distortions originating from the presence of dense objects (Panel (**d**) courtesy of Georg Schramm, Institute for Radiopharmaceutical Cancer Research, Helmholtz-Zentrum, Dresden-Rossendorf, Germany).

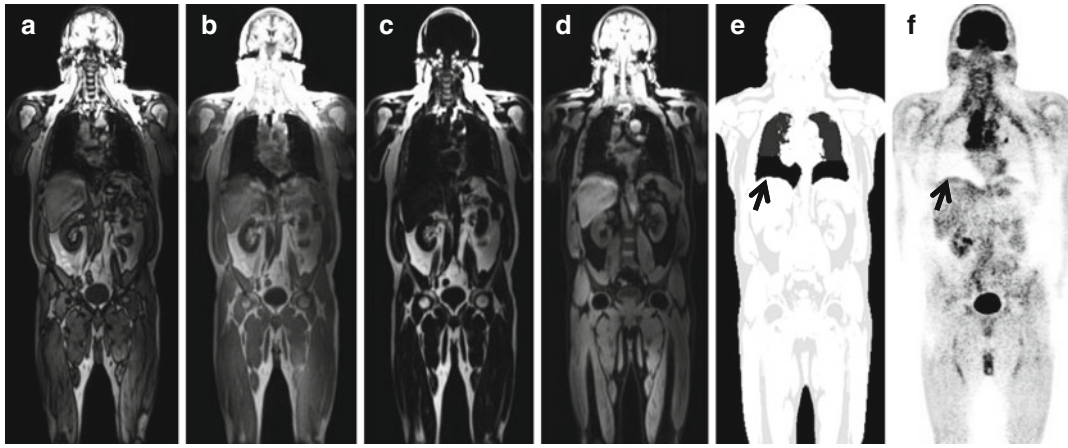

Fig. 2.16 Coronal views of whole-body [^{18}F]-FDG PET/MR study of a patient with metastatic lung cancer: (**a**) In-phase MR, (**b**) opposed-phase MR, (**c**) fat segmentation, (**d**) water segmentation, (**e**) standard 4-class MR-based attenuation map illustrating false air tissue assignment to lower thorax (*arrow*), and (**f**) AC-PET image following MR-AC showing areas of severe underestimation of PET activity in the lower thorax (*arrow*). (Courtesy of Bernhard Sattler, Dept. of Nuclear Medicine, University Hospital Leipzig, Germany)

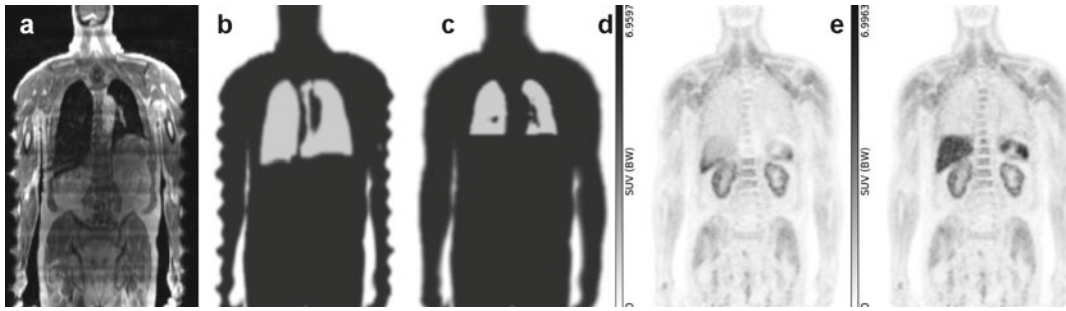

Fig. 2.17 Coronal views of a whole-body [^{18}F]-FDG PET/MRI study: (**a**) T1w-MR showing low signal from the liver, (**b**) corresponding 3-class MR-based attenuation map with liver tissue segmented as lungs, (**c**) manually corrected tissue composition in the thorax and liver region, (**d**) AC-PET following MR-AC using (**b**), and (**e**) AC-PET following MR-AC using (**c**) demonstrating markedly improved tracer recovery in the lower thorax and upper abdomen (Courtesy of Georg Schramm, Institute for Radiopharmaceutical Cancer Research, Helmholtz-Zentrum, Dresden-Rossendorf, Germany)

Figure 2.17 shows another example of a 3-class segmentation. Here, the signal from the liver on the *atMR* sequence was unusually low and, therefore, contributed to an incorrect assignment of lung tissue to the liver, which, in turn, caused a biased AC-PET image in the upper abdomen.

2.3.6.3 Solutions

So far, no standard correction method is available. Tissue inversion or misassignment can potentially be corrected retrospectively by using manual inpainting (Fig. 2.17d, e) or by resegmenting the MR images. Alternatively, the examination needs to be repeated without reinjection of the PET tracer.

2.3.7 Transformation of Attenuation Coefficients: MR Contrast Agents

2.3.7.1 Description

Much like PET/CT applications, the clinical adoption of PET/MR entails the use of contrast agents as part of integrated imaging protocols.

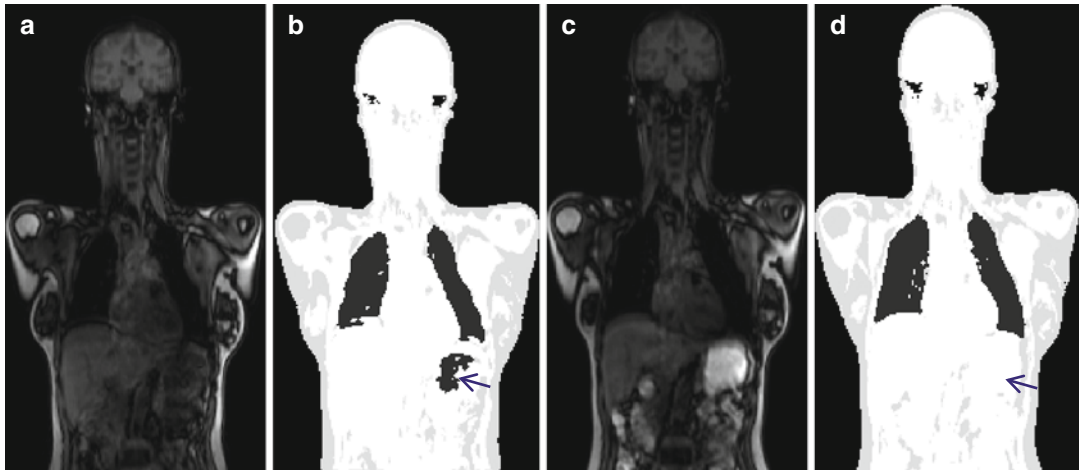

Fig. 2.18 Coronal MR images of volunteer following oral MR contrast intake: (**a**) T1w-MR (FLASH) following 300 mL oral MR contrast (Lumirem), (**b**) 4-class segmentation yielding air gaps (*arrow*) in the stomach region of standard MR-based attenuation map, (**c**) T1w-MR (FLASH) of the volunteer in a repeat study after drinking 400 mL of pineapple juice, and (**d**) corresponding MR-based attenuation map that has no air gaps in the fluid-filled stomach (This artifact is similar in nature to artifacts from metal implants (Fig. 2.12)). The *arrows* in (**b**) and (**d**) indicates the affected region

MR contrast agents are typically made up of iron oxide and Gd chelates for oral and intravenous (IV) administration, respectively.

Oral MR contrast, or ferumoxil (Lumirem®; Guerbet, Germany), is a negative oral contrast agent used to distinguish the loops of the bowel from other abdominal structures. It contains a colloid suspension of iron oxide particles and has superparamagnetic properties. IV MR contrast agents (e.g., Gadovist®, Bayer Group, Germany) are paramagnetic and cause a reduction of the T1 relaxation time, leading to a signal enhancement in a T1-weighted MRI.

Contrast agents could cause either a higher attenuation of 511 keV photons than that of water (soft tissue) and, therefore, lead to a bias of the AC-PET data, or they could cause indirect false tissue classification in DWFS-MR-AC (Figs. 2.18, 2.19).

2.3.7.2 Typical Finding

Lois et al. [43] argue that IV MR contrast does not create PET/CT-like artifacts in PET/MR images following DWFS-MR-AC if it is administered in clinically relevant concentrations, and that the attenuation values are not significantly different from that of water.

However, signal inversion leading to subsequent incorrect tissue assignment has been observed in PET/MR. PET attenuation maps may be biased after ingestion of standard iron oxide-based oral MR contrast agent when standard segmentation-based AC algorithms are used. Figure 2.18 shows a coronal MR image (Fig. 2.18a) and an MR-AC map (Fig. 2.18b) of a volunteer following the ingestion of Lumirem contrast. The standard 4-class DWFS segmentation assigns extended air pockets to the region of the stomach when acquired 15 min after the contrast ingestion. These signal voids can be avoided by the use of alternative contrast agents (Fig. 2.18c, d).

Further, DWFS may yield incorrect tissue assignment in the presence of IV contrast (Fig. 2.19a, b). In extreme cases, IV contrast administration, following standard MR protocols, may lead to incorrect tissue segmentation in standard MR-AC with liver being segmented as "air" and the lungs being partitioned into "air" and "lungs" (Fig. 2.19c, d, e, f). The patient was injected with Gd-based contrast material (Gadovist®) following a standard injection protocol: 1 mmol/kg at 0.5–2 mL/s plus 20 mL NaCl. The artifacts in Fig. 2.19 were observed in less than 10 % of patients.

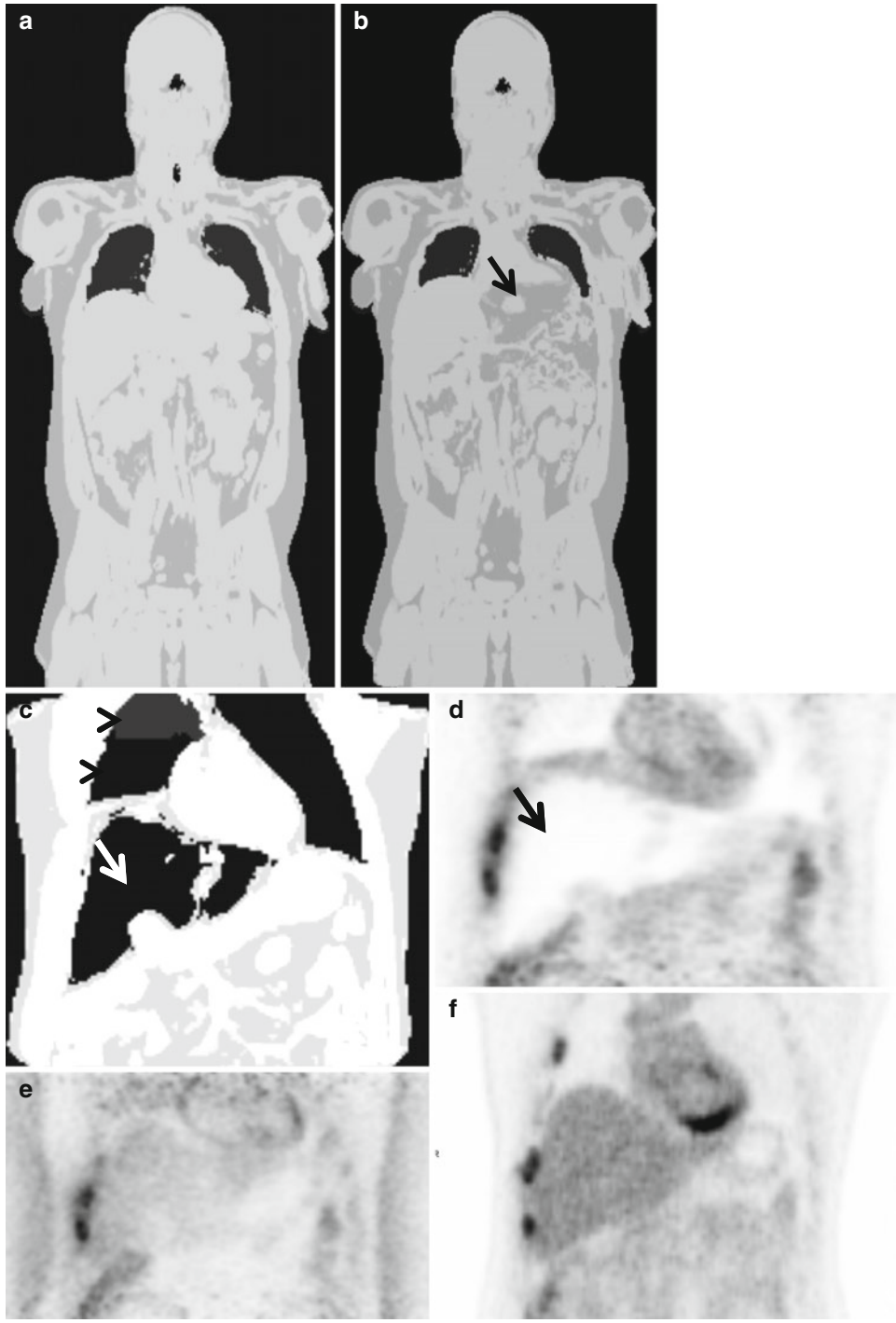

Fig. 2.19 IV MR contrast. Coronal attenuation images of clinical PET/MR patient before (**a**) and after (**b**) IV MR contrast administration demonstrating tissue inversion of the liver region following DWFS MR-AC. False tissue assignment is exemplified in another patient (**c**–**f**) where IV MR contrast administration leads to the incorrect assignment of "air" to the liver (**c**, *arrow*), while the right lung was assigned "air" and "lung" incorrectly (**c**, *arrowhead*). This leads to photopenic areas in the liver following MR-AC (**d**), in contrast to the original tracer distribution in no AC-PET (**e**) and PET following CT-AC (**f**) (Images courtesy Verena Hartung, MD (University Hospital Essen, Germany))

2.3.7.3 Solutions

The administration of an oral contrast agent may not be mandatory, or alternative oral agents, such as pineapple juice, could be used without biasing attenuation maps. Advanced AC algorithms, such as the atlas-based approach proposed by Hofmann and colleagues [39], can yield unbiased attenuation maps. The effects of IV contrast and subsequent reproducibility of MR-based attenuation maps deserve further attention.

Conclusion

Integrated, whole-body PET/MR has become clinically available, but the lack of CT-like transmission sources mandates new approaches for MR-based attenuation correction of the PET data in order to migrate the well-known, highly accurate quantification of metabolic and signaling pathways in PET to PET/MR. The currently implemented algorithms for attenuation correction may yield artifacts in PET/MR that in some cases are similar to distortions of PET/CT images.

It is recommended to routinely review the non-attenuation-corrected (NAC) and attenuation-corrected (AC) PET images together with the diagnostic MR images and the MR-based attenuation maps in order to reveal and interpret any image artifacts potentially arising from MR-based attenuation correction. This will help sharpen the eye of the observer and aid in the correct interpretation of PET/MR images. In addition, users are advised to consider following these points:

- Ensure appropriate and sufficient training of the expert readers and staff [44, 45].
- Perform daily quality control procedures [46].
- Adhere to imaging guidelines; so far no imaging guidelines on PET/MR exist, but guidelines on PET/CT [47] can serve as a guidance for the adoption of local standards.
- Test and adopt, if feasible, new MR sequences (for attenuation correction) reducing metal artifacts [48] and/or supporting the derivation of bone tissue [15].

The potential of PET/MR imaging can be explored more effectively if the sources of the most common artifacts are understood and if correction methods can be adopted. In either case, an interaction and collaboration of PET/MR users are required locally and globally to advance toward standardized and optimized PET/MR imaging.

Acknowledgments We gratefully acknowledge contributions from A Kalemis, F DiLalla and B Delattre (Philips Healthcare), MJ Ribeiro (CEA/SHFJ Orsay, France), B Sattler (Leipzig, Germany), FL Andersen (Copenhagen, DK), and G Schramm (Dresden, Germany).
Further, we thank our colleagues from Copenhagen for helpful advice and support: J Löfgren, K Stahr, J Poulsen, M Federspiel, and C Ladefoged.

Conflict of Interest None

References

1. Kuhl DE, Edwards RQ. Image separation radioisotope scanning. Radiology. 1963;80:653–61.
2. Phelps ME. Emission computed tomography. Semin Nucl Med. 1977;7:337–65.
3. Huang SC, Hoffman EJ, Phelps ME, et al. Quantitation in positron emission computed tomography: 2. Effects of inaccurate attenuation correction. J Comput Assist Tomogr. 1979;3:804–14.
4. Townsend DW. Multimodality imaging of structure and function. Phys Med Biol. 2008;53:R1–39.
5. Beyer T, Townsend DW, Brun T, Kinahan P, Charron M, Roddy R, Jerin J, Young J, Nutt R, Byars LG. A combined PET/CT scanner for clinical oncology. J Nucl Med. 2000;41:1369–79.
6. Beyer T, Townsend DW, Czernin J, Freudenberg LS. The future of hybrid imaging-part 2: PET/CT. Insights Imaging. 2011;2:225–34.
7. Czernin J, Allen-Auerbach M, Schelbert HR. Improvements in cancer staging with PET/CT: literature-based evidence as of September 2006. J Nucl Med. 2007;48:78S–88.
8. von Schulthess GK. Cost considerations regarding an integrated CT-PET system. Eur Radiol. 2000;10:S377–80.
9. Kinahan PE, Hasegawa BH, Beyer T. X-ray-based attenuation correction for positron emission tomography/computed tomography scanners. Semin Nucl Med. 2003;33:166–79.
10. Pichler BJ, Wehrl HF, Judenhofer MS. Latest advances in molecular imaging instrumentation. J Nucl Med. 2008;49:5S–23.

11. Beyer T, Freudenberg LS, Czernin J, et al. The future of hybrid imaging-part 3: PET/MR, small-animal imaging and beyond. Insights Imaging. 2011;2: 235–46.
12. Kalemis A, Delattre BM, Heinzer S. Sequential whole-body PET/MR scanner: concept, clinical use, and optimisation after two years in the clinic. The manufacturer's perspective. Magn Reson Mater Phys. 2013;26:5–23.
13. Delso G, Fürst S, Jakoby B, Ladebeck R, Ganter C, Nekolla SG, Schwaiger M, Ziegler SI. Performance measurements of the Siemens mMR integrated whole-body PET/MR scanner. J Nucl Med. 2011;52(12):1914–22.
14. Martinez-Möller A, Souvatzoglou M, Delso G, et al. Tissue classification as a potential approach for attenuation correction in whole-body PET/MRI: evaluation with PET/CT data. J Nucl Med. 2009;50: 520–6.
15. Bezrukov I, Mantlik F, Schmidt H, Schölkopf B, Pichler BJ. MR-Based PET attenuation correction for PET/MR imaging. Semin Nucl Med. 2013;43:45–59.
16. Schulz V, Torres-Espallardo I, Renisch S, et al. Automatic, three-segment, MR-based attenuation correction for whole-body PET/MR data. Eur J Nucl Med Mol Imaging. 2010;38:138–52.
17. Eiber M, Martinez-Möller A, Souvatzoglou M, et al. Value of a Dixon-based MR/PET attenuation correction sequence for the localization and evaluation of PET-positive lesions. Eur J Nucl Med Mol Imaging. 2011;38:1691–701.
18. Beyer T. Technical artifacts in PET/CT imaging. In: Shreve P, Townsend DW, editors. Clinical PET-CT in radiology. New York: Springer; 2011. p. 47–60. Chapter 5.
19. Keller SH, Holm S, Hansen AE, Sattler B, Andersen F, Klausen TL, Højgaard L, Kjær A, Beyer T. Image artifacts from MR-based attenuation correction in clinical, whole-body PET/MRI. Magn Reson Mater Phys. 2013;26:173–81.
20. Goerres GW, Kamel E, Seifert B, Burger C, Buck A, Hany TF, Von Schulthess GK. Accuracy of image coregistration of pulmonary lesions in patients with non-small cell lung cancer using an integrated PET/CT system. J Nucl Med. 2002;43(11):1469–75.
21. Beyer T, Antoch G, Müller S, Egelhof T, Freudenberg L, Debatin J, Bockisch A. Acquisition protocol considerations for combined PET/CT imaging. J Nucl Med. 2004;45:25S–35.
22. Delso G, Martinez-Möller A, Bundschuh RA, Nekolla SG, Ziegler SI. The effect of limited MR field of view in MR/PET attenuation correction. Med Phys. 2010;37:2804–12.
23. Nuyts J, Dupont P, Stroobants S, Benninck R, Mortelmans L, Suetens P. Simultaneous maximum a posteriori reconstruction of attenuation and activity distributions from emission sinograms. IEEE Trans Med Imaging. 1999;18:393–403.
24. Nuyts J, Bal G, Kehren F, Fenchel M, Michel C, Watson C. Completion of a truncated attenuation image from the attenuated PET emission data. IEEE Trans Med Imaging. 2013;32:237–46.
25. Jezzard P. The physical basis of spatial distortions in magnetic resonance images, handbook of medical imaging. San Diego: Academic; 2000. p. 425–38.
26. Blumhagen JO, Ladebeck R, Fenchel M, Scheffler K. MR-based field-of-view extension in MR/PET: B(0) homogenization using gradient enhancement (HUGE). Magn Reson Med. 2012. doi:10.1002/mrm.24555. Epub ahead of print.
27. Schwenzer NF, Schraml C, Müller M, Brendle C, Sauter A, Spengler W, Pfannenberg AC, Claussen CD, Schmidt H. Pulmonary lesion assessment: comparison of whole-body hybrid MR/PET and PET/CT imaging–pilot study. Radiology. 2012;264:551–8.
28. Klausen TL, Keller SH, Olesen OV, Aznar M, Andersen FL. Innovations in PET/CT. Q J Nucl Med Mol Imaging. 2012;56:268–79.
29. Catana C, Benner T, van der Kouwe A, Byars L, Hamm M, Chonde DB, Michel CJ, El Fakhri G, Schmand M, Sorensen AG. MRI-assisted PET motion correction for neurologic studies in an integrated MR-PET scanner. J Nucl Med. 2011;52:154–61.
30. Ullisch MG, Scheins JJ, Weirich C, Rota Kops E, Celik A, Tellmann L, Stöcker T, Herzog H, Shah NJ. MR-based PET motion correction procedure for simultaneous MR-PET neuroimaging of human brain. PLoS One. 2012;7:e48149.
31. Dikaios N, Izquierdo-Garcia D, Graves MJ, Mani V, Fayad ZA, Fryer TD. MRI-based motion correction of thoracic PET: initial comparison of acquisition protocols and correction strategies suitable for simultaneous PET/MRI systems. Eur Radiol. 2012;22: 439–46.
32. Robson MD, Bydder GM. Clinical ultrashort echo time imaging of bone and other connective tissues. NMR Biomed. 2006;19:765–80.
33. Andersen FL, Ladefoged CN, Beyer T, Keller SH, Hansen AE, Højgaard L, Kjær A, Law I, Holm S. Combined PET/MR imaging in neurology: MR-based attenuation correction implies a strong spatial bias when ignoring bone. Neuroimage. 2013;84C:206–16. doi:10.1016/j.neuroimage.2013.08.042 [Epub ahead of print].
34. Hitz S, Habekost C, Delso G, Souvatzoglou M, Grimmer T, Beer A, Fürst S, Ziegler S, Schwaiger M, Drzezga A. Evaluation of the qualitative performance of PET/MR versus PET/CT in patients with Alzheimer's disease. J Nucl Med. 2012;53 Suppl 1:1932.
35. Catana C, van der Kouwe A, Benner T, Michel CJ, Hamm M, Fenchel M, Fischl B, Rosen B, Schmand M, Sorensen AG. Toward implementing an MRI-based PET attenuation-correction method for neurologic studies on the MR-PET brain prototype. J Nucl Med. 2010;51:1431–8.
36. Keereman V, Fierens Y, Broux T, De Deene Y, Lonneux M, Vandenberghe S. MRI-based attenuation correction for PET/MRI using ultrashort echo time sequences. J Nucl Med. 2010;51:812–18.

37. Berker Y, Franke J, Salomon A, Palmowski M, Donker HC, Temur Y, Mottaghy FM, Kuhl C, Izquierdo-Garcia D, Fayad ZA, Kiessling F, Schulz V. MRI-based attenuation correction for hybrid PET/MRI systems: a 4-class tissue segmentation technique using a combined ultrashort-echo-time/Dixon MRI sequence. J Nucl Med. 2012;53:796–804.
38. Johansson A, Karlsson M, Nyholm T. CT substitute derived from MRI sequences with ultrashort echo time. Med Phys. 2011;38:2708–14.
39. Hofmann M, Bezrukov I, Mantlik F, Aschoff P, Steinke F, Beyer T, Pichler BJ, Schoelkopf B. MRI-based attenuation correction for whole-body PET/MRI: quantitative evaluation of segmentation- and atlas-based methods. J Nucl Med. 2011;52:1392–9.
40. Samarin A, Burger C, Wollenweber SD, Crook DW, Burger IA, Schmid DT, von Schulthess GK, Kuhn FP. PET/MR imaging of bone lesions–implications for PET quantification from imperfect attenuation correction. Eur J Nucl Med Mol Imaging. 2012;39:1154–60.
41. Defrise M, Rezaei A, Nuyts J. Time-of-flight PET data determine the attenuation sinogram up to a constant. Phys Med Biol. 2012;57:885–99.
42. Ladefoged CN, Andersen FL, Keller SH, Löfgren J, Hansen AE, Holm S, Højgaard L, Beyer T. PET/MR imaging of the pelvis in the presence of endoprostheses: reducing image artifacts and increasing accuracy through inpainting. Eur J Nucl Med Mol Imaging. 2013;40(4):594–601.
43. Lois C, Bezrukov I, Schmidt H, Schwenzer N, Werner MK, Kupferschläger J, Beyer T. Effect of MR contrast agents on quantitative accuracy of PET in combined whole-body PET/MR imaging. Eur J Nucl Med Mol Imaging. 2012;39:1756–66.
44. BischofDelaloye A, Carrió I, Cuocolo A, Knapp W, Gourtsoyiannis N, McCall I, Reiser M, Silberman B. White paper of the European Association of Nuclear Medicine (EANM) and the European Society of Radiology (ESR) on multimodality imaging. Eur J Nucl Med Mol Imaging. 2007;34:1147–51.
45. Gourtsoyiannis N, McCall I, Reiser M, Silberman B, BischofDelaloye A, Carrió I, Cuocolo A, Knapp W. White paper of the European Society of Radiology (ESR) and the European Association of Nuclear Medicine (EANM) on multimodality imaging. Eur Radiol. 2007;17:1926–30.
46. Sattler B, Jochimsen T, Barthel H, Sommerfeld K, Stumpp P, Hoffmann KT, Gutberlet M, Villringer A, Kahn T, Sabri O. Physical and organizational provision for installation, regulatory requirements and implementation of a simultaneous hybrid PET/MR-imaging system in an integrated research and clinical setting. Magn Reson Mater Phys. 2013;26:159–71.
47. Boellaard R, O'Doherty MJ, Weber WA, Mottaghy FM, Lonsdale MN, Stroobants SG, Oyen WJ, Kotzerke J, Hoekstra OS, Pruim J, Marsden PK, Tatsch K, Hoekstra CJ, Visser EP, Arends B, Verzijlbergen FJ, Zijlstra JM, Comans EF, Lammertsma AA, Paans AM, Willemsen AT, Beyer T, Bockisch A, Schaefer-Prokop C, Delbeke D, Baum RP, Chiti A, Krause BJ. FDG PET and PET/CT: EANM procedure guidelines for tumour PET imaging: version 1.0. Eur J Nucl Med Mol Imaging. 2010;37:181–200.
48. Olsen RV, Munk PL, Lee MJ, Janzen DL, MacKay AL, Xiang QS, Masri B. Metal artifact reduction sequence: early clinical applications. Radiographics. 2000;20:699–712.

Workflow and Practical Logistics

3

N.F. Schwenzer, H. Schmidt, and C.D. Claussen

Contents

N.F. Schwenzer • H. Schmidt • C.D. Claussen (✉)
Department of Radiology, University Hospital Tübingen, Tübingen, Germany
e-mail: claus.claussen@med.uni-tuebingen.de

3.1 Prologue

In contrast to PET/CT, several aspects concerning workflow have to be considered. In the following chapter, patient preparations as well as differences in comparison to PET/CT are discussed (i.e. metal implants, gadolinium-containing contrast agents). Furthermore, protocol recommendations are given for simultaneous as well as sequential MR-PET scanners. New methods for motion correction in PET open up in simultaneous MR-PET imaging. Finally, this new hybrid modality makes great demands on storage media and software solutions for image reading which will be addressed.

The new combination of PET and MRI raises several questions concerning workflow, data acquisition and data management. Especially the reading of the acquired images poses problems since PET/CT hybrid software developed in the last decade has to deal with a variety of new contrasts, functional analysis and regional morphological imaging. Other than in PET/CT imaging, the radiologists and nuclear medicine physicians are confronted with a number of image series for each body region instead of the well-known whole-body scan in PET and especially in CT. Therefore, data handling and visualisation tools need to be developed in order to optimise the workflow of this new hybrid modality.

Apart from reading and evaluation strategies, the conception of suitable MR protocols is essential. As the most common MR sequences are two-dimensional, the choice of the slice

I. Carrio, P. Ros (eds.), *PET/MRI*,
DOI 10.1007/978-3-642-40692-8_3, © Springer-Verlag Berlin Heidelberg 2014

orientation plays a role. Unlike in CT with thin collimation, the two-dimensional MR image quality drops substantially when reformatting MR images originally acquired in axial plane. Alternatively, three-dimensional sequences can be applied, which in turn goes along with longer acquisition times. Thus, the choice of sequence and slice orientation becomes crucial and depends on the preference of the reading physician and also on the needs of the referring clinician, i.e. high-resolution T2-weighted images of the prostate for biopsy or radiation planning.

At the moment, two different approaches for MR-PET imaging are available: first, the sequential approach which resembles the image acquisition of the sequentially performed PET/CT, and, second, the simultaneous approach. Here, the PET and MR acquisition can be performed simultaneously since the PET detector is integrated in the MR scanner. Both approaches require different workflow strategies.

Another challenge is the transfer of MR-PET from research to clinical routine: due to economical considerations in health system, an adequate throughput of patients is mandatory for adopting this new technique. At this point, we are confronted with the fact that high-resolution MR imaging and functional imaging is time consuming, thus limiting the patient number per day. Moreover, MR images are challenging to read due to the higher detail information gained by the excellent soft tissue contrast compared to CT. Thus, reading of MR-PET images certainly will be more time consuming in comparison to PET/CT: even on low-resolution MR images, we are confronted with a variety of anatomical details in several image weightings for each body region so that some organs (e.g. liver) have to be evaluated several times in order to make a conclusive diagnosis.

In light of these considerations, the following questions arise: How much 'morphological' and functional MR imaging do we need? At which time point do we integrate the MR-PET examination in the clinical workup of the patient? Which patient will profit from a MR-PET examination instead of a PET/CT examination?

Another important issue is the attenuation correction of the PET datasets. Since all commonly used MR-based methods for attenuation correction ignore bone, an additional inaccuracy is introduced in the PET quantification, namely, an underestimation of SUV. The severity of underestimation depends on the body region and the attenuation of surrounding tissues.

Concerning patient's safety during the MR-PET examination, several issues have to be addressed especially concerning metallic implants and devices which require special expertise and training of the operating personal.

3.2 What Can We Learn from the PET/CT Workflow?

In PET/CT a sequential workflow approach gained acceptance since it meets several requirements: the fast multi-detector CT gives the base for attenuation correction and offers a fast and robust anatomical imaging. The PET can directly be performed afterwards without repositioning the patient. Thus, in PET/CT two whole-body modalities meet without restraints or mutual interference. Modern PET/CT scanners allow for whole-body examinations within about 20 min depending on the imaging protocols. At the moment, two distinct imaging protocols can be applied:

- CT imaging with low dose (30 mAs, 120 kV) and low resolution which allows for attenuation correction and anatomical localisation of the PET findings.
- CT imaging according to 'CT-alone' diagnostic protocols, i.e. higher dose, contrast application and an additional chest examination in inspiration. Depending on the pathology examined, oral contrast and a muscle relaxant might be applied to improve bowel distension.

Accordingly, different imaging protocols can be applied for MR-PET imaging. First, a very fast imaging protocol is possible with no or very limited 'anatomical' imaging, and, second, a PET acquisition with additional comprehensive MR imaging. Further clinically relevant aspects concerning MR-PET protocols are discussed below.

3.3 Patient Preparation for MR-PET

For MR-PET imaging several workflow aspects can be adopted from PET/CT. This includes comprehensive information about the imaging procedure, especially concerning examination duration, positioning within the scanner and breathing commands. In contrast to PET/CT, the MR component requires additional information about the patient before the examination can take place.

Before the MR-PET examination can be scheduled, it is recommended to acquire all relevant information from the referring physician, especially regarding metallic implants, pace makers, claustrophobia, tinnitus and recent medical history as well as chronic diseases (particularly diabetes). Furthermore, if gadolinium-based contrast media injection is planned, the patient's renal function should be assessed to prevent renal-impaired patients from nephrogenic systemic fibrosis (NSF) which is a systemic fibrosis of the skin and joints. In severe forms, NSF may affect internal organs such as liver and lungs. First reported in 2000, NSF was observed mainly in patients on dialysis. In 2006 a strong association with gadolinium-based contrast medium administration was described [14]. Therefore, guidelines for gadolinium-based contrast application have been proposed by the European Society of Urogenital Radiology (ESUR) ('guidelines on contrast media' v7.0 2008 www.ESUR.org) and by the American College of Radiology (ACR) ('*manual on contrast media*' v7 ISBN: 978-1-55903-050-2 2010). They recommend identifying high-risk groups: Patients at highest risk are those who have severe chronic kidney disease (generally defined as patients who have eGFRs of <30 ml/min/1.73 m^2) or acute kidney injury [23]. If the administration of contrast is mandatory in a high-risk patient, the patient as well as the referring physician need to be informed about the potential risk. Of course, the lowest clinical possible dose of contrast media should be administered. As gadolinium-based MR contrast agents have different risk profile for NSF, those with the lowest risk for NSF should be preferred (see Table 3.1). In case of contrast administration, a history of previous allergic reaction following injection of gadolinium-containing contrast agents needs to be obtained.

Table 3.1 Groups of contrast agents sorted by incidence of NSF cases

Group I: Agents associated with the greatest number of NSF cases
Gadodiamide (Omniscan®, GE Healthcare)
Gadopentetate dimeglumine (Magnevist®, Bayer HealthCare Pharmaceuticals)
Gadoversetamide (OptiMARK®, Covidien)
Group II: Agents associated with few, if any, unconfounded cases of NSF
Gadobenate dimeglumine (MultiHance®, Bracco Diagnostics)
Gadoteridol (ProHance®, Bracco Diagnostics)
Gadoteric acid (Dotarem®, Guerbet)—as of this writing not FDA-approved for use in the USA
Gadobutrol (Gadavist® in the USA, Gadovist® in other parts of the world—Bayer HealthCare Pharmaceuticals)
Group III: Agents which have only recently appeared on the market
Gadofosveset (Ablavar®, Lantheus Medical Imaging)[a]
Gadoxetic acid (Eovist® in the USA, Primovist® in other parts of the world—Bayer HealthCare Pharmaceuticals)[a]

Adapted after the ACR manual on contrast media 2010
[a]Limited data for these agents, to date unconfounded cases of NSF

Standard 1.5 and 3 T MR scanners have superconducting magnets which means that the static magnetic field in the MR-PET suite is always active. Therefore, it is mandatory to keep all ferromagnetic items in an adequate distance from the scanner. The greatest danger in an MRI suite is the so-called missile effect which refers to the strength of strong magnetic fields to attract ferromagnetic objects. These missiles pose a substantial risk for the patient and the operating personnel. Furthermore, metallic objects have the potential risk of heating by the time-varying magnetic fields during the MR examination [8]. Therefore, all metallic objects (watches, hearing aids, body piercings, jewellery, eyeglasses, metal containing clothes, etc.) should be removed. Additionally, skin-to-skin contact points should be avoided during the examination to prevent the

formation of 'closed loops' inside the patient's body since body tissue is conductive. Only MR safe monitoring devices should be used within the MR-PET suite. All other conductive materials the patient may come with should be removed (ECG, EEG leads, cables, wires, etc.). Cables or wires which have to remain within the scanner must not form conductive loops. Before the examination, all removable metallic items should be left outside entering the MR-PET suite. Some tattoos and permanent cosmetics (i.e. permanent eyeliner) containing certain types of iron pigments can cause artefacts in the MR image. Furthermore, there are rare reports about tattoos causing burning sensations and skin burns, especially concerning decorative tattoos. Therefore, patients with tattoos need to be informed prior to the examination about the (rare) risk of heating and should be monitored carefully during the examination.

Regarding metallic implants, pacemakers and other devices, most manufacturers offer MR safety information. In urgent cases it might be mandatory to contact the manufacturer if a device or implant is MR safe, especially at 3 T. Ratings concerning MR compatibility can also be found in *Reference Manual for Magnetic Resonance Safety, Implants, and Devices* by Frank G. Shellock or on the website www.mrisafety.com. A comprehensive overview about MRI safety issues can also be found in Shellock and Crues [28].

3.4 Standard Tracer 18F-FDG

In oncological imaging, the standard tracer is 18F-FDG. Therefore, like in PET/CT, patient should fast for about 6 h prior to the examination. Plain water and unsweetened tea is allowed before the examination. Diabetic patients need additional monitoring: shortly before examination blood glucose level should be obtained. For the time of the examination, the blood glucose level should be ≤150 mg/dl [5]. Blood glucose levels above may lead to poor FDG-PET quality. In patients with markedly increased glucose levels, the examination might be rescheduled after consultation of a diabetes specialist. Diabetic patients should not take their diabetes medication near the FDG injection since insulin might cause increased FDG uptake in muscle whereas some oral diabetes medication such as metformin can lead to high bowel uptake of FDG [13].

For FDG injection the patient should be comfortably positioned. Before tracer injection the intravenous access should be flushed with saline to prevent paravasation of the PET tracer. A saline flush after FDG injection is useful to reduce venous retention of FDG which might create artefacts in the PET images. After FDG injection, walking should be avoided to prevent FDG uptake in the musculature. The documentation of patient's weight, injected dose, the residual dose as well as the exact uptake time is critical for a proper image decay correction and SUV uptake calculation [2].

What has to be kept in mind is that patient positioning might take longer in MR-PET than in PET/CT because of the placement of several local MR receive coils. Thus, technical assistants might be exposed to a higher radiation dose from the patient. Regarding the radiation safety, most dosimeters and many radiation shielding equipments are not usable in the scanner room because of the attraction to or interference with the magnetic field. Thus, special shielding equipment might be needed, staff has to be monitored by film dosimeters and contaminations can only be detected by wipe tests so far.

3.5 MR-PET Image Acquisition and Imaging Protocols

3.5.1 Whole-Body Examination

Principally, there are two different approaches to perform a MR-PET examination:

1. A very fast approach comprising the acquisition of the sequence for attenuation correction and the PET acquisition. Thus, a whole-body examination is possible within 15–20 min assuming 2–4 min PET acquisition per bed in simultaneous systems [11]. In sequential systems the time for the attenuation correction has to be added as well as the time for moving

the patient from one part of the scanner to the other.

2. In the second approach additional comprehensive MR imaging is performed. Especially for children, a whole-body examination with high-resolution imaging could be mandatory, since the MR might also be used for surgery planning, e.g. in sarcoma patients. Up to now, there are no standard protocols concerning the choice of sequences. Furthermore, the choice of MR sequences also depends on the scanner architecture (simultaneous versus sequential) since part of the MR imaging can be done during the PET acquisition at the simultaneous scanner systems.

For the simultaneous approach it depends on the duration of the PET acquisition per bed and what kind of MR imaging can be done during PET measurement. Assuming 4–6 min per bed, it is possible to perform T2-weighted STIR (short time inversion recovery) or single shot sequences of the whole body (i.e. HASTE; half Fourier acquisition single shot turbo spin echo). Additional sequences covering a certain region (i.e. T2-weighted imaging of the liver) should be done afterwards or before during the tracer uptake since the position of the MR field of view is restricted by the PET bed which might be different from reasonable anatomical landmarks in MR. Certainly, it is also possible to do additional whole-body MR imaging (e.g. after contrast injection) depending on clinical demands because it might not be possible to perform all whole-body MR sequences during the PET acquisition. A possible whole-body MR-PET protocol for simultaneous MR-PET is given in Table 3.2.

In sequential systems, the time of PET and MRI adds up. Therefore, the MR sequences should be chosen with care to prevent long examination times. It has to be considered that a comprehensive whole-body MR examination easily takes about 1.5 h. Until now, it is a matter of research which MR sequences can be skipped in combining MR and PET. Probably, region-dependent protocols have to be set up as it was supposed by Eiber et al. [12] who suggested an examination protocol for staging of head-and-neck cancer. However, an approach similar to simultaneous MR-PET is thinkable for sequential MR-PET systems: assuming about 8 min for attenuation correction, 25 min for PET acquisition and about 35 min for basic diagnostic MR imaging, the examination time sums up to about 70 min. In comparison to the simultaneous approach, all sequences for MR imaging have to be performed before or after the PET acquisition. A scheme illustrating the image acquisition in simultaneous and sequential MR-PET is given in Figs. 3.1 and 3.2. The user interface of a simultaneous MR-PET scanner is shown in Fig. 3.3.

Table 3.2 Simultaneous MR-PET protocol for whole-body imaging

	Basic examination		'MR-only'		
Body region	Simultaneous with PET		Native	Pre and post contrast (optional)	
Head	AC	STIR cor	FLAIR ax	T1 ax	T1 ax fs post contrast
Neck	AC	STIR cor	STIR ax	T1 fs ax	T1 ax fs post contrast
Thorax	AC	STIR cor	T1 VIBE/STIR ax		T1 ax (VIBE) fs after contrast
Abdomen	AC	STIR cor	T2 ax		Dynamic liver imaging (VIBE)
Pelvis	AC	STIR cor	T2 ax	T1 fs ax	T1 ax fs post contrast
Acquisition time[a]	~25 min		~20–30 min	~25 min	

[a]acquisition time strongly depends on the patient's weight and height. Additional bed positions might be mandatory depending on height and pathology influencing the acquisition time in MR

AC attenuation correction, *STIR* short time inversion recovery, *cor* coronal, *FLAIR* fluid attenuated inversion recovery, *ax* axial, *fs* fat-saturated, *VIBE* volumetric interpolated breath-hold examination

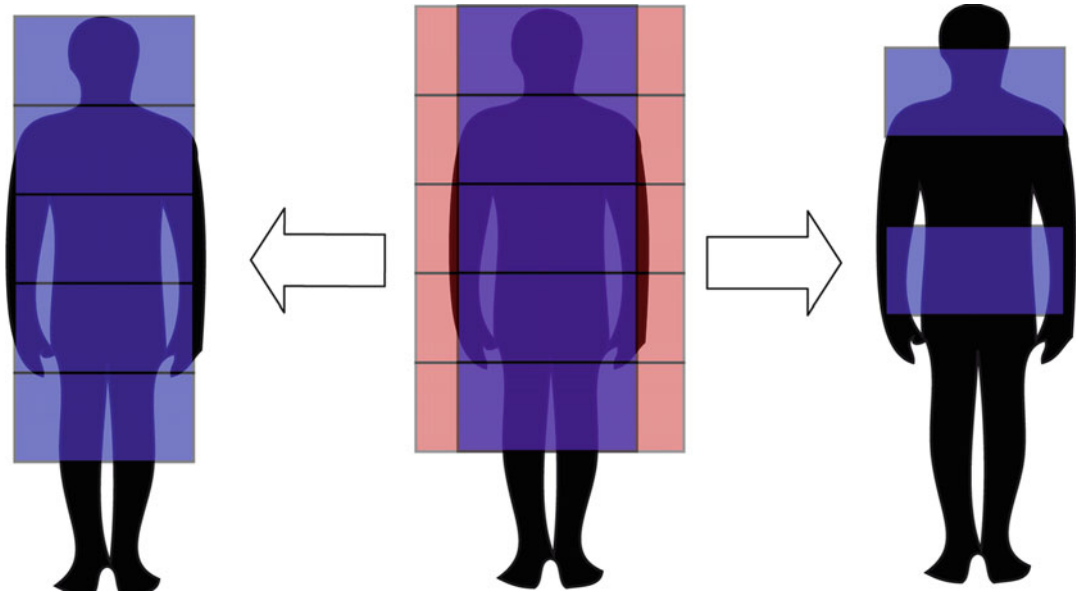

Fig. 3.1 Scheme illustrating the image acquisition in simultaneous MR-PET: first, a simultaneous MR-PET acquisition (including the attenuation correction) is performed (*middle*). Afterwards, either a regional examination (*right*) or an additional whole-body examination (*left*) can be performed comprising MR sequences which could not be performed during PET acquisition due to time constraints

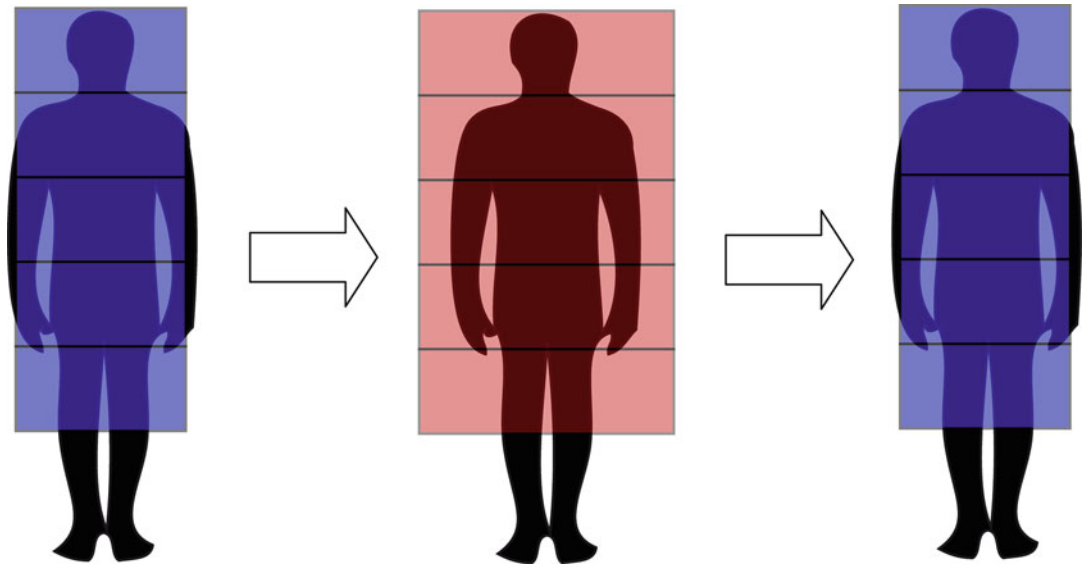

Fig. 3.2 Scheme illustrating the image acquisition in sequential MR-PET: First, MR imaging for attenuation correction (*AC*). Second, the PET acquisition is performed. Third, additional MR imaging can be performed (in this example, a whole-body MR examination)

Concerning the whole-body demands of oncological staging, the limited abilities of MR in lung staging might be critical. On the other hand, in standard PET/CT examinations performed with low-dose CT in expiration, small lung nodules might also be masked, especially in the basal lung. Another problem is calcified nodules which present with low signal in MRI. Therefore, an

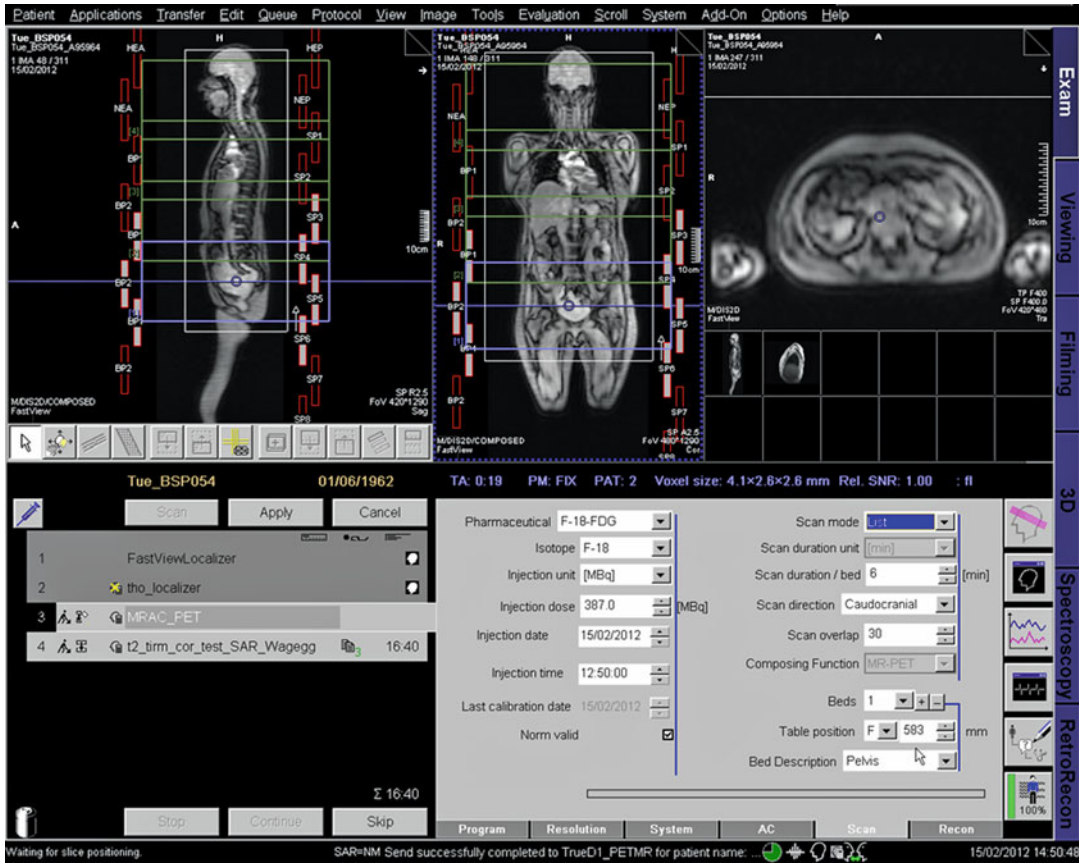

Fig. 3.3 User interface of the Biograph mMR (Siemens Healthcare) allowing for a simultaneous MR-PET examination. In the *upper row*, the MR field of view (*white frame*) as well as the PET field of view (*green frame*) are indicated. In this patient, four beds are planned. The activated bed is indicated by a change in colour (*blue frame*). The *lower row* shows the protocol window for the PET and MR parameters

additional CT of the lung might be necessary depending on the clinical demands.

In every MR-PET protocol sequences for attenuation, correction has to be incorporated. For whole-body examinations, all vendors offer a segmentation-based approach dividing the body in 3 to 4 tissue classes [24, 27]. Here, the question arises, if these sequences should be of low resolution but as fast as possible or if they should also be of diagnostic value. All these MR-based methods do not provide information about the osseous structures, since in conventional MR sequences, cortical bone offers only low signal intensity which makes it difficult to separate bone from air. Furthermore, there is no correlation of MR signal intensity and tissue density as it is known from CT. Since bone is ignored SUV in PET are underestimated to a certain degree with the greatest underestimation within the bone and in the head. Therefore, several groups try to overcome this limitations, for example, by using ultrashort echo time (UTE) sequences to visualise cortical bone [32] or atlas registration methods to predict attenuation maps from the MR images [16]. However, UTE imaging for whole-body examination is rather time demanding, and atlas-based methods suffer from the high anatomical inter-patient variation. Hoffmann et al. proposed a combined pattern recognition and atlas registration method [15] to overcome these problems but this method is computational demanding and still under investigation. The

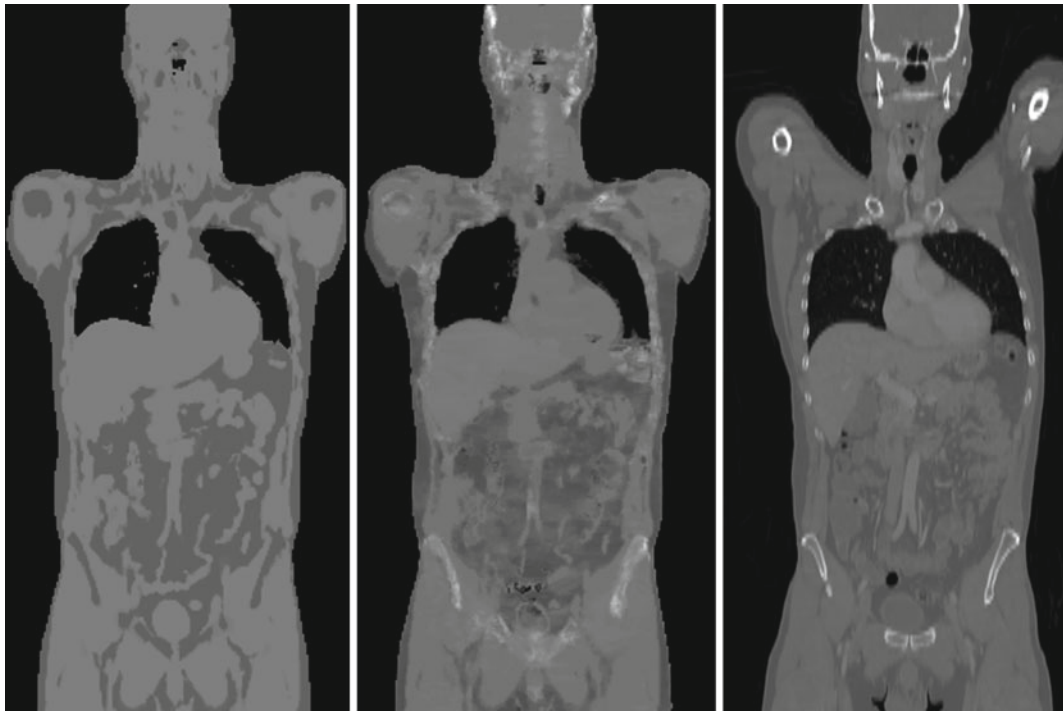

Fig. 3.4 Different types of MR-based attenuation maps for PET attenuation correction. *Left*: Attenuation map from MR-based segmentation. Different attenuation values are assigned to fat, soft tissue and lung; bone is ignored. *Middle*: Attenuation map based on atlas and pattern recognition. The image shows a more CT-like appearance with visible bone structures. Bone structures are visible here. *Right*: CT image of the same patient

problem of PET attenuation correction also leads to a reduced number of available MR coils and positioning aids for simultaneous systems, since these have to be optimised for minimum PET attenuation and/or corrected during image reconstruction [21, 22, 29]. An example of MR-based attenuation maps is given in Fig. 3.4.

3.5.2 MR-PET Examination of the Head

For examinations of the brain, more time can be invested for the PET acquisition since the head can be covered with one bed position. In this setting, the simultaneous PET and MR acquisition offers the possibility to perform a dynamic PET measurement during MR scanning. This approach is time effective and offers new possibilities for neurological research. However, especially for brain imaging and quantification sophisticated attenuation correction methods for PET are mandatory. Until now, all vendors offer segmentation-based methods for attenuation correction derived from MR images neglecting bony structures. Unfortunately, ignoring the bone leads to a distinct underestimation of PET SUVs severely limiting the PET quantification in MR-PET imaging. However, in case of brain imaging UTE measurements of cortical bone is feasible because only one bed position is usually acquired. For whole-body imaging UTE is not implemented so far. Furthermore, atlas methods can be used because of a reduced inter-patient variability in the head region.

3.6 Motion Correction for PET

There are several studies which underline the importance of motion correction in PET. It is known that especially respiratory motion can have a significant impact on static oncological PET/CT imaging of the thorax or upper abdomen where

SUV measurements are important for therapy response monitoring. Regarding the acquisition times of several minutes in PET, breath-hold acquisitions are impractical. Additionally, misalignments between the free-breathing PET and breath-hold CT acquisition can occur leading to difficult lesion identifications and incorrect PET attenuation correction maps. Different methods have been developed to manage respiratory motion in PET/CT, i.e. respiratory gating, use of external devices, examinations under breath-hold or several post-processing methods [1, 3, 6, 7, 9, 18–20, 25, 26]. The simplest approach is gating of PET data and using only data from a dedicated respiratory position for image reconstruction. However, this leads to a reduced number of counts and thus a decreased SNR in the resulting PET image. If all counts should be maintained, a description of the respiration-induced anatomical deformations is required and has to be applied after or during PET image reconstruction. These motion descriptions can be derived from PET data itself, however, the used radiotracer has to show enough background activity. Determination of motion from 4D CT scans is also possible but at the cost of increased ionisation radiation. Furthermore, the respiratory motion can change between CT and PET scan. Simultaneous MR-PET scanners offer the possibility to correct for motion using the MR data [4, 10, 17, 30, 31]. Most approaches try to avoid additional devices, i.e. using the 2D navigator from MRI which has to be adapted accordingly. However, if the MR scanner is used for motion detection for a substantial time, it is meanwhile blocked to other diagnostic imaging. Data from larger patient studies are missing on this evolving field and discussion is still going on about how much accuracy is needed for different clinical questions and how much MR scan time is bearable for motion measurements.

3.7 Software Requirements

In contrast to PET/CT, the amount of image data strongly depends on the chosen examination protocol. Additional MR images mostly cover one region only, i.e. the neck or the liver. The same holds true for additional functional imaging such as dynamic contrast-enhanced imaging of a region of interest. Therefore, fusion software has to be adapted for MR-PET reading since time-efficient navigation through this huge amount of data is important for the acceptance of this method in clinical settings. Furthermore, quantification of standardised parameters should be provided in PET and MRI. This includes region of interest or volume-of-interest SUV measurements as well as signal intensity and size measurements in MRI as basic demands. Additional functional MR analysis needs to be integrated in a reasonable manner. Preferably, it should be possible to arrange and superpose the MR sequences and PET by drag and drop. Since most fusion software solutions are adopted from PET/CT, none of the existing software is ideally suited to solve these problems in MR-PET up to now.

Conclusion

Overall, a lot of questions remain regarding MR-PET workflow. In the next years the amount of anatomical and functional imaging especially needed from the MR part has to be investigated. This is a crucial question since this does not only affect the measurement time but also the time needed for clinical reading of the data and thus the overall throughput of the systems. Also, prospective clinical studies have to address the question of potential patient collectives that benefit from this modality. The staff must be able to deal with both MR and nuclear medical applications and have to be familiar with radiation as well as MR safety aspects. Several problems have to be addressed regarding optimisation of MR-based attenuation and motion correction. Simultaneous acquisition of dynamic PET and functional MRI scans like perfusion measurements have the potential to give important insights into biochemical and metabolic processes but also generate a challenging demand on MR-PET workflow aspects.

References

1. Bai W, Brady M. Motion correction and attenuation correction for respiratory gated PET images. IEEE Trans Med Imaging. 2011;30:351–65.

2. Boellaard R. Standards for PET image acquisition and quantitative data analysis. J Nucl Med. 2009;50 Suppl 1:11S–20.
3. Buther F, Dawood M, Stegger L, et al. List mode-driven cardiac and respiratory gating in PET. J Nucl Med. 2009;50:674–81.
4. Catana C, Benner T, van der Kouwe A, et al. MRI-assisted PET motion correction for neurologic studies in an integrated MR-PET scanner. J Nucl Med. 2011;52:154–61.
5. Coleman RE. Clinical PET in oncology. Clin Positron Imaging. 1998;1:15–30.
6. Dawood M, Buther F, Lang N, et al. Respiratory gating in positron emission tomography: a quantitative comparison of different gating schemes. Med Phys. 2007;34:3067–76.
7. Dawood M, Buther F, Jiang X, et al. Respiratory motion correction in 3-D PET data with advanced optical flow algorithms. IEEE Trans Med Imaging. 2008;27:1164–75.
8. Dempsey MF, Condon B. Thermal injuries associated with MRI. Clin Radiol. 2001;56:457–65.
9. Dikaios N, Fryer TD. Improved motion-compensated image reconstruction for PET using sensitivity correction per respiratory gate and an approximate tube-of-response backprojector. Med Phys. 2011;38:4958–70.
10. Dikaios N, Izquierdo-Garcia D, Graves MJ, et al. MRI-based motion correction of thoracic PET: initial comparison of acquisition protocols and correction strategies suitable for simultaneous PET/MRI systems. Eur Radiol. 2012;22:439–46.
11. Eiber M, Martinez-Moller A, Souvatzoglou M, et al. Value of a Dixon-based MR/PET attenuation correction sequence for the localization and evaluation of PET-positive lesions. Eur J Nucl Med Mol Imaging. 2011;38:1691–701.
12. Eiber M, Souvatzoglou M, Pickhard A, et al. Simulation of a MR-PET protocol for staging of head-and-neck cancer including Dixon MR for attenuation correction. Eur J Radiol. 2012;81(10):2658–65.
13. Gontier E, Fourme E, Wartski M, et al. High and typical 18F-FDG bowel uptake in patients treated with metformin. Eur J Nucl Med Mol Imaging. 2008;35:95–9.
14. Grobner T. Gadolinium–a specific trigger for the development of nephrogenic fibrosing dermopathy and nephrogenic systemic fibrosis? Nephrol Dial Transplant. 2006;21:1104–8.
15. Hofmann M, Steinke F, Scheel V, et al. MRI-based attenuation correction for PET/MRI: a novel approach combining pattern recognition and atlas registration. J Nucl Med. 2008;49:1875–83.
16. Keereman V, Fierens Y, Broux T, et al. MRI-based attenuation correction for PET/MRI using ultrashort echo time sequences. J Nucl Med. 2010;51:812–18.
17. King AP, Buerger C, Tsoumpas C, et al. Thoracic respiratory motion estimation from MRI using a statistical model and a 2-D image navigator. Med Image Anal. 2012;16:252–64.
18. Koshino K, Watabe H, Hasegawa S, et al. Development of motion correction technique for cardiac (15) O-water PET study using an optical motion tracking system. Ann Nucl Med. 2010;24:1–11.
19. Lamare F, Ledesma Carbayo MJ, Cresson T, et al. List-mode-based reconstruction for respiratory motion correction in PET using non-rigid body transformations. Phys Med Biol. 2007;52:5187–204.
20. Liu C, Pierce 2nd LA, Alessio AM, et al. The impact of respiratory motion on tumor quantification and delineation in static PET/CT imaging. Phys Med Biol. 2009;54:7345–62.
21. MacDonald LR, Kohlmyer S, Liu C, et al. Effects of MR surface coils on PET quantification. Med Phys. 2011;38:2948–56.
22. Mantlik F, Hofmann M, Werner MK, et al. The effect of patient positioning aids on PET quantification in PET/MR imaging. Eur J Nucl Med Mol Imaging. 2011;38:920–9.
23. Marckmann P, Skov L, Rossen K, et al. Nephrogenic systemic fibrosis: suspected causative role of gadodiamide used for contrast-enhanced magnetic resonance imaging. J Am Soc Nephrol. 2006;17:2359–62.
24. Martinez-Moller A, Souvatzoglou M, Delso G, et al. Tissue classification as a potential approach for attenuation correction in whole-body PET/MRI: evaluation with PET/CT data. J Nucl Med. 2009;50:520–6.
25. Nehmeh SA, Erdi YE, Ling CC, et al. Effect of respiratory gating on quantifying PET images of lung cancer. J Nucl Med. 2002;43:876–81.
26. Nehmeh SA, Erdi YE, Meirelles GS, et al. Deep-inspiration breath-hold PET/CT of the thorax. J Nucl Med. 2007;48:22–6.
27. Schulz V, Torres-Espallardo I, Renisch S, et al. Automatic, three-segment, MR-based attenuation correction for whole-body PET/MR data. Eur J Nucl Med Mol Imaging. 2011;38:138–52.
28. Shellock FG, Crues JV. MR procedures: biologic effects, safety, and patient care. Radiology. 2004;232:635–52.
29. Tellmann L, Quick HH, Bockisch A, et al. The effect of MR surface coils on PET quantification in whole-body PET/MR: results from a pseudo-PET/MR phantom study. Med Phys. 2011;38:2795–805.
30. Tsoumpas C, Mackewn JE, Halsted P, et al. Simultaneous PET-MR acquisition and MR-derived motion fields for correction of non-rigid motion in PET. Ann Nucl Med. 2010;24:745–50.
31. Tsoumpas C, Buerger C, King AP, et al. Fast generation of 4D PET-MR data from real dynamic MR acquisitions. Phys Med Biol. 2011;56:6597–613.
32. Tyler DJ, Robson MD, Henkelman RM, et al. Magnetic resonance imaging with ultrashort TE (UTE) PULSE sequences: technical considerations. J Magn Reson Imaging. 2007;25:279–89.

MR-PET in Breast Cancer

4

Christian Buchbender, Thomas C. Lauenstein, Andreas Bockisch, Gerald Antoch, and Till A. Heusner

Contents

C. Buchbender, MD • G. Antoch, MD (✉)
T.A. Heusner, MD
Department of Diagnostic and Interventional Radiology, University of Dusseldorf,
D-40225 Dusseldorf, Germany
e-mail: christian.buchbender@med.uni-duesseldorf.de; antoch@med.uni-duesseldorf.de; heusner@med.uni-duesseldorf.de

T.C. Lauenstein, MD
Department of Diagnostic and Interventional Radiology and Neuroradiology,
University of Duisburg-Essen,
D-45147 Essen, Germany
e-mail: thomas.lauenstein@uk-essen.de

A. Bockisch, MD, PhD
Department of Nuclear Medicine,
University of Duisburg-Essen,
D-45147 Essen, Germany
e-mail: andreas.bockisch@uk-essen.de

Abstract

Breast cancer is a common cancer entity in Western countries and represents a major public health problem. A specific therapy and, therefore, chance for and duration of survival is strongly dependent on the cancer stage, for which reason an accurate staging is indispensable. This chapter describes the use and limitations of whole-body MR-PET imaging for staging the primary tumor, locoregional lymph nodes, as well as distant metastases. A dedicated whole-body MR-PET protocol is introduced, considering specific demands of breast cancer patients, including MR-PET

I. Carrio, P. Ros (eds.), *PET/MRI*,
DOI 10.1007/978-3-642-40692-8_4,

mammography. Moreover, aspects of MR imaging and functional FDG-PET are discussed with regard to restaging and treatment monitoring.

4.1 Introduction/Epidemiology

Breast cancer is a common cancer entity in Western countries and represents a major public health problem. In women it is the most frequent cancer entity and the second leading cause of cancer-related deaths [28]. The risk of a woman to develop breast cancer until the 74th year of life is about 8 %. In Europe breast cancer is diagnosed in more than 370,000 women each year accounting for about 30 % of all newly diagnosed cancer diseases in women. Approximately 130,000 women between 35 and 55 years die from breast cancer in Europe annually. These data emphasize that breast cancer represents a cancer entity that involves not only the elderly but also a high number of younger patients. The morbidity as well as survival of breast cancer patients is inversely correlated with the extension of the disease (size of the primary tumor, presence of metastatic lesions) [42]. For an overview of the TNM staging system, see Table 4.1. Axillary lymph node metastases have an effect on the prognosis of a breast cancer patient. The 10-year survival rate in patients with axillary lymph node metastases depends on the number of involved nodes and ranges from 30 % (>10 nodes) to 70 % (1–3 nodes) compared to 90 % in those patients without lymph node involvement. This chapter addresses the indication of MR-PET for staging, restaging, and treatment monitoring of breast cancer patients.

4.2 Initial Staging

4.2.1 Diagnostic Procedures for Initial Staging

Breast cancer patients are currently investigated using a multimodality, multistep imaging algorithm that includes X-ray mammography, breast

Table 4.1 TNM stage and anatomic stage/prognostic groups according to the American Joint Committee on Cancer (AJCC) Staging Manual, 7th edition

Primary tumor (T)	
TX	Primary tumor cannot be assessed
T0	No evidence of primary tumor
Tis	Carcinoma in situ
Tis (DCIS)	Ductal carcinoma in situ
Tis (LCIS)	Lobular carcinoma in situ
Tis (Paget's)	Paget's disease of the nipple not associated with invasive carcinoma and/or carcinoma in situ in the underlying breast parenchyma
T1	≤20 mm in greatest dimension
T1mi	≤1 mm in greatest dimension
T1a	>1 mm but ≤5 mm in greatest dimension
T1b	>5 mm but ≤10 mm in greatest dimension
T1c	>10 mm but ≤20 mm in greatest dimension
T2	>20 mm but ≤50 mm in greatest dimension
T3	>50 mm in greatest dimension
T4	Any size with direct extension to the chest wall and/or to the skin (ulceration or skin nodules)
T4a	Extension to the chest wall, not including only pectoralis muscle adherence/invasion
T4b	Ulceration and/or ipsilateral satellite nodules and/or edema (including péau d'órange) of the skin, which do not meet criteria for inflammatory carcinoma
T4c	Both T4a and T4b
T4d	Inflammatory carcinoma
Regional lymph nodes (N), clinical	
NX	Regional lymph nodes cannot be assessed
N0	No regional lymph node metastases
N1	Metastases to moveable ipsilateral level I, II axillary lymph node(s)
N2	Metastases in ipsilateral level I, II axillary lymph nodes that are clinically fixed or matted, or in clinically detected (e.g., by imaging studies) ipsilateral internal mammary nodes in the absence of clinically evident axillary lymph node metastases
N2a	Metastases in ipsilateral level I, II axillary lymph nodes fixed to one another (matted) or to other structures

Table 4.1 (continued)

N2b	Metastases only in clinically detected (e.g., by imaging studies) ipsilateral internal mammary lymph nodes and in the absence of clinically evident level I, II axillary lymph node metastases
N3	Metastases in ipsilateral infraclavicular (level III axillary) lymph node(s) with or without level I, II axillary lymph node involvement, or in clinically (e.g., by imaging) detected ipsilateral internal mammary lymph node(s) with clinically evident level I, II axillary lymph node metastases, or metastases in ipsilateral supraclavicular lymph node(s) with or without axillary or internal mammary lymph node involvement
N3a	Metastases in ipsilateral infraclavicular lymph node(s)
N3b	Metastases in ipsilateral internal mammary lymph node(s) and axillary lymph node(s)
N3c	Metastases in ipsilateral supraclavicular lymph node(s)
Distant metastases (M)	
M0	No clinical or radiographic evidence of distant metastases
cM0(I+)	No clinical or radiographic evidence of distant metastases, but deposits of molecularly or microscopically detected tumor cells in circulating blood, bone marrow, or other nonregional nodal tissue that are no larger than 0.2 mm in a patient without symptoms or signs of metastases
M1	Distant detectable metastases as determined by classic clinical and radiographic means and/or histologically proven larger than 0.2 mm

Anatomic stage/prognostic groups

Stage	T	N	M
0	Tis	N0	M0
IA	T1	N0	M0
IB	T0	N1mi	M0
	T1	N1mi	M0
IIA	T0	N1	M0
	T1	M1	M0
	T2	N0	M0
IIB	T2	N1	M0
	T3	N0	M0
IIIA	T0	N2	M0
	T1	N2	M0
	T2	N2	M0
	T3	N1	M0
	T3	N2	M0
IIIB	T4	N0	M0
	T4	N1	M0
	T4	N2	M0
IIIC	Any T	N3	M0
IV	Any T	Any N	M1

ultrasound, chest X-ray, ultrasound of the liver, bone scintigraphy, as well as invasive staging procedures in most European countries [30]. These invasive procedures include breast lesion biopsies, sentinel lymph node biopsy (SLNB), and axillary lymph node dissection (ALND). Cross-sectional imaging procedures such as computed tomography (CT), magnetic resonance imaging (MRI), positron emission tomography (PET), positron emission tomography/computed tomography (PET/CT), or magnetic resonance imaging/positron emission tomography (MR-PET) may be added to or replace some procedures of the established algorithm. Imaging guidelines differ from country to country and in-between different societies.

4.2.2 Evaluation of the Primary Tumor

4.2.2.1 X-Ray Mammography

X-ray mammography represents the basic investigation of the breasts and may be applied for screening purposes or clinical indication in the case of a symptomatic patient. As in many other cancer entities, the detection of early-stage disease or tumor precursors is highly desirable. For these purposes, X-ray mammography is used routinely. In contrast to other imaging techniques, it is able to detect microcalcifications that are associated with ductal in situ carcinomas. X-ray mammography as a screening tool may reduce the relative morbidity caused by breast cancer in 15 % of patients between 39

and 49 years [48]. European guidelines regarding quality assurance in mammography screening have been published in 2008 standardizing different performance indicators. At least 25 % of all detected invasive breast cancer lesions should measure less than 10 mm, and ductal in situ carcinomas should represent at least 10 % of all detected malignancies [52]. The sensitivity for the detection of breast cancer lesions strongly depends on the density of the breast tissue and ranges between 80 % in fatty breast and 30 % in very dense glandular tissue [39].

4.2.2.2 Ultrasound

Ultrasound using high-frequency transducers also represents a basic investigation for the evaluation of the breast [54]. Especially for the investigation of younger patients with a high proportion of dense glandular tissue, it may be favorable. Ultrasound has a relatively high sensitivity for the detection of invasive disease; for the detection of ductal in situ carcinoma, however, its sensitivity has been reported to be only 50 %. Breast ultrasound represents the imaging modality of choice for unclear clinical findings in young women during pregnancy and lactation. Especially for the identification of cysts within breast tissue, ultrasound has been proven a useful modality.

4.2.2.3 Magnetic Resonance Mammography (MR Mammography)

MR mammography is a very sensitive imaging method for the detection of primary lesions by using morphological and functional parameters [34, 35]. In the beginning, breast MRI suffered from limited specificity and positive predictive value for detection of invasive breast carcinomas but has reached a high specific level for the characterization of breast malignancies since then, offering a powerful diagnostic tool for breast imaging. The grade of specificity strongly depends on the readers' expertise and the use of adequate techniques [34, 35]. This holds true not only for initial lesion detection but also for the clarification of equivocal findings within other imaging methods, for the detection of synchronous carcinoma in the contralateral breast, as well as for the correct characterization of the architecture of a breast cancer lesion (solitary vs. multifocal vs. multicentric lesion). MR mammography performed in addition to X-ray mammography is able to further enhance the sensitivity for the detection of invasive breast cancer lesions as well as for the characterization of the extent of ductal carcinomas in situ. In 2008 the European Society of Breast Imaging (EUSOBI) delivered practical guidelines to ensure reliable breast imaging by MRI [40]. These guidelines defined indications and performance instructions for breast MRI. The most important indications were problem solving in case of inconclusive findings on conventional imaging, screening of the contralateral breast in women with histological evidence of unilateral breast cancer, evaluation of the breasts in case of metastases of an unknown primary carcinoma, evaluation of therapeutic response in patients treated with neoadjuvant chemotherapy, exclusion of local recurrence after breast-conserving surgery, and screening of women with a lifetime risk of 20 % or more to develop breast cancer (e.g., mutation carriers). Important performance instructions given by the EUSOBI are the following: A dedicated bilateral breast coil is mandatory for MR mammography; the spatial and temporal resolution must be sufficient; a T1-weighted sequence should be acquired at a minimum of three time points (one prior and two after contrast agent administration); reporting should be performed by a radiologist with experience in breast MRI, using the American College of Radiology (ACR) BI-RADS MRI lexicon; and MRI-guided breast biopsy should be available [40].

4.2.2.4 FDG-PET Mammography and FDG-PET/CT Mammography

[18F]-fluoro-deoxyglucose (FDG)-PET/CT is able to depict the primary tumor, although it is hampered by some substantial limitations: In one of the first key publications, Avril and colleagues demonstrated that many smaller tumors could not be imaged reliably by FDG-PET; pT1 tumors were detected with a sensitivity of only 68.2 %, whereas the sensitivity reached a level

of more than 90 % in pT2 tumors [4]. Partial volume effects as well as a varying metabolic activity due to histopathological tumor type were the most important factors for this limited sensitivity [4, 20]. In another study on 40 women using FDG-PET/CT, the detection rate of the untreated primary lesion was higher with a detection rate of 95 % of all breast lesions [27]. This difference most likely was a result of the different study populations investigated; also in this study, the detection rate of pT1b and pT1c cancer lesions was low with 50 and 72 %, respectively. This was the case even though image acquisition had been optimized to the clinical question by applying IV contrast agents with the breast positioned in a special positioning aid [23, 27]. Based on the high diagnostic accuracy and soft tissue resolution provided by MR mammography, FDG-PET/CT today cannot be recommended as the imaging modality of choice for imaging the primary lesion. In cases when the breast is imaged in an FDG-PET/CT scan, the investigation protocol may be optimized by positioning the patient prone ensuring pendant breast positioning leading to a better breast quadrant expansion, a better expansion of the axillary fossa and a separation of the tumor from the thoracic wall [23].

4.2.2.5 MR-PET Mammography

Currently, there is no sufficient data from larger series available regarding the performance of combined MR-PET in imaging primary breast cancer lesions and determining the local tumor extent. In recent years, several publications, however, have been published that deal with the performance of software-based, rigidly or dynamically fused FDG-PET datasets acquired prone and MR mammography datasets [24, 43–45]. Adding the functional FDG-PET information to morphology seems to enhance the specificity and PPV of MR mammography for the detection of malignant breast lesions; Moy and colleagues reported an increase in the specificity from 53 to 97 % by combining MR mammography with FDG-PET to PET/MR mammography. The PPV rose from 77 to 98 % after image fusion in the same study [43]. In opposite to these results, our own group did not find any statistically significant additional value of fusing FDG-PET with MR mammography [21]. Generally, all currently available data are based on small patient populations, inhomogeneities regarding the histopathological subentities, as well as limitations regarding the fusion techniques. Integrated PET/MR systems improve fusion accuracy but are subject to the same limitation when it comes to low PET sensitivity for detection of small breast lesions with FDG. To optimize the MR-PET protocol, it should contain a dedicated breast MR mammography as part of the whole-body MR-PET scan in the future. The design of such a protocol should enclose the recommendations of the EUSOBI guidelines. The protocol in use at our institution including whole-body FDG-MR-PET with integrated FDG-MR-PET mammography is shown in Fig. 4.1. For MR-PET specific reading recommendations have to be developed to classify lesions. These are not available yet. Considering false-negative findings with FDG-PET in small lesions and false positives with FDG-PET in lesions such as fibroadenomas or mastopathy development of these criteria seems of utmost importance [29, 66] (Fig. 4.2). An optimized MR protocol and a radiologist specialized in breast imaging must be considered indispensable for MR-PET reading to ensure correct image interpretation. Our initial experience with combined FDG-MR-PET for the evaluation of the primary tumor gives the impression that adding FDG-PET information to MR mammography does add relevant information to MR regarding the local tumor extent. The combination of FDG-PET and MR mammography can improve the discrimination of invasive and noninvasive breast cancer lesions using dual-time-point measurements: Zytoon et al. reported an increase of the SUVmax in invasive but not in noninvasive breast tumors between a baseline measurement and a follow-up after 16±10 days; the change of the SUVmax may also improve the detection of small tumors, especially in dense breasts [68]. However, lesion detection will primarily rely on MR information rather than PET. In addition, we learned from FDG-PET studies that the amount of FDG uptake is a relevant prognostic factor with higher SUV values indicating a poorer prognosis [61].

Whole-body MR-PET protocol for breast cancer staging	
Step 1: **FDG-MR-PET of the breast**	**Step 2:** **Whole-body FDG-MR-PET**
Prone position Dedicated breast MRI coil Field-of-view: Breasts and axillae	Supine position Body and surface coils Field-of-view: Head to thighs
(a) MR sequence for PET attenuation correction (e.g. DIXON) (b) STIR, axial (c) T2 TSE, axial (d) DWI (b0,500,1,500), axial (e) T1 DCE, axial (6 measurements every 2 min.) Simultaneous PET acquisition (20 min, Listmode)	(a) MR sequence for PET attenuation correction (e.g. DIXON) (b) T1 FLASH, contrast enhanced + fs, axial (c) STIR, sagittal (d) FLAIR, axial (brain) (e) T2 HASTE, axial (thorax) Simultaneous PET acquisition (8 min/bed position, Listmode)

Fig. 4.1 Whole-body FDG-MR-PET investigation protocol with integrated FDG-MR-PET mammography

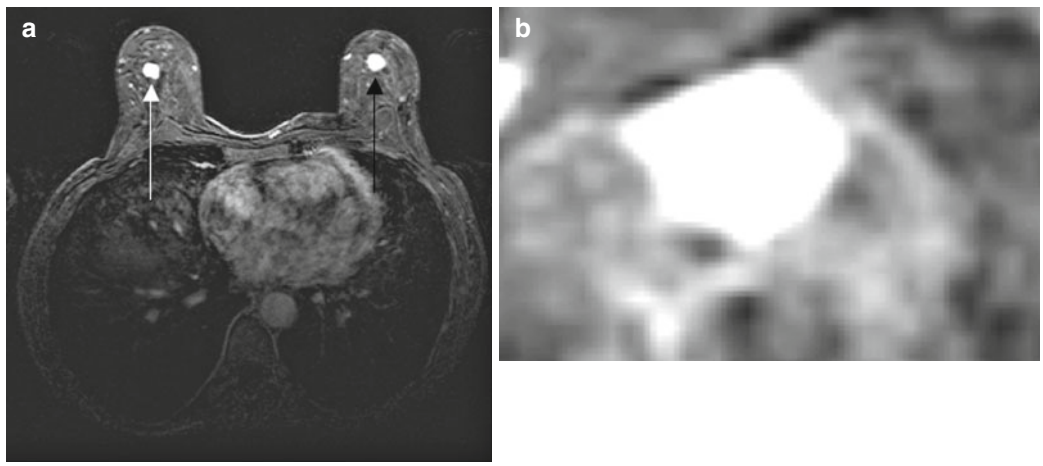

Fig. 4.2 A 49-year-old female with two contrast medium-avid tumors (*arrows*) (one in each breast) on MR (**a**, **b**, **e**). Both tumors were faintly FDG avid on PET (**c**, **f**) and fused FDG-MR-PET (**d**, **g**). Lesion within the left breast: SUVmax 1.6; lesion within the right breast: SUVmax 1.3. Only by a dedicated MR mammography reading taking dynamic contrast behavior into account the left lesion (**b**, **c**, **d**) was suspicious for a malignant carcinoma, whereas the lesion in the right breast was rated as possibly benign (**e**, **f**, **g**). Histopathology after breast-conserving resection revealed a highly differentiated tubular breast carcinoma (pT1c G1) in the left breast and a fibroadenoma in the right breast

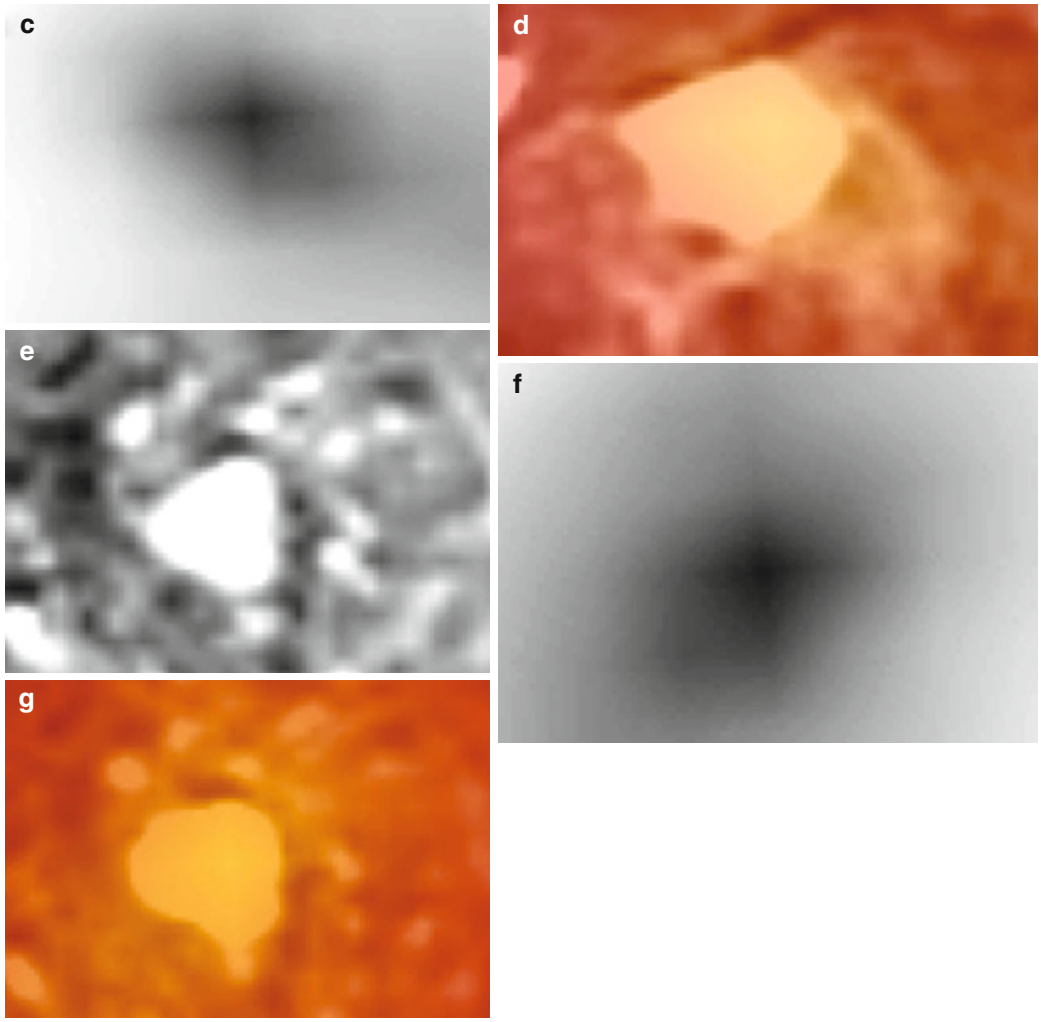

Fig. 4.2 (continued)

This information can be added to other predictors of a poor prognosis like tumor relapse, higher-grade tumors, and hormone receptor negativity [63]. FDG-MR-PET mammography thus not only might determine the local tumor extent but by SUVmax measurements also may help to predict the prognoses of patients. It has to be emphasized that – based on the lack of studies on the subject – the information given in this chapter represents the author's own experience that has been derived from a limited number of patients examined with MR-PET.

4.3 Evaluation of Locoregional Lymph Nodes

4.3.1 Ultrasound

Ultrasound represents a cost-effective noninvasive imaging method with a widespread use. In addition to the clinical examination, it is the standard procedure for the noninvasive axillary investigation. As on every ultrasound examination, its accuracy is strongly investigator dependent. Depending on the investigator's experience as well as on the criteria

defining a lymph node as metastatic, a sensitivity of up to 87 % and a specificity of up to 97 % have been reported [1]. However, small foci of disease may escape detection, even with contrast-enhanced ultrasound techniques [55]. Extra-axillary, locoregional infraclavicular lymph node metastases may be imaged by ultrasound but are not routinely covered. The detection of internal mammary lymph nodes is not possible reliably by ultrasound, if the nodes are not extensively enlarged.

4.3.2 Invasive Staging Procedures: Sentinel Lymph Node Biopsy/ Axillary Lymph Node Dissection

Invasive axillary staging is the most accurate staging modality and cannot be replaced by noninvasive imaging methods. The standard procedure to assess the axillary lymph node status has been ALND for a long time. This procedure is associated with the risk of morbidity such as lymphedema, arm pain, nerve injuries, hematoma, limitations of shoulder movement, and wound infections. A relevant amount of patients can be staged minimally invasively by SLNB. SLNB clearly represents a less invasive procedure compared with ALND. However, it cannot be used in patients with larger tumors, with multifocal or multicentric tumors, with inflammatory breast cancer, and with large ductal carcinoma in situ, after axillary surgery and after breast reconstruction surgery, or in patients with questionable lymph node status on ultrasound. The reason is a negative predictive value below 95 % in those patients for SLNB which is not accepted in most centers. Thus, in those patients, routinely an ALND with the risk of surgery-associated side effects is applied. The addition of a presurgical test such as FDG-PET/CT might triage those patients from unnecessary ALND to SLNB (see below).

4.3.3 PET/CT

The reported sensitivity, specificity, positive predictive value (PPV), negative predictive value (NPV), and accuracy of FDG-PET/CT for axillary lymph node detection are 58, 92, 82, 77, and 79 % [25]; for FDG-PEt alone, data are similar to these results [64]. Also when considering only patients with locally advanced breast cancer, FDG-PET/CT underestimates the amount of locoregional lymph nodes [19]. These data illustrate that FDG-PET/CT is not able to replace invasive staging procedures such as SLNB or ALND. FDG-PET/CT is, as opposed to invasive procedures, not able to detect micrometastatic disease sufficiently. In addition, the FDG uptake of low-grade carcinomas, lobular carcinomas, as well as other histopathological subentities may not be as high as the uptake of invasive ductal carcinomas with false-negative findings [4, 11]. PET/CT may be used to avoid unnecessary ALND in a specific subpopulation of breast cancer patients and to triage those patients to an SLNB if the pre-procedural FDG-PET/CT remains unremarkable for the existence of axillary lymph node metastases [25]. On the other hand, patients with metastases-suspicious findings on FDG-PET/CT may be referred primarily to ALND, based on the high specificity of FDG-PET and FDG-PET/CT.

FDG-PET/CT has been proven to be of favorable diagnostic accuracy for the detection of extra-axillary lymph node metastases compared to other modalities [3]. In a study on 60 patients, Aukema and colleagues investigated intramammary lymph nodes, lymph nodes at the internal mammary chain, intra- and interpectoral lymph nodes, and infraclavicular and mediastinal lymph nodes [3]. They found a direct impact on the clinical management caused by FDG-PET/CT findings.

4.3.4 MR-PET

MR imaging of the axilla can easily be combined with MR mammography imaging [6]. Nevertheless, MRI is – analogously to all other imaging modalities – also not able to compete with SLNB. Currently, MR-PET will also, due to the limited sensitivity of PET and despite current technical improvements such as time-of-flight PET scanning, not be able to replace SLNB or ALND. But most likely MR-PET may be used as a pretest before invasive staging with the chance to avoid unnecessary ALNDs or to triage patients to an immediate

ALNB if extended axillary metastases are detected [25]. When reviewing our initial experience with FDG-MR-PET in breast cancer patients, FDG-MR-PET seems to at least equal to FDG-PET/CT for the detection of axillary lymph node metastases. In individual cases we already experienced that MR-PET may even be of a higher diagnostic accuracy for this task, being in accordance with the results of MRI alone compared to FDG-PET/CT when it comes to the detection of axillary lymph node metastases [10]; however, both modalities have their limitations regarding micrometastases that are not detectable. Morphological criteria such as the small axis diameter of the lymph node, shape of the node, loss of a fatty hilum, central necrosis, or hypervascularization do not apply to micrometastatic disease as does FDG. A expected sensitivity of about 60 % of FDG-MR-PET for the detection of axillary lymph node metastases (on a patient basis) is far away from being "sensitive" (Fig. 4.3). For the detection of extra-axillary metastatic spread, it has to be expected that MR-PET will perform similar to FDG-PET/CT. When searching for lymph node metastases along the internal mammary artery, FDG-PET/CT seems to be of superior capability for detecting smaller metastases; the thinner slice thickness compared to FDG-MR-PET and the lower susceptibility of FDG-PET/CT to breathing artifacts enable for a more accurate detection of small nodes at the joints of the ribs and the sternum. To sum it up, a negative result on FDG-MR-PET regarding axillary or other locoregional lymphatic metastatic spread does not mean that the patient is free of metastases – invasive staging is still required; in the case of lymph nodes that are suspicious for metastatic spread, the chance for metastases is rather high, and invasive procedures are also required.

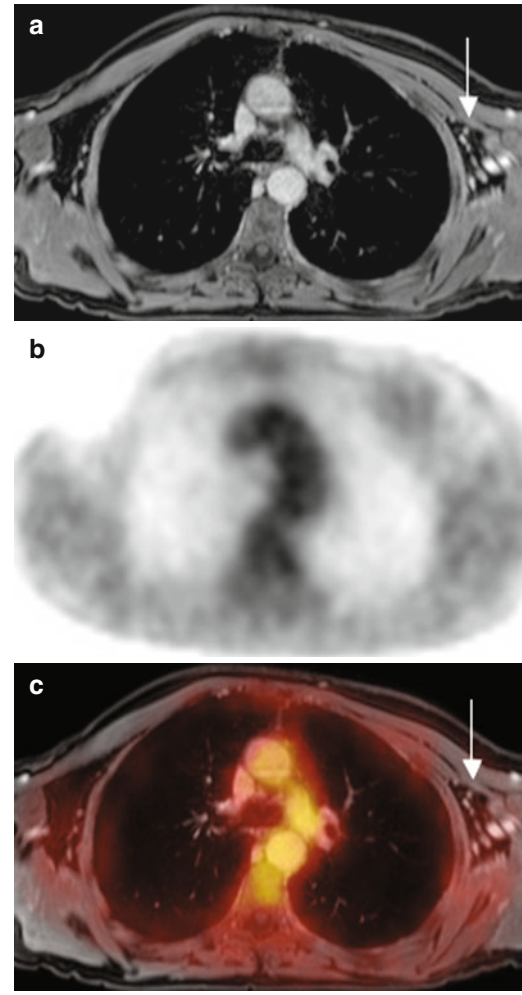

Fig. 4.3 A 65-year-old patient with histopathologically proven ipsilateral axillary lymph node metastases (pN1). Lymph nodes (*arrow*) were neither pathologically enlarged on MR (**a**) (maximum small axis diameter: 8 mm) nor exceedingly FDG avid (SUVmax 1.9) (**b**). FDG-MR-PET rated the axillary lymph nodes falsely as free of metastases (**c**)

4.4 Evaluation of Distant Metastases

4.4.1 PET/CT

FDG-PET/CT has its special diagnostic capability in the detection of distant metastases from breast cancer. Several studies have investigated the diagnostic accuracy of FDG-PET/CT for the detection of metastatic lesions. In a relevant number of patients – up to 12.5 % – the detection of previously unknown metastatic disease by FDG-PET/CT changed the therapeutic management [27]. The detection of additional disease might have consequences regarding the surgical strategy, radiation therapy planning, or switching from a curative intent to a palliative treatment concept. FDG-PET/CT clearly outperforms the conventional

modalities such as bone scintigraphy, ultrasound of the liver, chest X-ray, as well as CT [21, 27, 49]. In contrast to bone scintigraphy which frequently misses a relevant amount of osteolytic metastases (up to 30 %), FDG-PET/CT is able to detect both patterns of osseous metastases, osteolytic and osteoblastic [47].

4.4.2 MR-PET

Although currently no series with larger breast cancer patient numbers exists, MR-PET is expected to be a highly accurate staging tool for distant metastases. This is based on the fact that distant metastases from breast cancer are mainly located in the following compartments: the bone, liver, brain, and to a lower extent in other organs such as the lung. The aforementioned compartments – with the exception of the lung – can be imaged by MRI with a very high accuracy. Previous studies have provided evidence that MRI is superior to FDG-PET/CT when staging the bone, the brain, and the liver [2, 53, 67] (Figs. 4.4, 4.5, and 4.6). This is based on the fact that, on the one hand, these organs normally have a relatively high physiologic, basal FDG uptake, and, on the other hand, MRI with its detailed soft tissue contrast is superior to CT especially when detecting small lesions. Not only the lesion itself but also perifocal edema can be imaged more reliably using MRI by applying water-sensitive sequences. There is striking evidence that for brain imaging an MRI scan is indispensable: In a recently published study on bronchial carcinoma patients, FDG-PET/CT had a sensitivity for the detection of brain metastases of 27.3 % [33]. When searching for liver metastases, false-positive results from misinterpretation of benign tumors should be avoided. In these cases, the PET information will aid the correct diagnosis. The accuracy for the detection of liver metastases can be elevated compared to the use of non-hepatocyte-specific contrast agents if hepatocyte-specific contrast material (gadolinium-ethoxybenzyl-diethylenetriamine pentaacetic acid (Gd-EOB-DTPA), e.g., Primovist™, Bayer HealthCare, or gadobenate dimeglumine (Gd-BOPTA), e.g., MultiHance®, Bracco) is applied. Recent results showed that MRI of the liver using Gd-EOB-DTPA was significantly more accurate than FDG-PET/CT [13]; in this study, the fusion of MRI and FDG-PET datasets led to an increase of sensitivity and diagnostic confidence for the detection of liver metastases as compared to MRI alone. Whole-body MRI alone clearly outperforms the conventional staging algorithm including chest X-ray, ultrasound of the liver, and bone scintigraphy when it comes to the staging of distant metastases [22, 50]. Combining functional FDG-PET information with functional MRI information based on diffusion-weighted imaging (DWI) may be an interesting approach for further enhancing the diagnostic accuracy of MR-PET [26]. DWI alone has been reported to be rather unspecific for the detection of breast cancer metastases. Thus, adding PET data will improve specificity – probably at the cost of sensitivity. Although we only have initial experience with FDG-MR-PET for the detection of distant metastatic disease from breast cancer, our first results seem to be very suggestive for the diagnostic potential of FDG-MR-PET: Several brain metastases were only detected by the MRI part when comparing FDG-MR-PET and FDG-PET/CT; also for liver and bone metastases, this holds true; in the vast majority of the cases, the plain and/or contrast-enhanced MR sequences led to the correct diagnosis. Initial internal results indicate that FDG-MR-PET will lead to an even greater amount of therapeutic changes of breast cancer patients than is it known from FDG-PET/CT; this is mainly based on the fact that FDG-MR-PET is able to detect more distant metastases than other modalities which may change the tumor stage from M0 to M1.

4.5 Follow-Up

If the patient is without any clinical suspicion of tumor recurrence and tumor markers are not elevated after initial breast-conserving treatment, an X-ray mammography combined with ultrasound of the breast is the established method of choice to follow patients up. This algorithm is typically used by half-year periods for the first 3 years and annually thereafter. Ultrasound should cover the breasts as well as the axilla and the thoracic wall. If a local tumor recurrence has to be assumed, an MR mammography can be added. Due to cost

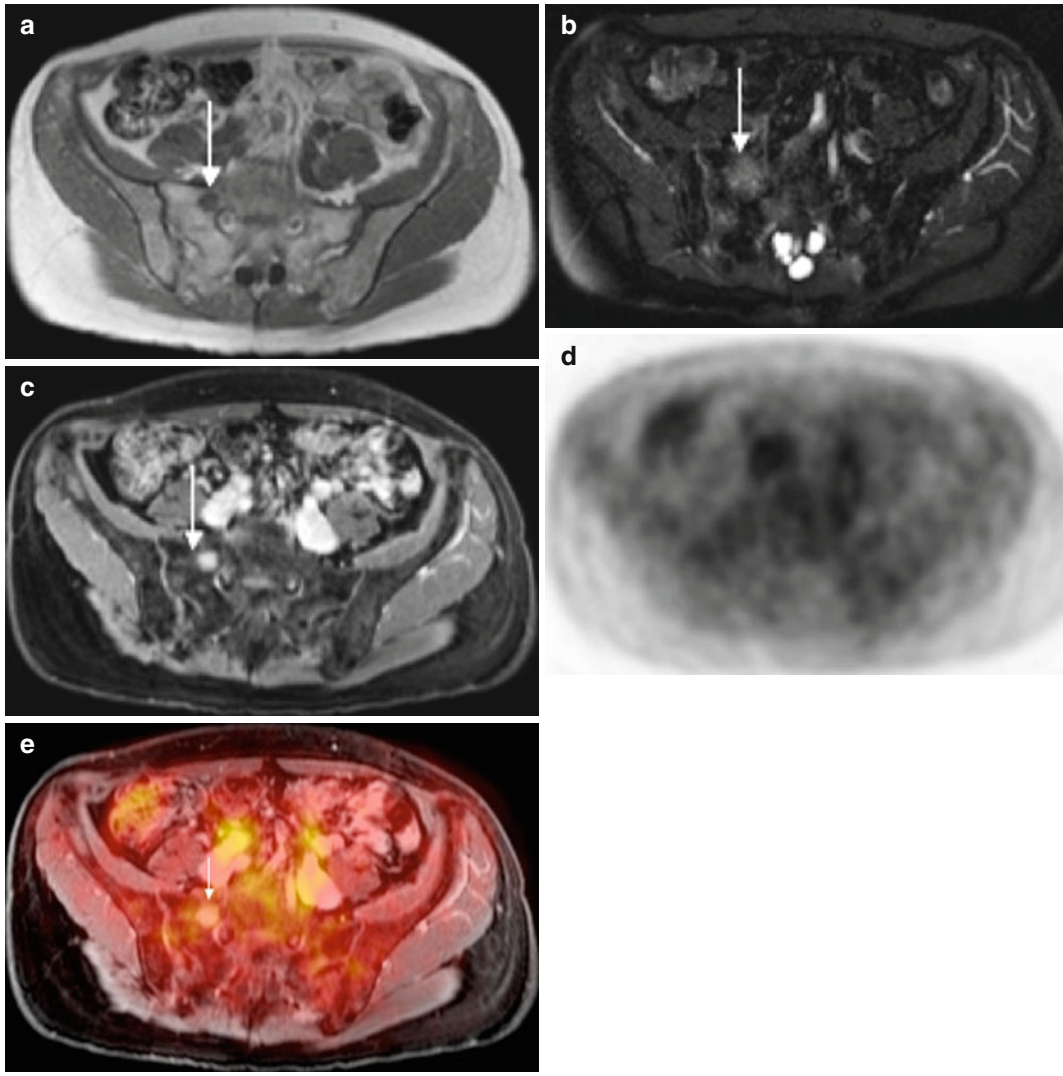

Fig. 4.4 Bone metastasis (*arrow*) of the right sacral bone that shows a typical behavior with a hypointense signal on the plain T1w image (**a**), a hyperintense signal on the images of the STIR sequence (**b**), and contrast material accumulation after IV gadolinium administration (**c**). Although the lesion is not visible on PET (**d**), the typical signal intensity on MR enables the correct classification of this lesion as a metastasis by FDG-MR-PET (**e**)

considerations as well as radiation burden caused by the PET part, MR-PET will not be a first-line modality in the follow-up setting.

4.6 Restaging

In the case of clinically suspected tumor recurrence, the patient has to be restaged. FDG-PET/CT has been proved to be a very accurate modality for whole-body restaging of patients with recurrent breast cancer. A sensitivity, a specificity, a PPV, an NPV, and an accuracy of 96, 91, 92, 95, and 94 % have been reported significantly outperforming FDG-PEt alone [46]. FDG-PET/CT has a great impact on the management of breast cancer patients in whom tumor recurrence is suspected based on the elevation of tumor markers but at the same time shows negative or equivocal findings on conventional imaging modalities

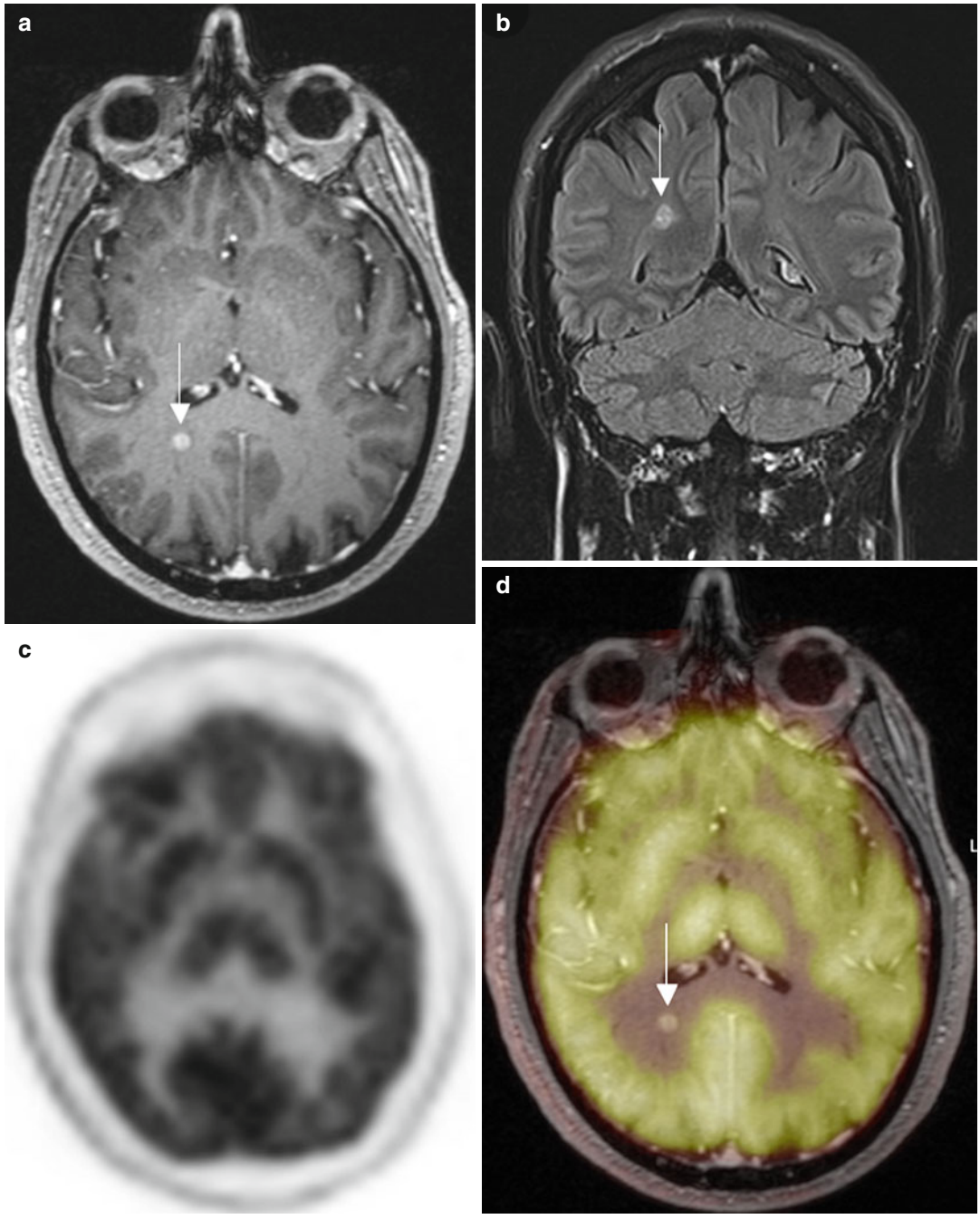

Fig. 4.5 Brain metastasis (*arrow*) in the right occipital lobe that is detectable only by the MR part of combined FDG-MR-PET (**d**). The lesion is visible not only on contrast-enhanced T1w images (**a**) but also on the images of the FLAIR sequence (**b**) that shows the perifocal edema. The metastasis is not FDG avid and thus cannot be detected by stand-alone FDG-PET (**c**) but is clearly depicted by combined MR-PET (**d**). This metastasis was the only distant metastasis in this 52-year-old patient

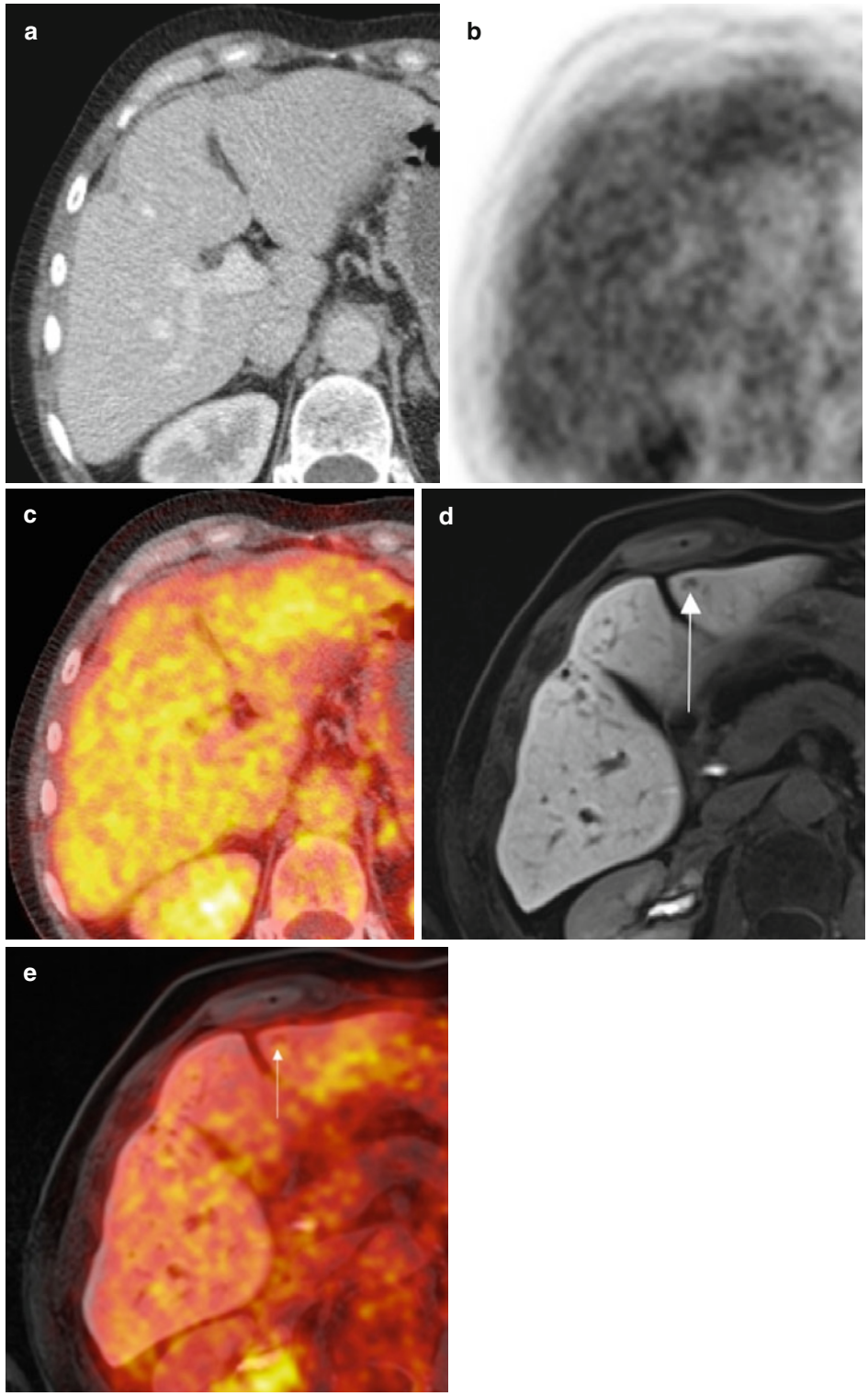

Fig. 4.6 Images of a 58-year-old patient suffering from a carcinoma of the right breast. The liver metastasis in segment 3 was detected neither by ultrasound (not shown) nor by FDG-PET/CT (**a**, **b**, **c**) but is clearly visible (*arrows* in **d**, **e**) through significant washout on Gd-EOB-DTPA-enhanced MR (**d**) and FDG-MR-PET (**e**)

[12, 18, 51, 57]. Today, however, it seems not clear whether FDG-PET/CT should be used as an adjunct to conventional imaging for restaging purposes or even as a replacement [51]. Due to the short time since MR-PET was introduced into clinical routine, currently no studies exist dealing with whole-body MRI or whole-body MR-PET for breast cancer restaging, providing a sufficient follow-up time. Whole-body MRI alone has been shown to represent a robust imaging modality for tumor recurrence imaging [16]. MR-PET is supposed to be at least as powerful as whole-body MRI and FDG-PET/CT because its morphological component undoubtedly has the potential to depict locoregional recurrent lesions with a higher contrast. Moreover, often recurrent metastatic disease is located in compartments such as the bone and liver which can be investigated more accurately by MRI than by CT.

4.7 Therapy Control

Both MR and FDG-PET imaging are excellent methods for neoadjuvant therapy control. MR imaging supplies important morphological information to the surgeon before tumor resection when breast-conserving therapy is the therapy of choice. MR imaging also is able to noninvasively predict pathological complete response to neoadjuvant therapy, to estimate the patients' prognoses, and to detect residual disease, especially in more aggressive cancers [9, 17, 37, 59]. While in the setting of a neoadjuvant chemotherapy the morphological information provided by MR is used to plan surgery, the FDG-PET information is able to predict therapeutic response to neoadjuvant therapy as early as after one or two chemotherapy cycles. Thus, with FDG-PET a sufficient response is seen earlier than by using common morphological methods [15, 31, 62]. This very early prediction of an adequate response to therapy is important as only up to 20 % of all patients achieve a pathological complete response [5]. The differentiation of responders from nonresponders has implications to the patients' management: Ineffective therapies with toxic side effects can be stopped and changed to alternative concepts very early, and costs can be saved. MR-PET joins the aforementioned benefits of both kinds of complementary information. A study on DWI furthermore showed the potential of functional MRI parameters to early monitor the response to neoadjuvant treatment [65]. Beyond neoadjuvant chemotherapy, FDG-PET is able to early monitor treatment in metastatic breast cancer disease. It has been reported in the literature that monitoring response to chemotherapy with FDG-PET can be performed as early as after the first cycle of chemotherapy offering optimized patient care by individualizing treatment and avoiding ineffective chemotherapy [14]. The role of whole-body MRI in this setting has to be investigated further. It seems likely that MRI will provide morphological information to allocate lesions to specific organs analogously to low-dose CT scans on PET/CT if only functional follow-up is needed. This may relevantly shorten the duration of the whole-body MR-PET investigation protocol. Though not yet clinical standard, we currently alter our imaging algorithm to FDG-MR-PET mammography when it comes to neoadjuvant therapy control.

4.8 Protocol Considerations: Whole-Body FDG-MR-PET with Integrated FDG-MR-PET Mammography

Generally, the FDG should be applied through a cubital vein at the contralateral side of the tumor to avoid an accumulation in the ipsilateral lymph nodes in case of an extravasation injury. PET scanning should be started 60 min after FDG injection. There are several reports in the literature that indicate the usefulness of scanning the patients even at a later time point (up to 3 h after tracer injection) or to perform two scans to document FDG uptake dynamics. Dual-time-point measurements of the SUVmax (interval 2–3 weeks) can be of value for the discrimination of invasive and noninvasive breast carcinomas as invasive, but not noninvasive, type tumors have been reported to show an increasing SUVmax [68]. Thus, using dual-time-point imaging, the discrimination between noninvasive and invasive cancers can be improved on FDG-PET/CT, inflammatory lesions with its falling

FDG uptake can more reliably be distinguished from malignant lesions, and the sensitivity for the detection of small cancers and cancers in dense breasts can be improved, especially in lesions with a low FDG uptake [7, 8, 36, 38, 41, 58, 69]. Up to 80 min after FDG injection, the tumor standardized uptake value (SUV) is known to behave more or less linearly, so mathematical time corrections are possible [60]. However, defining a clinical whole-body MR-PET scanning protocol, dual-time-point measurements seem to go beyond the tolerable time frame.

In contrast to the more or less restricted technical possibilities on whole-body PET/CT, there are tremendous options on whole-body MR-PET (due to the great variability of sequence parameters) to investigate the entire body of patients with breast cancer. Due to cost and compliance considerations, the protocol has to be limited to the required sequences that cover all demands on a whole-body investigation. A whole-body-MR-PET scan including an MR-PET mammography for initial staging can be divided into two steps and may contain the following sequences (Fig. 4.1):

4.8.1 First Step: Imaging the Breasts

For a thorough evaluation of the breasts, a dedicated prone MR mammography protocol with the use of a dedicated breast coil is essential. To use the complete capability of MR-PET for breast imaging, the protocol should cover the demands of the guidelines of the European Society of Breast Imaging [40]. The scan can be started 60 min after intravenous FDG injection and can be run as a synchronous MR scan and PET scan.

Breasts
- MR sequence for PET attenuation correction (e.g., DIXON)
- STIR, axial
- T2 TSE, axial orientation
- DWI, axial orientation with three diffusion weightings (b0, 500, 1,500)
- Dynamic contrast-enhanced T1w, axial orientation (six measurements per 2 min.) after rapid intravenous bolus injection of a gadolinium-containing contrast agent
- Simultaneous PET data acquisition, 20 min., Listmode

4.8.2 Second Step: Acquisition of Contrast-Enhanced Whole-Body MRI Sequences and Simultaneous FDG-PET Image in Supine Position

Brain
- Fluid-attenuated inversion recovery (FLAIR) sequence, axial orientation

Spine
- Short tau inversion recovery (STIR), sagittal orientation

Entire Body (Brain to Upper Thighs)
- MR sequence for PET attenuation correction (e.g., DIXON)
- T1 FLASH, contrast enhanced, fat suppressed, axial orientation
- T2 HASTE, axial (thorax)
- Simultaneous PET acquisition, 8 min. per bed position, Listmode

4.8.3 Tracers for Breast Cancer Imaging Beyond FDG

Although the broad use of FDG as the standard tracer for imaging breast cancer is well established, it has to be mentioned that other tracers might play a rising role when it comes to hybrid breast cancer imaging. Other tracers are able to more specifically address biological processes, e.g., 18F-3′-fluoro-3′-deoxy-L-thymidine (FLT) for the visualization of the tumor proliferation rate, [18F] fluoromisonidazole (FMISO) to image tumor hypoxia, [18F] annexin V to image apoptosis, matrix-metalloproteinase inhibitors to image matrix degeneration, or 16-[18F] fluorestradiol-17 (FES) to image estrogen receptors [32]. Recently, a study to predict the response to a human epidermal growth factor receptor (HER)-targeted therapy has been published

using C6.5 diabody (C6.5 dB), a noncovalent anti-HER2 single-chain Fv dimer as radiotracer [56]. It has to be awaited which specific tracers will qualify for a broader use in breast cancer patients in the future.

Conclusion

Whole-body FDG-MR-PET with integrated FDG-MR-PET mammography is expected to be a very accurate tool for whole-body breast cancer staging, restaging, and therapy control. Assessing the primary lesion, a radiologist with dedicated experience in breast imaging is indispensable, especially to avoid false-positive results. For assessing the axillary fossa, invasive staging procedures will still be required. However, FDG-MR-PET might help to triage patients either to sentinel lymph node biopsy or to axillary lymph node dissection. For the detection of distant metastases, FDG-MR-PET is expected to outperform other modalities, mainly due to the typical pattern of distant metastatic spread from breast cancer that can be imaged by MR-PET in an outstanding way; initial results definitely account for this estimation. It moreover will prove as very accurate tool for restaging as well as for early therapeutic monitoring in the next years.

References

1. Alvarez S, Anorbe E, et al. Role of sonography in the diagnosis of axillary lymph node metastases in breast cancer: a systematic review. AJR Am J Roentgenol. 2006;186(5):1342–8.
2. Antoch G, Vogt FM, et al. Whole-body dual-modality PET/CT and whole-body MRI for tumor staging in oncology. JAMA. 2003;290(24):3199–206.
3. Aukema TS, Straver ME, et al. Detection of extra-axillary lymph node involvement with FDG PET/CT in patients with stage II-III breast cancer. Eur J Cancer. 2010;46(18):3205–10.
4. Avril N, Rose CA, et al. Breast imaging with positron emission tomography and fluorine-18 fluorodeoxyglucose: use and limitations. J Clin Oncol. 2000; 18(20):3495–502.
5. Avril N, Sassen S, et al. Response to therapy in breast cancer. J Nucl Med. 2009;50 Suppl 1:55S–63.
6. Baltzer PA, Dietzel M, et al. Application of MR mammography beyond local staging: is there a potential to accurately assess axillary lymph nodes? Evaluation of an extended protocol in an initial prospective study. AJR Am J Roentgenol. 2011;196(5):W641–7.
7. Basu S, Mavi A, et al. Implications of standardized uptake value measurements of the primary lesions in proven cases of breast carcinoma with different degree of disease burden at diagnosis: does 2-deoxy-2-[F-18] fluoro-D-glucose-positron emission tomography predict tumor biology? Mol Imaging Biol. 2008;10(1):62–6.
8. Caprio MG, Cangiano A, et al. Dual-time-point [18F]-FDG PET/CT in the diagnostic evaluation of suspicious breast lesions. Radiol Med. 2010;115(2): 215–24.
9. Chen JH, Bahri S, et al. Breast cancer: evaluation of response to neoadjuvant chemotherapy with 3.0-T MR imaging. Radiology. 2011;261(3):735–43.
10. Cooper KL, Meng Y, et al. Positron emission tomography (PET) and magnetic resonance imaging (MRI) for the assessment of axillary lymph node metastases in early breast cancer: systematic review and economic evaluation. Health Technol Assess. 2011;15(4):iii–iv, 1–134.
11. Crippa F, Agresti R, et al. Prospective evaluation of fluorine-18-FDG PET in presurgical staging of the axilla in breast cancer. J Nucl Med. 1998;39(1):4–8.
12. Dirisamer A, Halpern BS, et al. Integrated contrast-enhanced diagnostic whole-body PET/CT as a first-line restaging modality in patients with suspected metastatic recurrence of breast cancer. Eur J Radiol. 2010;73(2):294–9.
13. Donati OF, Hany TF, et al. Value of retrospective fusion of PET and MR images in detection of hepatic metastases: comparison with 18F-FDG PET/CT and Gd-EOB-DTPA-enhanced MRI. J Nucl Med. 2010;51(5):692–9.
14. Dose Schwarz J, Bader M, et al. Early prediction of response to chemotherapy in metastatic breast cancer using sequential 18F-FDG PET. J Nucl Med. 2005;46(7):1144–50.
15. Duch J, Fuster D, et al. 18F-FDG PET/CT for early prediction of response to neoadjuvant chemotherapy in breast cancer. Eur J Nucl Med Mol Imaging. 2009;36(10):1551–7.
16. Eiber M, Holzapfel K, et al. Whole-body MRI including diffusion-weighted imaging (DWI) for patients with recurring prostate cancer: technical feasibility and assessment of lesion conspicuity in DWI. J Magn Reson Imaging. 2011;33(5):1160–70.
17. Fangberget A, Nilsen LB, et al. Neoadjuvant chemotherapy in breast cancer-response evaluation and prediction of response to treatment using dynamic contrast-enhanced and diffusion-weighted MR imaging. Eur Radiol. 2011;21(6):1188–99.
18. Filippi V, Malamitsi J, et al. The impact of FDG-PET/CT on the management of breast cancer patients with elevated tumor markers and negative or equivocal conventional imaging modalities. Nucl Med Commun. 2011;32(2):85–90.
19. Fuster D, Duch J, et al. Preoperative staging of large primary breast cancer with [18F]fluorodeoxyglucose

positron emission tomography/computed tomography compared with conventional imaging procedures. J Clin Oncol. 2008;26(29):4746–51.
20. Grabellus F, Sheu SY, et al. The XbaI G>T polymorphism of the glucose transporter 1 gene modulates 18F-FDG uptake and tumor aggressiveness in breast cancer. J Nucl Med. 2010;51(8):1191–7.
21. Hahn S, Heusner T, et al. Comparison of FDG-PET/CT and bone scintigraphy for detection of bone metastases in breast cancer. Acta Radiol. 2011;52(9):1009–14.
22. Hausmann D, Jochum S, et al. Comparison of the diagnostic accuracy of whole-body MRI and whole-body CT in stage III/IV malignant melanoma. J Dtsch Dermatol Ges. 2011;9(3):212–22.
23. Heusner TA, Freudenberg LS, et al. Whole-body PET/CT-mammography for staging breast cancer: initial results. Br J Radiol. 2008;81(969):743–8.
24. Heusner TA, Hahn S, et al. Diagnostic accuracy of fused positron emission tomography/magnetic resonance mammography: initial results. Br J Radiol. 2011;84(998):126–35.
25. Heusner TA, Kuemmel S, et al. Diagnostic value of full-dose FDG PET/CT for axillary lymph node staging in breast cancer patients. Eur J Nucl Med Mol Imaging. 2009;36(10):1543–50.
26. Heusner TA, Kuemmel S, et al. Diagnostic value of diffusion-weighted magnetic resonance imaging (DWI) compared to FDG PET/CT for whole-body breast cancer staging. Eur J Nucl Med Mol Imaging. 2010;37(6):1077–86.
27. Heusner TA, Kuemmel S, et al. Breast cancer staging in a single session: whole-body PET/CT mammography. J Nucl Med. 2008;49(8):1215–22.
28. Jemal A, Siegel R, et al. Cancer statistics, 2010. CA Cancer J Clin. 2010;60(5):277–300.
29. Kang BJ, Lee JH, et al. Clinical significance of incidental finding of focal activity in the breast at 18F-FDG PET/CT. AJR Am J Roentgenol. 2011;197(2):341–7.
30. Kataja V, Castiglione M. Primary breast cancer: ESMO clinical recommendations for diagnosis, treatment and follow-up. Ann Oncol. 2009;20 Suppl 4:10–4.
31. Keam B, Im SA, et al. Early metabolic response using FDG PET/CT and molecular phenotypes of breast cancer treated with neoadjuvant chemotherapy. BMC Cancer. 2011;11:452.
32. Krause BJ, Schwarzenbock S, et al. Tracers in oncology – preclinical and clinical evaluation. Nuklearmedizin. 2010;49 Suppl 1:S41–5.
33. Kruger S, Mottaghy FM, et al. Brain metastasis in lung cancer. Comparison of cerebral MRI and 18F-FDG-PET/CT for diagnosis in the initial staging. Nuklearmedizin. 2011;50(3):101–6.
34. Kuhl C. The current status of breast MR imaging. Part I. Choice of technique, image interpretation, diagnostic accuracy, and transfer to clinical practice. Radiology. 2007;244(2):356–78.
35. Kuhl CK. Current status of breast MR imaging. Part 2. Clinical applications. Radiology. 2007;244(3):672–91.
36. Kumar R, Loving VA, et al. Potential of dual-time-point imaging to improve breast cancer diagnosis with (18) F-FDG PET. J Nucl Med. 2005;46(11):1819–24.
37. Li SP, Makris A, et al. Use of dynamic contrast-enhanced MR imaging to predict survival in patients with primary breast cancer undergoing neoadjuvant chemotherapy. Radiology. 2011;260(1):68–78.
38. Maguire Jr GQ, Noz ME, et al. Prone breast dual-time-point PET/CT compared with MRI for determining breast cancer. AJR Am J Roentgenol. 2009;193(1):W77; author reply W78.
39. Mandelson MT, Oestreicher N, et al. Breast density as a predictor of mammographic detection: comparison of interval- and screen-detected cancers. J Natl Cancer Inst. 2000;92(13):1081–7.
40. Mann RM, Kuhl CK, et al. Breast MRI: guidelines from the European Society of Breast Imaging. Eur Radiol. 2008;18(7):1307–18.
41. Mavi A, Urhan M, et al. Dual time point 18F-FDG PET imaging detects breast cancer with high sensitivity and correlates well with histologic subtypes. J Nucl Med. 2006;47(9):1440–6.
42. Miller WR, Ellis IO, et al. ABC of breast diseases. Prognostic factors. BMJ. 1994;309(6968):1573–6.
43. Moy L, Noz ME, et al. Role of fusion of prone FDG-PET and magnetic resonance imaging of the breasts in the evaluation of breast cancer. Breast J. 2010; 16(4):369–76.
44. Moy L, Noz ME, et al. Prone mammoPET acquisition improves the ability to fuse MRI and PET breast scans. Clin Nucl Med. 2007;32(3):194–8.
45. Moy L, Ponzo F, et al. Improving specificity of breast MRI using prone PET and fused MRI and PET 3D volume datasets. J Nucl Med. 2007;48(4):528–37.
46. Murakami R, Kumita SI, et al. FDG-PET/CT in the diagnosis of recurrent breast cancer. Acta Radiol. 2012;53(1):12–6.
47. Nakai T, Okuyama C, et al. Pitfalls of FDG-PET for the diagnosis of osteoblastic bone metastases in patients with breast cancer. Eur J Nucl Med Mol Imaging. 2005;32(11):1253–8.
48. Nelson HD, Tyne K, et al. Screening for breast cancer: an update for the U.S. Preventive Services Task Force. Ann Intern Med. 2009;151(10):727–37, W237-742.
49. Niikura N, Costelloe CM, et al. FDG-PET/CT compared with conventional imaging in the detection of distant metastases of primary breast cancer. Oncologist. 2011;16(8):1111–19.
50. Ohlmann-Knafo S, Kirschbaum M, et al. Diagnostic value of whole-body MRI and bone scintigraphy in the detection of osseous metastases in patients with breast cancer–A Prospective Double-Blinded Study at two Hospital Centers. Rofo. 2009;181(3):255–63.
51. Pennant M, Takwoing Y, et al. A systematic review of positron emission tomography (PET) and positron emission tomography/computed tomography (PET/CT) for the diagnosis of breast cancer recurrence. Health Technol Assess. 2010;14(50):1–103.
52. Perry N, Broeders M, et al. European guidelines for quality assurance in breast cancer screening and

diagnosis. Fourth edition–summary document. Ann Oncol. 2008;19(4):614–22.
53. Pfannenberg C, Aschoff P, et al. Prospective comparison of 18F-fluorodeoxyglucose positron emission tomography/computed tomography and whole-body magnetic resonance imaging in staging of advanced malignant melanoma. Eur J Cancer. 2007;43(3):557–64.
54. Piccoli CW, Forsberg F. Advanced ultrasound techniques for breast imaging. Semin Roentgenol. 2011;46(1):60–7.
55. Podkrajsek M, Hocevar M. The role of contrast enchanced axillary ultrasonography in early breast cancer patients. Coll Antropol. 2011;35(1):33–7.
56. Reddy S, Shaller CC, et al. Evaluation of the anti-HER2 C6.5 diabody as a PET radiotracer to monitor HER2 status and predict response to trastuzumab treatment. Clin Cancer Res. 2011;17(6):1509–20.
57. Rosen EL, Eubank WB, et al. FDG PET, PET/CT, and breast cancer imaging. Radiographics. 2007;27 Suppl 1:S215–29.
58. Sanz-Viedma S, Torigian DA, et al. Potential clinical utility of dual time point FDG-PET for distinguishing benign from malignant lesions: implications for oncological imaging. Rev Esp Med Nucl. 2009;28(3): 159–66.
59. Schwarz-Dose J, Untch M, et al. Monitoring primary systemic therapy of large and locally advanced breast cancer by using sequential positron emission tomography imaging with [18F]fluorodeoxyglucose. J Clin Oncol. 2009;27(4):535–41.
60. Stahl AR, Heusner TA, et al. Time course of tumor SUV in 18F-FDG PET of breast cancer: presentation of a simple model using a single reference point for time corrections of tumor SUVs. J Nucl Med. 2010;52(1):18–23.
61. Ueda S, Tsuda H, et al. Clinicopathological and prognostic relevance of uptake level using 18F-fluorodeoxyglucose positron emission tomography/computed tomography fusion imaging (18F-FDG PET/CT) in primary breast cancer. Jpn J Clin Oncol. 2008;38(4):250–8.
62. Ueda S, Tsuda H, et al. Early reduction in standardized uptake value after one cycle of neoadjuvant chemotherapy measured by sequential FDG PET/CT is an independent predictor of pathological response of primary breast cancer. Breast J. 2010;16(6):660–2.
63. Uematsu T, Kasami M, et al. Comparison of FDG PET and MRI for evaluating the tumor extent of breast cancer and the impact of FDG PET on the systemic staging and prognosis of patients who are candidates for breast-conserving therapy. Breast Cancer. 2009;16(2):97–104.
64. Wahl RL, Siegel BA, et al. Prospective multicenter study of axillary nodal staging by positron emission tomography in breast cancer: a report of the staging breast cancer with PET Study Group. J Clin Oncol. 2004;22(2):277–85.
65. Wang XH, Peng WJ, et al. Value of diffusion weighted imaging (DWI) in evaluating early response to neoadjuvant chemotherapy in locally advanced breast cancer. Zhonghua Zhong Liu Za Zhi. 2010;32(5):377–81.
66. Yamaguchi R, Futamata Y, et al. Mastopathic-type fibroadenoma and ductal adenoma of the breast with false-positive fluorodeoxyglucose positron emission tomography. Jpn J Radiol. 2009;27(7):280–4.
67. Yi CA, Shin KM, et al. Non-small cell lung cancer staging: efficacy comparison of integrated PET/CT versus 3.0-T whole-body MR imaging. Radiology. 2008;248(2):632–42.
68. Zytoon AA, Murakami K, et al. Dual time point FDG-PET/CT imaging. Potential tool for diagnosis of breast cancer. Clin Radiol. 2008;63(11):1213–27.
69. Zytoon AA, Murakami K, et al. Breast cancer with low FDG uptake: characterization by means of dual-time point FDG-PET/CT. Eur J Radiol. 2009;70(3): 530–8.

5 PET/MRI in Evaluating Lymphomas: Preliminary Experience and Potential Future Applications

Maria Chiara Gaeta and Karin Anna Herrmann

Contents

5.1 Introduction

Hodgkin's and non-Hodgkin's lymphomas (HL and NHL) are a heterogeneous group of lymphoproliferative disorders, representing the fifth most frequent type of cancer in the western world [1].

Imaging has a paramount role in the initial staging of the disease identifying lymph node groups affected by the disease and the involvement of extra-lymphatic organs. In addition, imaging is successfully used to evaluate therapy response and follow-up [2, 3].

Computed tomography (CT) represented in the past the dominant radiologic modality for lymphoma assessment [4]. However, the morphologic evaluation of potentially affected organs is currently considered not sufficient, as malignant cells may be present in normal-sized lymph nodes or in residual non-infiltrating masses often observed after therapy [4, 5]. MRI, so far, has played a rather minor role in the standard of care imaging of lymphoma patients. Currently, only the assessment of primary central nervous system (CNS) lymphoma is preferentially performed with MRI and CT [6–14].

Both cross-sectional imaging techniques, CT and magnetic resonance imaging (MRI), rely to a large extent on morphologic imaging criteria. Positron emission tomography (PET) with 18-F-fluorodeoxyglucose (FDG) provides functional information assessing tissue metabolism. Due to the increased glucose metabolism of most lymphoma subtypes, PET with FDG has become

M.C. Gaeta (✉) • K.A. Herrmann
Department of Radiology, UH Case Medical Center, Cleveland, OH 44106, USA
e-mail: mc.gaeta@gmail.com

I. Carrio, P. Ros (eds.), *PET/MRI*,
DOI 10.1007/978-3-642-40692-8_5, © Springer-Verlag Berlin Heidelberg 2014

an established and well-accepted staging tool for this disease entity. It has demonstrated high efficacy in predicting therapy outcomes and restaging after therapy.

With the introduction of ^{67}Ga-citrate imaging for both Hodgkin's and non-Hodgkin's lymphomas, the spectrum of molecular imaging has broadened for the assessment of lymphomas [15]; however, ^{67}Ga imaging has not gained widespread attention because of its poor spatial resolution and low diagnostic accuracy [16].

On the other hand, many authors have proved that FDG-PET is the most sensitive and specific imaging technique available for patients with lymphoma [4, 17–20]. Nowadays, FDG-PET is routinely performed with integrated PET/CT scanners. Providing co-registered functional PET and anatomical CT information, PET/CT represents now the standard of care.

In this scenario, the recently developed PET/MRI systems, at a first glance, seem to have a limited future. However, a deeper analysis of the advantages of PET/MRI, its potential applications, and innovative approaches to staging algorithms of lymphoma may lead to the opposite consideration discovering PET/MRI as an important adjunct in the imaging tool box for diagnosing and staging lymphoma patients.

5.2 Current Diagnostic Workup and Dosimetric Considerations

Current diagnostic algorithms for lymphoma staging, assessment of treatment response, and follow-up require repetitive imaging. According to the current clinical practice and guidelines [21], the established imaging strategy for HL and NHL patients requires a high number of sequentially performed X-ray-based imaging procedures. On average, patients undergo one chest X-ray, one CT of neck/chest/abdomen and pelvis, and one FDG-PET/CT for the initial staging of their disease. During the course of their therapy, another one or two chest X-rays, one or two CTs of neck/chest/abdomen/pelvis, and one or two PET/CT scans may follow. An average of seven CTs and four chest X-rays during the follow-up are not unusual. Multiple repetitive imaging with modalities using ionizing radiation results in considerable radiation exposure and cumulative effective dose (CED). Nievelstein RA et al. calculated a cumulative effective dose from medical imaging in adults with non-Hodgkin's lymphoma of 97 mSv at 2.5 years after diagnosis.

Repetitive imaging with X-ray-based imaging modalities harbors a distinct risk in pediatric patient populations. It is well known that children are more sensitive to radiation-induced carcinogenesis than adults because their cells divide more rapidly and because they have a potential for a longer life relative to adults. Thus, radiation-exposed children are more likely to manifest radiation-induced cancer within their lifetime [22, 23]. Replacing PET/CT with PET/MRI in the evaluation of lymphoma patients, the cumulative effective dose would be significantly reduced as the radiation exposure would be limited to radiation dose from the PET tracer alone.

5.3 Conventional and Advanced MRI Evaluating Lymphoma Patients

Whole-body (WB) MRI has shown potential for the staging of a variety of malignancies [24–27]. Two studies reported the feasibility of WB MRI using STIR in adult and pediatric population with malignant lymphoma [28, 29]. The authors conclude that WB MRI-STIR enables disease staging and is superior to blind bone marrow biopsy and conventional imaging (including CT, gallium-67 scintigraphy, and bone scintigraphy) in detecting bone marrow involvement at initial diagnosis. However, WB MRI-STIR showed a low specificity for recurrent or residual disease.

Diffusion-weighted imaging (DWI) is a technique exploiting the random, translational motion

of water molecules in biological tissues [30]. On diffusion-sensitive sequences, this motion results in a signal loss and can be quantified by calculating the apparent diffusion coefficient (ADC). The ADC reflects the specific diffusion capacity of water protons of a biological tissue that is low in densely packed tumor tissues [31, 32]. The increased cellular density within lymphoma lesions is correlated with a high signal on diffusion-weighted images expressing a reduced ADC [33]. Several studies comparing DWI with PET/CT in terms of diagnostic accuracy for staging lymphoma showed reasonable results for DWI [34–36] and a strong inverse correlation between ADC and PET SUV [37].

Kwee et al. [38] studied prospectively 31 patients with newly diagnosed malignant lymphoma with WB MRI (T1-weighted and short inversion time inversion recovery and DWI) and CT. Results showed that WB MRI (without DWI and with DWI) for initial staging of malignant lymphoma equals CT in most of the patients. In a not negligible percentage of cases, WB MRI overstaged relative to CT, suggesting a possible advantage of using DWI.

In a recent study [36], WB MRI including DWI has been compared with FDG-PET/CT in the staging of newly diagnosed lymphoma. While WB MRI-DWI compared to FDG-PET/CT did not fail to depict lesions, it overstaged disease in a minority of cases.

Another aspect that can be addressed with DWI is disease response assessment. Punwani et al. [37] studied the incremental information derived from DWI for predicting local treatment response in Hodgkin's lymphoma patients evaluated with PET/CT. The rationale of this study is that currently no method is considered reliable for predicting the response of an individual disease site prior to commencing treatment. Punwani S et al. showed that sites with an adequate response to chemotherapy had a significantly lower median pretreatment ADC (1.0×10^{-3}mm^2 s^{-1}) than those with an inadequate response (1.26×10^{-3}mm^2 s^{-1}; $p<0.01$). Thus, lesions with a lower cellularity showed a worse response compared to those with a higher cellularity, which reflect a plausible behavior considering the mechanism of action of the chemotherapy drugs. Authors conclude that DWI may complement PET for prediction of site-specific interim response to chemotherapy, potentially facilitating earlier therapy stratification and tailored treatment plans.

Despite the significant impact of DWI in WB MRI on image diagnosis of lymphoma, current literature does not advocate or support MRI as a potential replacement test for PET/CT. FDG-PET/CT remains the reference standard staging and restaging malignant lymphoma.

The advent of integrated PET/MRI systems, however, may challenge this fact again and opens up the exciting possibility of exploring the potential complementary role of the two modalities.

5.4 Central Nervous System Lymphoma

Primary and secondary central nervous system lymphomas (PCNSL and SCNSL) are predominantly tumors of the diffuse large B-cell type and represent aggressive diseases necessitating early diagnosis for proper management of patients. PCNL is usually confined to the brain, and leptomeninges, eyes, and spinal cord are less often involved. It represents about 3 % of all brain tumors in immunocompetent patients. On the other hand, SCNSL originates from systemic lymphoma spreading to the CNS, usually occurring at disease progression or relapse [39, 40].

The imaging technique of choice to detect SCNSL is contrast-enhanced MRI [41]. The initial diagnosis of PCNSL, as well as detection of recurrence, requires non-enhanced (i.e., T1-weighted, T2-weighted, FLAIR, diffusion-weighted imaging (DWI)) and contrast-enhanced MRI [42].

Despite promising advances in imaging techniques, including DWI and ADC maps, MR spectroscopy, perfusion imaging and diffusion

tensor imaging, and conventional non-enhanced and contrast-enhanced MRI remain the imaging test of choice in CNSL [42] until there is stronger evidence of added value of these procedures.

Although CNS lymphomas may have characteristic imaging findings, conventional MRI cannot clearly differentiate CNS lymphoma from other brain lesions and SCNSL from PCNSL [43].

FDG-PET/CT is uncommonly used for imaging malignant brain tumors because of the high physiologic glucose metabolism in normal brain tissue. However, PET with FDG typically reveals hypermetabolic lesions with increased uptake of FDG in CNS lymphoma [44]. Some authors demonstrated its application to detect common enhancing brain lesions on MRI. In the study of Kosaka et al. [45], semiquantitative parameters of FDG-PET were significantly higher for lymphoma than for other tumors ($p < 0.01$), concluding that FDG-PET can help for differential diagnosis between lymphoma and other malignant enhancing brain tumors and is recommended when the MRI findings are not conclusive.

18F-FDG-PET is also considered helpful to distinguish malignant lymphoma from nonmalignant cerebral lesions such as toxoplasmosis in patients with HIV [46].

Finally, 18F-FDG-PET is advocated to represent an independent predictor for treatment response of primary central nervous system lymphoma [47]. Using a ten-step semiquantitative visual rating system (metabolic imaging lymphoma aggressiveness scale, or MILAS) to assess primary CNS lymphoma metabolism as a marker of clinical aggressiveness, a cutoff of 3 was helpful tool to separate progression-free survival and overall survival [47].

For primary lymphoma of the central nervous system, other tracers than 18F-FDG deserve a special mentioning. Initial experience is reported with 11C-FET PET showing encouraging results and complementary information in the treatment follow-up of PCNSL [48].

The combination of N-ammonia and F-FDG imaging is demonstrated to help distinguishing PCNSLs and solid gliomas and making an accurate prediction of PCNSL due to their different metabolic profiles [49].

For diagnosis and management of primary and secondary lymphoma to the central nervous system, both imaging modalities PET and MRI have their independent value. What PET/MRI has to offer as a combined imaging modality remains to be determined.

PET/MRI systems have the potential to combine all available functional information from PET and MRI and high-resolution soft tissue information from MRI. The combined assessment might help to improve diagnostic accuracy in differentiating SNC lymphoma from other brain tumors and SCNSL from PCNSL. It might also help to easier and comprehensively assess systemic disease in its disease extent.

These hopes and expectations however need to undergo investigation, and no data is currently available to support a preliminary statement on this.

5.5 Bone Marrow Involvement Evaluation

Bone marrow involvement in patients with lymphoma has crucial prognostic and therapeutic consequences. The gold standard for its evaluation is the bone marrow biopsy (BMB) that is an invasive procedure with a not negligible risk of complications and showing a not sufficient sensitivity due to possible sampling errors [50].

FDG-PET has high sensitivity and specificity detecting focal or multifocal bone marrow involvement, even in those patients with a false-negative BMB due to sampling error [51].

However, it is important to note that FDG-PEt alone is not accurate in detecting small bone marrow lesions or bone marrow involvement by low-grade lymphomas. Thus, a negative PET scan cannot rule out lymphomatous involvement [52]. On the other hand, diffuse or heterogeneous bone marrow uptake of radiotracer in a pretreatment scan should not immediately suggest bone

marrow involvement by lymphoma as this pattern of uptake can be seen in reactive myeloid hyperplasia [53]. Diffuse increase in FDG uptake can also be observed in patients treated with granulocyte colony-stimulating factors, leading to a possible false-positive interpretation of PET scans [8]. The use of PET/MRI systems may overcome these limitations, taking advantage of the complementary information provided by both modalities. Conventional MRI (T1w, T2w, and short inversion time inversion recovery, STIR, as indispensable sequences for the evaluation of the bone marrow) and DWI may be able to detect small lymphomatous bone marrow lesions [54, 55]. MRI may also detect lymphomatous bone marrow lesions in patients with low-grade lymphomas that are negative at FDG-PET. On the other hand, the information provided by FDG-PET would increase MRI specificity discriminating between reconverted or red marrow, benign bone marrow pathologies, and lymphomatous bone marrow lesions that may show an overlap in signal intensities [56].

5.6 PET/MRI and Lymphomas: First Experiences with Integrated and Sequential Dedicated PET/MR Systems

The current status of the literature on PET/MRI reflects very sparse experience with imaging lymphoma patients. Available data are based on small patient populations.

In a recent retrospective study [57], the feasibility of FDG-PET/MR for response evaluation of malignant lymphoma has been evaluated in nine patients with malignant lymphoma. All patients underwent FDG-PET/MR twice, once for staging and once for therapy response assessment. PET/MR of all patients was performed with the Ingenuity TF PET/MR (Philips Medical Systems, Best, Netherlands). In two patients, both the initial exam and the follow-up exam included an additional diffusion-weighted MR scan (diffusion-weighted imaging with background suppression). Two nuclear medicine physicians, who evaluated independently the PET scans, reported high interobserver agreement of lymphoma staging. In addition, all PET datasets were found to have very good or excellent image quality. The additional diffusion-weighted images performed in two patients confirmed its technical feasibility. However, authors conclude that its clinical role still has to be defined.

A clinical experience with integrated whole-body PET/MRI (Biograph mMR; Siemens Healthcare) is reported by Drzezga et al. [58] who assessed scans of 32 patients with different oncologic diagnoses, including two patients with lymphoma. Patients underwent a dual-imaging protocol consisting of a PET/CT and subsequent PET/MR scan. Corresponding PET/CT and PET/MRI images did not show significant difference regarding the numbers of suspicious lesions or lesion positive, with a comparable anatomical allocation.

A promising first experience evaluating lymphoma patients with PET/MRI can be reported from our own experience (unpublished data). We retrospectively evaluated ten patients with malignant lymphoma who first underwent FDG-PET/CT (Philips Gemini TF PET/CT, Philips Healthcare, Andover, MA) followed by a PET/MRI (Philips Ingenuity TF PET/MRI, Philips Healthcare, Andover, MA) without an additional FDG injection. Our results in a multireader analysis demonstrated that assessment of lymphomatous lesions is feasible with high interobserver agreement. Detection and localization of lesions correlated well between the two modalities. Figure 5.1 illustrates an example of PET/MRI. Of special interest was that PET/MRI, unlike PET/CT, was able to confidently show the involvement of bone marrow which had impact on the stage of disease according to the Ann Arbor classification.

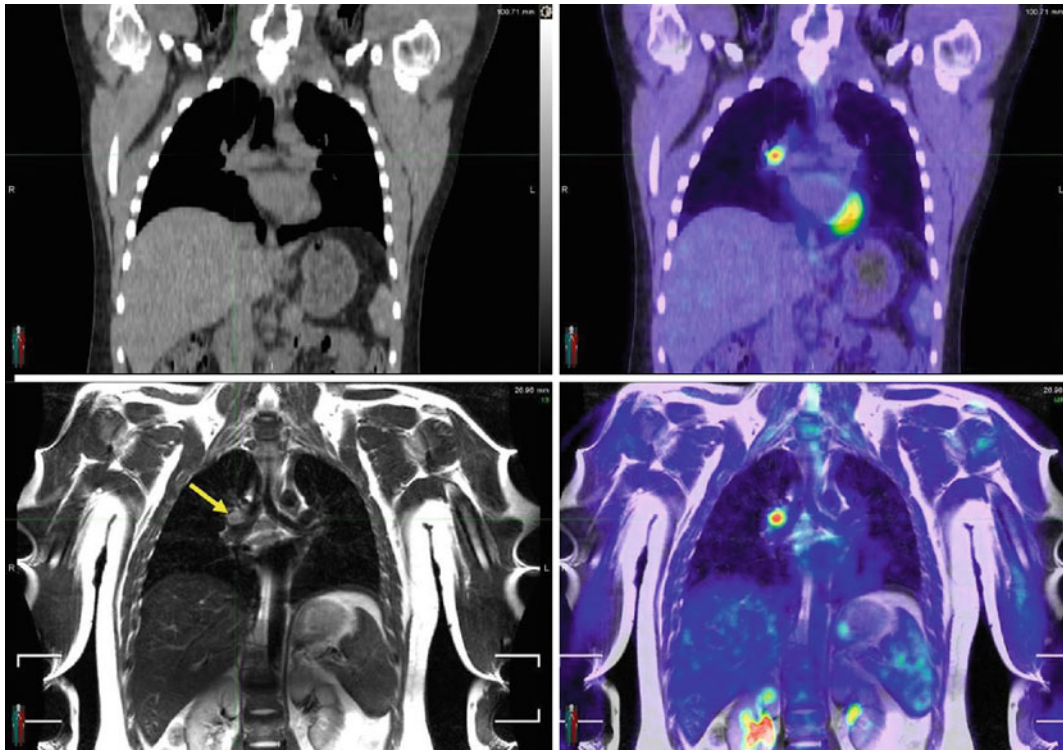

Fig. 5.1 Low-dose PET/CT (*upper row* of images, CT and fused CT and PET) and PET/MRI (*lower row* of images, coronal T2-weighted fast spin echo FSE sequence and fused MRI and PET) in a 49-year-old patient with NHL. An FDG avid lymph adenopathy is identified in the right hilum by both modalities. Note that in MRI the lymph node can be more easily distinguished from vascular structures and bronchus than in CT given the signal void in both structures. Conspicuity of lymph nodes in the hilum with this MR sequence is superior non-enhanced low-dose CT which has clearly low contrast resolution

Conclusions

Initial clinical experiences with integrated and sequential PET/MRI systems show promising results in evaluating lymphoma patients. The experience at current times however is limited to generalized statements in patients with oncologic disease and preliminary data on small patient samples.

Both PET and MRI are individually valuable as imaging techniques; however, further dedicated research is needed to determine the role of PET/MRI in the various clinical scenarios of lymphoma.

The value of radiotracers other than 18F-FDG remains to be determined for this particular disease entity. Focusing on the combined and hopefully complementary information from these two modalities may offer in the future to improve the diagnostic accuracy in diagnosing and staging CNS lymphoma, bone marrow involvement, and extra-nodal lymphoma. Such exciting clinical applications remain to be explored.

What can be expected from current preliminary data is that replacing PET/CT with PET/MRI in the diagnostic algorithm would lead to a lower radiation exposure which is particularly important for sequential treatment monitoring and surveillance as well as in pediatric patients.

References

1. Jhanwar YS, Straus DJ. The role of PET in lymphoma. J Nucl Med. 2006;47(8):1326–34.
2. Armitage JO. Staging non-Hodgkin lymphoma. CA Cancer J Clin. 2005;55(6):368–76.

3. Connors JM. State-of-the-art therapeutics: Hodgkin's lymphoma. J Clin Oncol. 2005;23(26):6400–8.
4. Juweid ME. FDG-PET/CT in lymphoma. Methods Mol Biol. 2011;727:1–19.
5. Kwee TC, Kwee RM, Nievelstein RA. Imaging in staging of malignant lymphoma: a systematic review. Blood. 2008;111(2):504–16.
6. Bodet-Milin C, et al. FDG-PET in follicular lymphoma management. J Oncol. 2012;370272(10):30.
7. Park S, et al. The impact of baseline and interim PET/CT parameters on clinical outcome in patients with diffuse large B cell lymphoma. Am J Hematol. 2012; 87(9):937–40.
8. Shelly MJ, et al. 18-Fluorodeoxyglucose positron emission tomography/computed tomography in the management of aggressive non-Hodgkin's B-cell lymphoma. ISRN Hematol. 2012;456706(10):11.
9. Connors JM. Positron emission tomography in the management of Hodgkin lymphoma. Hematology Am Soc Hematol Educ Program. 2011;2011:317.
10. Hosein PJ, et al. Utility of positron emission tomography scans in mantle cell lymphoma. Am J Hematol. 2011;86(10):841–5.
11. Zinzani PL. PET in T-cell lymphoma. Curr Hematol Malig Rep. 2011;6(4):241–4.
12. Cimarelli S, et al. Use of F-18 FDG PET/CT in non-Hodgkin lymphoma with central nervous system involvement. Clin Nucl Med. 2011;36(6):e45–9.
13. Mohile NA, Deangelis LM, Abrey LE. The utility of body FDG PET in staging primary central nervous system lymphoma. Neuro Oncol. 2008;10(2):223–8.
14. Seam P, Juweid ME, Cheson BD. The role of FDG-PET scans in patients with lymphoma. Blood. 2007;110(10):3507–16.
15. Kaplan WD, et al. Gallium-67 imaging: a predictor of residual tumor viability and clinical outcome in patients with diffuse large-cell lymphoma. J Clin Oncol. 1990;8(12):1966–70.
16. Tsukamoto N, et al. The usefulness of (18) F-fluorodeoxyglucose positron emission tomography ((18)F-FDG-PET) and a comparison of (18)F-FDG-pet with (67)gallium scintigraphy in the evaluation of lymphoma: relation to histologic subtypes based on the World Health Organization classification. Cancer. 2007;110(3):652–9.
17. Karam M, et al. Role of fluorine-18 fluorodeoxyglucose positron emission tomography scan in the evaluation and follow-up of patients with low-grade lymphomas. Cancer. 2006;107(1):175–83.
18. Kostakoglu L, et al. Interim [(18)F]fluorodeoxyglucose positron emission tomography imaging in stage I-II non-bulky Hodgkin lymphoma: would using combined positron emission tomography and computed tomography criteria better predict response than each test alone? Leuk Lymphoma. 2012;53(11): 2143–50.
19. Isasi CR, Lu P, Blaufox MD. A metaanalysis of 18F-2-deoxy-2-fluoro-D-glucose positron emission tomography in the staging and restaging of patients with lymphoma. Cancer. 2005;104(5):1066–74.
20. Munker R, et al. Contribution of PET imaging to the initial staging and prognosis of patients with Hodgkin's disease. Ann Oncol. 2004;15(11): 1699–704.
21. Nievelstein RA, et al. Radiation exposure and mortality risk from CT and PET imaging of patients with malignant lymphoma. Eur Radiol. 2012;22(9): 1946–54.
22. Brix G, et al. Radiation exposure of patients undergoing whole-body dual-modality 18F-FDG PET/CT examinations. J Nucl Med. 2005;46(4):608–13.
23. Fahey FH. Dosimetry of pediatric PET/CT. J Nucl Med. 2009;50(9):1483–91.
24. Lauenstein TC, Semelka RC. Emerging techniques: whole-body screening and staging with MRI. J Magn Reson Imaging. 2006;24(3):489–98.
25. Schmidt GP, et al. High-resolution whole-body magnetic resonance imaging applications at 1.5 and 3 Tesla: a comparative study. Invest Radiol. 2007;42(6): 449–59.
26. Lauenstein TC, et al. Whole-body MR imaging: evaluation of patients for metastases. Radiology. 2004; 233(1):139–48.
27. Antoch G, et al. Whole-body dual-modality PET/CT and whole-body MRI for tumor staging in oncology. JAMA. 2003;290(24):3199–206.
28. Brennan DD, et al. A comparison of whole-body MRI and CT for the staging of lymphoma. AJR Am J Roentgenol. 2005;185(3):711–16.
29. Kellenberger CJ, et al. Initial experience with FSE STIR whole-body MR imaging for staging lymphoma in children. Eur Radiol. 2004;14(10):1829–41.
30. Koh DM, Collins DJ. Diffusion-weighted MRI in the body: applications and challenges in oncology. AJR Am J Roentgenol. 2007;188(6):1622–35.
31. Szafer A, et al. Diffusion-weighted imaging in tissues: theoretical models. NMR Biomed. 1995;8(7–8): 289–96.
32. Lyng H, Haraldseth O, Rofstad EK. Measurement of cell density and necrotic fraction in human melanoma xenografts by diffusion weighted magnetic resonance imaging. Magn Reson Med. 2000;43(6):828–36.
33. Barajas Jr RF, et al. Diffusion-weighted MR imaging derived apparent diffusion coefficient is predictive of clinical outcome in primary central nervous system lymphoma. AJNR Am J Neuroradiol. 2010;31(1):60–6.
34. Gu J, et al. Whole-body diffusion-weighted imaging: the added value to whole-body MRI at initial diagnosis of lymphoma. AJR Am J Roentgenol. 2011; 197(3):W384–91.
35. Abdulqadhr G, et al. Whole-body diffusion-weighted imaging compared with FDG-PET/CT in staging of lymphoma patients. Acta Radiol. 2011;52(2): 173–80.
36. van Ufford HM, et al. Newly diagnosed lymphoma: initial results with whole-body T1-weighted, STIR, and diffusion-weighted MRI compared with 18F-FDG PET/CT. AJR Am J Roentgenol. 2011;196(3): 662–9.
37. Punwani S, et al. Diffusion-weighted MRI of lymphoma: prognostic utility and implications for PET/MRI? Eur J Nucl Med Mol Imaging. 2012;30:30.
38. Kwee TC, et al. Whole-body MRI, including diffusion-weighted imaging, for the initial staging of

malignant lymphoma: comparison to computed tomography. Invest Radiol. 2009;44(10):683–90.
39. Baraniskin A, et al. Current strategies in the diagnosis of diffuse large B-cell lymphoma of the central nervous system. Br J Haematol. 2012;156(4):421–32.
40. Haldorsen IS, et al. Diagnostic delay in primary central nervous system lymphoma. Acta Oncol. 2005;44(7):728–34.
41. Bierman P, Giglio P. Diagnosis and treatment of central nervous system involvement in non-Hodgkin's lymphoma. Hematol Oncol Clin North Am. 2005;19(4):597–609.
42. Haldorsen IS, et al. CT and MR imaging features of primary central nervous system lymphoma in Norway, 1989-2003. AJNR Am J Neuroradiol. 2009;30(4): 744–51.
43. Haldorsen IS, Espeland A, Larsson EM. Central nervous system lymphoma: characteristic findings on traditional and advanced imaging. AJNR Am J Neuroradiol. 2011;32(6):984–92.
44. Go JL, Lee SC, Kim PE. Imaging of primary central nervous system lymphoma. Neurosurg Focus. 2006; 21(5):E4.
45. Kosaka N, et al. 18F-FDG PET of common enhancing malignant brain tumors. AJR Am J Roentgenol. 2008;190(6):W365–9.
46. Westwood TD, Hogan C, Julyan PJ, Coutts G, Bonington S, Carrington B, Taylor B, Khoo S, Bonington A. Utility of FDG-PETCT and magnetic resonance spectroscopy in differentiating between cerebral lymphoma and non-malignant CNS lesions in HIV-infected patients. Eur J Radiol. 2013;82(8):e374–9. doi:10.1016/j.ejrad.2013.03.008. pii: S0720-048X(13)00137-X.
47. Kasenda B, Haug V, Schorb E, Fritsch K, Finke J, Mix M, Hader C, Weber WA, Illerhaus G, Meyer PT. 18F-FDG PET is an independent outcome predictor in primary central nervous system lymphoma. J Nucl Med. 2013;54(2):184–91. doi:10.2967/jnumed.112.108654. Epub 2012 Dec 18.
48. Jang SJ, Lee KH, Lee JY, Choi JY, Kim BT, Kim SJ, Kim WS. (11)C-methionine PET/CT and MRI of primary central nervous system diffuse large B-cell lymphoma before and after high-dose methotrexate. Clin Nucl Med. 2012;37(10):e241–4.
49. Shi X, Zhang X, Yi C, Wang X, Chen Z, Zhang B. The combination of 13N-ammonia and 18F-FDG in predicting primary central nervous system lymphomas in immunocompetent patients. Clin Nucl Med. 2013;38(2):98–102. doi:10.1097/RLU.0b013e318279b6cc.
50. Pelosi E, et al. FDG-PET in the detection of bone marrow disease in Hodgkin's disease and aggressive non-Hodgkin's lymphoma and its impact on clinical management. Q J Nucl Med Mol Imaging. 2008;52(1):9–16.
51. Moog F, et al. 18-F-fluorodeoxyglucose-positron emission tomography as a new approach to detect lymphomatous bone marrow. J Clin Oncol. 1998; 16(2):603–9.
52. Pakos EE, Fotopoulos AD, Ioannidis JP. 18F-FDG PET for evaluation of bone marrow infiltration in staging of lymphoma: a meta-analysis. J Nucl Med. 2005;46(6):958–63.
53. Cronin CG, et al. Clinical utility of PET/CT in lymphoma. AJR Am J Roentgenol. 2010;194(1): W91–103.
54. Mirowitz SA, et al. MR imaging of bone marrow lesions: relative conspicuousness on T1-weighted, fat-suppressed T2-weighted, and STIR images. AJR Am J Roentgenol. 1994;162(1):215–21.
55. Yasumoto M, et al. MR detection of iliac bone marrow involvement by malignant lymphoma with various MR sequences including diffusion-weighted echo-planar imaging. Skeletal Radiol. 2002;31(5): 263–9.
56. Kwee TC, de Klerk JM, Nievelstein RA. Imaging of bone marrow involvement in lymphoma: state of the art and future directions. Scientific World Journal. 2011;11:391–402.
57. Drzezga A, et al. First clinical experience with integrated whole-body PET/MR: comparison to PET/CT in patients with oncologic diagnoses. J Nucl Med. 2012;53(6):845–55.
58. Platzek I, et al. PET/MR for therapy response evaluation in malignant lymphoma: initial experience. MAGMA. 2012;16:16.

PET/MRI of the Liver

6

Raj Mohan Paspulati and Andres A. Kohan

Contents

6.1 Introduction

Current imaging methods for liver disease include the use of US, CT, MRI and PET/CT. While US and CT are the initial and more cost-effective imaging methods worldwide, MR imaging has become the modality of choice for liver imaging due to its high sensitivity and specificity in characterizing liver lesions. Introduction of liver-specific MR contrast agents has further increased the role of MR imaging of liver in primary and secondary liver malignancy lesion detection, treatment planning, and follow-up. Similarly, ^{18}F-FDG PET/CT imaging has established a place in staging and follow-up of liver malignancies, especially of liver metastases. Due to decreased sensitivity of ^{18}F-FDG PET in primary hepatocellular carcinoma, focus is being made on introduction of new radiotracers.

Despite these recent advances in both MRI and PET/CT, contrast-enhanced CT is still the most widely used method for liver imaging, probably secondary to the availability, cost, and easiness of the method. There is increased concern about radiation exposure from CT especially from repeated CT imaging as seen in cancer imaging. This latter issue will not only accelerate the replacement of CT in areas where MR has already proven superior but also create a perfect background for introduction of PET/MR into the available spectrum of imaging modalities.

Integrated PET/MR imaging has several potential advantages over PET/CT. There is no additional exposure to ionizing radiation and is believed to provide better co-registration, higher

R.M. Paspulati, MD (✉) • A.A. Kohan, MD
Department of Radiology, University Hospitals,
Case Western Reserve University, Cleveland,
OH 44106, USA
e-mail: raj.paspulati@uhhospitals.org

I. Carrio, P. Ros (eds.), *PET/MRI*,
DOI 10.1007/978-3-642-40692-8_6,

Table 6.1 MR sequences

MRI with gadolinium	MRI with gadoxetic acid	MRI with gadobenate dimeglumine
T2 TSE breathing triggered	T1w FFE in/opp phase or mDIXON	T1w FFE in/opp phase or mDIXON
Fat-suppressed T2w SSH	T2w SSH	T2w SSH
DWI	*Contrast*	*Contrast*
T1w FFE in/opp phase or mDIXON	Dynamic T1w FFE thrive	Dynamic T1w FFE thrive
Fat-suppressed T1w FFE or mDIXON	T2 TSE breathing triggered	T2 TSE breathing triggered
Contrast	DWI	DWI
Dynamic T1w FFE thrive	mDIXON (20 min delay)	mDIXON (120 min delay)

accuracy, and more comprehensive information than MR or PET/CT in their stand-alone configurations. Combining high sensitivity of dedicated liver MRI with molecular imaging of PET in PET/MRI as a single examination will be beneficial in whole-body staging of malignancy.

However, PET/MR has only been recently introduced into the clinical arena with little evidence available to support or reject the potential clinical applications of this technology. In this chapter, we will try to go over the different aspects that have to be taken into account for the use of PET/MR in liver disease, while reviewing the available evidence for MRI, PET/CT, and retrospectively fused PET/MR.

6.2 PET/MR Technique and Protocol

Currently there are only two commercial PET/MR scanners, and while one performs simultaneous acquisition of the PET and the MR, the other does it in a sequential way. There are at least two possible methods to perform a PET/MR when following usual guidelines, where a 60 min distribution time for ^{18}F-FDG is required before acquiring the PET. One method is inject ^{18}F-FDG and wait for 60 min and perform the PET/MR. The other method is to utilize this 60 min distribution time after tracer injection for MR component of the PET/MR followed by PET acquisition.

There are two specific situations to decide the type of imaging protocol:

1. Whole-body (WB) PET/MR including the liver without liver-specific MR

   When there is no need for liver-specific imaging, the MR sequences that should be performed ought to be directed to localize whatever lesion is found in the study and help characterize it. For these purposes some of the sequences suggested are:
   - WB 2-point Dixon which, besides providing the MRAC in the simultaneous scanner, has shown equal anatomical localization capabilities when compared to PET/CT [1].
   - WB STIR coronal allows for the detection of lesions in the bone [2].
   - WB DWI helps characterize lesions and has shown to provide enhanced lesion conspicuity and improved diagnostic accuracy for lymphomas [3].
   - Other non-WB sequences for specific organs for basic diagnostic purposes depending on the diagnosis of the patient.
2. WB PET/MR with liver-specific MR

There are many different possible MRI protocols for liver imaging that could be integrated into a PET/MR scan, and it usually varies from institution to institution. The ones suggested in Table 6.1 were drafted from our own experience and those published in the literature.

By integrating these into the PET/MR scanning protocol, they could be implemented either during the distribution of the tracer, as long as they last less than 60 min, or after the PET acquisition if more time is needed. Whichever protocol is selected, a WB sequence has to be performed as well for attenuation correction purposes.

6.3 Imaging

6.3.1 Primary Liver Tumors

Hepatocellular carcinoma (HCC), cholangiocarcinoma (CC), and gallbladder carcinoma (GBC) constitute the main primary malignant tumors of the liver. HCC is the fourth most common cause

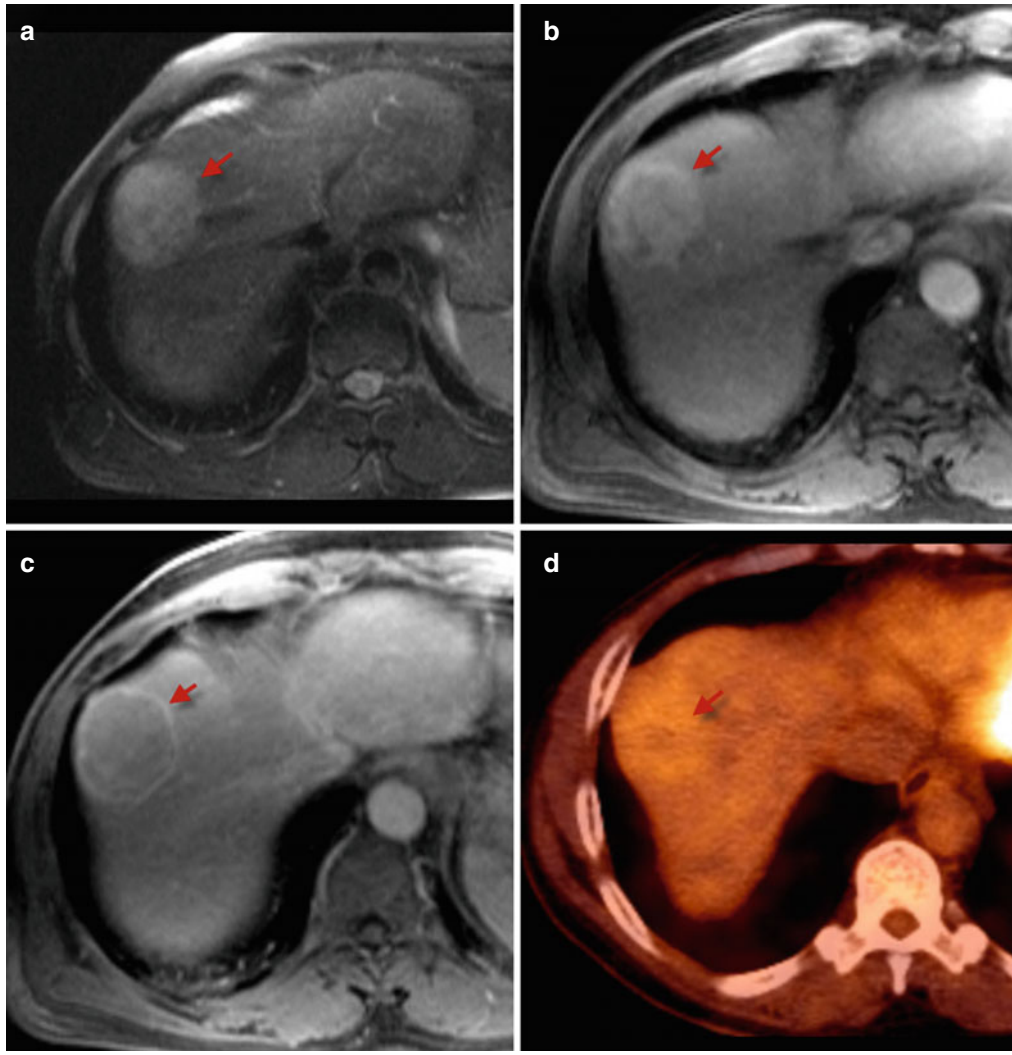

Fig. 6.1 Well-differentiated HCC. T2-weighted fat-saturated FSE (**a**) arterial (**b**) and delayed (**c**) gadolinium-enhanced T1 GRE images show a well-defined T2w hyperintense mass with enhancement in the arterial phase and washout on delayed post-gadolinium images. Corresponding ^{18}F-FDG PET/CT image (**d**) shows no significant uptake

of cancer-related death worldwide, and it is highly associated with chronic hepatic infection by hepatitis C and B virus and cirrhosis. CC is the second most common hepatobiliary malignancy after HCC and is frequently associated with a poor prognosis. Based on anatomical location, CC is classified as peripheral or intrahepatic, central or hilar, and extrahepatic. While the peripheral type of CC is asymptomatic and presents at an advanced stage, hilar and extrahepatic present clinically with signs of biliary obstruction. Finally, GBC is the fifth most common cancer of the gastrointestinal tract and has a very poor prognosis because of delayed diagnosis due to clinically silent nature and nonspecific presentation similar to cholelithiasis and cholecystitis.

6.3.1.1 ^{18}F-FDG

In HCC, several studies have shown that the sensitivity of ^{18}F-FDG is inversely related to the grade of differentiation of the tumor, with an overall reported sensitivity of 55 % [4]. The more undifferentiated the tumor is, the more ^{18}F-FDG avidity it shows. This is mainly related to a loss of glucose-6-phosphatase production, an enzyme that renders ^{18}F-FDG ineffectual (Fig. 6.1) in

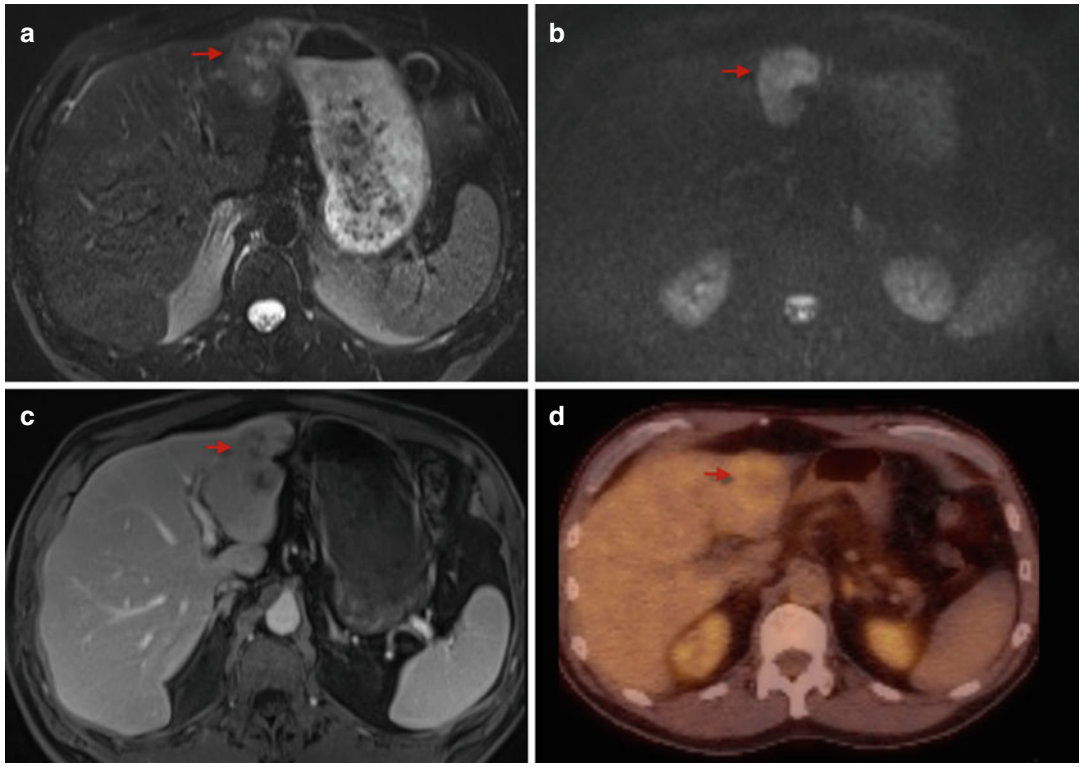

Fig. 6.2 Cholangiocarcinoma. T2-weighted fat-saturated (**a**) DWI (**b**) and gadolinium-enhanced T1 GRE images (**c**) show a well-defined enhancing mass with heterogeneous T2w signal intensity, diffusion restriction in the left lobe. Corresponding ^{18}F-FDG PET/CT image (**d**) shows minimal peripheral uptake of the mass

well-differentiated HCC tumors. This inverse relationship between ^{18}F-FDG avidity and tumor differentiation makes PET/CT a great tool for detecting distant metastasis and to predict prognosis, since both are highly influenced by the degree of tumor differentiation. This is especially true when combined in a ratio with alpha-fetoprotein blood levels according to some reports [5]. It is also believed that ^{18}F-FDG PET/CT could be a good tool for recurrence surveillance following local treatments, for example, Paudyal et al. showed that PET was able to detect recurrence after RFA earlier than CT in 92 % of his sample after only 4–6 weeks of treatment [6]. On the contrary, following therapies targeting the tumor blood supply, false-negative ^{18}F-FDG uptake can occur due to reduced tumor vascularity, thus limiting its use. Finally, ^{18}F-FDG uptake by the tumor has also shown to be a strong predictive factor for recurrence when used for pre-operative liver transplant evaluation [5]. Regardless of all of these characteristics, PET/CT is not considered a first-line imaging method for HCC in any of the areas mentioned. ^{18}F-FDG is believed to play a role in staging and detecting metastatic spread of CC and GB carcinoma, although there is less supporting evidence for GBC. ^{18}F-FDG PET/CT has proven to be more sensitive (93 % vs. 55 %) and specific (80 % vs. 33 %) for intrahepatic-type than extrahepatic [7]-type CC and in the first category, more specifically, for mass-forming type of CC rather than the infiltrative subtype [8] (Fig. 6.2). On the other hand, ^{18}F-FDG has shown poor sensitivity in locoregional staging of GBC.

^{18}F-FDG PET/CT has also been reported to be useful in some cases of rare primary liver tumors such as sarcomatous HCC and combined HCC-CC. There are only few case reports showing ^{18}F-FDG uptake in combined HCC-CC

lesions smaller than 2 cm and with low serum levels of CA 19.9, two independent prognostic factors. Hence, ^{18}F-FDG uptake might be an additional important factor, as studies have shown that an SUV ≥5 is a predictive factor of early recurrence or poor prognosis [9]. Further studies should be done in these rare tumors to better understand the usefulness of ^{18}F-FDG in that context.

6.3.1.2 Other Tracers

Due to limited sensitivity of ^{18}F-FDG for well-differentiated HCC, other radiotracers may be used to improve the sensitivity.

11C-Acetate is a tracer whose uptake is closely related with de novo lipid synthesis. The main problem related with this tracer is its short half-life (20 min) which requires the need for an onsite cyclotron. It is reported to have high sensitivity of 78–87 % [4] for both well and poorly differentiated HCC. However, sensitivity is much lower for HCC smaller than 2 cm. Choline, as either 11C-choline or 18F-choline, is another tracer being studied. Abnormal choline metabolism is closely related with oncogenesis and tumor progression, since its uptake is increased to keep up with the demands of phospholipids for the cell membrane. While 11C-choline is biochemically indistinguishable from normal choline, allowing for a better evaluation of the choline pathway, it suffers from a short half-life (20 min) which makes this tracer hard to use in a clinical setting. On the other hand, 18F-choline, besides having a longer half-life (118 min), is shown to be useful in detecting HCC when they are well differentiated, although sensitivity drops when dealing with poorly differentiated HCC [10]. Because of this characteristic, it has been suggested by some authors to do a double scan with ^{18}F-FDG and 18F-choline, thus covering both well and poorly differentiated HCC.

18 F-FCH (fluoromethylcholine) is another tracer derived from choline that has shown high sensitivity and specificity in differentiating hepatic adenoma (HCA) and focal nodular hyperplasia (FNH) when using a 1.13 SUV cutoff, seeing higher uptake in FNH. Theoretically it could also prove useful in detecting malignant change in HCA, since in well-differentiated HCC there is uptake of this tracer [11].

^{18}F-FDGal (fluoro-deoxy-galactose) is a tracer that can show galactose metabolism and has avid uptake in the liver. Generation of this tracer from nucleophilic fluorination of commercially available Talose triflate has been reported as safe for human use [12]. In an initial report of the use of ^{18}F-FDGal in humans for HCC, the authors conclude that this tracer has high sensitivity and specificity, although no percentages are shown, for HCC and extrahepatic spread when compared to conventional dynamic contrast-enhanced CT [13]. More studies have to be undertaken before determining its utility.

18 F-FLT (fluorothymidine) is a tracer that shows tissue proliferation and has been used mainly for brain tumor imaging. There are reports showing a sensitivity of around 70 % for detecting HCC, which is similar to that of conventional ^{18}F-FDG PET imaging. Larger studies are required for better assessment of its utility in increasing the specificity by combined use of both tracers [14].

6.3.1.3 Treatment Response

While ^{18}F-FDG is shown to be useful (Fig. 6.3) in tumor response assessment, false-negative uptake is seen in therapies targeting the tumor blood supply. Meanwhile, MRI multiparametric imaging is not as dependent as ^{18}F-FDG on blood flow, thus allowing them to assess tumor response in a wider range of treatments.

Quantitative dynamic contrast enhancement (DCE) is a technique where by using one or two compartment PK models, the constant tumor tissue transfer (K^{trans}) and the extravascular extracellular volume fraction (V_e) can be computed. The imaging technique relies on the sequential scanning of the liver before and immediately after contrast injection on predetermined periods of time. The analysis of these images with dedicated software provides the K^{trans} and the V_e, allowing detection of areas of the tumor perfusion as an indicator for cell viability. The two main problems with DCE, is the inability to differentiate viable tumoral from reactive granulation tissue and in assessment of tumoral lesions with areas of necrosis. The

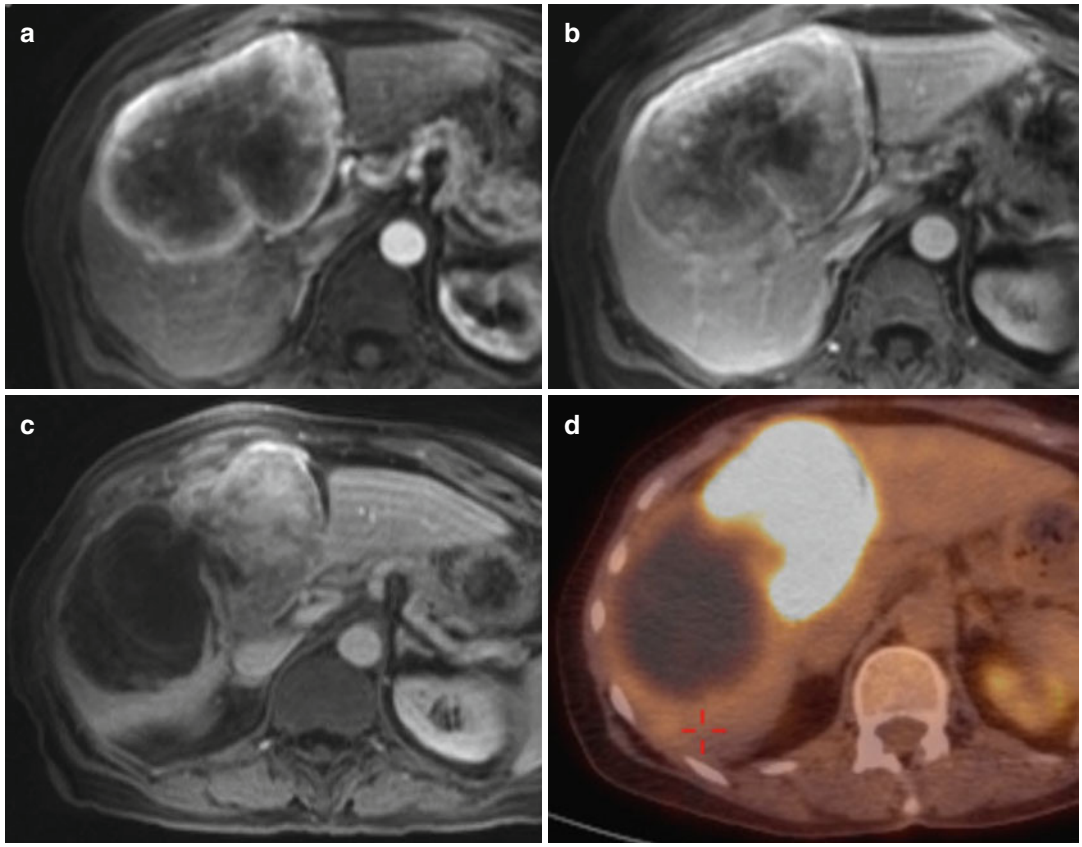

Fig. 6.3 Chemoembolization (TACE) of HCC. Pretreatment post-gadolinium T1 GRE images in arterial (**a**) and delayed (**b**) show a large left hepatic lobe mass with peripheral enhancement. Post-TACE gadolinium-enhanced T1 GRE image (**c**) shows no enhancement of right half of the lesion. ^{18}F-FDG PET/CT image (**d**) shows no uptake in the corresponding right half of the mass indicating partial response to treatment

main issue with necrosis is that contrast enhancement of these areas is obtained through contrast diffusion and that mechanism can influence the recorded agent concentration curves.

Other multiparametric sequences that can also determine tumor perfusion and vascularity are arterial spin labeling (ASL), blood oxygenation level-dependent (BOLD) imaging, and intravoxel incoherent motion (IVIM) imaging. These are being tested in renal cell carcinoma with no documented utility in hepatic malignancy. There is potential application of these MR techniques in the future, once difficulties such as the quantification in a tri-compartment model, exact arterial input function, respiratory gating, absolute quantification, and reproducibility are sorted out.

For assessment of tumor viability, independent of blood flow, DWI and the ADC maps obtained from it have shown to be useful in the longitudinal monitoring of tumor response to a vascular disrupting agent. Based on the capability of this sequence to determine the diffusivity of the free water molecules, DWI can depict with high-sensitivity tissues with high cellular component. It has to be taken into account that when evaluating well-perfused tumors, the ADC maps should be obtained from *b* values >100 to suppress the perfusion component of the analyzed tissue.

6.3.2 Metastases

The liver is an organ that is commonly involved by metastatic disease, especially with primary tumors of the digestive tract because of the portal drainage of these organs into the liver. It is known

that 30–40 % of colorectal cancer (CRC) patients with a resectable primary lesion at the time of initial diagnosis will develop recurrent disease in the liver, within the first 2 years [15]. Over all about 50 % of the CRC patients will develop hepatic metastasis [15]. Two different patient populations have to be distinguished regarding treatment approaches to metastatic disease to the liver in CRC: patients who are amenable for partial liver resection and those who do not qualify for a surgical approach. Of the 50 % of CRC patients who develop liver metastases, only 20–25 % [16] will be candidates for surgical resection. The importance of this relies in that survival of CRC patients has been significantly improved when abdominal imaging is implemented in their diagnostic workup and follow-up. This is mainly due to liver resection of metastasis detected at an early stage. To those patients who are not surgical candidates, other options such as transarterial embolization (TAE), transarterial chemoembolization (TACE), radiofrequency ablation, and transarterial radio-embolization with Y90 are available. In this fraction of patients, the focus is no longer on disease detection but on assessment of treatment response.

Diagnostic workup for the patient population where surgery is an option should focus on sensitivity to detect early disease, as surgical resection provides absolute cure and improved survival. While usually triple-phase CT is the most commonly used diagnostic procedure, PET/CT has proven more sensitive for detection of both hepatic and extrahepatic metastatic diseases. At the same time, MRI is evolving as a more accurate tool to assess liver metastasis when compared to CT. With the advent of hepatocyte- and liver-specific contrast agents (gadoxetic acid, SPIO, etc.), accuracy of MRI has surpassed triple-phase CT [17] and PET/CT for lesions below 10 mm [18] (Fig. 6.4). For detection of hepatic malignant lesions, MRI with DWI has a reported detection rate of 97.5 % (Fig. 6.5) and which has increased to 100 % with the additional use of liver-specific agents [19]. Hence, MRI is the single best imaging option for detection of hepatic metastases. While PET/CT is limited in spatial resolution in the liver (Fig. 6.6), it definitely has its strengths in the detection of extrahepatic disease (Fig. 6.7) which is essential to determine appropriate therapeutic approach.

In the second patient population, with non-resectable liver metastases, the major challenge is to determine success or failure of treatment and to determine local recurrence in previously treated locations. Triple-phase CT, though not the best imaging modality, is a more common option in this patient population, because of its availability and reasonable sensitivity and specificity. While efficacy of multiparametric MRI with DWI and ADC maps is still being tested on these patients, response to chemotherapy on F-FDG PET/CT has shown good correlation to disease-free survival [20]. PET/CT has shown a sensitivity of 65 % on detecting residual tumors in livers treated with radiofrequency ablation [21].

6.3.2.1 Other Tracers

Another tumor entity to frequently metastasize to the liver is neuroendocrine tumors (NET) of the pancreas and gastrointestinal tract. NET are slow growing and have a slow metabolic rate. Because of their slow-growing pace and the fact that they are usually asymptomatic, they are most often diagnosed at a late stage when metastatic spread is already present. Because of the slow-growing rate and, hence, low metabolic rate of most of these tumors, ^{18}F-FDG-based PET is not a good tool to diagnose or stage. Nonetheless it could be useful on determining prognosis since ^{18}F-FDG uptake by these tumors is directly related to a shift in differentiation from well to poorly differentiated which in turn is related to poorer prognosis [22]. Expression of somatostatin receptors by these tumors allows the use of labeled somatostatin analogues for detection and staging of NET. The tracer used for SPECT is ^{111}In-DTPAOC (111In-DTPA-octreotide) (Fig. 6.8), while ^{68}Ga-DOTATOC is the tracer for PET/CT ([68Ga]-DOTA-D-Phe (1)-Tyr (3)-octreotide). The latter tracer has shown higher sensitivity than CT and SPECT because ^{68}Ga-DOTATOC has higher affinity to somatostatin receptors than ^{111}In-DTPAOC and PET has a higher spatial resolution than SPECT. It has also been noted that the retrospective fusion of ^{68}Ga-DOTATOC

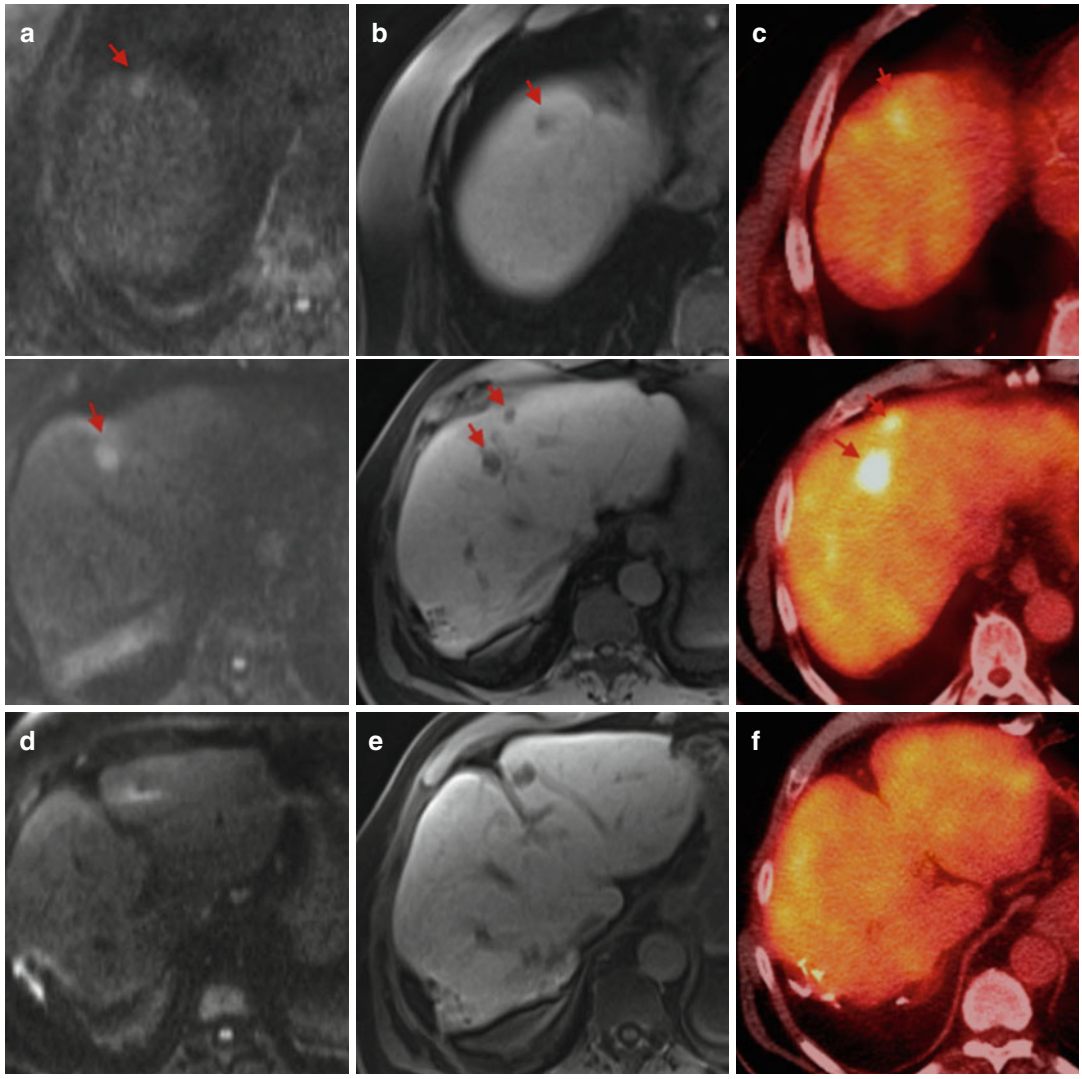

Fig. 6.4 Hepatic metastases from colon cancer. DWI (**a**) delayed hepatobiliary phase T1 GRE following Eovist (**b**) and ^{18}F-FDG PET/CT (**c**) images show multiple hepatic lesions in segment 4 with FDG uptake. DWI (**d**) delayed hepatobiliary phase T1 GRE following Eovist (**e**) and ^{18}F-FDG PET/CT (**f**) images show another metastatic lesion in segment 3 on delayed post-Eovist images without diffusion restriction or uptake on FDG-PET images

PET with MRI using gadoxetic acid has higher sensitivity (91 %) than ^{68}Ga-DOTATOC PET/CT alone (74 %), especially with lesions under 10 mm. On the other hand, MRI alone has a sensitivity of 88 % [23]. One should be aware that poorly differentiated neuroendocrine tumors can express low levels of somatostatin receptors 2 and 5, which are the ones that are targeted by the aforementioned radiotracers. In this latter population, there would be a benefit of using MRI conjointly with ^{18}F-FDG PET/CT, since MRI can still detect these lesions with a high sensitivity, independently of the tumor grade, and avid uptake of ^{18}F-FDG by undifferentiated NET, as opposed to the other tracers.

Other radiotracers such as 18 F-FLT (fluorothymidine) have been tested for the detection and characterization of liver metastatic lesions with promising results when assessing treatment response [24]. As FLT is metabolized to

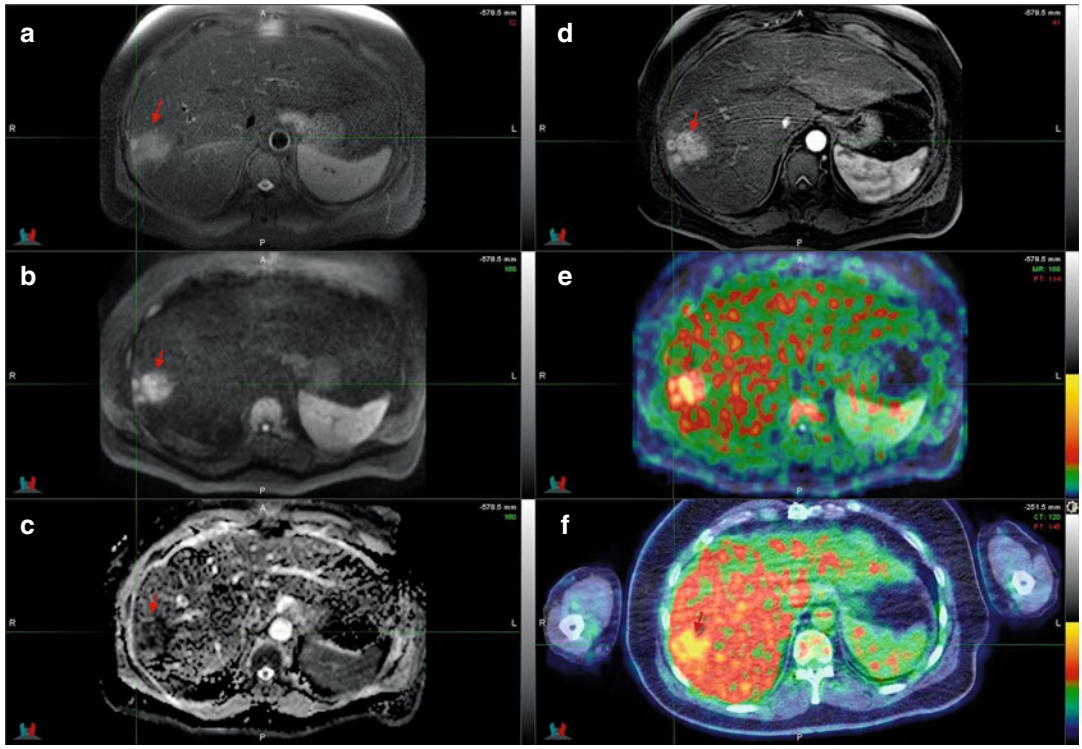

Fig. 6.5 Hepatic metastases from rectal cancer. T2-weighted fat-saturated FSE (**a**) DWI (**b**) ADC (**c**) and gadolinium-enhanced T1 GRE images (**d**) show a cluster of three metastatic lesions in the right lobe. Fusion images of FDG PET/MR (**e**) and FDG PET/CT (**f**) demonstrate increased uptake in this region though identification of three distinct lesions is difficult due to low spatial resolution

FLT-glucuronide in liver tissue leading to a high physiological uptake, its utility for assessing proliferation in patients with liver tumors is limited, and further experience is needed before any conclusions can be drawn from these experiences.

6.3.3 Infections

Use of ^{18}F-FDG PET/CT is reserved for specific hepatic infections.

Reports have been published on the role of ^{18}F-FDG in imaging alveolar echinococcal disease and fungal liver abscesses. However, no evidence can be drawn from them regarding its use in either disease. Though there is potential role of F-FDG-PET CT in monitoring response to treatment and to decide the appropriate drug therapy of fungal liver abscesses, there is no supporting evidence from large-scale studies. Regarding alveolar echinococcal disease, there were unsuccessful attempts to link the ^{18}F-FDG uptake of the lesions to the pathogen viability, since there are reports showing pathogen viability even in the absence of ^{18}F-FDG uptake. Nonetheless some authors reported the ^{18}F-FDG PET/CT to be useful in differentiating between alveolar and cystic echinococcal diseases.

6.4 Pitfalls and Artifacts

PET/MRI pitfalls and artifacts related to the imaging of the liver are mostly related to breathing motion. When no measures are taken to prevent breathing-related artifacts, they can show in up to two thirds of patients. Breathing artifacts can result in either misalignment of lesions or incorrect attenuation correction of the PET acquisition (Fig. 6.9). Ideally, the liver is imaged in the

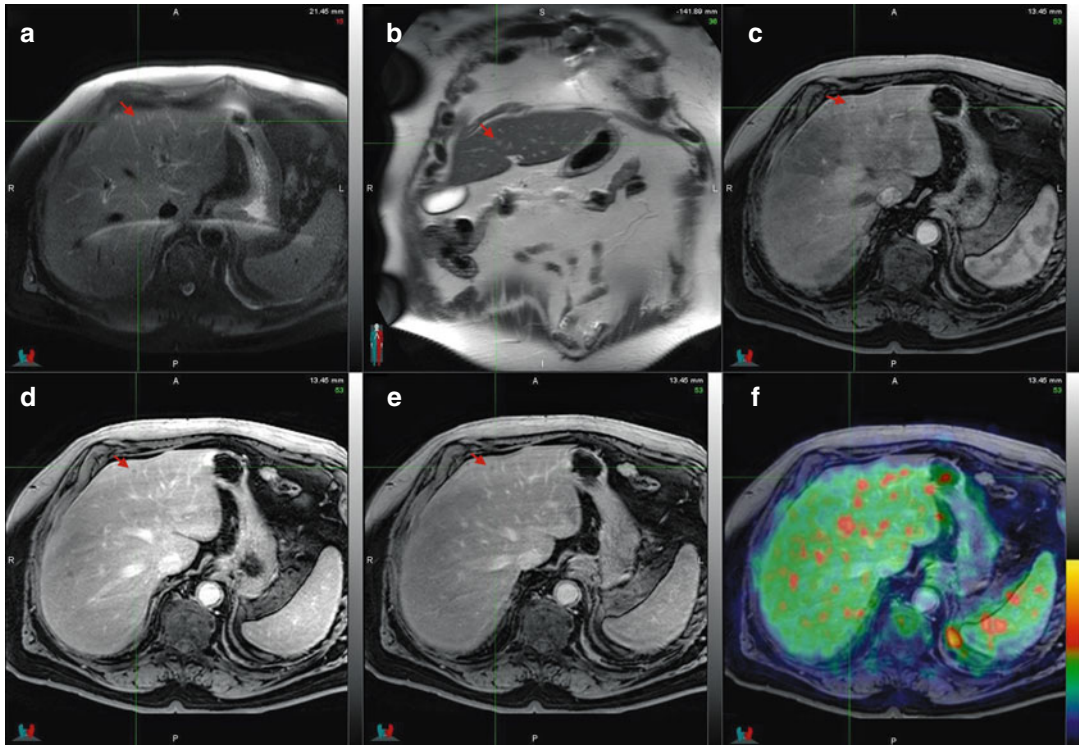

Fig. 6.6 Small hepatic metastasis from colon cancer. T2-weighted axial (**a**) and coronal (**b**) gadolinium-enhanced T1 GRE images in arterial (**c**) portal (**d**) and delayed (**e**) phases show the presence of a subcentimeter liver metastasis in segment 4. The lesion is not detectable in the corresponding PET/MR fusion image (**f**)

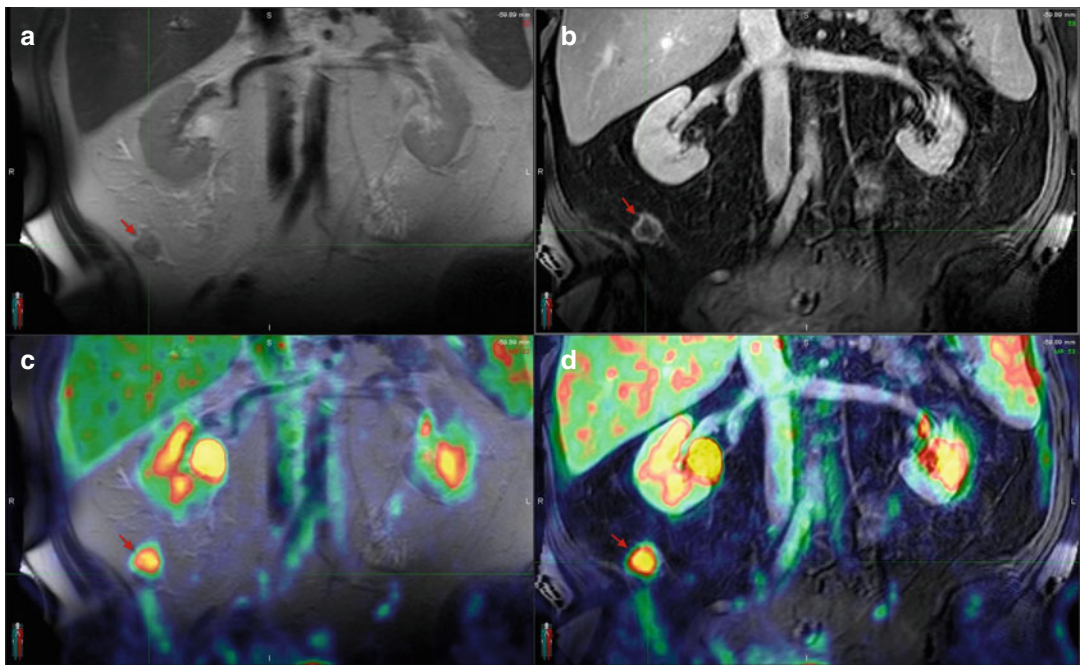

Fig. 6.7 Extrahepatic metastases from colon cancer. Coronal T2-weighted (**a**) and gadolinium-enhanced T1 GRE (**b**) images demonstrate an enhancing lesion in the right lower quadrant. Corresponding coronal ^{18}F-FDG PET/CT images (**c** & **d**) show significant uptake within this lesion

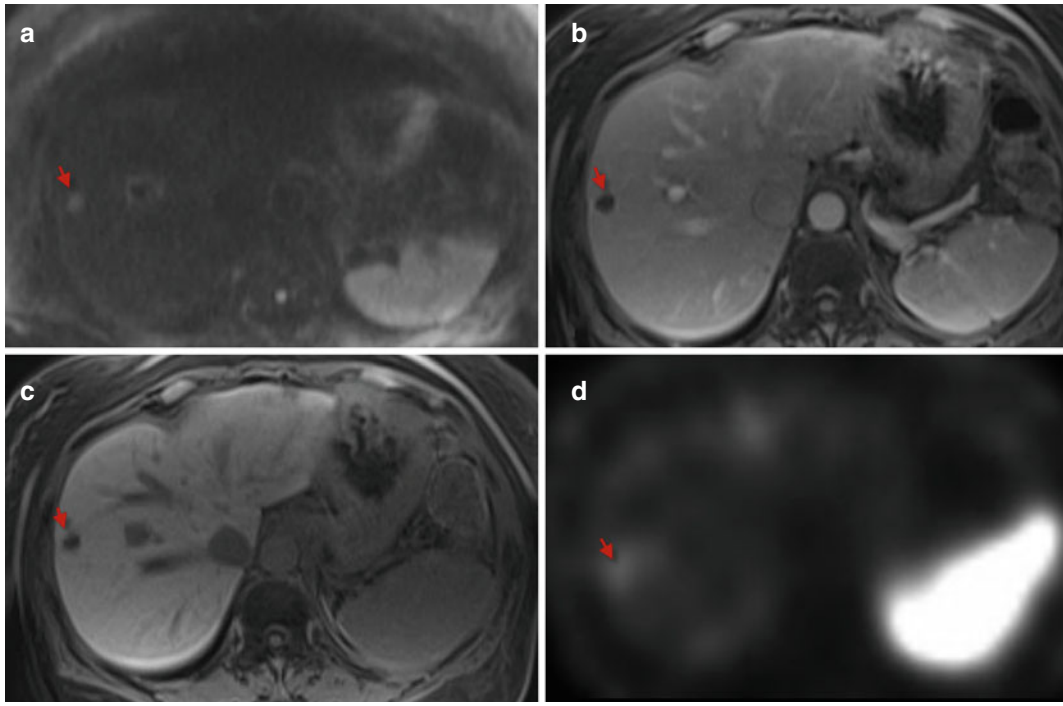

Fig. 6.8 Hepatic metastases from neuroendocrine tumor of the pancreas. DWI (**a**) T1 GRE in portal venous (**b**) and delayed hepatobiliary phase (**c**) images following Eovist show a well-defined hypointense lesion in segment VIII with diffusion restriction. Indium-111 octreotide scan (**d**) shows faint uptake of the tracer in the same region

exact same position in both MRI and PET. However, in reality, image acquisition is slightly different in MRI and PET so that exact co-registration is actually challenging. As in PET/CT, the acquisition in PET is done over 1–3 min, typically per bed position, and in free breathing which averages an intermediate respiratory position. In MRI, image acquisition is typically performed in one single breath hold during which the entire liver can be covered.

The first relates to the position of the liver during the anatomical acquisition, be it MRI or CT, and the mismatch of the position of the organ in comparison with the position of the organ in the PET. In PET/CT, where CT acquisition happens in a few seconds with the current CT technology, attempts have been made to diminish breathing artifact by instructing the patient to breath-hold in intermediate inspiration or in expiration. In MRI, most of the relevant sequences for liver imaging are acquired in breath hold. Thus, a similar approach could be chosen as in PET/CT, since image acquisition in MRI however may take between 20 and 30 s and more than one acquisition may be necessary in some cases to cover the entire liver.

As both attenuation correction sequences, 2-point Dixon and the T1w 3D, are scanned as volume data sets, there is no possibility to gate the acquisition. Nonetheless, breathing instructions do help, and efforts can be made to make the breath hold last shorter, like increasing the number of acquisitions to cover the whole length of the liver by diminishing the number of slices per acquisition.

Albeit the impact breathing artifact has on lesion localization, it can also impact on the SUV values of the PET data (Fig. 6.10), given that the anatomical acquisition is used to correct the PET. In this case a misalignment of the PET data and the CT or MRI data generates the misinterpretation of photons that proceed from liver tissue as photons that proceed from the lung; since both tissues have attenuation correction coefficients

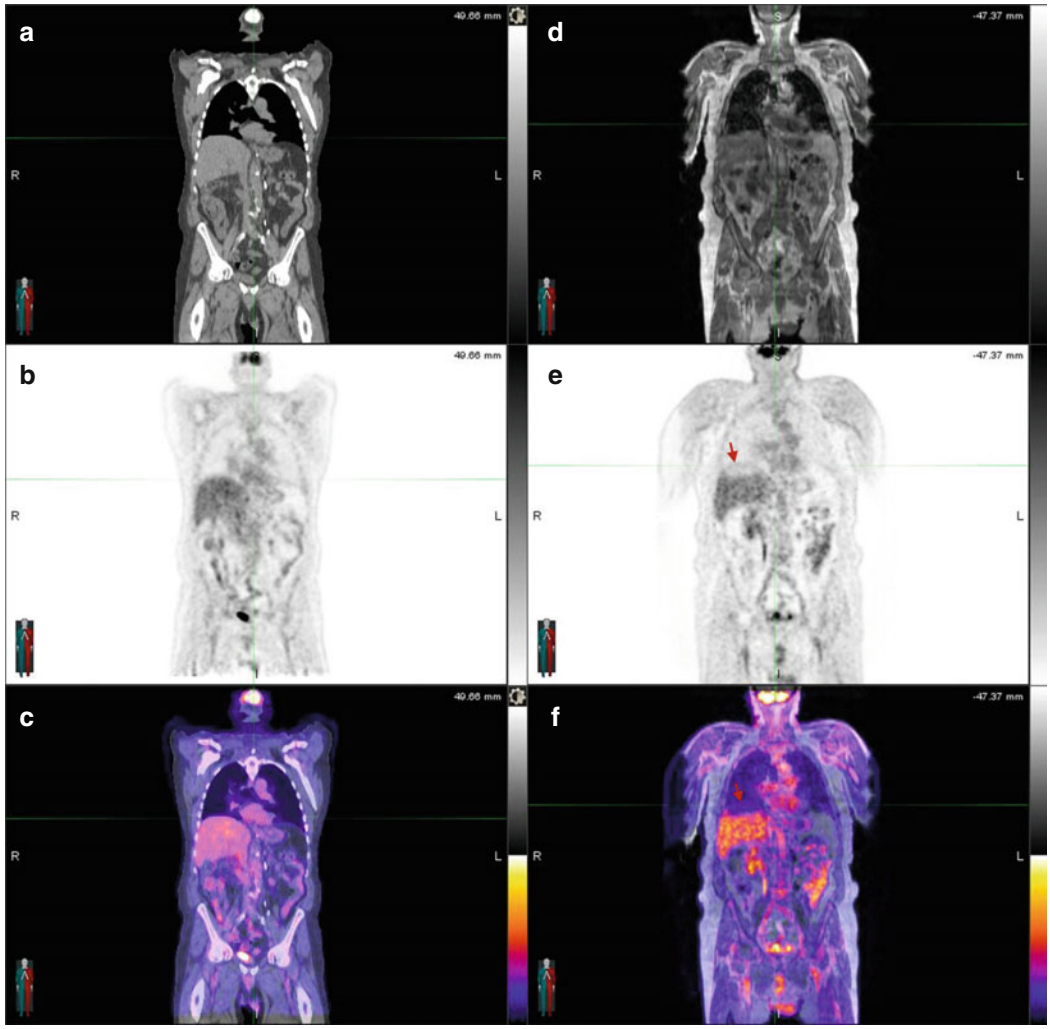

Fig. 6.9 Respiratory misregistration artifact. Side-by-side comparison of PET/CT attenuation correction (**a**) FDG-PET (**b**) PET/CT fusion (**c**) PET/MR attenuation correction (**d**) FDG-PET (**e**) and PET/MR fusion (**f**) images showing a photopenic band in the PET/MR images (*arrows* in images **d** & **e**) near the dome of the liver due to the lower position of the liver in the images used for MR attenuation correction

which are very different, the resulting SUV is underestimated and a photopenic band is seen.

While the breathing-based artifacts are of a technical nature in the sense that are related to how the image is acquired by the scanner, other artifacts can be generated from physiological conditions of the patient, like the one related to tissues with physiologically increased ^{18}F-FDG uptake. In the case of the liver, there has been studies showing that at higher serum glucose levels at the time of ^{18}F-FDG injection, higher SUV values will be seen in the liver, especially upon delayed imaging (>1 h) [25]. In this context guidelines [26] suggest to image with glucose levels below 120 mg/dl, especially because the liver is already an organ with high ^{18}F-FDG uptake, making it sometimes difficult to visualize lesions with uptake.

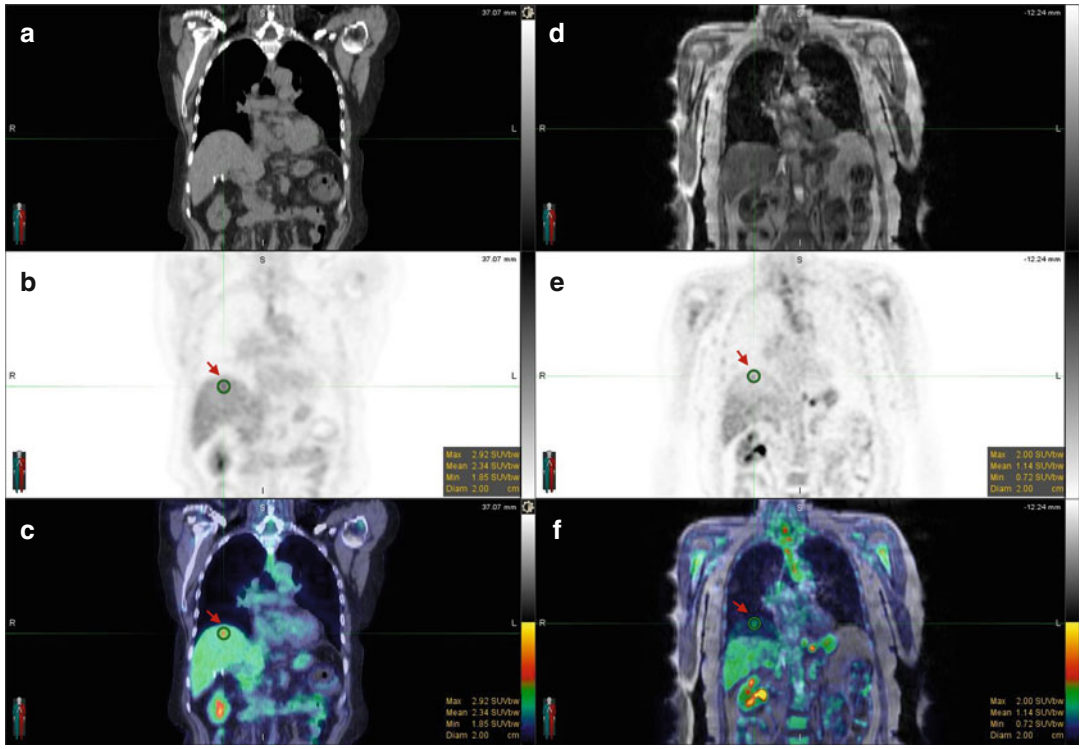

Fig. 6.10 Low SUV value from respiratory misregistration. Side-by-side comparison of PET/CT attenuation correction (**a**) FDG-PET (**b**) PET/CT fusion (**c**) PET/MR attenuation correction (**d**) FDG-PET (**e**) and PET/MR fusion (**f**) images show low SUV of the metastatic lesion at the dome of the liver in PET/MR images (**d** & **e**) due to the lower position of the liver in the images used for MR attenuation correction

Conclusion

MRI and molecular imaging, using ^{18}F-FDG and other tracers, are the two best independent imaging methods in evaluation of both metastatic and primary hepatic tumors. It is also evident that in most of these situations, neither imaging modality hinders the performance of the other, allowing coupling into a single-imaging modality (PET/MRI).

Patients being studied for metastatic spread of CRC, or breast cancer, or melanoma, or other tumor will have the opportunity to get the best diagnostic capabilities in the liver (MRI) (Fig. 6.11); at the same time they can be screened for extrahepatic disease with the best imaging method available (PET). Another example would be a patient with a primary tumor of the liver, where MRI multiparametric imaging, alongside with PET and its multiple tracers available, not only will work synergically to diagnose the type of the tumor and extrahepatic metastases but will also be able to thoroughly assess tumor response to treatment and screen for relapse.

PET/MRI is still a fairly new technology, and though preliminary studies have shown great potential for this new hybrid imaging, further studies have to be undertaken to establish its role and its cost-effectiveness.

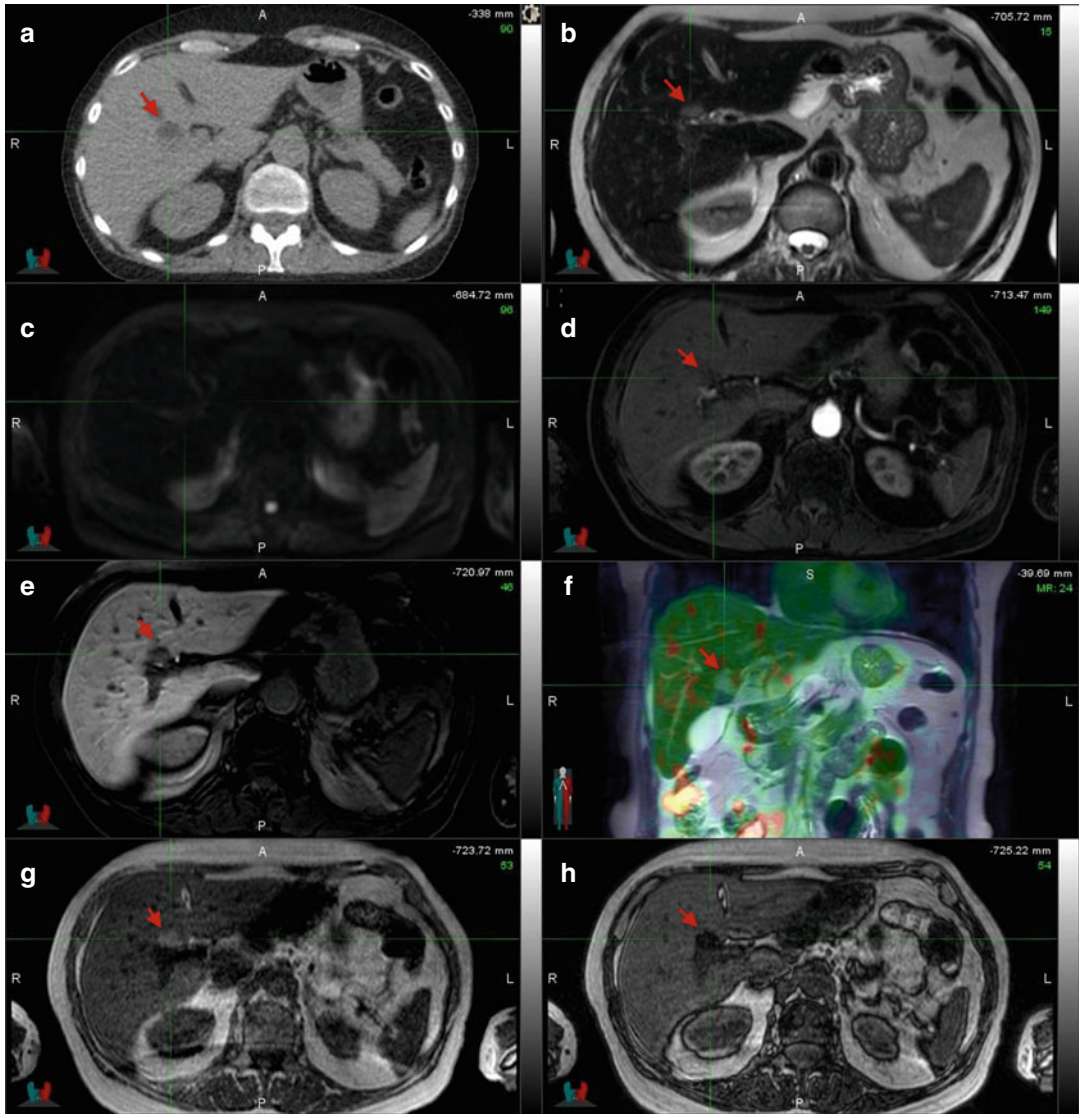

Fig. 6.11 Focal hepatic steatosis. A patient with colon cancer for staging demonstrates indeterminate focal hypodense lesion on a contrast-enhanced CT (**a**); T2-weighted MR image (**b**) without fat saturation demonstrates a hyperintense focus; DWI (**c**) shows no diffusion restriction, no enhancement in the early (**d**) and delayed hepatobiliary phase (**e**) T1 GRE images following Eovist, no uptake on fused FDG-PET MR image (**f**); chemical shift T1-weighted MR images demonstrate drop in signal intensity of this lesion between the in-phase (**g**) and out-of-phase (**h**) images

References

1. Drzezga A, Souvatzoglou M, Eiber M, et al. First clinical experience with integrated whole-body PET/MR: comparison to PET/CT in patients with oncologic diagnoses. J Nucl Med. 2012;53(6):845–55.
2. Siegel MJ, Acharyya S, Hoffer FA, et al. Whole-body MR imaging for staging of malignant tumors in pediatric patients: results of the American College of Radiology Imaging Network 6660 trial. Radiology. 2013;266(2):599–609.
3. Gu J, Chan T, Zhang J, et al. Whole-body diffusion-weighted imaging: the added value to whole-body MRI at initial diagnosis of lymphoma. AJR Am J Roentgenol. 2011;197(3):W384–91.
4. He YX, Guo QY. Clinical applications and advances of positron emission tomography with fluorine-18-fluorodeoxyglucose (^{18}F-FDG) in the diagnosis of liver neoplasms. Postgrad Med J. 2008;84(991):246–51.

5. Lee SD, Kim SH, Kim YK, et al. (18)F-FDG-PET/CT predicts early tumor recurrence in living donor liver transplantation for hepatocellular carcinoma. Transpl Int. 2013;26(1):50–60.
6. Paudyal B, Oriuchi N, Paudyal P, et al. Early diagnosis of recurrent hepatocellular carcinoma with ^{18}F-FDG PET after radiofrequency ablation therapy. Oncol Rep. 2007;18(6):1469–73.
7. Lan BY, Kwee SA, Wong LL. Positron emission tomography in hepatobiliary and pancreatic malignancies: a review. Am J Surg. 2012;204(2):232–41.
8. Shiomi S, Kawabe J. Clinical applications of positron emission tomography in hepatic tumors. Hepatol Res. 2011;41(7):611–17.
9. Ijichi H, Shirabe K, Taketomi A, et al. Clinical usefulness of (18) F-fluorodeoxyglucose positron emission tomography/computed tomography for patients with primary liver cancer with special reference to rare histological types, hepatocellular carcinoma with sarcomatous change and combined hepatocellular and cholangiocarcinoma. Hepatol Res. 2013;43(5): 481–7.
10. Treglia G, Giovannini E, Di Franco D, et al. The role of positron emission tomography using carbon-11 and fluorine-18 choline in tumors other than prostate cancer: a systematic review. Ann Nucl Med. 2012; 26(6):451–61.
11. Bieze M, Bennink RJ, El-Massoudi Y, et al. The use of 18F-fluoromethylcholine PET/CT in differentiating focal nodular hyperplasia from hepatocellular adenoma: a prospective study of diagnostic accuracy. Nucl Med Commun. 2013;34(2):146–54.
12. Frisch K, Bender D, Hansen SB, et al. Nucleophilic radiosynthesis of 2-[18F]fluoro-2-deoxy-D-galactose from Talose triflate and biodistribution in a porcine model. Nucl Med Biol. 2011;38(4):477–83.
13. Sorensen M, Frisch K, Bender D, et al. The potential use of 2-[(1)(8)F]fluoro-2-deoxy-D-galactose as a PET/CT tracer for detection of hepatocellular carcinoma. Eur J Nucl Med Mol Imaging. 2011;38(9): 1723–31.
14. Eckel F, Herrmann K, Schmidt S, et al. Imaging of proliferation in hepatocellular carcinoma with the in vivo marker 18F-fluorothymidine. J Nucl Med. 2009;50(9):1441–7.
15. Jones C, Badger SA, McKie LD, et al. PET-CT accurately predicts the pre-operative characteristics of colorectal hepatic metastases. Eur J Surg Oncol. 2012;38(12):1184–8.
16. Georgakopoulos A, Pianou N, Kelekis N, et al. Impact of ^{18}F-FDG PET/CT on therapeutic decisions in patients with colorectal cancer and liver metastases. Clin Imaging. 2013;37(3):536–41.
17. Bipat S, van Leeuwen MS, Comans EF, et al. Colorectal liver metastases: CT, MR imaging, and PET for diagnosis–meta-analysis. Radiology. 2005; 237(1):123–31.
18. Strasberg SM, Dehdashti F. Role of FDG-PET staging in selecting the optimum patient for hepatic resection of metastatic colorectal cancer. J Surg Oncol. 2010;102(8):955–9.
19. Lowenthal D, Zeile M, Lim WY, et al. Detection and characterisation of focal liver lesions in colorectal carcinoma patients: comparison of diffusion-weighted and Gd-EOB-DTPA enhanced MR imaging. Eur Radiol. 2011;21(4):832–40.
20. Small RM, Lubezky N, Shmueli E, et al. Response to chemotherapy predicts survival following resection of hepatic colo-rectal metastases in patients treated with neoadjuvant therapy. J Surg Oncol. 2009;99(2):93–8.
21. Veit P, Antoch G, Stergar H, et al. Detection of residual tumor after radiofrequency ablation of liver metastasis with dual-modality PET/CT: initial results. Eur Radiol. 2006;16(1):80–7.
22. Kumar R, Sharma P, Garg P, et al. Role of (68) Ga-DOTATOC PET-CT in the diagnosis and staging of pancreatic neuroendocrine tumours. Eur Radiol. 2011;21(11):2408–16.
23. Schreiter NF, Nogami M, Steffen I, et al. Evaluation of the potential of PET-MRI fusion for detection of liver metastases in patients with neuroendocrine tumours. Eur Radiol. 2012;22(2):458–67.
24. Contractor K, Challapalli A, Tomasi G, et al. Imaging of cellular proliferation in liver metastasis by [18F] fluorothymidine positron emission tomography: effect of therapy. Phys Med Biol. 2012;57(11):3419–33.
25. Kubota K, Watanabe H, Murata Y, et al. Effects of blood glucose level on FDG uptake by liver: a F-FDG-PET/CT study. Nucl Med Biol. 2011;38(3):347–51.
26. Boellaard R, O'Doherty MJ, Weber WA, et al. F-FDG PET and PET/CT: EANM procedure guidelines for tumour PET imaging: version 1.0. Eur J Nucl Med Mol Imaging. 2010;37(1):181–200.

PET/MR in Colorectal Cancer

7

Sasan Partovi, Andres Kohan, Raj Mohan Paspulati, Pablo R. Ros, and Karin A. Herrmann

Contents

S. Partovi • A. Kohan • R.M. Paspulati, MD
P.R. Ros • K.A. Herrmann (✉)
Department of Radiology, University Hospitals Case Medical Center, Cleveland, OH, USA
e-mail: raj.paspulati@uhhospitals.org; pablo.ros@uhhospitals.org; karin.herrmann@uhhospitals.org

7.1 Introduction

Colorectal cancer (CRC) is the third most common malignant neoplasm in mankind with slightly less than 1.2 million new cases and more than 600,000 deaths worldwide in 2008 [1, 2]. Colorectal cancer is frequently associated with metastatic disease – either synchronous or metachronous – with the highest number of metastases to the lymph nodes and liver. In CRC patients' early detection of metastases has a strong impact on prognosis since effective interventional as weäll as surgical treatment options can be offered leading to relatively high survival rates [3]. If disease course is followed closely with imaging, survival can be significantly improved [4].

Diagnostic imaging plays a crucial role in the initial staging, treatment monitoring, and disease follow-up. The cornerstones of diagnostic imaging in this setting are computed tomography (CT), magnetic resonance imaging (MRI), and positron-emission tomography (PET), today mostly performed as PET/CT. Conventional colonoscopy is the mainstay for the detection and primary diagnosis of disease.

In addition to contrast-enhanced CT of the chest, abdomen, and pelvis, other cross-sectional imaging methods and PET are well established in the current CRC workup. Foremost, PET/CT has gained a crucial role in primary staging and surveillance of colorectal cancer [5]. What makes PET/CT a successful modality for this disease is the accuracy for assessment of M and N staging with minor limitations for the detection of liver

I. Carrio, P. Ros (eds.), *PET/MRI*,
DOI 10.1007/978-3-642-40692-8_7, © Springer-Verlag Berlin Heidelberg 2014

metastases. In a post-treatment setting, PET/CT is able to differentiate post-therapeutic changes from cancer recurrence or residual malignancy with a high level of confidence [6]. This hybrid imaging modality is therefore of particular value for colorectal cancer patients who present with an unexplained rise in CEA [6].

In addition, PET/CT leads frequently to the correction of staging results established by other noninvasive staging imaging modalities and helps to appropriately adjust the overall therapeutic strategy in individual patients [7–10].

MRI, historically, is an imaging technique focusing on a specific organ or body region like the brain, liver, or pelvic organs with dedication to tissue specification and spatial detail.

In imaging colorectal cancer, the role of MRI is paramount in the workup of rectal cancer and less prominent in the workup of colon cancer except for the assessment of metastatic disease to the liver.

With the arrival of new scanner technology for faster imaging – particularly parallel imaging techniques – whole-body MRI has been successfully applied for CRC staging with comparable results to PET/CT [11]. Functional, multiparametric MR imaging has further broadened the spectrum of applications of diagnostic MRI [12]. Diffusion-weighted imaging (DWI), a surrogate parameter for tissue cellularity, perfusion imaging with dynamic contrast-enhanced (DCE)-MRI, blood oxygen level-dependent (BOLD) imaging for hypoxia mapping, as well as MR spectroscopy which give information about the molecular tissue composition [13, 14] all have helped MRI to gain attention as an essential tool for oncology imaging beyond the mere desire to image anatomic detail and morphology. In PET/MR, local and whole-body imaging is combined, and the molecular and biological information from PET is added to the equation. This combination raises hope for further improvement of diagnostic capacity of this new modality compared to the current standard of care. The noninvasive approach and lack of ionizing radiation are additional advantages even over the very successful modality PET/CT. To assess the value of PET/MR, to determine the accuracy as compared to standard of care and PET/CT, and to elucidate the incremental benefit of combining the two modalities in one are currently work in progress.

7.2 Technical Considerations for PET/MR in CRC

7.2.1 Scanner Design

The design of currently commercially available hybrid PET/MRI systems is that of either an integrated system [15] or a “tandem” sequential solution of PET and MRI [16]. In the integrated system, the PET is built into the MRI scanner. Image acquisition of PET and MRI occurs simultaneously. In the tandem approach, PET and MRI are located in close vicinity to each other in the same room and connected by a common table that moves between the two units. In the tandem approach PET/MR, the images in PET and MRI are acquired sequentially but in the same imaging examination as in PET/CT. Whether there is advantage of one approach over the other is not proven, yet.

Based on the limited literature available, some authors claim that simultaneous integrated PET/MR may overcome challenges in image interpretation in the abdomen related to tissue movement in structures like the bowel [17]. Other authors of a recently published review about applications of PET/MRI in the abdomen state that the sequential “tandem” approach is sufficient for the majority of cases in clinical settings.

According to our own experience with a tandem system PET/MR and sequential imaging, the quality of alignment for abdominal lesions depends essentially on the imaging sequences and the patient motion for exact matching. Based on our experience and the limited literature available, there is no clinically relevant difference for localization of lesions between sequential and simultaneous PET/MR approach in abdominal oncology applications [18]. Further studies in larger patient cohorts however are warranted.

7.2.2 Attenuation Correction

The three major tasks of MRI in the context of PET/MR are the following: (1) to generate data for tissue attenuation correction, (2) to provide anatomic reference for foci of abnormal tracer uptake, and (3) to deliver morphologic and functional diagnostic information dedicated to detect, characterize, and stage disease.

Various MR sequences are being used as a source for tissue attenuation maps and subsequent quantification of standardized uptake values (SUV). Most common MR attenuation (atMR) sequences include T1w 3D gradient echo, mDIXON, ultrashort echo time (UET), and double UTE sequences. mDIXON has the advantage to provide an in-phase, out-of-phase, water- and fat-balanced image, all in one breath hold. This sequence has been successfully used for both attenuation correction and anatomic localization. With the mDIXON a four-class tissue segmentation is possible accounting for the fat, soft tissue, air, and lung but not bone [19, 20]. This may result in quantization errors in bone and adjacent structures. On the other hand, 2-point mDIXON has demonstrated to be most suitable for the delivery of anatomic reference in PET/MRI [18]. Even for the visualization of pulmonary nodules, mDIXON was considered sufficient for diagnostic purposes with PET/MRI [21] although slightly inferior to PET/CT in a direct comparison.

UTE sequences with exceedingly short spin-spin T2 relaxation times are able to detect bone, tendons, and ligaments [22]. These properties of UTE have been applied in the brain and skull to distinguish bone from air and soft tissue for the purpose of attenuation correction. This might be distinctly helpful in the pelvis where attenuation correction is challenging due to surrounding bone and possible air in the rectum and bowel [23, 24]. A recently published manuscript combined successfully the Dixon sequence for water vs. fat detection with the UTE approach leading to four-class tissue segmentation for attenuation correction in PET/MRI [25]. This has however only been shown for head and neck cancers, primarily.

T1-weighted 3D GRE sequences – as used in other protocols – seem to suffer from higher sensitivity to motion artifacts which occasionally limit exact anatomic localization. With T1w 3D GRE, a 3-segment model is used distinguishing the air, soft tissue, and lung. Again, bone is not accounted for. A recent article by Kershah et al. reporting on the use of T1w 3D GRE for MR attenuation correction has shown that SUV deviations between PET/CT and PET/MRI are most pronounced in areas close to the bone such as the psoas muscle [26, 27]; the latter may be a region which potentially will be affected for the assessment of SUV measurements in lymphadenopathies of malignancies in the pelvis. Deviations of SUV values up to 25 % have been reported in the pelvis. However, this remains to be proven.

Other than the mDIXON sequence, the T1w 3D GRE which is used for attenuation correction in our protocol is not sufficient for anatomic reference in all areas of the body due to sensitivity to respiratory and other motion artifacts and T1w signal and contrast only. A combined approach with T1w 3D GRE for attenuation correction and mDIXON is therefore desirable.

Further characteristics of these atMR sequences are discussed elsewhere in this book in more detail.

7.2.3 Workflow Design and Image Protocol

One of the major logistic challenges encountered with PET/MR in imaging and staging colorectal cancer is the management of time intensive imaging protocols on both ends. Imaging protocols are different if focus is desired on a specific area as compared to a whole-body approach as in PET/CT. The individual arrangement of the imaging protocol, however, will substantially differ for scanners with simultaneous vs. sequential image acquisition. In both instances, examination time has to be intelligently utilized not to exceed reasonable examination time on one side and not to jeopardize image quality, patient comfort, and diagnostic outcome on the other side. Therefore, appropriate CRC-specific PET/MR protocols need to be developed for use in clinical settings [28].

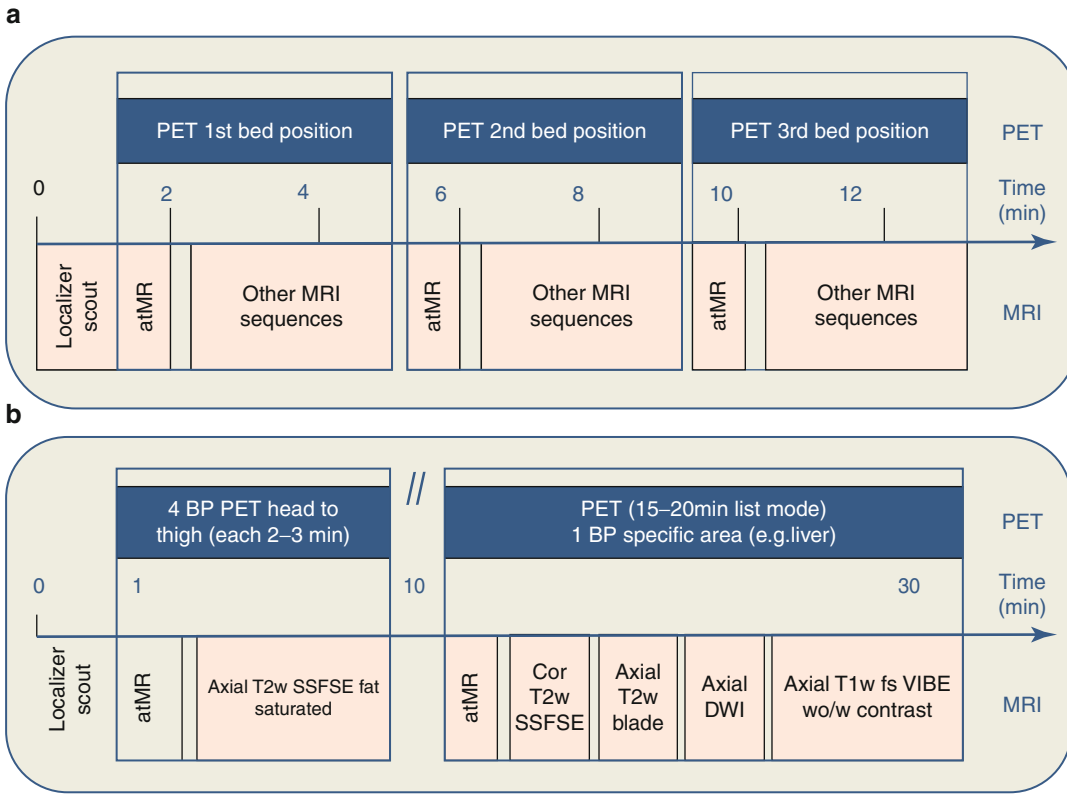

Fig. 7.1 29Workflow in a setting of simultaneous PET and MRI data acquisition. (**a**) Represents the workflow combining PET acquisition with morphologic whole-body MRI; (**b**) demonstrates an example of combined whole-body and organ-focused imaging protocol (Modified after Martinez-Moeller et al. [29])

For both scenarios, the patient preparation, the tracer kinetics, patient positioning on the table, and time for scanner operation and planning are comparable. In the integrated system, the PET and MRI data are acquired simultaneously. Martinez-Moeller et al. have proposed a workflow for optimal use of examination time in this integrated setting (Fig. 7.1) [29]. The atMR and morphologic MRI sequences are acquired while PET acquisition is running over approximately 4 min per bed position. This procedure is repeated for each bed position. Diligent selection of MRI sequences has to be made in order to intelligently use the given 4 min per bed position. If multiple sequences with variable weightings including functional imaging are desired at a certain body level – as it is likely the case in oncologic imaging – this may exceed the given time frame per bed position.

In the sequential setting, PET and MRI are acquired as separate examinations but one immediately after the other with a table shift in between. With time of flight PET technology, not available in the simultaneous design, accelerated scanning in PET is possible [16], and the total examination time for the PET component can be shortened. This leaves more time for the MRI component. In addition, in this setting, the time immediately after injection of the tracer can already be used to acquire MRI data while waiting for the tracer distribution in the body. Particularly, if whole-body MR imaging for anatomic localization is added to the equation, this may be performed during this time period. Taking advantage of the time of tracer distribution may shorten patients' overall time of visit and improve workflow.

For colorectal cancer applications, whole-body imaging for M staging might ideally be combined with focused MR imaging of the liver and/or rectum.

Typical sequences used in rectal cancer imaging include the T2-weighted sequences SSFSE and TSE in three planes with and without fat saturation and T1-weighted fat-saturated 2D or 3D sequences with and without the application of contrast material. Standard phased-array surface coils are sufficient, and an endorectal coil is not required [30].

A typical imaging protocol for colorectal cancer staging PET/MR with the sequential scanner approach includes T2w SSH imaging in two planes for the liver, abdomen, and pelvis, T2w SSH with fat saturation for the liver, and DWI for the liver and pelvis in axial orientation as well as T2w FSE (TSE) imaging in three planes for the pelvis and rectum if the primary cancer is rectal cancer. Pre- and post-contrast images are acquired for the liver including dynamic scanning 25 s, 70 s, and 5 min post injection of the contrast agent and pre- and post-contrast imaging of the pelvis. In order to cover the whole body and provide anatomic reference for M staging, the whole-body 2-point mDIXON can be performed both pre and post gadolinium. This adds only a few minutes to the total protocol and the comprehensive local and whole-body protocol can be performed in 35–40 min dependent on the body size of the patient. In a sequential approach, the PET component adds another approximately 15 min, and most of the examination can be performed within one hour.

If one would want to include primary detection of colon cancer in this setting of PET/MR, MR colonoscopy would have to be performed. MR colonoscopy includes steady-state free precession sequences (SSFP), T2w SSFSE in two planes, and T1w 3D GRE in coronal plane. SSFP sequences, although generally robust in 1.5 T MRI systems, are less desirable in a 3 T setting since they suffer from banding artifacts due to greater magnetic field heterogeneity at higher field strengths [31]. They have shown to be more motion sensitive at 3 T leading to reduced image quality [32]. The T1-weighted contrast-enhanced 3D gradient echo sequences benefit most from the higher SNR [33]. These sequences are essential for colorectal polyp and cancer diagnosis [34, 35].

Since in the setting of PET/MRI it is crucial to optimize the workflow and decrease the MR acquisition time, every approach to reduce acquisition time is welcome. Recently published data propose for rectal imaging to substitute 2D sequences in three orthogonal planes with 3D sequences in one plane followed by post-acquisition 3D image reconstruction and multiplanar reformations [36, 37]. Implementing these benefits of 3 T MR imaging may be relevant for PET/MR imaging but have not been properly evaluated yet.

7.3 Current Role of PET/CT and MRI and Potential Role of PET/MR

In current standard of care, both PET/CT and MRI have preeminent value for the diagnostic workup of CRC. The role of PET/MR is likely to be different for colon cancer as compared to rectal cancer.

7.3.1 T Staging in Colon Cancer and Rectal Cancer

The reference standard for detection of polyps as precursors of colon cancer is currently still optical colonoscopy (OC) [38, 39]. OC however is an invasive method involving anesthesia and is related to procedural risks even if minor. MR colonography (MRC) has been performed successfully and proposed as a noninvasive method to screen for polyps and detect and stage colon cancer. MRC is capable to detect colorectal adenomatous polyps as well as fully established cancer [40]. At 1.5 T field strength, a polyp of 5 mm or larger in size can be depicted with a sensitivity and specificity of 93 and 100 %, respectively [41]. 3 T MR imaging (commercially available PET/MR hybrid systems are 3 T systems) may further decrease this threshold for polyp detection [40, 42] but will also face the intrinsic challenges of

high field strength imaging. Air generates larger susceptibility artifacts at 3 T than at 1.5 T. MRC still requires the preparation of the colon and will likely not entirely avoid the issue of air in the colon. Despite the fact that a recent publication has mastered these challenges and found a sensitivity of 78.4 % and a specificity of 95.3 % for MRC at 3 T in detecting colonic polyps >6 mm [43], this technique has never been truly established in clinical routine, as of yet [31, 34, 35].

PET alone has significant limitations in detecting cancerous polyps and primary colon cancer for several reasons. First, precancerous adenomatous polyps can be detected with FDG-PET, but it is difficult to determine whether they are benign or malignant [44]. Detection rate of PET improves in larger colonic polyps and in those with a higher grade of dysplasia [45]. False-negative lesions may occur with PET specifically if these lesions are (I) mucinous tumors with poor cellularity [46] and (II) serosal metastases, because these are difficult to discern from physiological bowel activity. Furthermore, PET has limited inherent spatial resolution which does not allow accurate T staging with regard to mural invasion.

In a setting of PET/MR, the high soft tissue contrast of MRI and functional information from PET could possibly improve overall performance in detection and characterization of polyps. While there is an overt advantage of PET/MR over PET/CT in reducing radiation dose, both the feasibility of MR colonography in a setting of PET/MR and its diagnostic benefit beyond the current methods for the detection and T staging colon cancer remain to be determined.

In distinguishing inflammatory from malignant disease, PET is relatively nonspecific; this occasionally leads to a false-positive interpretation in PET images. One of the major interpretation pitfalls, however, is the physiological bowel activity which may mimic colon cancer. At this point it is important to emphasize that PEt alone is not an appropriate imaging modality for colon cancer screening due to high costs, limited availability, and lack of specificity [47].

Following our own initial experience with PET/MR, issues of bowel activity and distinction of inflammatory from malignant tissue are a similar dilemma. Additional challenges in PET/MR lie in a reproducible quantification and consistency of standardized uptake values. Since tissue attenuation correction in PET/MR is not performed with CT but based on MRI, the SUV quantification and tissue attenuation correction in PET/MRI is currently particularly dependent on the sequence type used for attenuation correction [48].

In summary, MRC and MRI nowadays play a minor role in the primary detection of colon cancer despite its noninvasive character, high potential, and fairly high accuracy [34, 43]. T staging of colon cancer remains a domain of conventional optical colonoscopy which has maintained its role as a reference standard likely due to the significant advantage to provide histopathology and options for treatment at the same time.

In contrast to the setting for colon cancer, MRI plays a major role in the primary assessment of rectal cancer. Local staging of rectal cancer and patient treatment outcome have significantly improved with the arrival of high-resolution MRI. To assess the degree of infiltration in the bowel wall and mesorectum is of paramount importance for clinicians and surgeons in order to decide for appropriate therapy. This information can be obtained either with invasive endorectal ultrasonography or with noninvasive MRI [49]. Studies comparing histology as reference standard with T staging conducted by MRI revealed agreement rates of up to 94 % [50, 51].

Beyond primary local T staging of rectal cancer, MRI alone has gained increasing importance in the evaluation of *treatment response* and *local recurrence*. Adding DWI to the protocol has improved diagnostic accuracy for detection of rectal cancer [52–56], has fostered predictive capacities of MRI [57, 58], and has been successful assessing treatment response when combined with T2-weighted images [55, 59]. As DWI with its ADC values gives information about viability of tissue and potentially about the hypoxic state, it can be used to predict treatment response [57, 58]. This is explained by the fact that hypoxia hampers the effect of radiochemotherapy. Furthermore, DWI helps to distinguish fibrosis from recurrence [56].

7.3.2 N Staging

Nodal staging remains a challenge for any imaging modality – in both colon and rectal cancer. Looking at the surgical strategy, however, preoperative assessment of nodal involvement seems more critical and relevant in rectal cancer. Prior to mesorectal excision, detection of lymphadenopathy is essential. For partial colectomy, lymph node dissection is encompassed in the resection of the mesenteric pathways.

Local N staging of rectal cancer is currently done with MRI in clinical settings. T2-weighted sequences are cornerstone both for T staging and for the assessment of local lymph node involvement before as well as after initiation of therapy [60–62]. For N staging, agreement between MRI results and histological standard of reference are high at around 85 % [63]. The size of the node remains one main criterion with those nodes greater than 1 cm considered as malignant. DWI can add information in calculating the ADC value ratio between lymph node and tumor [64]. In all instances the signal intensity and signal pattern of the lymph node is an essential feature to assess metastatic involvement. While MRI for N staging (also outside the local tumor environment) can be improved with application of iron containing nanoparticles [61, 62], this contrast agent is not universally available.

PET delivers molecular information and is an important adjunct to morphologic imaging in the case of positive uptake. However, its inherent limitation of spatial resolution reduces its value in smaller-sized nodes. One recently published paper showed superior N staging when combining the reading of PET/CT and MRI leading to high lymph node metastases detection rate [65]. These data justify the hope for an improved N staging in rectal cancer with PET/MR. Despite the mentioned limitations, nodal staging is most likely to benefit from the arrival of PET/MR as a combined imaging modality.

7.3.3 M Staging

The preeminent advantages of PET/CT for colorectal cancer staging arise from its capability of whole-body imaging with detection of metastatic spread. While performance is very sound in solid organs and soft tissue, PET has limitations in the liver, brain, and bone. In the liver, the PET component is limited for M staging due to the physiological uptake of the liver parenchyma, the low spatial resolution, and the lack of clear anatomic landmarks [66]. Lesions measuring less than 1.3 cm might be overseen due to volume averaging effects [67]. High liver background activity may lead to masking of small hepatic metastases. Additionally, it is challenging to detect micrometastases with PET/CT, in particular when unselective tracers such as FDG are used [68]. In these cases the MR component can be of specific value.

MRI has shown to be more accurate in the detection of small liver metastases than both CT and PET/CT [69, 70]. Colon cancer diagnostic reliability of metastases can be increased when adding MRI which has shown to be better than CT for this indication [71, 72]. In a meta-analysis of 39 articles with over 3,000 patients, MRI had a sensitivity of 80.3 % on a per-lesion basis and a sensitivity of 88.2 % on a per-patient basis. For lesions less than 10 mm in size, the sensitivity in MRI was higher in comparison to CT [73].

MRI is also particularly useful for the detection of brain metastases [74]. MRI with the use of contrast agents can depict small metastases in the brain and proved to have a higher sensitivity for this indication in comparison to PET/CT or CT alone [75]. Due to the nonspecific uptake of FDG in the brain, PET is not suitable to assess simultaneous metastases to the brain.

Other areas which presumably benefit from both MRI and PET in a whole-body setting are bone metastases. One study showed a sensitivity of 94 %, a specificity of 76 %, and a diagnostic accuracy of 91 % when applying whole-body MRI for bone metastases detection. Smaller malignant bone lesions were depicted with whole-body MRI in comparison to PET/CT [76].

PET/MR may improve the detection of metastases to the liver, brain, and bone. In combining the outstanding sensitivity of MRI in the detection of even small liver lesions and the more specific metabolic information of PET, this will likely result in a significant benefit of PET/MRI for M staging of CRC.

7.3.4 Surveillance

Beyond the initial staging of the primary cancer, there are multiple scenarios regarding the follow-up of diagnosed colorectal cancer including the setting of neoadjuvant therapy and treatment response, postoperative treatment monitoring, and long-term surveillance.

Neoadjuvant radiochemotherapy is established in the clinical workflow of rectal cancer patients for downstaging of advanced-stage tumors [77]. In this treatment setting, DWI combined with morphologic MRI helps to predict clearance of the mesorectal fascia from the neoplasm, important information required by the clinician [78]. The metabolic imaging of PET together with the MR component proved to be useful in rectal cancer for differentiations of recurrent tumor vs. scar tissue [79].

Another important role of imaging in the workup of CRC is the *monitoring* of treatment. Both MRI and PET/CT have proven value to accurately assess response to therapy for appropriate therapeutic decisions. DWI was proven to aid in assessment response to radiochemotherapy [55, 56, 58]. Degree of SUV decrease in FDG-PET prior to and after radiochemotherapy in advanced rectal cancer revealed to be a prognostic outcome parameter: patients with higher degree of SUV decrease demonstrated a favorable outcome in this study [80].

The *surveillance* of colon cancer is important to detect tumor recurrence or progress. Historically, chemotherapy was the therapy of choice for recurrent cancer. With the introduction of minimally invasive therapy options like radiofrequency ablation, innovative adjuvant radiochemotherapy regimens, and surgical metastatic resection, the clinician is able to treat recurrence and progress of colon cancer successfully if it is detected at an early stage [73, 81]. The role of CEA as a screening method for recurrent CRC is debated. Elevated CEA levels do not provide information about the location of recurrent or progressive disease; thus, imaging is needed, and currently CT of the chest, abdomen, and pelvis is standard. If a rising CEA tumor marker in patient with a history of colorectal cancer leads to a negative diagnostic workup, PET is recommended to reveal the recurrence site [82, 83].

In the presence of posttreatment changes, the diagnosis of rectal cancer recurrence can be challenging. CT with its poor soft tissue resolution is extremely limited in providing accurate information. Morphologic MRI with higher soft tissue resolution is superior to CT in these cases. Nonetheless, after treatment in the pelvis, it can be difficult to distinguish tumor recurrence or residual from treatment-induced fibrotic or desmoplastic or necrotic and inflammatory changes with MRI alone [84]. DWI MRI is an important adjunct in these conditions to detect and stage rectal cancer appropriately [85] and has shown to improve assessment [56]. Recently published data demonstrated better detection of posttreatment tumor recurrence and residual as well as superior identification of positive lymph nodes in this patient population when adding DWI datasets [55, 56, 86, 87]. Another study could show DWI as a surrogate marker for the biological behavior of rectal cancer [54]. The combination with information from PET is even more promising.

In PET/MR both local and distant recurrence can be investigated in one single examination. Combining the functional metabolic information from PET with the multiparametric and morphologic information from MRI, PET/MR might be superior for follow-up after treatment enabling improved diagnosis of recurrent or residual tumor vs. therapy-induced changes. The incremental value of this approach, however, remains to be determined.

7.4 Initial Results and Future Perspectives of PET/MR in CRC

Some clear advantages and benefits are obvious and can be expected from PET/MR; others remain to be proven and may crystallize over time as evidence is increasing.

First, benefit can be seen in the potential for dose reduction with PET/MR avoiding the radiation dose for CT.

Second, PET/MR may offer, specifically in rectal cancer, a comprehensive diagnostic approach for T, N, and M staging and head toward a "one-stop-shop" modality with improved workflow and patient management.

Third and most importantly, there is great hope, that combining functional information of PET with functional multiparametric capacities of MRI will enhance diagnostic accuracy and provide predictive factors to guide therapy.

For all these fields, current literature is sparse. Current approaches to analyze the value of PET/MRI are limited to comparing PET/CT and PET/MR in the detection, localization, and characterization of FDG-positive lesions and the accuracy of MR-based attenuation correction.

In a recent paper, the value of software fusion between PET/CT and PET/MR (PET data fused to MRI) was analyzed for metastatic lesions. This approach is prospecting the potential gain from simultaneous or sequential imaging in one device. The data yielded sensitivities of 84.2 and 98.3 % for PET/CT and PET/MRI, respectively, and stated that PET/MR efficiently detected more metastatic lesions than PET/CT ($p < 0.05$) among those with diameter <1 cm.

Initial studies are available from true simultaneously acquired data in PET/MR looking at the value of PET/MR in oncologic indications. Oncologic imaging with PET/MRI so far yielded promising in studies including patients with a variety of tumors [17]. Detection of FDG-avid lesions suspicious for neoplastic involvement seems comparable between PET/MR and PET/CT in the majority of these studies reporting on the initial experience with the new hybrid modality [18, 88].

For example, in the series of Drzezga et al. [18], a total of 32 patients were included in the study, four of which presented colorectal cancer. These patients had seven lesions in the liver and three in lymph nodes. Overall conclusion in this study was that the reliability of PET/MR was comparable to that of PET/CT in allowing the detection of hypermetabolic lesions suspicious for malignancy in patients with oncologic disease.

Quick et al. [88] report on 80 patients who underwent a double-scanning protocol with PET/MR and PET/CT looking qualitatively at the correlation of 195 tracer-avid lesions between the two modalities and rating image quality. The authors conclude that integrated PET/MR hybrid imaging is feasible in a clinical setting with similar detection rates as those of PET/CT. Attenuation correction can be performed sufficiently with Dixon sequences, although bone is disregarded.

In none of these studies, colorectal cancer is specifically addressed separately as disease entity.

Our own experience with PET/MR in oncologic patients is based on 120 patients with various primary neoplasms who underwent double-scanning protocol with PET/MR in a sequential design and PET/CT following a single-tracer injection of FDG. This oncologic patient population included 13 patients with colorectal cancer at various stages of disease. From this limited experience we can summarize at least three distinct advantages of PET/MR that might prove value over current standard imaging approach in colorectal cancer:

1. Increase the confidence in the characterization of focal liver lesions. Limitations of PET in confidently identifying small lesions are compensated for with MRI. On the other hand, even faint uptake in a small lesion which would be considered nonspecific in PET/CT imaging alone can reinforce the diagnostic confidence in a lesion not fully characterized by MRI.
2. Improvement to identify lymph nodes suspicious for metastatic involvement.
3. Increase the diagnostic confidence in identifying residual tumor after treatment. Synergistic behavior of ADC and PET may be a powerful tool to describe treatment response with even higher confidence than either modality alone.

The future topics to be addressed with PET/MR on the horizon of CRC imaging are manifold.

No experience is so far reported on combining the molecular information from multiparametric MRI and PET in colorectal cancer. Initial tests suggest there is sufficient quality of alignment of data in the abdomen approach for comprehensive image analysis from both device components. More specifically, to assess the

potentially synergistic information from PET and DWI in the assessment of treatment response in colorectal cancer will be an intriguing topic.

More data is warranted to prove the potential benefits and questionable superiority of simultaneous image acquisition in an integrated over sequential acquisition. To date, no clear advantage has been demonstrated, in the specific indication of colorectal cancer imaging staging.

There needs to be more effort in exploring the potential of currently existing multiparametric imaging capacities of MRI for CRC imaging. For instance, PET-based perfusion measurements or hypoxia tracer might be correlated with BOLD imaging. PET tracer uptake might be compared with DWI as shown in earlier preliminary tests [89, 90]. Parameters determined from dynamic contrast-enhanced DCE-MRI [91–93] may be correlated with PET information.

With upcoming, new, and innovative treatment strategies for CRC, imaging is challenged to provide adequate reflection of the effectiveness of these agents. Angiogenic inhibitor treatment has started to play a role in CRC. How to illustrate, quantify, and interpret the effect of these treatments beyond the purely morphologic description will be one of the major tasks in the future. New radiotracers for PET are already nowadays available to show the effect of anti-angiogenetic drugs. How their results can be further complemented with MRI remains to be determined. For this purpose, PET/MR seems the ideal and most integrative imaging modality. Since PET/MR involves less radiation burden, more frequent imaging to determine treatment response may be less problematic. The role and value of PET/MR in view of these achievements, however, need to be determined.

Finally, different and new radiotracers may be explored as for their value in PET imaging of colorectal cancer. New predictive factors, biomarkers, parameters, and measures may emerge from their use to enrich the landscape of diagnostic imaging for CRC patients.

References

1. Ferlay J, Parkin DM, Steliarova-Foucher E. Estimates of cancer incidence and mortality in Europe in 2008. Eur J Cancer. 2010;46(4):765–81.
2. Ferlay J, Shin HR, Bray F, Forman D, Mathers C, Parkin DM. Estimates of worldwide burden of cancer in 2008: GLOBOCAN 2008. Int J Cancer. 2010;127(12):2893–917.
3. Kemeny NE, Gonen M. Hepatic arterial infusion after liver resection. N Engl J Med. 2005;352(7):734–5.
4. Figueredo A, Rumble RB, Maroun J, Earle CC, Cummings B, McLeod R, Zuraw L, Zwaal C, Gastrointestinal Cancer Disease Site Group of Cancer Care Ontario's Program in Evidence-based Care. Follow-up of patients with curatively resected colorectal cancer: a practice guideline. BMC Cancer. 2003;3:26.
5. Grassetto G, Marzola MC, Minicozzi A, Al-Nahhas A, Rubello D. F-18 FDG PET/CT in rectal carcinoma: where are we now? Clin Nucl Med. 2011;36(10):884–8.
6. Sanli Y, Kuyumcu S, Ozkan ZG, Kilic L, Balik E, Turkmen C, Has D, Isik G, Asoglu O, Kapran Y, Adalet I. The utility of FDG-PET/CT as an effective tool for detecting recurrent colorectal cancer regardless of serum CEA levels. Ann Nucl Med. 2012;26(7):551–8.
7. Selzner M, Hany TF, Wildbrett P, McCormack L, Kadry Z, Clavien PA. Does the novel PET/CT imaging modality impact on the treatment of patients with metastatic colorectal cancer of the liver? Ann Surg. 2004;240(6):1027–34.
8. Davey K, Heriot AG, Mackay J, Drummond E, Hogg A, Ngan S, Milner AD, Hicks RJ. The impact of 18-fluorodeoxyglucose positron emission tomography-computed tomography on the staging and management of primary rectal cancer. Dis Colon Rectum. 2008;51(7):997–1003.
9. Gearhart SL, Frassica D, Rosen R, Choti M, Schulick R, Wahl R. Improved staging with pretreatment positron emission tomography/computed tomography in low rectal cancer. Ann Surg Oncol. 2006;13(3):397–404.
10. Wiering B, Krabbe PF, Jager GJ, Oyen WJ, Ruers TJ. The impact of fluor-18-deoxyglucose-positron emission tomography in the management of colorectal liver metastases. Cancer. 2005;104(12):2658–70.
11. Schmidt GP, Baur-Melnyk A, Haug A, Utzschneider S, Becker CR, Tiling R, Reiser MF, Hermann KA. Whole-body MRI at 1.5 T and 3 T compared with FDG-PET-CT for the detection of tumour recurrence in patients with colorectal cancer. Eur Radiol. 2009;19(6):1366–78.
12. Ichikawa T, Erturk SM, Motosugi U, Sou H, Iino H, Araki T, Fujii H. High-B-value diffusion-weighted MRI in colorectal cancer. AJR Am J Roentgenol. 2006;187(1):181–4.

13. Morita N, Harada M, Otsuka H, Melhem ER, Nishitani H. Clinical application of MR spectroscopy and imaging of brain tumor. Magn Reson Med Sci. 2010;9(4):167–75.
14. Zhong JH, Gore JC. Studies of restricted diffusion in heterogeneous media containing variations in susceptibility. Magn Reson Med. 1991;19(2):276–84.
15. Heusch P, Buchbender C, Beiderwellen K, Nensa F, Hartung-Knemeyer V, Lauenstein TC, Bockisch A, Forsting M, Antoch G, Heusner TA. Standardized uptake values for [^{18}F] FDG in normal organ tissues: comparison of whole-body PET/CT and PET/MRI. Eur J Radiol. 2013;82(5):870–6.
16. Kalemis A, Delattre BM, Heinzer S. Sequential whole-body PET/MR scanner: concept, clinical use, and optimisation after two years in the clinic. The manufacturer's perspective. MAGMA. 2013;26(1):5–23.
17. Schwenzer NF, Schmidt H, Claussen CD. Whole-body MR/PET: applications in abdominal imaging. Abdom Imaging. 2012;37(1):20–8.
18. Drzezga A, Souvatzoglou M, Eiber M, Beer AJ, Fürst S, Martinez-Möller A, Nekolla SG, Ziegler S, Ganter C, Rummeny EJ, Schwaiger M. First clinical experience with integrated whole-body PET/MR: comparison to PET/CT in patients with oncologic diagnoses. J Nucl Med. 2012;53(6):845–55.
19. Coombs BD, Szumowski J, Coshow W. Two-point Dixon technique for water-fat signal decomposition with B0 inhomogeneity correction. Magn Reson Med. 1997;38(6):884–9.
20. Martinez-Möller A, Souvatzoglou M, Delso G, Bundschuh RA, Chefd'hotel C, Ziegler SI, Navab N, Schwaiger M, Nekolla SG. Tissue classification as a potential approach for attenuation correction in whole-body PET/MRI: evaluation with PET/CT data. J Nucl Med. 2009;50(4):520–6.
21. Stolzmann P, Veit-Haibach P, Chuck N, Rossi C, Frauenfelder T, Alkadhi H, von Schulthess G, Boss A. Detection rate, location, and size of pulmonary nodules in trimodality PET/CT-MR: comparison of low-dose CT and Dixon-based MR imaging. Invest Radiol. 2013;48(5):241–6.
22. Wagenknecht G, Kaiser HJ, Mottaghy FM, Herzog H. MRI for attenuation correction in PET: methods and challenges. MAGMA. 2013;26(1):99–113.
23. Keereman V, Fierens Y, Broux T, De Deene Y, Lonneux M, Vandenberghe S. MRI-based attenuation correction for PET/MRI using ultrashort echo time sequences. J Nucl Med. 2010;51(5):812–18.
24. Keereman V, Holen RV, Mollet P, Vandenberghe S. The effect of errors in segmented attenuation maps on PET quantification. Med Phys. 2011;38(11):6010–19.
25. Berker Y, Franke J, Salomon A, Palmowski M, Donker HC, Temur Y, Mottaghy FM, Kuhl C, Izquierdo-Garcia D, Fayad ZA, Kiessling F, Schulz V. MRI-based attenuation correction for hybrid PET/MRI systems: a 4-class tissue segmentation technique using a combined ultrashort-echo-time/Dixon MRI sequence. J Nucl Med. 2012;53(5):796–804.
26. Kershah S, Partovi S, Traughber BJ, Muzic RF Jr., Schluchter MD, O'Donnell JK, Faulhaber P. Comparison of standardized uptake calues in normal structures between PET/CT and PET/MRI in an oncology patient population. Mol Imaging Biol. 2013;15(6):776–85.
27. Partovi S, Kohan A, Gaeta C, Rubbert C, Vercher-Conejero JL, Jones RS, O'Donnell JK, Wojtylak P, Faulhaber P. Image quality assessment of automatic three-segment MR attenuation correction vs. CT attenuation correction. Am J Nucl Med Mol Imaging. 2013;3(3):291–9.
28. Buchbender C, Heusner TA, Lauenstein TC, Bockisch A, Antoch G. Oncologic PET/MRI, part 1: tumors of the brain, head and neck, chest, abdomen, and pelvis. J Nucl Med. 2012;53(6):928–38.
29. Martinez-Möller A, Eiber M, Nekolla SG, Souvatzoglou M, Drzezga A, Ziegler S, Rummeny EJ, Schwaiger M, Beer AJ. Workflow and scan protocol considerations for integrated whole-body PET/MRI in oncology. J Nucl Med. 2012;53(9):1415–26.
30. Sani F, Foresti M, Parmiggiani A, D'Andrea V, Manenti A, Amorotti C, Scotti R, Gallo E, Torricelli P. 3-T MRI with phased-array surface coil in the local staging of rectal cancer. Radiol Med. 2011;116(3):375–88.
31. Lauenstein TC, Saar B, Martin DR. MR colonography: 1.5T versus 3T. Magn Reson Imaging Clin N Am. 2007;15(3):395–402.
32. Dagia C, Ditchfield M, Kean M, Catto-Smith A. Feasibility of 3-T MRI for the evaluation of Crohn disease in children. Pediatr Radiol. 2010;40(10):1615–24.
33. Boll DT, Merkle EM. Imaging at higher magnetic fields: 3 T versus 1.5 T. Magn Reson Imaging Clin N Am. 2010;18(3):549–64.
34. Hartmann D, Bassler B, Schilling D, Adamek HE, Jakobs R, Pfeifer B, Eickhoff A, Zindel C, Riemann JF, Layer G. Colorectal polyps: detection with dark-lumen MR colonography versus conventional colonoscopy. Radiology. 2006;238(1):143–9.
35. Saar B, Gschossmann JM, Bonel HM, Kickuth R, Vock P, Netzer P. Evaluation of magnetic resonance colonography at 3.0 T regarding diagnostic accuracy and image quality. Invest Radiol. 2008;43(8):580–6.
36. Fütterer JJ, Yakar D, Strijk SP, Barentsz JO. Preoperative 3T MR imaging of rectal cancer: local staging accuracy using a two-dimensional and three-dimensional T2-weighted turbo spin echo sequence. Eur J Radiol. 2008;65(1):66–71.
37. Kim HJ, Park SH, Pickhardt PJ, Yoon SN, Lee SS, Yee J, Kim DH, Kim AY, Kim JC, Yu CS, Ha HK. CT colonography for combined colonic and extracolonic surveillance after curative resection of colorectal cancer. Radiology. 2010;257(3):697–704.
38. Winawer SJ, Zauber AG, Fletcher RH, Stillman JS, O'Brien MJ, Levin B, Smith RA, Lieberman DA, Burt RW, Levin TR, Bond JH, Brooks D, Byers T, Hyman N, Kirk L, Thorson A, Simmang C, Johnson D, Rex DK, US Multi-Society Task Force on Colorectal Cancer; American Cancer Society. Guidelines for colonoscopy surveillance after polypectomy: a con-

sensus update by the US Multi-Society Task Force on Colorectal Cancer and the American Cancer Society. Gastroenterology. 2006;130(6):1872–85.
39. Bond JH. Colon polyps and cancer. Endoscopy. 2003;35(1):27–35.
40. Herrmann KA, Paspulati RM, Lauenstein T, Reiser MF. Benefits and challenges in bowel MR imaging at 3.0 T. Top Magn Reson Imaging. 2010;21(3): 165–75.
41. Ajaj W, Pelster G, Treichel U, Vogt FM, Debatin JF, Ruehm SG, Lauenstein TC. Dark lumen magnetic resonance colonography: comparison with conventional colonoscopy for the detection of colorectal pathology. Gut. 2003;52(12):1738–43.
42. Wessling J, Fischbach R, Borchert A, Kugel H, Allkemper T, Osada N, Heindel W. Detection of colorectal polyps: comparison of multi-detector row CT and MR colonography in a colon phantom. Radiology. 2006;241(1):125–31.
43. Graser A, Melzer A, Lindner E, Nagel D, Herrmann K, Stieber P, Schirra J, Mansmann U, Reiser MF, Göke B, Kolligs FT. Magnetic resonance colonography for the detection of colorectal neoplasia in asymptomatic adults. Gastroenterology. 2013;144(4):743–50.
44. Yasuda S, Fujii H, Nakahara T, Nishiumi N, Takahashi W, Ide M, Shohtsu A. 18F-FDG PET detection of colonic adenomas. J Nucl Med. 2001;42(7):989–92.
45. van Kouwen MC, Nagengast FM, Jansen JB, Oyen WJ, Drenth JP. 2-(18F)-fluoro-2-deoxy-D-glucose positron emission tomography detects clinical relevant adenomas of the colon: a prospective study. J Clin Oncol. 2005;23(16):3713–17.
46. Berger KL, Nicholson SA, Dehdashti F, Siegel BA. FDG PET evaluation of mucinous neoplasms: correlation of FDG uptake with histopathologic features. AJR Am J Roentgenol. 2000;174(4):1005–8.
47. Vikram R, Iyer RB. PET/CT imaging in the diagnosis, staging, and follow-up of colorectal cancer. Cancer Imaging. 2008;8(Spec No A):S46–51.
48. Eiber M, Martinez-Möller A, Souvatzoglou M, Holzapfel K, Pickhard A, Löffelbein D, Santi I, Rummeny EJ, Ziegler S, Schwaiger M, Nekolla SG, Beer AJ. Value of a Dixon-based MR/PET attenuation correction sequence for the localization and evaluation of PET-positive lesions. Eur J Nucl Med Mol Imaging. 2011;38(9):1691–701.
49. Lambregts DM, Beets GL, Maas M, Curvo-Semedo L, Kessels AG, Thywissen T, Beets-Tan RG. Tumour ADC measurements in rectal cancer: effect of ROI methods on ADC values and interobserver variability. Eur Radiol. 2011;21(12):2567–74.
50. Beets-Tan RG, Beets GL, Vliegen RF, Kessels AG, Van Boven H, De Bruine A, von Meyenfeldt MF, Baeten CG, van Engelshoven JM. Accuracy of magnetic resonance imaging in prediction of tumour-free resection margin in rectal cancer surgery. Lancet. 2001;357(9255):497–504.
51. Bipat S, Glas AS, Slors FJ, Zwinderman AH, Bossuyt PM, Stoker J. Rectal cancer: local staging and assessment of lymph node involvement with endoluminal US, CT, and MR imaging–a meta-analysis. Radiology. 2004;232(3):773–83.
52. Rao SX, Zeng MS, Chen CZ, Li RC, Zhang SJ, Xu JM, Hou YY. The value of diffusion-weighted imaging in combination with T2-weighted imaging for rectal cancer detection. Eur J Radiol. 2008;65(2):299–303.
53. Muhi A, Ichikawa T, Motosugi U, Sou H, Sano K, Araki T. Diffusion- and T_2-weighted MR imaging of the liver: effect of intravenous administration of gadoxetic acid disodium. Magn Reson Med Sci. 2012;11(3):185–91.
54. Curvo-Semedo L, Lambregts DM, Maas M, Beets GL, Caseiro-Alves F, Beets-Tan RG. Diffusion-weighted MRI in rectal cancer: apparent diffusion coefficient as a potential noninvasive marker of tumor aggressiveness. J Magn Reson Imaging. 2012;35(6):1365–71.
55. Lambregts DM, Vandecaveye V, Barbaro B, Bakers FC, Lambrecht M, Maas M, Haustermans K, Valentini V, Beets GL, Beets-Tan RG. Diffusion-weighted MRI for selection of complete responders after chemoradiation for locally advanced rectal cancer: a multicenter study. Ann Surg Oncol. 2011;18(8):2224–31.
56. Lambregts DM, Cappendijk VC, Maas M, Beets GL, Beets-Tan RG. Value of MRI and diffusion-weighted MRI for the diagnosis of locally recurrent rectal cancer. Eur Radiol. 2011;21(6):1250–8.
57. Dzik-Jurasz A, Domenig C, George M, Wolber J, Padhani A, Brown G, Doran S. Diffusion MRI for prediction of response of rectal cancer to chemoradiation. Lancet. 2002;360(9329):307–8.
58. Sun YS, Zhang XP, Tang L, Ji JF, Gu J, Cai Y, Zhang XY. Locally advanced rectal carcinoma treated with preoperative chemotherapy and radiation therapy: preliminary analysis of diffusion-weighted MR imaging for early detection of tumor histopathologic downstaging. Radiology. 2010;254(1):170–8.
59. Curvo-Semedo L, Lambregts DM, Maas M, Thywissen T, Mehsen RT, Lammering G, Beets GL, Caseiro-Alves F, Beets-Tan RG. Rectal cancer: assessment of complete response to preoperative combined radiation therapy with chemotherapy–conventional MR volumetry versus diffusion-weighted MR imaging. Radiology. 2011;260(3):734–43.
60. Koh DM, Chau I, Tait D, Wotherspoon A, Cunningham D, Brown G. Evaluating mesorectal lymph nodes in rectal cancer before and after neoadjuvant chemoradiation using thin-section T2-weighted magnetic resonance imaging. Int J Radiat Oncol Biol Phys. 2008;71(2):456–61.
61. Koh DM, George C, Temple L, Collins DJ, Toomey P, Raja A, Bett N, Farhat S, Husband JE, Brown G. Diagnostic accuracy of nodal enhancement pattern of rectal cancer at MRI enhanced with ultrasmall superparamagnetic iron oxide: findings in pathologically matched mesorectal lymph nodes. AJR Am J Roentgenol. 2010;194(6):W505–13.
62. Lahaye MJ, Engelen SM, Kessels AG, de Bruïne AP, von Meyenfeldt MF, van Engelshoven JM, van de Velde CJ, Beets GL, Beets-Tan RG. USPIO-enhanced MR imaging for nodal staging in patients with

primary rectal cancer: predictive criteria. Radiology. 2008;246(3):804–11.
63. Brown G, Radcliffe AG, Newcombe RG, Dallimore NS, Bourne MW, Williams GT. Preoperative assessment of prognostic factors in rectal cancer using high-resolution magnetic resonance imaging. Br J Surg. 2003;90(3):355–64.
64. Yasui O, Sato M, Kamada A. Diffusion-weighted imaging in the detection of lymph node metastasis in colorectal cancer. Tohoku J Exp Med. 2009; 218(3):177–83.
65. Kim DJ, Kim JH, Ryu YH, Jeon TJ, Yu JS, Chung J. Nodal staging of rectal cancer: high-resolution pelvic MRI versus ^{18}F-FDGPET/CT. J Comput Assist Tomogr. 2011;35(5):531–4.
66. Osman MM, Cohade C, Nakamoto Y, Marshall LT, Leal JP, Wahl RL. Clinically significant inaccurate localization of lesions with PET/CT: frequency in 300 patients. J Nucl Med. 2003;44(2):240–3.
67. Mawlawi O, Podoloff DA, Kohlmyer S, Williams JJ, Stearns CW, Culp RF, Macapinlac H, National Electrical Manufacturers Association. Performance characteristics of a newly developed PET/CT scanner using NEMA standards in 2D and 3D modes. J Nucl Med. 2004;45(10):1734–42.
68. Stoeckli SJ, Steinert H, Pfaltz M, Schmid S. Is there a role for positron emission tomography with ^{18}F-fluorodeoxyglucose in the initial staging of nodal negative oral and oropharyngeal squamous cell carcinoma. Head Neck. 2002;24(4):345–9.
69. Kong G, Jackson C, Koh DM, Lewington V, Sharma B, Brown G, Cunningham D, Cook GJ. The use of 18F-FDG PET/CT in colorectal liver metastases–comparison with CT and liver MRI. Eur J Nucl Med Mol Imaging. 2008;35(7):1323–9.
70. Sahani DV, Kalva SP, Fischman AJ, Kadavigere R, Blake M, Hahn PF, Saini S. Detection of liver metastases from adenocarcinoma of the colon and pancreas: comparison of mangafodipir trisodium-enhanced liver MRI and whole-body FDG PET. AJR Am J Roentgenol. 2005;185(1):239–46.
71. Regge D, Campanella D, Anselmetti GC, Cirillo S, Gallo TM, Muratore A, Capussotti L, Galatola G, Floriani I, Aglietta M. Diagnostic accuracy of portal-phase CT and MRI with mangafodipir trisodium in detecting liver metastases from colorectal carcinoma. Clin Radiol. 2006;61(4):338–47.
72. Bartolozzi C, Donati F, Cioni D, Procacci C, Morana G, Chiesa A, Grazioli L, Cittadini G, Cittadini G, Giovagnoni A, Gandini G, Maass J, Lencioni R. Detection of colorectal liver metastases: a prospective multicenter trial comparing unenhanced MRI, MnDPDP-enhanced MRI, and spiral CT. Eur Radiol. 2004;14(1):14–20.
73. Niekel MC, Bipat S, Stoker J. Diagnostic imaging of colorectal liver metastases with CT, MR imaging, FDG PET, and/or FDG PET/CT: a meta-analysis of prospective studies including patients who have not previously undergone treatment. Radiology. 2010;257(3):674–84.
74. Antoch G, Bockisch A. Combined PET/MRI: a new dimension in whole-body oncology imaging? Eur J Nucl Med Mol Imaging. 2009;36 Suppl 1:S113–20.
75. Eustace SJ, Walker R, Blake M, Yucel EK. Whole-body MR imaging. Practical issues, clinical applications, and future directions. Magn Reson Imaging Clin N Am. 1999;7(2):209–36.
76. Schmidt GP, Schoenberg SO, Schmid R, Stahl R, Tiling R, Becker CR, Reiser MF, Baur-Melnyk A. Screening for bone metastases: whole-body MRI using a 32-channel system versus dual-modality PET-CT. Eur Radiol. 2007;17(4):939–49.
77. Sauer R, Becker H, Hohenberger W, Rödel C, Wittekind C, Fietkau R, Martus P, Tschmelitsch J, Hager E, Hess CF, Karstens JH, Liersch T, Schmidberger H, Raab R, German Rectal Cancer Study Group. Preoperative versus postoperative chemoradiotherapy for rectal cancer. N Engl J Med. 2004;351(17):1731–40.
78. Park MJ, Kim SH, Lee SJ, Jang KM, Rhim H. Locally advanced rectal cancer: added value of diffusion-weighted MR imaging for predicting tumor clearance of the mesorectal fascia after neoadjuvant chemotherapy and radiation therapy. Radiology. 2011; 260(3):771–80.
79. Ito K, Kato T, Tadokoro M, Ishiguchi T, Oshima M, Ishigaki T, Sakuma S. Recurrent rectal cancer and scar: differentiation with PET and MR imaging. Radiology. 1992;182(2):549–52.
80. Guillem JG, Moore HG, Akhurst T, Klimstra DS, Ruo L, Mazumdar M, Minsky BD, Saltz L, Wong WD, Larson S. Sequential preoperative fluorodeoxyglucose-positron emission tomography assessment of response to preoperative chemoradiation: a means for determining longterm outcomes of rectal cancer. J Am Coll Surg. 2004;199(1):1–7.
81. Smith MD, McCall JL. Systematic review of tumour number and outcome after radical treatment of colorectal liver metastases. Br J Surg. 2009;96(10):1101–13.
82. Flanagan FL, Dehdashti F, Ogunbiyi OA, Kodner IJ, Siegel BA. Utility of FDG-PET for investigating unexplained plasma CEA elevation in patients with colorectal cancer. Ann Surg. 1998;227(3):319–23.
83. Flamen P, Hoekstra OS, Homans F, Van Cutsem E, Maes A, Stroobants S, Peeters M, Penninckx F, Filez L, Bleichrodt RP, Mortelmans L. Unexplained rising carcinoembryonic antigen (CEA) in the postoperative surveillance of colorectal cancer: the utility of positron emission tomography (PET). Eur J Cancer. 2001;37(7):862–9.
84. Vliegen RF, Beets GL, Lammering G, Dresen RC, Rutten HJ, Kessels AG, Oei TK, de Bruïne AP, van Engelshoven JM, Beets-Tan RG. Mesorectal fascia invasion after neoadjuvant chemotherapy and radiation therapy for locally advanced rectal cancer: accuracy of MR imaging for prediction. Radiology. 2008;246(2):454–62.
85. Hosonuma T, Tozaki M, Ichiba N, Sakuma T, Hayashi D, Yanaga K, Fukuda K. Clinical usefulness of diffusion-weighted imaging using low and high

b-values to detect rectal cancer. Magn Reson Med Sci. 2006;5(4):173–7.
86. Song I, Kim SH, Lee SJ, Choi JY, Kim MJ, Rhim H. Value of diffusion-weighted imaging in the detection of viable tumour after neoadjuvant chemoradiation therapy in patients with locally advanced rectal cancer: comparison with T2 weighted and PET/CT imaging. Br J Radiol. 2012;85(1013):577–86.
87. Kim SH, Lee JM, Hong SH, Kim GH, Lee JY, Han JK, Choi BI. Locally advanced rectal cancer: added value of diffusion-weighted MR imaging in the evaluation of tumor response to neoadjuvant chemo- and radiation therapy. Radiology. 2009;253(1):116–25.
88. Quick HH, von Gall C, Zeilinger M, Wiesmüller M, Braun H, Ziegler S, Kuwert T, Uder M, Dörfler A, Kalender WA, Lell M. Integrated whole-body PET/MR hybrid imaging: clinical experience. Invest Radiol. 2013;48(5):280–9.
89. Makino K, Hirai T, Nakamura H, Murakami R, Kitajima M, Shigematsu Y, Nakashima R, Shiraishi S, Uetani H, Iwashita K, Akter M, Yamashita Y, Kuratsu J. Does adding FDG-PET to MRI improve the differentiation between primary cerebral lymphoma and glioblastoma? Observer performance study. Ann Nucl Med. 2011;25(6):432–8.
90. Ewelt C, Floeth FW, Felsberg J, Steiger HJ, Sabel M, Langen KJ, Stoffels G, Stummer W. Finding the anaplastic focus in diffuse gliomas: the value of Gd-DTPA enhanced MRI, FET-PET, and intraoperative, ALA-derived tissue fluorescence. Clin Neurol Neurosurg. 2011;113(7):541–7.
91. Alonzi R, Padhani AR, Allen C. Dynamic contrast enhanced MRI in prostate cancer. Eur J Radiol. 2007;63(3):335–50.
92. Chen K, Cai W, Li ZB, Wang H, Chen X. Quantitative PET imaging of VEGF receptor expression. Mol Imaging Biol. 2009;11(1):15–22.
93. Gore JC, Manning HC, Quarles CC, Waddell KW, Yankeelov TE. Magnetic resonance in the era of molecular imaging of cancer. Magn Reson Imaging. 2011;29(5):587–600.

PET/MR in Brain Imaging

8

Wolf-Dieter Heiss and Alexander Drzezga

Contents

Abstract

The new hybrid PET/MR systems permit optimal spatial and temporal coregistration of structural, functional, and molecular data. The real-time high-resolution multiparametric imaging improves the clinical evaluation of disorders of the brain and offers new options for research in the central nervous system. This review discusses the advantages of integrated PET/MR for brain imaging and indicates possible applications in dementia, degenerative disorders, epilepsy, brain tumors, cerebrovascular disease, and inflammatory diseases. The integrated assessment of various parameters additionally will improve partial volume correction of metabolic and functional values and facilitate the modeling of dynamic data. PET/MR may also help to understand complex metabolic processes and permit insight into functional and structural connectivity in the brain. The multiple noninvasive investigative approaches offered simultaneously by PET/MR might gain a special impact in translational brain research.

8.1 Introduction

Multimodality imaging, especially the combination of PET and CT, has become an important diagnostic tool [3], but its application to the brain has been limited by the low soft tissue sensitivity of CT. The high resolution and excellent soft tissue contrast of MRI and the multifunctional

W.-D. Heiss (✉)
Max Planck Institute for Neurological Research,
Gleueler Str. 50, 50931 Köln, Germany
e-mail: wdh@nf.mpg.de

A. Drzezga
Department of Nuclear Medicine,
University Hospital of Cologne, Kerpener Str. 62,
50937 Cologne, Germany

I. Carrio, P. Ros (eds.), *PET/MRI*,
DOI 10.1007/978-3-642-40692-8_8,

options it offers, such as assessment of diffusion, permeability, and changes in blood oxygenation levels after neuronal activation, identification of intracranial vessels and differentiation of tissue after injection of contrast agents, and determination of endogenous molecules by MRS as well as identification of metabolites using chemical shift analysis, render this technology the ideal imaging modality for the brain. PET can complement the information obtained from MRI procedures by visualizing molecular tracers with picomolar sensitivity and providing quantitative measurements of blood flow, cell metabolism, proliferation, receptor status, synaptic transmission, transporter activity, gene expression, and molecular abnormalities such as pathological protein aggregates (e.g., ß-amyloid plaques). Multimodality imaging therefore is a promising field, although examinations are usually performed on separate machines making them time-consuming and logistically demanding for patients and staff: patient repositioning causes inaccurate anatomical matching and side-by-side interpretation of images results in inaccuracies. Additionally, software fusion of images is affected by differences in image properties, such as spatial resolution, shifting, tilting, rotation, distortion, partial volume effects, and organ deformation. Even the combination of PET and CT which was realized successfully to avoid many of these limitations has a major drawback as imaging is performed sequentially rather than simultaneously. A similar approach by installing a high-resolution PET system adjacent to high-field MRI which allows the utilization of high-sensitivity molecular/biochemical and high-resolution anatomical imaging for brain research [11] (Philips whole-body MRI PET) suffers from the problems inherent in studies performed at different time points and under different circumstances. Simultaneous and isochronous PET and MR data acquisition can only be achieved by a fully integrated PET/MR system.

The development of integrated PET/MR scanners has been aggravated by the fact that conventional PET photomultiplier technology does not work in the strong magnetic field of the MR scanner. Only the development of the so-called avalanche photodiodes (APDs), which are insensitive to magnetic fields, opened the opportunity to build PET scanners able to operate in a strong magnetic field.

The feasibility of simultaneous PET and MR data acquisition was demonstrated by Schmand et al. [40], and MR and PET images of the brain were acquired for the first time simultaneously in a prototype with a PET insert into a MR tomograph [39]. The high impact of integrated PET/MR scanners for experimental research was demonstrated by several groups applying locally developed equipment in small animals [9, 10, 54] (Pichler, see Chap. 2).

Since end of 2010, fully integrated PET/MR instrumentation is available for human whole-body imaging (Siemens Biograph mMR) [13].

Recent studies were able to demonstrate that the application of this technology is clinically feasible with comparable quality of the PET data as in conventional state-of-the-art PET scanners [16]. This novel technique may represent the method of choice for brain imaging for a number of reasons, which we will try to address in this chapter. Some of the potential applications and preliminary results with PET/MR in brain imaging are presented in this review.

8.2 Advantages of Integrated PET/MR in Clinical Application

The integrated imaging modality permits the simultaneous acquisition of a combination of various biological parameters (Table 8.1). With the exception of blood flow or blood volume, which can be assessed rapidly, usually the quantitative determination of metabolic, molecular, or functional measures by PET can require considerable time, during which several MR procedures can be performed.

For example, according to the official guidelines, minimum acquisition times of 10–15 min for a [18F]FDG brain scan and of 20 min for a [18]FET brain scan are recommended [50, 51].

Correspondingly, it has already been demonstrated that a complete set of MR data can be

Table 8.1 Assessment of biological properties by MRI and PET

MRI	PET
Anatomy and pathology	Flow (H215O)
Water motion in tissue (DWI)	Metabolism (FDG)
Perfusion	Blood volume (C15O)
Vascular structure	Oxygen consumption (15O)
Cerebral blood flow	Protein synthesis (labeled AA)
Fiber tracts	Vascular permeability (labeled AA)
Functional activation (fMRI)	Nucleic acid synthesis (FLT)
Metabolites in tissue (MRS)	Transmitters (e.g. DOPA)
Oxygen consumption (17O)	Receptors (e.g. raclopride)
Migration of cells (Fe labeling)	Enzymatic activity (e.g. MP4A) Angiogenesis (e.g. 18F-RGB) Distribution and kinetics of tracers and drugs (labeled compounds) Pathological protein aggregations (e.g. β-amyloid) Enzymatic activity in transfected cells

accumulated during one measurement of glucose metabolism by FDG-PET in the first volunteer investigated with the prototype insert brain PET/MR [39] (Fig. 8.1). It is thereby possible to quantify various functional parameters by PET in the picomolar range (see Table 8.1) and correctly correlate these measures to normal and pathologically altered anatomy and additionally complement this with dynamic and spectroscopic information from MR. Special benefits can be expected from the following applications:

8.2.1 Practical/Work Flow Advantages

With regard to clinical application, there are a number of obvious practical advantages of integrated PET/MR technology, as compared to separate diagnostic modalities. Often PET and MR examinations are required in the same patient anyway, sometimes even repetitively (e.g., in follow-up of brain tumor patients). The option to perform two examinations at the same time in the same scanner represents a major increase in patient comfort. This so-called one stop shop decreases the number of examinations, i.e., the number of visits of the patient to the imaging departments, and it also reduces the overall imaging time. These facts also represent an advantage for clinicians/medical personnel by reducing the required time of presence at the scanners. It may even contribute to shorter hospitalization of patients and thus potentially lead to improved cost efficiency.

8.2.2 Apparent Clinical Advantages

PET represents a highly sensitive imaging procedure but it provides limited anatomical information. Thus, the high-resolution MR data can be used for MR-guided interpretation and evaluation of PET data, given that the two modalities are exactly coregistered. Regions of interest can be clearly defined, partial volume effects can be avoided, and artifacts due to motion or distortion can be corrected. This is particularly important for the identification of small regions of interest; e.g., it is essential for assessing the metabolism, transmitter concentration, or enzyme expression in small nuclei at the base of the brain (e.g., thalamic nuclei [12] or nucleus basalis of Meynert [22]) or in the brain stem. So far this has only been possible by coregistration of images from different investigations (Fig. 8.2).

Potential added value may exist for specific clinical indications.

8.2.2.1 Dementia/Neurodegeneration

In the workup of patients with cognitive impairment or suspected dementia, non-neurodegenerative and potentially treatable causes for the symptomatic appearance have to be excluded, i.e., brain tumors and vascular or inflammatory abnormalities. Thus, usually patients undergo morphological imaging procedures such as CT or MRI anyway. Whereas MR is valuable to exclude the mentioned abnormalities, it is not well suited to provide a positive proof of a specific neurodegenerative disorder.

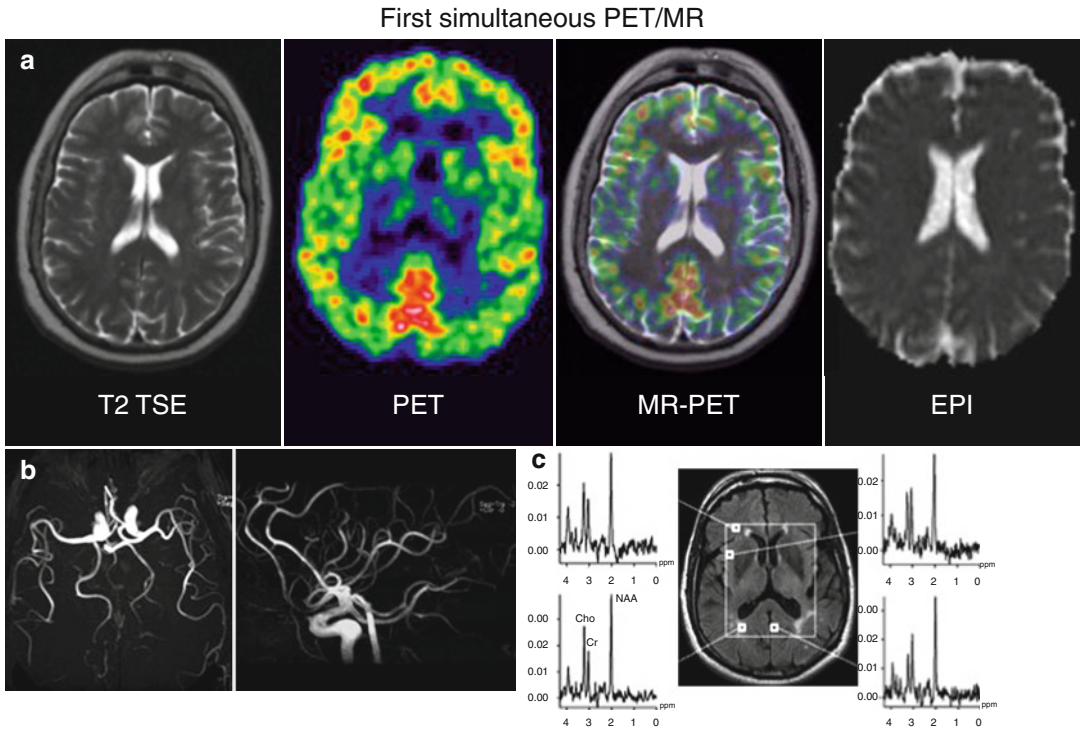

Fig. 8.1 Complete set of acquired MR and PET data of a 66-year-old man after injection of 370 MBq of FDG. (**a**) T2-TSE, tracer distribution in PET recorded for 20 min at steady-state, superimproved combined PET/MR and EPI; (**b**) time-of-flight MR angiography; (**c**) proton MR spectroscopy showing increased choline relative to creatine in white matter areas (*left spectra*) compared to normal gray matter (*right spectra*) (Modified from Schlemmer et al. [39])

Characteristic patterns of atrophy visible on the MR scans have been described for different types of neurodegenerative disorders, but their actual sensitivity and specificity in clinical routine is not utterly high. A potential reason for this can be found in the assumption that structural/atrophic changes in the brain represent a downstream phenomenon in the process of neurodegeneration [24].

On the other hand, PET procedures have been demonstrated to allow reliable diagnosis and differential diagnosis of dementing disorders as well as prediction in pre-dementia stages. This includes specific patterns of regional glucose metabolism indicating neuronal dysfunction and recently also the detection of ß-amyloid plaques, a neuropathological hallmark of Alzheimer's disease [15, 34] (Fig. 8.3).

Thus, it seems obvious that it may be very beneficial to systematically combine MR for exclusion of non-neurodegenerative causes of cognitive impairment with PET methods allowing a sensitive and specific diagnosis of the type of neurodegeneration, respectively the underlying neuropathology.

8.2.2.2 Epilepsy

In epilepsy, high-resolution MRI brain scans are required for focus localization, particularly ahead of epilepsy surgery. However, sometimes even on high-resolution MRI, no clearly defined lesion can be found, or several structural abnormalities are present, which hampers the identification of the actual epiloptogenic focus.

It is known that regional hypometabolic lesions detected in FDG-PET are highly probable to represent epileptogenic foci, even in MRI-negative cases, or to select the responsible focus out of several structural abnormalities present on the MRI findings [32] (Fig. 8.4).

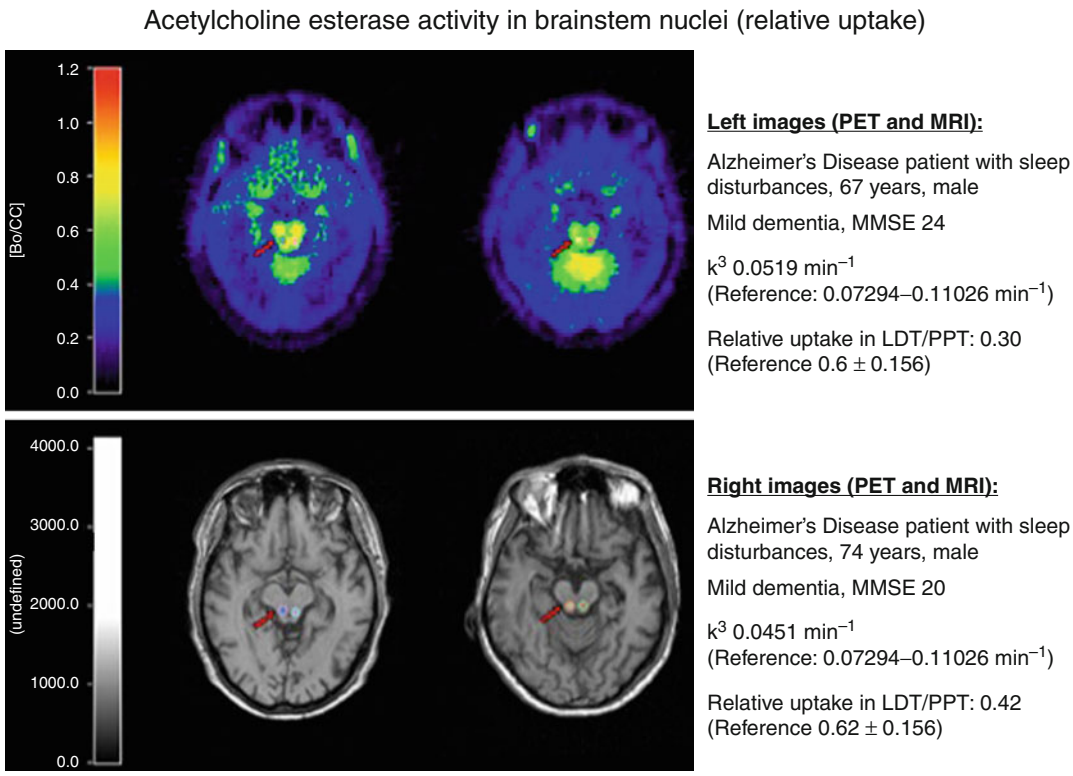

Fig. 8.2 11C-*N*-methyl-4-piperidyl-acetate (*MP4A*)-positron emission tomography (*PET*) and coregistered T1-magnetic resonance imaging (*MRI*) of Alzheimer's disease (*AD*) patients without (*left*) and with (*right*) sleep disturbance; *arrows*, regions of interest (*ROIs*) in cholinergic regions in the brain stem: lateral dorsal tegmental nuclei and pedunculopontine tegmental nuclei (From Eggers et al. [17])

Exact coregistration of the PET data with the MRI is of particular importance with regard to surgery planning, i.e., not to remove too little or too much of the brain tissue. Combination of PET and functional MRI may also allow to detect eloquent brain areas and the topographical association to the epileptogenic material. A major advantage of integrated PET/MR for epilepsy diagnosis may be found in the fact that the number of required sedations/anesthesias can be reduced, particularly in smaller children who usually would not lie still during the PET and the MR scan.

8.2.2.3 Brain Tumors

Systematic combination of PET and MR information could also help to improve the quality of brain tumor diagnosis. MR allows the location of brain tumor tissue on the basis of contrast enhancement, equivalent to a disrupture of the blood–brain barrier. The extent of brain edema can be assessed and MR spectroscopy may provide information on the tissue, i.e., presence/level of malignancy. Furthermore, the integrity of white matter tracts in the neighborhood of tumors can be assessed by MR fiber tracking procedures. However, MRI has some limitations. (1) It is well accepted today that brain tumors may extend into brain tissue significantly beyond the areas affected by blood–brain barrier disruption. (2) Following therapy (e.g., radiation) a blood–brain barrier disruption may persist without the actual presence of underlying brain tumor tissue (so-called radiation necrosis). (3) The performance of MR spectroscopy is limited in borderline areas, i.e., close to the skull or the ventricles, and it is not well suited to cover the entire brain.

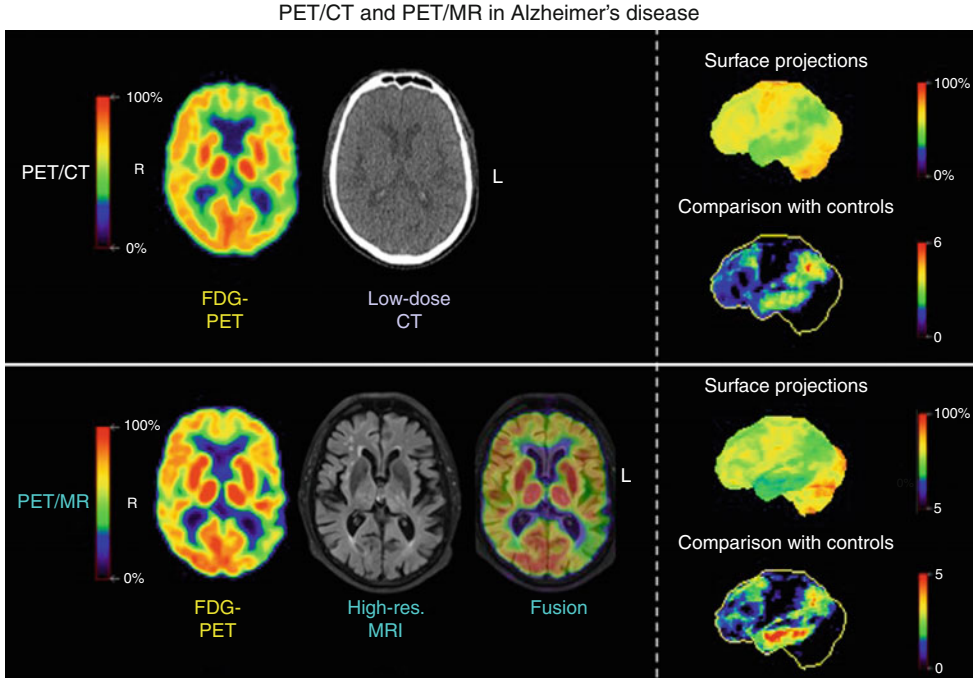

Fig. 8.3 [18F]FDG-PET in a patient with Alzheimer's disease. *Upper row*, conventional PET/CT scanner (Siemens Biograph 64, 30–45 min p.i.); from left to right, axial PET and low-dose CT slices. *Lower row*, same patient examined on an integrated PET/MR scanner (Siemens Biograph mMR, 60–74 min p.i.); from left to right, axial PET, high-resolution MRI, and fusion image. Areas with reduced metabolism (*green color*) representing impaired neuronal function are visible in the left temporoparietal cortex with both modalities, but brain anatomy can only be displayed in high resolution with the PET/MR. Cerebral atrophy is apparent in widespread regions, predominantly on the left side and on the fusion image regional allocation of hypometabolism and brain substance loss is possible. Right half of the image: surface projections of cerebral metabolism and of Z-score images (comparison with controls) in left lateral aspects. Similar patterns of abnormality are visible for both modalities. *L* left, *R* right

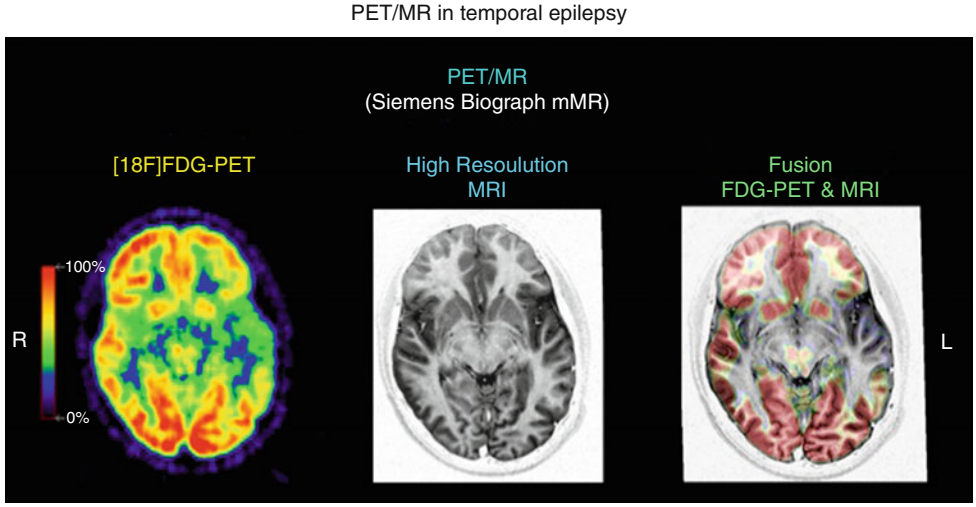

Fig. 8.4 [18F]FDG-PET/MR in a patient with epilepsy, acquired on an integrated PET/MR scanner (Siemens Biograph mMR, 60–75 min p.i.). From left to right: axial PET, high-resolution MRI scan, and fusion image. Distinct hypometabolism is visible in the polar region of the left temporal lobe, typically corresponding to the epileptogenic focus. The fusion image allows exact anatomical allocation of the functional changes, e.g., for surgery planning. *L* left, *R* right

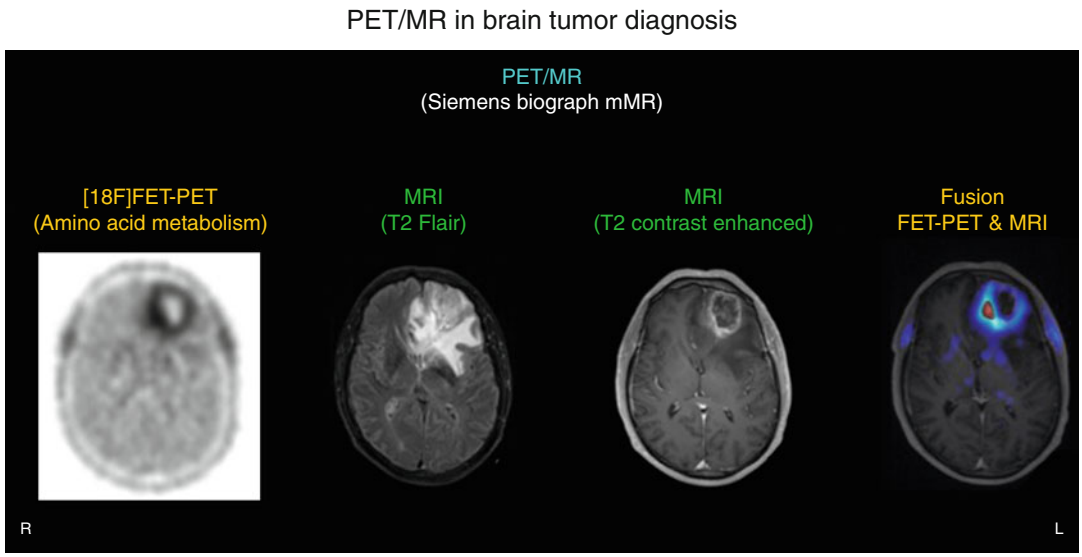

Fig. 8.5 [18F]FET-PET/MR in a patient with a brain tumor, acquired on an integrated PET/MR scanner (Siemens Biograph mMR, 50–65 min p.i.). From left to right: axial PET, T2-FLAIR, contrast-enhanced MR images, and fusion image. The differences between the abnormalities on the MR images and the PET signal are illustrated. The fusion image allows identification and anatomical allocation of a "hot spot" potentially helpful, e.g., for biopsy planning. *L* left, *R* right

PET and particularly PET using amino acids/analogues as tracers (e.g., [18F]FET, [11C] methionine) can help to circumvent the limitations of the MRI for brain tumor diagnosis. It has been demonstrated that vital brain tumor tissue with correspondingly increased amino acid metabolism can be detected outside of the regions associated with a blood–brain barrier disruption [21]. It allows to cover the entire brain and – due to the tracer uptake mechanism which is independent from the blood–brain barrier – it also helps to differentiate between radiation necrosis and tumor recurrence [37] (Fig. 8.5).

In consequence, the combination and exact anatomical coregistration between PET and MR information can be of crucial value for primary diagnosis, biopsy planning, assessment of tumor extent, and differentiation between recurrence and unspecific findings [36].

In combination, the PET and MR data can be used for surgery and radiation therapy planning. It has been demonstrated that the combination of both modalities results in changes of the tumor volume used for definition of the radiation therapy, which may have relevant effects on patient outcome [19].

An integrated imaging device becomes especially important when areas of critical neurofunction must be identified in the vicinity of tumors for planning of radiation therapy of the extent of a surgical intervention [46]. Similarly as for epilepsy surgery, the simultaneous acquisition of the PET information with fMRI activation studies can help to establish the locoregional association between tumor tissue and eloquent brain regions.

In first studies the value of PET/MR for intracerebral lesions has been already evaluated. A comparison to PET/CT images obtained in the same diagnostic session showed similar diagnostic quality of the hybrid PET/MR and PET/CT studies. The computed tumor-to-reference tissue ratios exhibited an excellent accordance between the PET/MR and PET/CT systems with a Pearson correlation coefficient of 0.98, and no significant artifacts or distortions were detected in the simultaneously acquired MR images using the PET/MR scanner [7].

8.2.2.4 Stroke/Cerebrovascular Disorders

In experimental focal ischemia and ischemic stroke, coregistration of regional values for

cerebral blood flow, oxygen utilization, and glucose metabolism on MRI early and late after the insult has permitted the differentiation of irreversibly damaged tissue and functionally impaired but morphologically preserved areas; these findings formed the basis for the concept of the penumbra, which significantly affected treatment strategies (review in Heiss [20]).

Currently, PET procedures are not routinely integrated into the first-line diagnostic evaluation of patients with suspected cerebrovascular issues or stroke. This is in part due to the need for a fast diagnosis, particularly regarding differentiation between ischemia and intracerebral bleeding, because different therapeutic strategies result. This diagnosis is usually obtained by CT or increasingly also by means of MR imaging. MR procedures offer multiple insights into the cerebrovascular status, including perfusion, diffusion, cerebral blood flow, and blood volume. The acquisition of these MR sequences is not carried out within seconds (as opposed to the CT) but within several minutes. If an integrated PET/MR scanner is available, this would in principle allow the acquisition of a PET scan during the collection of the MR data. PET imaging using tracers such as 15O and H215O would, e.g., allow to assess the extent of the penumbra, respectively, to obtain a baseline situation for comparison with follow-up data, e.g., after intervention. However, it has to be kept in mind that some tracers such as FDG require an uptake period (>30 min) to reach a relatively steady state in the brain. This fact could lead to an intolerable delay in the start of the imaging procedures, if not organized well.

In the future, further insights into the pathophysiology of ischemia and potential strategies for treatment and rehabilitation might result from simultaneous studies of blood flow, perfusion, vascular status, tissue water content, metabolism, and receptor activity in the course after acute stroke.

8.2.2.5 Inflammation

Different pathological changes associated with cerebral inflammation can be measured with PET methods (e.g., increased glucose metabolism or microglial activation and even demyelination) as well as with MR (e.g., edema, changes in perfusion, or postinflammatory residuals). The combination of both measures may allow more reliable diagnosis by the accumulation of evidence, such as in limbic encephalitis (Fig. 8.6). Furthermore, approaching the effects of inflammation from different perspectives may allow improving the understanding of the complex pathomechanisms involved (e.g., in multiple sclerosis) [6, 35, 44].

In general, the combined acquisition of clinical PET and MR data may help to directly compare the diagnostic value of the two modalities and to identify if one of the two or a combination of both represents the optimal approach for a specific indication.

8.3 Special Methodological and Scientific Advantages

8.3.1 Atrophy/Partial Volume Correction

Regarding the fact that the PET signal intensity is influenced by the actual volume of underlying brain substance, integrating this structural information in the evaluation of the PET findings may improve the quantification of abnormalities and improve the diagnostic value. Particularly in brain disorders associated with cerebral atrophy, such as dementia, judging the PET signal on the basis of the underlying structural framework may be of utmost value (see Fig. 8.3). This refers, for example, to FDG-PET used to assess regional glucose metabolism and to modern amyloid imaging procedures, such as [11C] PiB. For FDG-PET imaging, gray matter atrophy may lead to overestimation of cortical hypometabolism. Reversely for amyloid imaging atrophy may lead to underestimation of amyloid tracer uptake.

Combining PET and MRI systematically, without additional radiation exposure or loss of examination time, may allow performing atrophy correction of the PET data on a systematic basis, i.e., using the MR information reliably acquired on the same scanner and using the same sequences. The lack of this type of consistent information may have hampered the introduction of atrophy/partial volume correction into clinical application in the past.

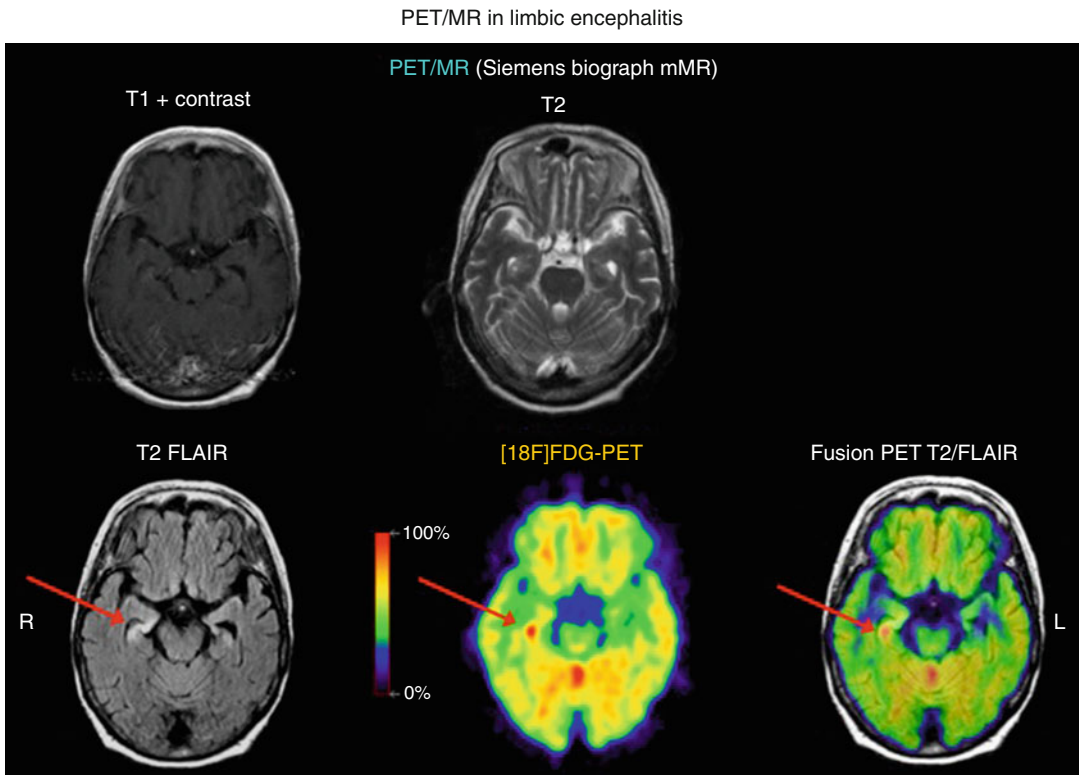

Fig. 8.6 [18F]FET-PET/MR in a patient with limbic encephalitis, acquired on an integrated PET/MR scanner (Siemens Biograph mMR, 60–75 min p.i.). From left to right, *upper row*: axial contrast-enhanced and T2-weighted MR scans, *lower row*: T2-FLAIR MRI, PET, and fusion image. On the PET image, a lesion with increased glucose metabolism is visible in the right mesial temporal lobe (*red arrow*), typically representing inflammatory changes associated with limbic encephalitis. Regarding the MR sequences, on the T2-FLAIR image, a signal enhancement is visible in similar location, adding evidence to the suspected diagnosis. *L* left, *R* right

Apart from using structural information obtained with MRI for partial volume correction, it can also be used for direct regional correlation between atrophy and specific PET findings. For example, recent studies were able to demonstrate a direct regional correlation between PET findings of regional amyloid load and brain atrophy in healthy elderly subjects [2].

8.3.2 Motion Correction

For simultaneous PET/MR acquisition, it has already been demonstrated that it may be possible to perform MR monitoring of patient head movement during the entire PET scan and correct the PET data for this motion afterward. In a recent publication, it has been shown that this may lead to an optimization of the image quality of the PET scan [8].

Particularly in patients with neurological disorders such as dementia or Parkinson's disease or in children, the option to perform motion correction may be highly valuable. This option is only available for data acquired simultaneously.

8.3.3 Modeling and Validation of Dynamic Data

The supply of PET tracers to various brain regions depends on the regional perfusion, and the tracer distribution can also be strongly influenced by the integrity of the blood–brain barrier. These effects

are important with regard to quantitatively translating the PET signal into an accurate biological measure. Often, it may be of critical importance to obtain objective information from a PET imaging study, e.g., on receptor occupancy or on metabolism, independently from accompanying effects of perfusion or blood–brain barrier disruption. MR procedures offer a number of insights into cerebrovascular parameters such as cerebral blood flow, blood volume, mean transit time, permeability, and blood–brain barrier disruption. This includes imaging procedures depending on the injection of contrast media (such as DCE-MRI or DSC-MRI) but also noninvasive methods such as arterial spin labeling (ASL). To combine this wealth of available information with data obtained by PET imaging may offer numerous valuable options:

The high temporal resolution of MRI can be utilized for the acquisition of dynamic data required for quantification of parametric values by PET. For instance, flow-dependent kinetic constants can be determined by PWI (perfusion-weighted imaging) and used for compartmental analysis of PET data (e.g., FDG, FLT) [41] or for the assessment of the kinetics of the distribution of tracers or labeled drugs in various brain structures [53].

Vascular regions of interest defined by MRI time-of-flight (TOF) angiography may be used to observe the dynamics of PET tracer supply to the brain and potentially to help replacing the invasive monitoring of an arterial input function, e.g., for receptor imaging studies.

In research on stroke, PWI and DWI (diffusion-weighted imaging) by MR has been used extensively during the last decade for the identification of critically perfused tissue (a surrogate of the penumbra) as the basis for reperfusion therapy. However, since PWI does not yield tissue flow but vascular perfusion, a validation of this method by quantitative measurement of blood flow is necessary, by which critical thresholds for functional and morphological damage can be determined (Fig. 8.7).

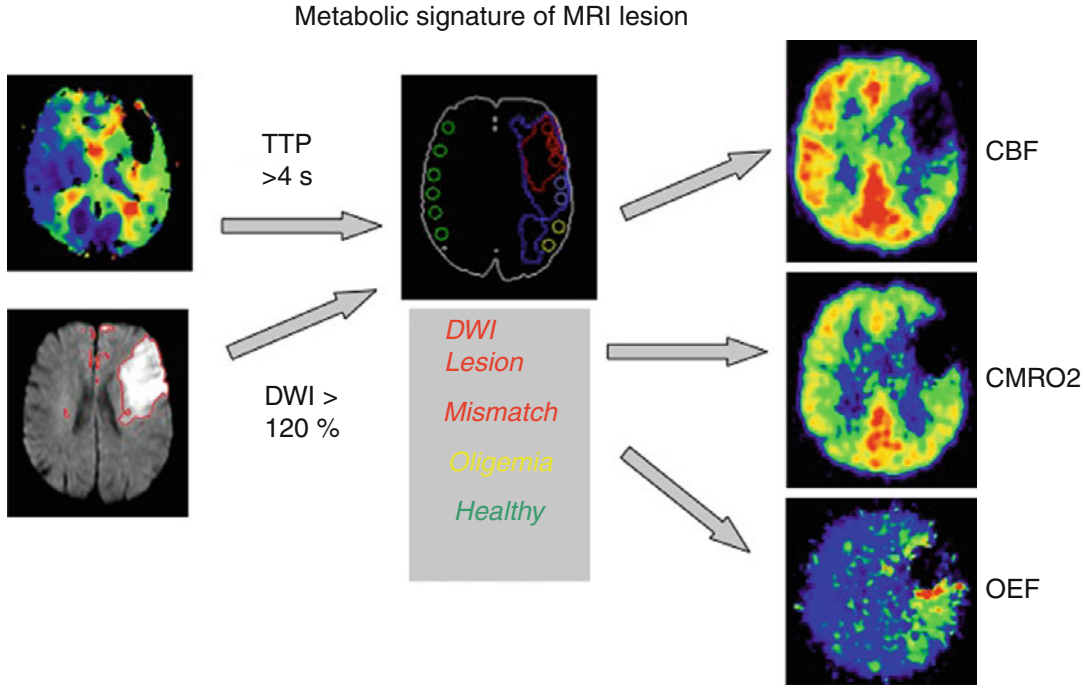

Fig. 8.7 Coregistered images of PW/DW MRI and multitracer PET in a patient with an acute right-side hemiparesis. The ROIs were placed according to the MRI criteria and then transferred to the PET images (ROI colors: *red* indicates DWI lesion; *blue*, mismatch; *yellow*, oligemia; *green*, reference region)

In sequential investigations of patients with acute ischemic stroke perfusion delays as surrogate measures of penumbra flow were obtained (review in Heiss [20]), but simultaneous acquisition of these parameters would certainly improve the validity of these results. Additionally, the vascular origin of the ischemic lesion can be detected by MRA and effects of reopening the vessel on blood flow and energy metabolism can be shown.

Regarding studies on brain tumors, the quantification of regional PET-tracer uptake could be corrected for effects of regional blood–brain barrier disrupture and perfusion. Effects of antiangiogenetic therapy in brain tumors (e.g., on tumor viability, metabolism, or proliferation) could be monitored independently from changes in vascular permeability [5].

Simultaneous data acquisition by MRI and PET could also be used to develop and validate new methods. Values of cerebral blood flow obtained by ASL-MRI can be validated by $H_2{}^{15}O$-PET [30], and ^{17}O as a potential tracer for oxygen utilization [45] could be compared to the cerebral metabolic rate of oxygen as determined by PET. Additionally, vascular lesions seen in MRA and perfusion disturbances detected by PWI could be related to hypoxic markers from 18F-MISO-PET. Certainly, also other new methods to quantify oxygen consumption by MRI (pulsed arterial spin labeling – PASL-MR, deoxyhemoglobin MR) need to be validated by ^{15}O-PET procedures.

8.3.4 Monitoring Different Stages of Metabolic Processes

PET as well as magnetic resonance spectroscopy (MRS) can be used to monitor metabolic processes and products, but these methods differ in their detection sensitivity. 18-Fluorodeoxyglucose (FDG) is the most widely used PET tracer and is routinely applied to measure glucose consumption in the brain. However, since turnover of FDG is blocked at FDG-6-phosphate, FDG-PET only permits the quantification of glycolysis. MRS is able to image substrates of the tricarboxylic acid cycle including lactate and pyruvate and therefore can supplement the metabolic information obtained by PET [33]. This complimentary insight into different stages of the glucose metabolism is of special interest in brain tumors [23]. A combination of spectroscopic detection of choline with ^{11}C- or 18F-choline PET might deliver important hints on membrane properties of special tumors [28, 29]. Metabolic changes induced by drugs, e.g., by the interaction with the dopaminergic system, can also be visualized with PET or MRS [52] permitting the combined visualization of receptor binding and increased energy demand by neuronal activation.

8.3.5 Functional Activation

Patterns of activation due to different stimuli or interactions can be studied by PET (regional blood flow or metabolism) and by fMRI (usually by utilizing the BOLD effect), but the observed changes actually come from different substrates. The BOLD (blood oxygen level dependent) MRI uses activity-induced change of the signal which is the sum of changes in cerebral blood flow (increase) and in cerebral metabolic rate of oxygen (smaller and delayed increase); the BOLD signal during activation actually indicates the increased blood oxygenation due to the overshoot of blood supply [18, 27]. Simultaneous PET/MR measurement at the same physiological and stimulus conditions could reveal small differences between results from PET and MR and also demonstrate the differences in the localization of the activation patterns (intravascular vs. tissue signals). Complex MR activation studies observed a large task-induced augmentation of cerebral blood flow (60 %) not mediated by increased oxygen consumption but only a small energy demand (15 % increase in ATP production), which is met through oxidative metabolism [31].

A highly interesting scientific option of PET/MR may be found in the combined measurement of neurochemical changes as assessed by PET and changes in regional brain activity as assessed by BOLD fMRI.

This includes effects of activation by specific tasks on transmitter release or receptor binding

of, e.g., DOPA or raclopride. For example, during learning of motor skills, effects of regional neuronal activation might be followed by BOLD MRI, and simultaneously it could be detected by PET where a dopamine receptor ligand is displaced from the receptor site [1]. Using opiate receptor PET displacement studies, effects of drugs or of endogenous endorphin release could be monitored simultaneously with regional brain activation. These findings of multimodal imaging could then also be related with task performance, behavior, hormone levels, etc. In contrast to previous approaches using sequential imaging of activation and neurochemical changes, simultaneous acquisition is not prone to habituation effects regarding the task and to differences in performance, changes in mood, hormonal status, and wakefulness, which can occur even within a few hours. This will open new perspectives in the analysis of functional networks and also in the evaluation of the interaction of drugs with behavior.

8.3.6 Functional and Structural Connectivity

New insights into brain function in health and disease and into the effects of interventions on functional networks might be gained by introducing diffusion tensor imaging (DTI) by MRI into the investigative procedures: diffusion tensor imaging in an integrated PET/MR system will add new dimensions since it can be performed in close temporal relation to activation studies mapping the effects on transmitter release and receptor occupancy as well as on metabolism in connected areas of functional networks [43]. Diffusion tensor imaging (DTI) showed good quality in seven volunteers with simultaneous PET data readout in the hybrid PET/MR scanner dedicated for brain and head imaging ([7]). In four patients with brain tumors, DTI provided information on displacement and integrity of peritumoral fiber tracts which in addition to the metabolic grading by PET was important for treatment planning.

Another useful application for integrated PET and structural connectivity MR imaging may be to improve the understanding of the effects of deep brain stimulation. With this approach the effect of deep brain stimulation of the nucleus accumbens — which is a means to ameliorate neurological symptoms and improve abnormal behavior in several brain disorders [49] — on metabolism, and on transmitter/receptor interaction in defined regions together with the connecting fiber tracts can be demonstrated (Fig. 8.8). Another study was able to delineate the networks responsible for cognitive changes of patients with Parkinson's disease after stimulation of the subthalamic nucleus [26]. A further application might be the analysis of effects of repetitive transcranial magnetic stimulation (rTMS) or of direct current stimulation (DCS), which can be used to activate or inhibit selected areas of the cortex, on regional metabolism, and on the involvement of transmitter/receptor systems with the connecting networks [48].

Recently, increased microglia activation was observed in ischemic infarcts but also in periinfarct regions as well as in the fiber tracts originating from the affected areas (Fig. 8.9); the inflammation of the corticospinal tract was closely related to its atrophy and predicted the further course of persisting deficits [47].

In addition to information on structural connectivity, modern resting state functional MRI procedures allow the identification of the functional connectivity between different brain areas. Several studies have already been performed comparing functional connectivity information with PET. For example, reductions in functional connectivity have been demonstrated in patients with Alzheimer's disease and even in healthy controls with PET-proven amyloid deposition in the brain [42].

Furthermore regional overlap of hypometabolic abnormalities (as measured with [18F] FDG-PET) with impaired functional connectivity (as measured by fMRI) has been demonstrated in patients with mild cognitive impairment and also in amyloid-positive healthy controls [14].

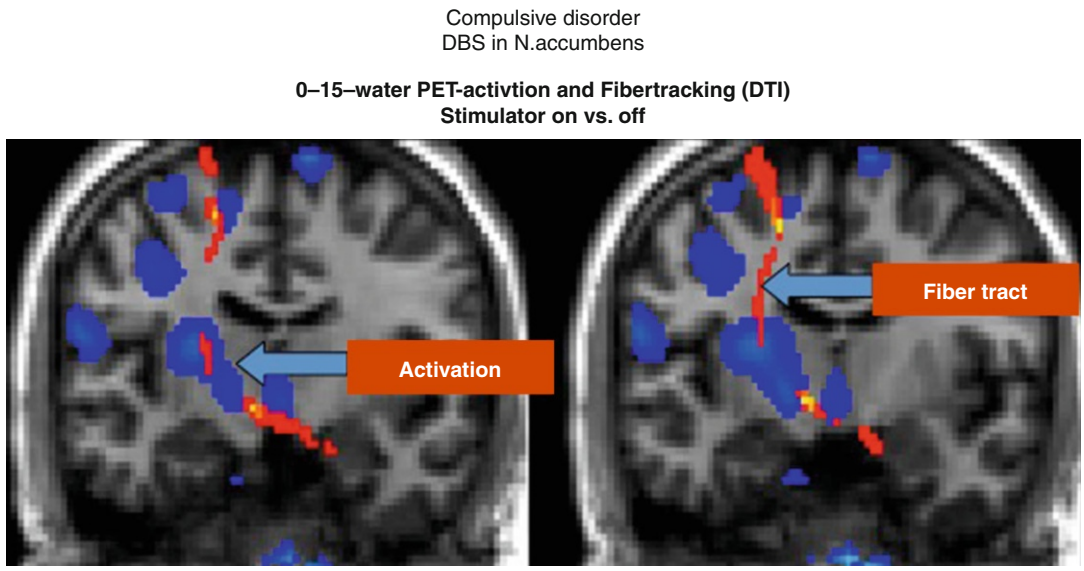

Fig. 8.8 Coregistration of MRI with diffusion tensor tracking and PET 15O water activation studies demonstrates the effect of stimulation of the nucleus accumbens by flow increase in the striatum and various cortical regions. Diffusion tractography depicts the anatomical pathways between the stimulated region and the activated subcortical and cortical areas

8.4 PET/MR for Translational Research

Molecular and cellular imaging is a new field opening up with combined micro-PET and MR devices for animal studies [54]. For the transfer of these findings and the development of innovative treatment strategies to humans integrated PET/MR will be of great value. Topics for which simultaneous assessment of various parameters is essential include:

- Targeted gene transfer by various vectors for induction of foreign enzyme expression in selected cells. These foreign enzymes can render the induced cells susceptible to specific drugs which then are converted into toxic compounds. This approach was applied for experimental treatment of glioblastoma by transferring the herpes simplex thymidine kinase gene which made the cells susceptible for ganciclovir. The expression of the transferred gene as well as the effect on tumor metabolism and growth could be followed by PET and MRI [25].
- Simultaneous PET/MR can be used to show the viability and differentiation of transplanted cells and their effect on the neuronal network. Embryonic stem cells can be implemented into brain lesions, e.g., the destroyed striatum. The proliferation and differentiation of dopaminergic cells can be followed by coregistering MRI and PET of specific dopamine transporter ligands. The restored functional activity of the transplanted cells can be demonstrated by the response to amphetamine causing increase in rCBV due to dopamine release [4].
- Cell replacement approaches for treatment of various neurological disorders, e.g., ischemic stroke. For this strategy it is essential to monitor the location and follow the migration of grafted stem or progenitor cells. For labeling these cells, various methods can be used making them detectable by MRI, e.g., iron oxide particles [23]. The migration of these cells to the border zone of damaged brain tissue in the lesioned hemisphere can be followed by MRI, and PET can demonstrate their viability and

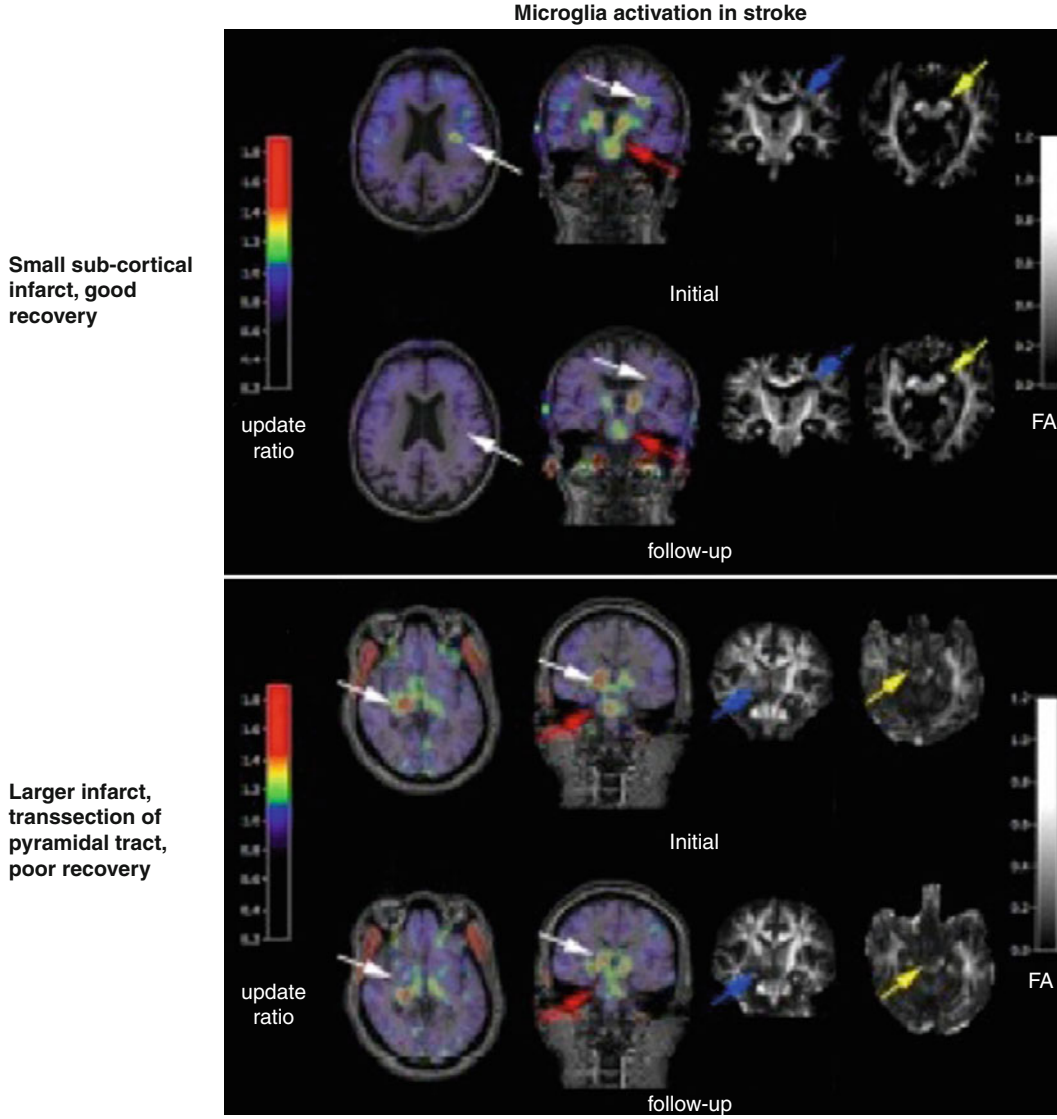

Fig. 8.9 (**a**) Microglial activation in patient with small subcortical infarct and good recovery. Initial activated microglia in infarct decreased over 6 months (*white arrows*), whereas microglial activation in the brain stem persisted (*red arrows*). DTI showed decreased FA primarily in infarct (*blue arrows*) and less along tract at level of cerebral peduncles (*yellow arrows*). (**b**) Patient with complete transection of PT and poor recovery. Microglial activity in infarct decreased but still persisted after 6 months (*white arrows*), as did activity in brain stem (*red arrows*). FA decreased in area of infarct (*blue arrows*) and along tract in cerebral peduncle (*yellow arrows*). Microglial activity in patient in whom PT was not affected decreased over 6 months (*white arrows*). No tracer uptake at level of brain stem was observed, and FA along tracts was not decreased (From Thiel et al. [47] with permission)

their integration into functional networks [38]. Monitoring viability and migration as well as integration of cells into functional networks by integrated PET/MR might become a qualifying step in strategies relying on transplantation of fetal grafts in various neurological diseases.

8.5 Summary

Integrated PET/MR imaging offers a number of promising options regarding the clinical evaluation of disorders of the brain. The high diagnostic value of MR and PET procedures for neuropsychiatric conditions may turn PET/MR into the hybrid imaging modality of choice for diagnostic questions directed toward pathologies inside the brain. It may help to improve the diagnostic value compared to each of the individual diagnostic procedures and it may optimize work flow efficiency and patient comfort. Generally, the integrated PET/MR technology will eventually prompt the diagnostic disciplines to generate a combined report including findings from both modalities and interpreting them together. This may lead to a surge in the diagnostic quality and avoid that the referring physicians obtain two reports with eventually incompatible or mismatching results.

From a scientific perspective, PET/MR may help to improve the physiological understanding of healthy brain function and open new insights into the pathophysiological interrelation between different parameters involved in disorders of the central nervous system in human and small animal studies.

Acknowledgment WDH has been supported by the Max Planck Society and by the WDH Foundation. AD has been supported by the DFG (Deutsche Forschungsgemeinschaft, Großgeräteinitiative), who funded the installation of the PET/MR scanner at the Technische Universität München. The scanner is operated by a consortium of the Departments of Nuclear Medicine and Radiology of the Technische Universität München, Munich, and of the Ludwig-Maximilians-Universität München, Munich. Furthermore, this work was supported by grants of the DFG [DR 445/3-1, 4-1 to A.D.]

References

1. Badgaiyan RD, Fischman AJ, et al. Striatal dopamine release in sequential learning. Neuroimage. 2007; 38(3):549–56.
2. Becker JA, Hedden T, et al. Amyloid-beta associated cortical thinning in clinically normal elderly. Ann Neurol. 2011;69(6):1032–42.
3. Beyer T, Townsend DW, et al. A combined PET/CT scanner for clinical oncology. J Nucl Med. 2000; 41(8):1369–79.
4. Bjorklund LM, Sanchez-Pernaute R, et al. Embryonic stem cells develop into functional dopaminergic neurons after transplantation in a Parkinson rat model. Proc Natl Acad Sci U S A. 2002;99(4):2344–9.
5. Bjornerud A, Sorensen AG, et al. T(1)- and T(2)(*)-dominant extravasation correction in DSC-MRI: part I–theoretical considerations and implications for assessment of tumor hemodynamic properties. J Cereb Blood Flow Metab. 2011;31(10):2041–53.
6. Blinkenberg M, Mathiesen HK, et al. Cerebral metabolism, magnetic resonance spectroscopy and cognitive dysfunction in early multiple sclerosis: an exploratory study. Neurol Res. 2012;34(1):52–8.
7. Boss A, Bisdas S, et al. Hybrid PET/MRI of intracranial masses: initial experiences and comparison to PET/CT. J Nucl Med. 2010;51(8):1198–205.
8. Catana C, Benner T, et al. MRI-assisted PET motion correction for neurologic studies in an integrated MR-PET scanner. J Nucl Med. 2011;52(1):154–61.
9. Catana C, Procissi D, et al. Simultaneous in vivo positron emission tomography and magnetic resonance imaging. Proc Natl Acad Sci U S A. 2008;105(10):3705–10.
10. Cherry SR. The 2006 Henry N. Wagner lecture: of mice and men (and positrons)–advances in PET imaging technology. J Nucl Med. 2006;47(11):1735–45.
11. Cho ZH, Son YD, et al. A fusion PET-MRI system with a high-resolution research tomograph-PET and ultra-high field 7.0 T-MRI for the molecular-genetic imaging of the brain. Proteomics. 2008;8(6):1302–23.
12. Cho ZH, Son YD, et al. Observation of glucose metabolism in the thalamic nuclei by fusion PET/MRI. J Nucl Med. 2011;52(3):401–4.
13. Delso G, Furst S, et al. Performance measurements of the Siemens mMR integrated whole-body PET/MR scanner. J Nucl Med. 2011;52(12):1914–22.
14. Drzezga A, Becker JA, et al. Neuronal dysfunction and disconnection of cortical hubs in non-demented subjects with elevated amyloid burden. Brain. 2011; 134(Pt 6):1635–46.
15. Drzezga A, Grimmer T, et al. Prediction of individual clinical outcome in MCI by means of genetic assessment and (18)F-FDG PET. J Nucl Med. 2005;46(10): 1625–32.
16. Drzezga A, Souvatzoglou M, et al. First clinical experience of integrated whole-body PET/MR. Comparison to PET/CT in patients with oncological diagnoses. J Nucl Med. 2012;53(6):845–55.
17. Eggers C, et al. Imaging of acetylcholine esterase activity in brainstem nuclei involved in regulation of sleep and wakefulness. Eur J Neurol. 2007;14:690–3.
18. Fox PT, Raichle ME. Focal physiological uncoupling of cerebral blood flow and oxidative metabolism during somatosensory stimulation in human subjects. Proc Natl Acad Sci U S A. 1986;83:1140–4.

19. Grosu AL, Weber WA, et al. Reirradiation of recurrent high-grade gliomas using amino acid PET (SPECT)/CT/MRI image fusion to determine gross tumor volume for stereotactic fractionated radiotherapy. Int J Radiat Oncol Biol Phys. 2005; 63(2):511–19.
20. Heiss WD. The ischemic penumbra: correlates in imaging and implications for treatment of ischemic stroke. The Johann Jacob wepfer award 2011. Cerebrovasc Dis. 2011;32(4):307–20.
21. Herholz K, Coope D, et al. Metabolic and molecular imaging in neuro-oncology. Lancet Neurol. 2007; 6(8):711–24.
22. Herholz K, Weisenbach S, et al. In vivo study of acetylcholine esterase in basal forebrain, amygdala, and cortex in mild to moderate Alzheimer disease. Neuroimage. 2004;21:136–43.
23. Hoehn M, Wiedermann D, et al. Cell tracking using magnetic resonance imaging. J Physiol. 2007;584(Pt 1): 25–30.
24. Jack Jr CR, Vemuri P, et al. Evidence for ordering of Alzheimer disease biomarkers. Arch Neurol. 2011; 68(12):1526–35.
25. Jacobs A, Voges J, et al. Positron-emission tomography of vector-mediated gene expression in gene therapy for gliomas. Lancet. 2001;358:727–9.
26. Kalbe E, Voges J, et al. Frontal FDG-PET activity correlates with cognitive outcome after STN-DBS in Parkinson disease. Neurology. 2009;72(1):42–9.
27. Kida I, Hyder F. Physiology of functional magnetic resonance imaging: energetics and function. Methods Mol Med. 2006;124:175–95.
28. Kwee S, Ernst T. Total choline at 1H-MRS and [18F]-fluoromethylcholine uptake at PET. Mol Imaging Biol. 2010;12(4):424–5; author reply 426.
29. Kwee SA, Coel MN, et al. Combined use of F-18 fluorocholine positron emission tomography and magnetic resonance spectroscopy for brain tumor evaluation. J Neuroimaging. 2004;14(3):285–9.
30. Leontiev O, Buxton RB. Reproducibility of BOLD, perfusion, and CMRO2 measurements with calibrated-BOLD fMRI. Neuroimage. 2007;35(1):175–84.
31. Lin AL, Fox PT, et al. Nonlinear coupling between cerebral blood flow, oxygen consumption, and ATP production in human visual cortex. Proc Natl Acad Sci U S A. 2010;107(18):8446–51.
32. Lopinto-Khoury C, Sperling MR, et al. Surgical outcome in PET-positive, MRI-negative patients with temporal lobe epilepsy. Epilepsia. 2012;53(2):342–8.
33. Morris P, Bachelard H. Reflections on the application of 13C-MRS to research on brain metabolism. NMR Biomed. 2003;16(6–7):303–12.
34. Okello A, Koivunen J, et al. Conversion of amyloid positive and negative MCI to AD over 3 years: an 11C-PIB PET study. Neurology. 2009;73(10):754–60.
35. Owen DR, Piccini P, et al. Towards molecular imaging of multiple sclerosis. Mult Scler. 2011;17(3): 262–72.
36. Pauleit D, Floeth F, et al. O-(2-[18F]fluoroethyl)-l-tyrosine PET combined with MRI improves the diagnostic assessment of cerebral gliomas. Brain. 2005;128(Pt 3):678–87.
37. Rachinger W, Goetz C, et al. Positron emission tomography with O-(2-[18F]fluoroethyl)-L-tyrosine versus magnetic resonance imaging in the diagnosis of recurrent gliomas. Neurosurgery. 2005;57(3): 505–11; discussion 505–511.
38. Rueger MA, Backes H, et al. Noninvasive imaging of endogenous neural stem cell mobilization in vivo using positron emission tomography. J Neurosci. 2010;30(18):6454–60.
39. Schlemmer HP, Pichler BJ, et al. Simultaneous MR/PET imaging of the human brain: feasibility study. Radiology. 2008;248(3):1028–35.
40. Schmand M, Burbar Z, et al. BrainPET: first human tomograph for simultaneous (functional) PET and MR imaging. J Nucl Med Abstr Book. 2007;48:45P, No. 151.
41. Schmidt KC, Turkheimer FE. Kinetic modeling in positron emission tomography. Q J Nucl Med. 2002;46(1):70–85.
42. Sheline YI, Raichle ME, et al. Amyloid plaques disrupt resting state default mode network connectivity in cognitively normal elderly. Biol Psychiatry. 2010;67(6):584–7.
43. Song AW, Harshbarger T, et al. Functional activation using apparent diffusion coefficient-dependent contrast allows better spatial localization to the neuronal activity: evidence using diffusion tensor imaging and fiber tracking. Neuroimage. 2003;20(2):955–61.
44. Stankoff B, Freeman L, et al. Imaging central nervous system myelin by positron emission tomography in multiple sclerosis using [methyl-(1)(1)C]-2-(4′-methylaminophenyl)- 6-hydroxybenzothiazole. Ann Neurol. 2011;69(4):673–80.
45. Tailor DR, Baumgardner JE, et al. Proton MRI of metabolically produced H2 17O using an efficient $17O_2$ delivery system. Neuroimage. 2004;22(2):611–18.
46. Thiel A, Habedank B, et al. From the left to the right: how the brain compensates progressive loss of language function. Brain Lang. 2006;98:57–65.
47. Thiel A, Radlinska BA, et al. The temporal dynamics of poststroke neuroinflammation: a longitudinal diffusion tensor imaging-guided PET study with 11C-PK11195 in acute subcortical stroke. J Nucl Med. 2010;51(9):1404–12.
48. Thiel A, Schumacher B, et al. Direct demonstration of transcallosal disinhibition in language networks. J Cereb Blood Flow Metab. 2006;26(9):1122–7.
49. van Kuyck K, Gabriels L, et al. Behavioural and physiological effects of electrical stimulation in the nucleus accumbens: a review. Acta Neurochir Suppl. 2007;97(Pt 2):375–91.
50. Vander Borght T, Asenbaum S, et al. EANM procedure guidelines for brain tumour imaging using labelled amino acid analogues. Eur J Nucl Med Mol Imaging. 2006;33(11):1374–80.
51. Varrone A, Asenbaum S, et al. EANM procedure guidelines for PET brain imaging using [18F]FDG, version 2. Eur J Nucl Med Mol Imaging. 2009; 36(12):2103–10.

52. Volkow ND, Wang G-J, et al. Addiction circuitry in the human brain. Annu Rev Pharmacol Toxicol. 2012;52:321–36.
53. Weber WA, Czernin J, et al. Technology Insight: novel imaging of molecular targets is an emerging area crucial to the development of targeted drugs. Nat Clin Pract Oncol. 2008;5(1): 44–54.
54. Wehrl HF, Judenhofer MS, et al. Pre-clinical PET/MR: technological advances and new perspectives in biomedical research. Eur J Nucl Med Mol Imaging. 2009;36 Suppl 1:S56–68.

MR-PET in Cardiology: An Overview and Selected Cases

9

Stephan G. Nekolla and Christoph Rischpler

Contents

Abstract

Since the turn of the millennium, PET/CT devices evolved as the first generation of hybrid imaging systems integrating nuclear and radiological imaging from a valuable research tool into a clinically useful and accepted technique. These innovative devices combined morphological and metabolic-functional information in an elegant way and reached widespread distribution. Therefore, it seemed quite obvious to develop a PET/MR system. However, the technical hurdles for this kind of integration were for physic's reasons much higher – but were finally solved: for more than 2 years, integrated whole-body systems are now available and, in view of the success of PET/CT, the expectations are high that PET/MR provides an actual clinical benefit. MRI's advantage of an excellent soft tissue contrast and the capability of functional imaging at the molecular level by PET should have the potential to create a unique multimodality imaging. However, PET/MR in general and in cardiac imaging in particular needs to demonstrate its suitability in everyday clinical practice. In this review we give an overview of the requirements and features of this new hybrid imaging system and provide an outlook based on clinical examples, in which areas PET/MR could potentially find a place in the armamentarium of cardiac imaging.

S.G. Nekolla (✉) • C. Rischpler
Nuklearmedizinische Klinik und Poliklinik,
Klinikum rechts der Isar der Technischen Universität München, Ismaninger Strasse 22,
81675 Munich, Germany
e-mail: stephan.nekolla@tum.de

I. Carrio, P. Ros (eds.), *PET/MRI*,
DOI 10.1007/978-3-642-40692-8_9, © Springer-Verlag Berlin Heidelberg 2014

9.1 Introduction

Cardiac imaging is in the fortunate situation that a wide variety of noninvasive imaging modalities is available. This includes echocardiography, computed tomography (CT), magnetic resonance imaging (MRI), single-photon emission computed tomography (SPECT), and positron emission tomography (PET). Each of these methods has certain advantages and disadvantages. Through the combination of single modalities into hybrid imaging systems (such as SPECT/CT or PET/CT), the disadvantages of each component can not only be mitigated or eliminated but can yield synergistic value. Thus, the PET/CT has experienced an impressive growth since its introduction in 2000, and several thousand systems were installed worldwide. This is primarily driven by oncological imaging, where the added value of hybrid imaging with PET/CT compared to stand-alone PET was demonstrated [1]. The increased availability of PET/CT systems resulted also in an increased utilization in cardiac imaging. Those devices provided rapid assessment of the data needed for attenuation correction which is the prerequisite of any image quantification up to the delineation of myocardial blood flow. In addition, CT angiography allowed the visualization and quantification of the coronary anatomy, which yielded incremental diagnostic value over perfusion information alone [2]. Thus, the questions arise whether integrated PET/MR systems can repeat the success of PET/CT in general and whether such a hybrid device adds incremental value in cardiac imaging in particular.

This review will provide (a) an overview over the technical challenges and implementations in the context of thoracic imaging, (b) report on our initial experiences, and based on those (c) outline areas of interest and relevance for cardiac PET/MR.

9.2 PET/MR in Cardiac Imaging: Technical Considerations

As part of a major research initiative of the Deutsche Forschungsgesellschaft (DFG: German Research Foundation), an integrated whole-body PET/MR scanner was installed in our department in late 2010. Since then we gained considerable experience with this novel and complex imaging approach – although no final evaluation or assessment in comparison to the established modalities such as PET/CT and pure MRI systems was possible [3, 4].

From a technical point of view, two fundamental implementations are available today: Philips Healthcare (Best, Netherlands) provides a system with two separated units, which are connected with a common patient table [5]. Siemens Healthcare (Erlangen, Germany) implemented a fully integrated PET/MR system based on earlier prototypes of brain-only PET inserts [6], which is housed directly within the bore of a conventional 3 T magnet.

9.3 Attenuation Correction

As mentioned before, the correction of attenuated and scattered annihilation photons is a cornerstone in PET quantification. In PET/MR, this topic is of particular interest as both system designs lack the conventional (PET-only) approach, namely, rotating germanium rod sources, and also have no access to the technique used in PET/CT systems, i.e., extrapolating the attenuation for the 511 keV annihilation photons from the CT data acquired with 80–140 keV. Without access to such an attenuation map or "μ-map," PET quantification – which is a fundamental building block of cardiac PET – is impossible. In the special case of cardiac PET/CT, this is of even higher importance as even modest alignment errors between PET and CT decrease the diagnostic accuracy [7, 8], Consequently, the generation of the attenuation map for 511-keV photons poses a new challenge, as there is no physical relationship between MR images and the attenuation coefficients for biological tissues. In order to address this problem, various approaches are being pursued: (a) image segmentation and value mapping, (b) template- or atlas-based, or (c) utilizing the PET data itself. Image segmentation is currently the technique utilized on both available systems and is described briefly: image data is classified into different

types of tissue, which then are associated with fixed attenuation coefficients [9] using DIXON image sequences [10]. Water and fat images are generated and each voxel is assigned to be either air, lung tissue, fat, or soft tissue. As cortical bone is basically invisible in these images, it is ignored (which was also the case of the "classic" PET scanner with rotating rod sources). For every bed position, the acquisition time is about 18 s. The major limitations of this technique are the small number of tissue classes with a general (not patient-specific) attenuation coefficient which is of particular relevance in cardiac studies as in some cases significant fluctuations in the lung tissue signal can be seen. The advantages of this approach are, however, that the attenuation map may be computed relatively quickly and in a reproducible way. The Siemens Biograph mMR uses a variant of this approach [9], and we could already show a good correlation of tracer uptake between PET/CT and PET/MR examinations in oncological studies [11, 12]. The Philips PET/MR device uses a similar approach integrating soft and fat tissue into one class, however [13]. Of special relevance is the fact that the transaxial field of the MR unit typically is only 40–45 cm. This results in a potential truncation of the attenuation map in some parts of the body – especially the arms, which are positioned usually next to the body [14]. An extension of the MR's field-of-view is technically very complex [15], and in the current Biograph mMR, the following approach is implemented to compensate for this effect: in the truncated parts, PET emission data is utilized to estimate the presence of tissue as many PET tracers show nonspecific uptake. This data is also segmented and included in the attenuation map [7, 16]. Finally, it should be mentioned that the MR imaging-related equipment such as patient's bed (which is more massive than the one found in PET/CT scanners), MRI coils which can be freely placed, and positioning and monitoring devices such as ECG electrodes, headphones, and respiratory belts all contribute to scattering and attenuation of the 511 keV annihilation photons. Since these parts are not visible in conventional MR sequences and thus are not used in the attenuation map, they may lead to image inhomogeneities and adversely affect quantification. Despite these technical problems, the data obtained so far in cardiac PET/MR imaging in general show a relatively good correlation between PET/CT and PET/MR [17, 18], but larger studies are clearly warranted.

9.4 Applications in Cardiac Imaging

It has to be acknowledged that in the past, the probability that a patient underwent MR and PET sequentially was rather low – the only moderate body of literature to be found reflects this. The main reasons were the availability of both techniques in spatial and temporal proximity as well as cost issues. Realistically, if both MR and PET were used in the same patients, the objective was the comparison of methods and the proof of superiority or at least non-inferiority of one approach over the other. However, there are quite some aspects where the combination of both modalities could be advantageous.

9.5 Myocardial Viability and Tissue Characterization

The imaging-based assessment of myocardial viability is a standard approach applied in patients with advanced coronary heart disease or in those who are in early or advanced states of heart failure. The diagnostic goal is to distinguish between under-perfused but vital heart tissue (so-called hibernating myocardium) and poorly perfused but nonvital tissue (scar). Patients in the first group would benefit from invasive revascularization, whereas patients in the latter group have no advantage of this intervention. Of the various imaging methods, PET using 18 F-fluorodeoxyglucose (FDG) is widely considered as the clinical gold standard. In such an examination, both myocardial perfusion (e.g., with the 13 N-ammonia as tracer) and the glucose metabolism using FDG are investigated ideally applying the euglycemic-hyperinsulinemic clamp technique [19]. From a conceptual point

of view, hypoxia or ischemia leads to a change in myocardial metabolism from the utilization of free fatty acids toward glucose metabolism. It could also be shown that the extent of the ischemically compromised myocardium is associated with a poorer long-term outcome [20]. Furthermore, this approach allows the classification of the myocardial tissue into fully viable, partially vital, and nonvital tissue – however, always within the limits of PET's modest spatial resolution. MR imaging could provide here a valuable addition to PET. Late gadolinium enhancement (LGE) which is acquired using T1-weighted inversion recovery sequences 5–20 min after the administration of gadolinium-DTPA directly represents myocardial scar tissue [21–23]. Normal myocardium can be "nulled" and infarcted tissue shows a hyperintense signal due to different washout constants in normal versus abnormal tissue. MRI's high spatial resolution allows not only the distinction between transmural and nontransmural myocardial infarction (MI), it can also detect even small subendocardial infarcts, which is common in patients with suspected coronary artery disease without previous MI and shows prognostic significance [24]. Whereas the specificity of PET and MRI is comparable (63 %), PET shows a higher sensitivity (92 % vs. 84 %) [25]. This stems from the fundamentally different processes in the imaging process: while the LGE signal is based solely on an increased interstitial volume of distribution (gadolinium chelates are too large to enter a cell), the PET signal is truly metabolic. Furthermore, the PET also allows the identification of myocardium at a metabolical risk – thus, the PET provides an indication of therapeutic relevance in addition to the known relationship of infarct size and prognosis [26]. In summary, for the assessment of myocardial viability, both methods provide similar information [18]. However, a potentially relevant opportunity of hybrid imaging could arise from the observation that myocardial tissues that were classified as vital prior to the revascularization show no contractile improvement [27]. Here, the PET/MR imaging could offer an interesting approach. By integrating the information from morphology and left ventricular wall motion from the MR and the functional information from PET, a better understanding of the underlying mechanisms as well as an improved prediction of myocardial recovery could arise. Figure 9.1 shows an example of multimodality imaging with PET/MRI of a patient after acute MI.

In addition to the conventional approach of viability imaging, recently, interesting insights were gained into the inflammatory process after acute MI. The compromised ischemic myocardium undergoes a complex healing process, which includes inflammation, neoangiogenesis, fibroblast proliferation, and collagen deposition. Studies indicate that an excessive inflammatory response could increase myocardial remodeling after acute MI and thus directly affect the prognosis [28]. This inflammatory response is primarily maintained by different subpopulations of monocytes. In a recent study in mice, it has been shown that the (sequentially measured) PET and MR scans can be used to describe and monitor this inflammatory response [29]. It was shown that FDG is taken up mainly by monocytes in the acutely infarcted myocardium. However, to reliably determine this particular FDG uptake, it is necessary to suppress its uptake in the healthy (remote) myocardium. This can be achieved by a special low-carbohydrate diet (so-called Atkins diet) in combination with "glucose fasting." [30] PET/MRI could play an important role in elucidating the underlying pathophysiology of the inflammatory response after acute MI in humans as well as in facilitating such a complex protocol as the FDG signal can be only moderate and an improved morphological co-localization is crucial. In addition, patient compliance is improved if only one examination is performed shortly after myocardial infarction.

The same fasted protocol is applicable in hybrid PET/MR imaging for myocardial tissue characterization. These applications target pathological entities such as sarcoidosis or Takotsubo cardiomyopathy. Those applications are clearly not for everyday clinical use, but they can point into a direction where a complex imaging system such as the PET/MRI could show its potential.

Cardiac sarcoidosis represents an inflammatory cardiomyopathy where, in the case of car-

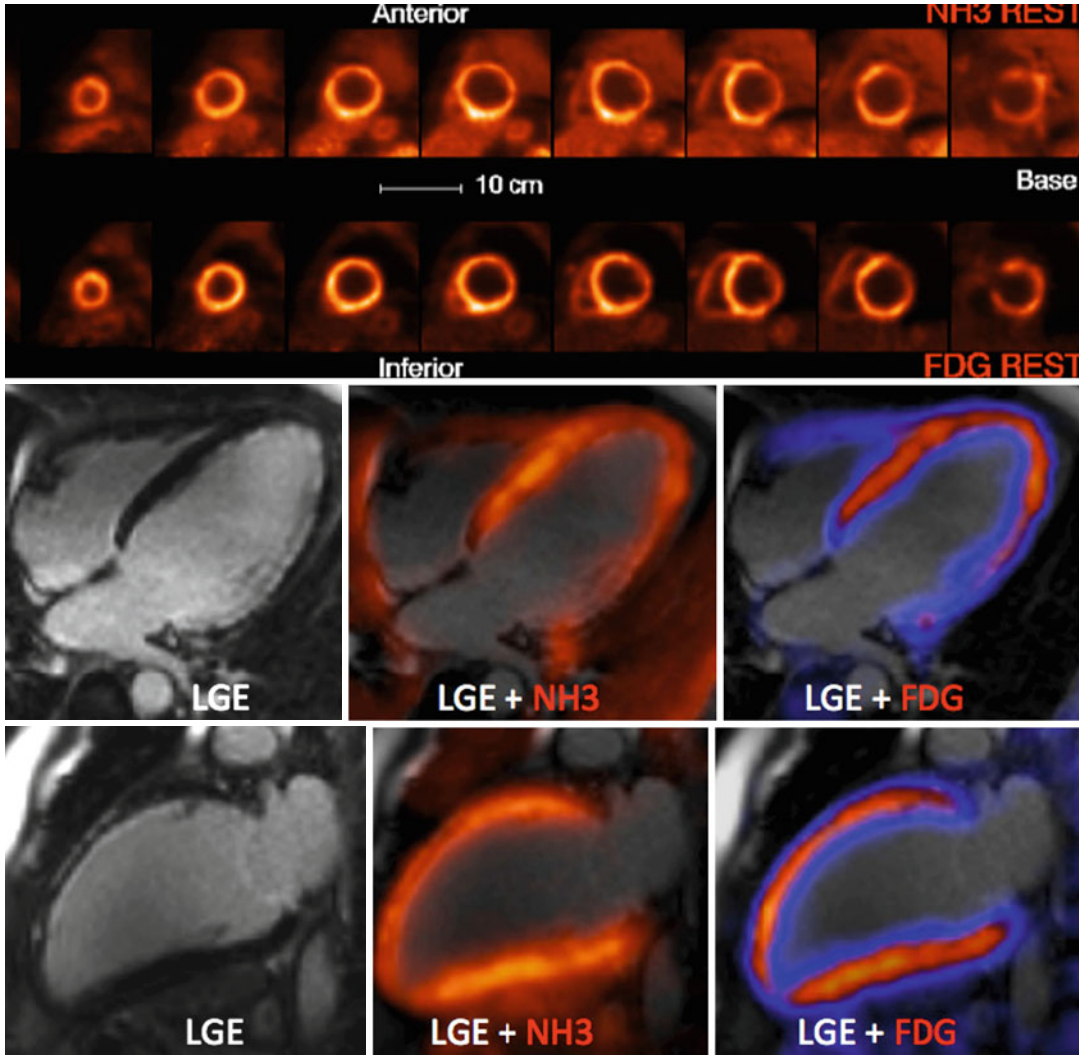

Fig. 9.1 Short-axis images of myocardial perfusion and glucose metabolism (*top*). Both reduced 13N-ammonia and 18F-FDG uptake are clearly depicted in the basal areas of the anterior, anterolateral, and lateral wall. Four-chamber and two-chamber views show large areas of transmural LGE in the anterior and lateral wall (*middle* and *bottom rows*). While clearly reduced perfusion and glucose metabolism is observed in the basal lateral wall, the majority of the anterior wall still shows significant amount of 18F-FDG and 13N-ammonia uptake

diac involvement, the myocardium is replaced by fibrotic, fibrogranulomatous tissue. MR using LGE can image those fibrotic changes of the heart [31]. In sarcoidosis, LGE is patchy and appears primarily in subepicardial regions but only rarely in the subendocardium. In PET, different patterns of glucose metabolism under fasting conditions and myocardial perfusion are known [32] (Fig. 9.2). Vivid glucose metabolism and normal perfusion indicate active inflammation, whereas reduced perfusion and high glucose metabolism represent an advanced stage of the disease. Absent or reduced perfusion and lack of glucose uptake indicate end-stage disease. Thus, hybrid PET/MR not only allows the quantification of the amount of affected myocardium but also helps to assess the disease stage and might be suited to guide therapy.

Takotsubo cardiomyopathy is an increasingly recognized syndrome with symptoms

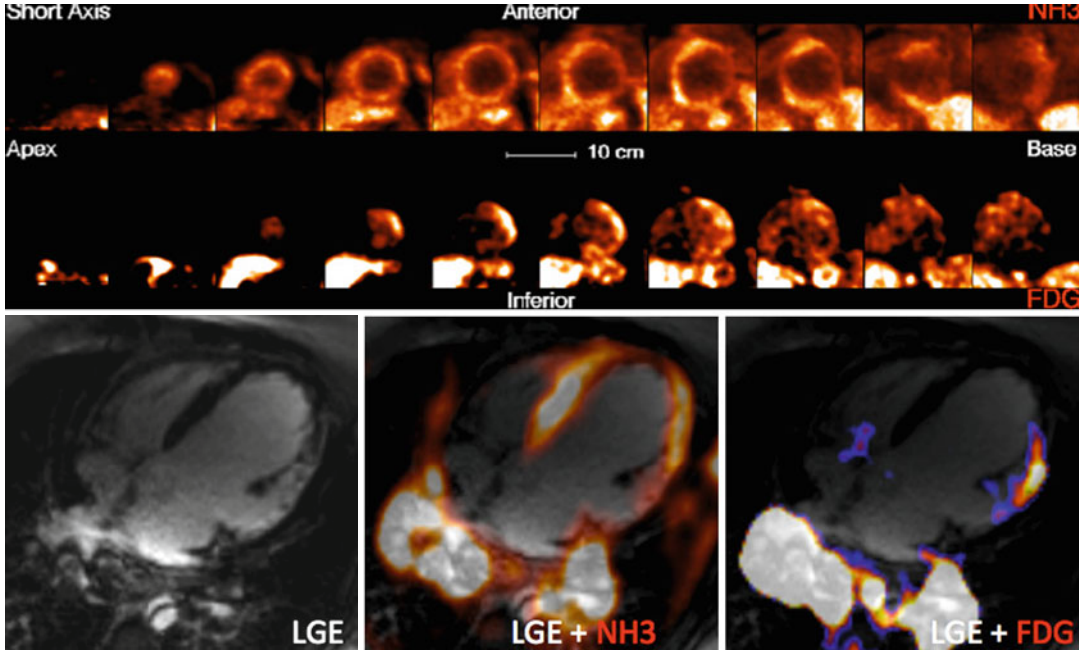

Fig. 9.2 Illustration of short-axis images of myocardial perfusion (*top row*) and inflammation (*bottom row*). Both reduced 13N-ammonia and upregulated 18F-FDG uptake are clearly depicted in the anterolateral and lateral wall as a sign of active cardiac sarcoidosis in these regions (*top*). Four-chamber view shows an area of transmural LGE in the lateral wall (*left*). Here, clearly reduced perfusion (*middle*) and upregulated glucose metabolism (*right*) are observed as a sign of active inflammation. Note increased 18F-FDG uptake in bilateral hilar lymph nodes (*bottom*)

similar to acute MI, including chest pain and electrocardiographic ST segment elevation, but in the absence of relevant stenosis. It occurs in the majority of cases in postmenopausal women of an advanced age and is characterized by transient left ventricular apical wall motion abnormalities associated with emotional or physical stress. Its pathophysiology is not well understood and the available literature focuses primarily on case studies – however, hybrid imaging offers attractive opportunities [33, 34] and PET/MRI using the fasted FDG protocol as described above shows promising results (Fig. 9.3).

9.6 Myocardial Ischemia

The most widespread application in nuclear cardiology is the detection (or exclusion) of a hemodynamically significant coronary artery disease (CAD). Although the majority of patients are examined with SPECT, PET offers certain advantages. It shows a sensitivity and specificity of about 90 % for this indication [35, 36] and has proven suitable to make quantitative statements for the prognostic assessment of patients and guidance for treatment [37, 38]. MRI researchers introduced "first-pass" MRI almost two decades ago where significant coronary stenoses are detected visually after the injection of a fast bolus of a contrast agent such as gadolinium-DTPA using the different wash-in rates at rest and during exercise. The sensitivity and specificity of this method vary substantially in the literature but can reach values of about 91 and 81 % [39–41]. Most SPECT and PET studies are also analyzed in a visual manner; however, PET's major advantage is the possibility to quantify myocardial blood flow in absolute terms. This allows the determination of blood flow at rest and during exercise and consequently the calculation of the myocardial flow reserve. This is particularly of interest in patients with 3-vessel disease or myocardial dysfunction, since a reduced perfusion under stress might be missed if only a visual or semiquantitative assessment is utilized due to the phenomenon of

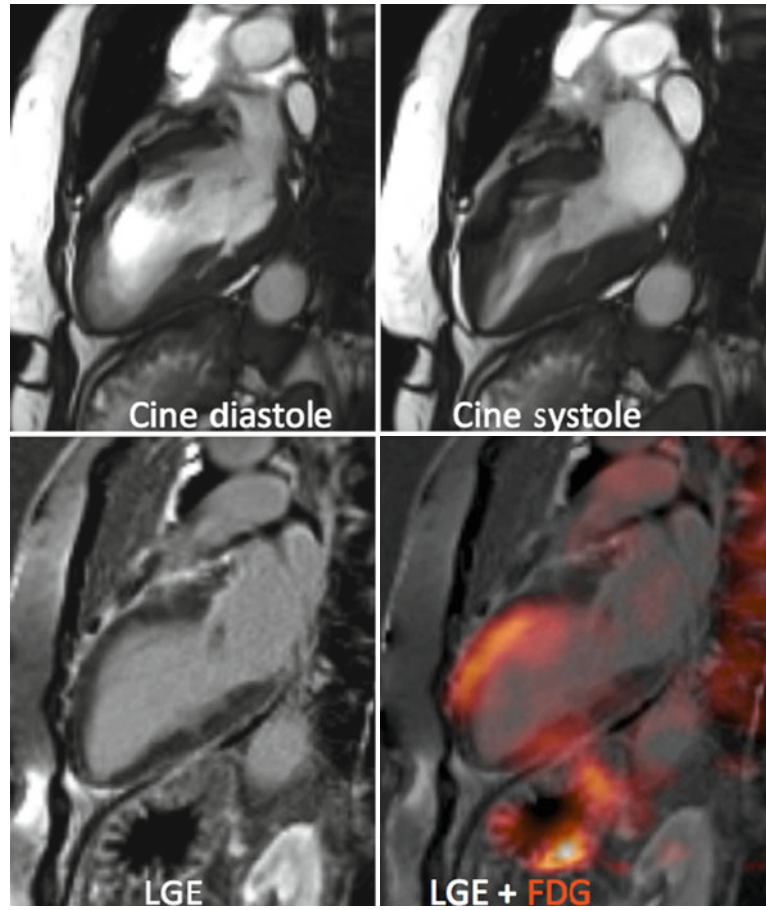

Fig. 9.3 Two-chamber views during diastole (*top left*) and systole (*top right*) show midventricular hypokinesia with marked ballooning during systole. Left ventricular ejection fraction was reduced (46 %). LGE shows no enhancement of the myocardium (*bottom left*). 18F-FDG PET demonstrates an upregulated glucose metabolism in the hypokinetic midventricular segments while glucose consumption is suppressed in remote myocardium (*bottom right*)

"balanced ischemia." [42] While the absolute quantification of blood flow is increasingly used in many hospitals (especially in the United States) with PET due to the availability of FDA-approved software, dynamic perfusion MR is still in clinical trials and exclusively for research purposes. Consequentially, the body of literature is rather sparse although a good correlation with 13N- ammonia PET was shown [41, 43].

Indeed, both methods have limitations which could point to a mutual benefit, if combined: MRI's weak part is the reliable definition of the arterial input function (as a prerequisite for absolute flow delineation), the relatively low "volume of distribution" for gadolinium-DTPA, the very rapid diffusion of gadolinium-DTPA into the extracellular space, and the limited spatial coverage of the left ventricle during acquisition (usually 3–5 slices and not the entire ventricle). The biggest disadvantage of PET is that no morphological information is obtained, but only data about the perfused myocardium. Therefore, PET cannot distinguish whether a reduced blood flow is a result due to an epicardial stenosis or a microvascular dysfunction (e.g., diabetes). Furthermore, PET cannot clearly determine whether such a perfusion defect is caused by thin scar tissue, which often poses a problem in dilated cardiomyopathy [44].

Thus, parallel PET/MR imaging allows for the first time a direct comparison of the delineation of myocardial blood flow using PET and MR under identical physiological (resting or stress) conditions. In addition to validation studies, this permits the combination of MRI-derived information such as morphology (e.g., coronary anatomy (MR angiography)), wall thickness, or scar (LGE) with the functional PET data so that an improved tissue characterization becomes possible.

9.7 Considerations for the Clinical Workflow

It is important to remember that hybrid scanners always require close collaboration between nuclear medicine physicians, radiologists, cardiologists, and technical personnel. This holds especially true for MR imaging, as the methodological complexity (different contrasts, image geometry, artifacts, etc.) and the patient-specific adjustments are higher and more time consuming than those found in stand-alone PET and/or CT systems.

But also technical workflow aspects need to be addressed: any reading of hybrid data requires PET and MR images to be superimposed as accurately as possible. In thoracic imaging in general and in cardiac imaging in particular, this represents a challenge as was learned already from cardiac PET/CT. Both cardiac motion due to contraction of the heart as well as thorax movement due to respiration have to be taken into account [7]. As mentioned before, any misalignment between emission and "transmission" negatively affects the accuracy of attenuation correction: but in contrast to PET/CT, MRI does not require ionizing radiation and thus the attenuation map can be generated as often as needed. In general, we found a good agreement between the PET data, which is acquired over many respiratory cycles, and the MR attenuation map, which is acquired in 18 s at end-expiration. It is relevant to keep in mind that alignment issues are present both for fully integrated as well as for integrated PET/MR systems. Even in the latter design, PET and MR data will be acquired often not simultaneously but rather in parallel. MR imaging is usually done sequentially, i.e., the image data represents a volume usually acquired sequentially slice by slice with slice acquisition times ranging from about 50 m s for perfusion scans up to several seconds for high-resolution images. This differs in PET where truly volumetric acquisitions with typical frame times – depending on the protocol – from 5 s to 20 min are acquired. Basically, this translates into the fact that fully simultaneous acquisitions using PET/MR are not trivial and thus continue to pose a major problem with respect to patient movement. However, integrated PET/MR scanners could offer real-time motion correction and partial volume correction in the future.

A major advantage of parallel imaging, however, is the patient management, because sequential imaging of PET and MR is not only uncomfortable for the patient but also for the operating personnel. Consequently, cardiac PET/MR imaging could lead to both increased patient compliance as well as to better device utilization, and thus better cost-effectiveness.

9.8 Clinical Cases

9.8.1 Acute Infarction

Clinical History: A 31-year-old male patient presented to his general practitioner (GP) because of chest pain. While talking to the GP, the patient suddenly collapsed. The GP immediately started cardiopulmonary resuscitation and called the ambulance which transported the patient to our emergency department where myocardial infarction was suspected. Cardiac catheterization confirmed left main occlusion, and subsequently PCI was performed. 13 days later the patient underwent PET/MR viability imaging (Fig. 9.1).

Findings: MR images indicate mostly transmural myocardial infarction of the anterior, lateral, and anteroseptal wall. LV ejection fraction was significantly reduced. PET images show both reduced glucose metabolism and perfusion in the basal regions indicating transmural myocardial infarction. However, PET confirms still a large amount of viable myocardium.

Advantages of PET/MR: The integrated information of PET and MR may allow more accurate prediction of the left ventricular remodeling and outcome after acute myocardial infarction.

9.8.2 Cardiac Sarcoidosis

Clinical History: A 30-year-old male patient was referred to our institution because of suspected cardiac involvement of a newly diagnosed

sarcoidosis. Coronary angiography excluded coronary artery disease and showed a severely reduced left ventricular function. A CT of the chest demonstrated bihilar lymphadenopathy. Subsequently, the patient was transferred to our institution to confirm cardiac involvement of the sarcoidosis by PET/MR (Fig. 9.2).

Findings: Bihilar lymphadenopathy with increased FDG uptake in the lymph nodes confirms the diagnosis of sarcoidosis. Areas in the left ventricle with increased FDG uptake and reduced perfusion indicate active inflammation and reveal cardiac involvement of the sarcoidosis. Also, a severely reduced left ventricular ejection fraction with severe hypokinesia of the lateral wall demonstrates dilated cardiomyopathy (DCM) as a consequence of cardiac sarcoidosis. Furthermore, areas demonstrating late gadolinium enhancement (LGE) indicate myocardial infiltration and scarring.

Advantages of PET/MR: The integrated information of PET and MR may thus not only allow assessing the amount of affected myocardium by LGE but also exact assessment of the stage and inflammatory state of the disease, and consequently therapy monitoring is feasible.

9.8.3 Takotsubo Cardiomyopathy

Clinical History: A 70-year-old woman presented with acute chest pain to our institution. She reported of progressive dyspnea while experiencing personal stress during this time. Angiographically inconspicuous epicardial coronary arteries were found during cardiac catheterization. The ventriculography, however, showed midventricular dilatation and a hypercontractile apex and base. Because of these findings a variant of Takotsubo cardiomyopathy (TTC) was suspected and the patient was referred for PET/MR (Fig. 9.3).

Findings: Left midventricular hypokinesia was found on cine MR images; however, no late gadolinium enhancement (LGE) could be depicted in the entire left ventricular myocardium. FDG PET showed a markedly increased glucose metabolism in the dysfunctional midventricular myocardium while FDG uptake was suppressed in the remote area.

Advantages of PET/MR: Takotsubo cardiomyopathy is a rare but increasingly recognized, reversible disease of which the underlying pathophysiology is unclear. However, stress-induced catecholamine excess to the myocardium seems to play an important role in pathophysiology. PET/MR allows the integrated imaging of hypokinetic areas of the myocardium, which demonstrate a metabolic shift from fatty acid to glucose consumption in the fasted state while no myocardial enhancement (LGE) after MR contrast application is seen.

9.8.4 Outlook: Advanced Molecular Imaging and Neoangiogenesis

In addition to those more clinically motivated imaging approaches, previous work with sequential PET and MR imaging identified potential applications. Although those come mostly from preclinical work, their translation would be greatly facilitated by the use of a hybrid imaging system.

9.8.4.1 Stem Cell Therapy

After an acute MI many of the affected cardiomyocytes die and the ischemically compromised myocardium loses its function and thus contractility – which may eventually lead to heart failure. A promising therapeutic approach is the use of stem cells. Here, the transplanted cells (e.g., embryonic stem cells or bone marrow stem cells) will replace the lost cardiomyocytes and thus contribute to the regeneration of the myocardium. A frequently observed problem is that only a fraction of the transplanted cells remains actually in the myocardium [45]. PET/MR could assist for a better understanding of "stem cell engraftment" and the underlying cellular and molecular processes. Our group demonstrated earlier the advantage of a (sequential) hybrid imaging approach [46]. In this rodent study, human endothelial precursor cells were labeled with iron particles. In addition, the cells were

modified using a viral vector in such a way that they expressed the human sodium iodide symporter (NIS) and then were transplanted into immunodeficient rats. The MR was well suited to represent the left ventricular morphology and to identify the location of transplanted cells. The vitality of the cells was shown by PET, which delineated uptake of radionuclide 124I only in living cells. Basically, the iron particles were taken up by macrophages after the death of the transplanted cells and thus were still visible on the MR. The PET signal (I-124), however, was only visible if the transplanted cells were still vital, which involves a sustained expression of the NIS.

9.8.4.2 Imaging of Neoangiogenesis

This seems to play a key role after myocardial infarction and accordingly is an attractive target for molecular imaging. Integrins are of importance in cell migration, the regulation of cell proliferation, cell survival, as well as in cell differentiation. 18F-labeled galacto-RGD was initially developed for oncological PET imaging [47] but was investigated also for imaging of $\alpha v\beta 3$ integrin expression after acute MI, both in animals and humans [48, 49]. In these studies the co-visualization of this "hot spot" PET imaging using MRI for anatomical localization and functional correlation was helpful. Furthermore, a recent study revealed that significant F-18 galacto-RGD uptake was a predictor for the absence of left ventricular remodeling after MI in rats [50]. Thus, whole-body PET/MR has the potential to facilitate further research, especially since it allows the delineation of scar extent, left ventricular function, and the integrin expression within a single examination.

Conclusion

Both PET and MRI as stand-alone modalities are accepted imaging methods for the assessment of myocardial perfusion and vitality. Hybrid PET/MR combines these two methods in one system, but it remains to be seen whether this integration provides synergistic, diagnostic value. Currently, PET/MR is mostly used for research purposes, where it provides an excellent tool for cross-validation of new imaging methods under identical experimental conditions. However, it seems not unlikely that PET/MR could become an indispensable method for the development of radiopharmaceuticals and contrast agents. However, it requires complex workflows and excellent interdisciplinary cooperation. The latter factor in addition to the proof of cost-effectiveness will determine a wider distribution.

References

1. Von Schulthess GK, Hany TF. Imaging and pet-pet/ct imaging. J Radiol. 2008;89:438–47; quiz 448.
2. Knuuti J, Saraste A. Combined functional and anatomical imaging for the detection and guiding the therapy of coronary artery disease. Eur Heart J. 2013;34:1954–7.
3. Nekolla SG, Martinez-Moeller A, Saraste A. Pet and mri in cardiac imaging: from validation studies to integrated applications. Eur J Nucl Med Mol Imaging. 2009;36 Suppl 1:S121–30.
4. Rischpler C, Nekolla SG, Dregely I, Schwaiger M. Hybrid pet/mr imaging of the heart: potential, initial experiences, and future prospects. J Nucl Med. 2013; 54:402–15.
5. Zaidi H, Ojha N, Morich M, Griesmer J, Hu Z, Maniawski P, Ratib O, Izquierdo-Garcia D, Fayad ZA, Shao L. Design and performance evaluation of a whole-body ingenuity tf pet-mri system. Phys Med Biol. 2011;56:3091–106.
6. Schlemmer HP, Pichler BJ, Schmand M, Burbar Z, Michel C, Ladebeck R, Jattke K, Townsend D, Nahmias C, Jacob PK, Heiss WD, Claussen CD. Simultaneous mr/pet imaging of the human brain: feasibility study. Radiology. 2008;248:1028–35.
7. Martinez-Moller A, Souvatzoglou M, Navab N, Schwaiger M, Nekolla SG. Artifacts from misaligned ct in cardiac perfusion pet/ct studies: frequency, effects, and potential solutions. J Nucl Med. 2007;48: 188–93.
8. Gould KL, Pan T, Loghin C, Johnson NP, Guha A, Sdringola S. Frequent diagnostic errors in cardiac pet/ct due to misregistration of ct attenuation and emission pet images: a definitive analysis of causes, consequences, and corrections. J Nucl Med. 2007;48: 1112–21.
9. Martinez-Moller A, Souvatzoglou M, Delso G, Bundschuh RA, Chefd'hotel C, Ziegler SI, Navab N, Schwaiger M, Nekolla SG. Tissue classification as a potential approach for attenuation correction in whole-body pet/mri: evaluation with pet/ct data. J Nucl Med. 2009;50:520–6.

10. Coombs BD, Szumowski J, Coshow W. Two-point dixon technique for water-fat signal decomposition with b0 inhomogeneity correction. Magn Reson Med. 1997;38:884–9.
11. Drzezga A, Souvatzoglou M, Eiber M, Beer AJ, Furst S, Martinez-Moller A, Nekolla SG, Ziegler S, Ganter C, Rummeny EJ, Schwaiger M. First clinical experience with integrated whole-body pet/mr: comparison to pet/ct in patients with oncologic diagnoses. J Nucl Med. 2012;53:845–55.
12. Souvatzoglou M, Eiber M, Takei T, Furst S, Maurer T, Gaertner F, Geinitz H, Drzezga A, Ziegler S, Nekolla SG, Rummeny EJ, Schwaiger M, Beer AJ. Comparison of integrated whole-body [c]choline pet/mr with pet/ct in patients with prostate cancer. Eur J Nucl Med Mol Imaging. 2013;40(10):1486-99.
13. Schulz V, Torres-Espallardo I, Renisch S, Hu Z, Ojha N, Bornert P, Perkuhn M, Niendorf T, Schafer WM, Brockmann H, Krohn T, Buhl A, Gunther RW, Mottaghy FM, Krombach GA. Automatic, three-segment, mr-based attenuation correction for whole-body pet/mr data. Eur J Nucl Med Mol Imaging. 2011;38:138–52.
14. Delso G, Martinez-Moller A, Bundschuh RA, Nekolla SG, Ziegler SI. The effect of limited mr field of view in mr/pet attenuation correction. Med Phys. 2010;37:2804–12.
15. Blumhagen JO, Ladebeck R, Fenchel M, Scheffler K. Mr-based field-of-view extension in mr/pet: B(0) homogenization using gradient enhancement (huge). Magn Reson Med. 2012. doi:10.1002/mrm.24555.
16. Nuyts J, Bal G, Kehren F, Fenchel M, Michel C, Watson C. Completion of a truncated attenuation image from the attenuated pet emission data. IEEE Trans Med Imaging. 2013;32:237–46.
17. Lau JM, Sharma S, Laforest R, McConathy J, Barnwell J, Priatna A, Becker LM, Foster GJ, Gropler RJ, Woodard PK. Feasibility of mri attenuation correction in cardiac fdg-pet. J Cardiovasc Magn Reson. 2013;15 Suppl 1:O61.
18. Nensa F, Poeppel TD, Beiderwellen K, Schelhorn J, Mahabadi AA, Erbel R, Heusch P, Nassenstein K, Bockisch A, Forsting M, Schlosser T. Hybrid pet/mr imaging of the heart: feasibility and initial results. Radiology. 2013;268(2):366–73.
19. Knuuti MJ, Nuutila P, Ruotsalainen U, Saraste M, Harkonen R, Ahonen A, Teras M, Haaparanta M, Wegelius U, Haapanen A, et al. Euglycemic hyperinsulinemic clamp and oral glucose load in stimulating myocardial glucose utilization during positron emission tomography. J Nucl Med. 1992;33:1255–62.
20. Beanlands RSB, Hendry PJ, Masters RG, de Kemp RA, Woodend K, Ruddy TD. Delay in revascularization is associated with increased mortality rate in patients with severe left ventricular dysfunction and viable myocardium on fluorine 18-fuorodeoxyglucose positron emission tomography imaging. Circulation. 1998;98:Ii51–6.
21. Klein C, Nekolla SG, Balbach T, Schnackenburg B, Nagel E, Fleck E, Schwaiger M. The influence of myocardial blood flow and volume of distribution on late gd-dtpa kinetics in ischemic heart failure. J Magn Reson Imaging. 2004;20:588–93.
22. Klein C, Nekolla SG, Bengel FM, Momose M, Sammer A, Haas F, Schnackenburg B, Delius W, Mudra H, Wolfram D, Schwaiger M. Assessment of myocardial viability with contrast-enhanced magnetic resonance imaging: comparison with positron emission tomography. Circulation. 2002;105:162–7.
23. Klein C, Schmal TR, Nekolla SG, Schnackenburg B, Fleck E, Nagel E. Mechanism of late gadolinium enhancement in patients with acute myocardial infarction. J Cardiovasc Magn Reson. 2007;9:653–8.
24. Kwong RY, Chan AK, Brown KA, Chan CW, Reynolds HG, Tsang S, Davis RB. Impact of unrecognized myocardial scar detected by cardiac magnetic resonance imaging on event-free survival in patients presenting with signs or symptoms of coronary artery disease. Circulation. 2006;113:2733–43.
25. Schinkel AFL, Poldermans D, Elhendy A, Bax JJ. Assessment of myocardial viability in patients with heart failure. J Nucl Med. 2007;48:1135–46.
26. Ibrahim T, Hackl T, Nekolla SG, Breuer M, Feldmair M, Schomig A, Schwaiger M. Acute myocardial infarction: serial cardiac mr imaging shows a decrease in delayed enhancement of the myocardium during the 1st week after reperfusion. Radiology. 2010;254:88–97.
27. Wu YW, Tadamura E, Yamamuro M, Kanao S, Marui A, Tanabara K, Komeda M, Togashi K. Comparison of contrast-enhanced mri with (18)f-fdg pet/201tl spect in dysfunctional myocardium: relation to early functional outcome after surgical revascularization in chronic ischemic heart disease. J Nucl Med. 2007;48:1096–103.
28. van der Laan AM, Nahrendorf M, Piek JJ. Healing and adverse remodelling after acute myocardial infarction: Role of the cellular immune response. Heart. 2012;98:1384–90.
29. Lee WW, Marinelli B, van der Laan AM, Sena BF, Gorbatov R, Leuschner F, Dutta P, Iwamoto Y, Ueno T, Begieneman MPV, Niessen HWM, Piek JJ, Vinegoni C, Pittet MJ, Swirski FK, Tawakol A, Di Carli M, Weissleder R, Nahrendorf M. Pet/mri of inflammation in myocardial infarction. J Am Coll Cardiol. 2012;59:153–63.
30. Williams G, Kolodny GM. Suppression of myocardial 18f-fdg uptake by preparing patients with a high-fat, low-carbohydrate diet. AJR Am J Roentgenol. 2008;190:W151–6.
31. Watanabe E, Kimura F, Nakajima T, Hiroe M, Kasai Y, Nagata M, Kawana M, Hagiwara N. Late gadolinium enhancement in cardiac sarcoidosis: characteristic magnetic resonance findings and relationship with left ventricular function. J Thorac Imaging. 2013;28:60–6.
32. Mc Ardle BA, Leung E, Ohira H, Cocker MS, de Kemp RA, DaSilva J, Birnie D, Beanlands RS, Nery PB. The role of f(18)-fluorodeoxyglucose positron emission tomography in guiding diagnosis

and management in patients with known or suspected cardiac sarcoidosis. J Nucl Cardiol. 2013;20: 297–306.
33. Kurisu S, Kihara Y. Tako-tsubo cardiomyopathy: clinical presentation and underlying mechanism. J Cardiol. 2012;60:429–37.
34. Hasbak P, Kjaer A, Skovgaard D, Bang LE, Grande P, Holmvang L. Preserved myocardial blood flow in the apical region involved in takotsubo cardiomyopathy by quantitative cardiac pet assessment. J Nucl Cardiol. 2012;19:169–71.
35. Klocke FJ, Baird MG, Lorell BH, Bateman TM, Messer JV, Berman DS, O'Gara PT, Carabello BA, Russell RO, Cerqueira MD, Sutton MGS, DeMaria AN, Udelson JE, Kennedy JW, Verani MS, Williams KA, Antman EM, Smith SC, Alpert JS, Gregoratos G, Anderson JL, Hiratzka LF, Faxon DP, Hunt SA, Fuster V, Jacobs AK, Gibbons RJ, Russell RO, Heart ACCA. Acc/aha/asnc uidelines for the clinical use of cardiac radionuclide imaging - executive summary - a report of the american college of cardiology/american heart association task force on practice guidelines (acc/aha/asnc committee to revise the 1995 guidelines for the clinical use of cardiac radionuclide imaging). J Am Coll Cardiol. 2003;42: 1318–33.
36. Parker MW, Iskandar A, Limone B, Perugini A, Kim H, Jones C, Calamari B, Coleman CI, Heller GV. Diagnostic accuracy of cardiac positron emission tomography versus single photon emission computed tomography for coronary artery disease a bivariate meta-analysis. Circ Cardiovasc Imaging. 2012;5:700–7.
37. Yoshinaga K, Chow BJW, Williams K, Chen L, Dekemp RA, Garrard L, Szeto ALT, Aung M, Davies RA, Ruddy TD, Beanlands RSB. What is the prognostic value of myocardial perfusion imaging using rubidium-82 positron emission tomography? J Am Coll Cardiol. 2006;48:1029–39.
38. Merhige ME, Breen WJ, Shelton V, Houston T, D'Arcy BJ, Perna AF. Impact of myocardial perfusion imaging with pet and rb-82 on downstream invasive procedure utilization, costs, and outcomes in coronary disease management. J Nucl Med. 2007;48:1069–76.
39. Manning WJ, Atkinson DJ, Grossman W, Paulin S, Edelman RR. First-pass nuclear magnetic resonance imaging studies using gadolinium-dtpa in patients with coronary artery disease. J Am Coll Cardiol. 1991;18:959–65.
40. Nandalur KR, Dwamena BA, Choudhri AF, Nandalur MR, Carlos RC. Diagnostic performance of stress cardiac magnetic resonance imaging in the detection of coronary artery disease: a meta-analysis. J Am Coll Cardiol. 2007;50:1343–53.
41. Morton G, Chiribiri A, Ishida M, Hussain ST, Schuster A, Indermuehle A, Perera D, Knuuti J, Baker S, Hedstrom E, Schleyer P, O'Doherty M, Barrington S, Nagel E. Quantification of absolute myocardial perfusion in patients with coronary artery disease: comparison between cardiovascular magnetic resonance and positron emission tomography. J Am Coll Cardiol. 2012;60:1546–55.
42. Bengel FM. Leaving relativity behind: quantitative clinical perfusion imaging. J Am Coll Cardiol. 2011;58:749–51.
43. Schwitter J, Nanz D, Kneifel S, Bertschinger K, Buchi M, Knusel PR, Marincek B, Luscher TF, von Schulthess GK. Assessment of myocardial perfusion in coronary artery disease by magnetic resonance: a comparison with positron emission tomography and coronary angiography. Circulation. 2001;103:2230–5.
44. O'Neill JO, McCarthy PM, Brunken RC, Buda T, Hoercher K, Young JB, Starling RC. Pet abnormalities in patients with nonischemic cardiomyopathy. J Card Fail. 2004;10:244–9.
45. Terrovitis J, Lautamaki R, Bonios M, Fox J, Engles JM, Yu JH, Leppo MK, Pomper MG, Wahl RL, Seidel J, Tsui BM, Bengel FM, Abraham MR, Marban E. Noninvasive quantification and optimization of acute cell retention by in vivo positron emission tomography after intramyocardial cardiac-derived stem cell delivery. J Am Coll Cardiol. 2009; 54:1619–26.
46. Higuchi T, Anton M, Dumler K, Seidl S, Pelisek J, Saraste A, Welling A, Hofmann F, Oostendorp RAJ, Gansbacher B, Nekolla SG, Bengel FM, Botnar RM, Schwaiger M. Combined reporter gene pet and iron oxide mri for monitoring survival and localization of transplanted cells in the rat heart. J Nucl Med. 2009;50:1088–94.
47. Beer AJ, Schwaiger M. Imaging of integrin alphav-beta3 expression. Cancer Metastasis Rev. 2008;27: 631–44.
48. Higuchi T, Bengel FM, Seidl S, Watzlowik P, Kessler H, Hegenloh R, Reder S, Nekolla SG, Wester HJ, Schwaiger M. Assessment of alpha(v) beta(3) integrin expression after myocardial infarction by positron emission tomography. Cardiovasc Res. 2008;78:395–403.
49. Makowski MR, Ebersberger U, Nekolla S, Schwaiger M. In vivo molecular imaging of angiogenesis, targeting alpha(v)beta(3) integrin expression, in a patient after acute myocardial infarction. Eur Heart J. 2008;29:2201.
50. Sherif HM, Saraste A, Nekolla SG, Weidl E, Reder S, Tapfer A, Rudelius M, Higuchi T, Botnar RM, Wester HJ, Schwaiger M. Molecular imaging of early alpha(v)beta(3) integrin expression predicts long-term left-ventricle remodeling after myocardial infarction in rats. J Nucl Med. 2012;53:318–23.

Risks and Safety Aspects of MR-PET

10

Gunnar Brix, Elke Nekolla, and Dietmar Nosske

Contents

Abstract

The introduction of MR-PET systems into medical practice not only may lead to a gain in clinical diagnosis as compared to PET-CT imaging due to the superior soft tissue contrast of the MR technology but can also substantially reduce exposure of patients to ionizing radiation. On the other hand, there are also risks and health effects associated with the use of diagnostic MR devices that have to be considered carefully. In this chapter, the biophysical and biological aspects relevant for the assessment of health effects related to the use of ionizing radiation in PET and (electro)magnetic fields in MR are summarized. On this basis, the current safety standards will be presented – which, however, do not address the possibility of synergistic effects of ionizing radiation and (electro)magnetic fields. In the light of the developing MR-PET technology, it is of utmost importance to investigate this aspect in more detail for exposure levels that will occur at MR-PET systems. Finally, some considerations concerning the justification and optimization of MR-PET examination will be made.

10.1 Introduction

Clinical adoption of combined PET-CT imaging has been surprisingly rapid, and, despite continuing debate, this technology has advanced the use of metabolic and molecular imaging [49],

G. Brix (✉) • E. Nekolla • D. Nosske
Department of Medical and Occupational Radiation Protection, Federal Office for Radiation Protection, Oberschleissheim, Germany
e-mail: gbrix@bfs.de

I. Carrio, P. Ros (eds.), *PET/MRI*,
DOI 10.1007/978-3-642-40692-8_10,

particularly for oncology [11, 39, 40, 43]. However, when discussing the immediate benefits of combined PET-CT examinations, the issue of patient exposure must be taken into account as well. As shown in a multicenter study, whole-body PET-CT examinations – comprising a PET scan after the administration of the glucose analogue 2-[^{18}F] fluoro-2-deoxy-D-glucose (FDG) and a fully diagnostic contrast-enhanced CT scan – result in an effective dose to patients in the order of 25 mSv and thus mandate a thorough medical justification for each individual patient [5, 8]. A detailed analysis of protocols, which are representative for the imaging scenarios reported in the literature, revealed that up to 70 % of the total exposure is contributed by CT [8]. It would thus be very welcome from a radiation protection point of view if PET-CT could be replaced whenever possible by MR-PET as soon as the methodological challenges of this new imaging technology have been overcome.

As no ionizing radiation is used in MR, it is generally deemed safer than CT or PET in terms of associated health risks. Nevertheless, there are possible risks and health effects associated with the use of diagnostic MR devices that have to be considered carefully [4, 45]. In this context, a fundamental difference between ionizing and nonionizing radiation has to be noted: Radiation doses related to CT or PET procedures may result in stochastic effects (occurring many years later), whereas biological effects of (electro)magnetic fields used in MR are of deterministic nature (occurring immediately). A stochastic process is one where the exposure determines the probability of the occurrence of an event but not the severity of the effect. In contrast, the severity of a deterministic effect is related to the level of exposure and a threshold may be defined [21]. As a consequence, the probability of detrimental effects caused by PET or CT examinations performed over many years accumulate, whereas biophysical and biological effects induced by (electro)magnetic fields used for MR examinations (such as cardiovascular reactions or peripheral nerve stimulation) are related to the acute exposure levels of a particular examination and does, to our present knowledge, not accumulate over years.

Following the presentation in Brix et al. [9], this chapter presents (a) an overview on biophysical and biological aspects relevant for the assessment of detrimental health effects related to the exposure of patients to ionizing radiation in PET and to (electro)magnetic fields in MR as well as (b) some preliminary considerations on the justification and optimization of MR-PET procedures. A comprehensive discussion of aspects which are beyond the scope of this chapter – as, for example, layout and shielding of a PET facility or protection of the staff – can be found in a safety report issued by the "International Atomic Energy Agency" [19] and guidelines of the "International Commission on Non-Ionizing Radiation Protection" [20, 24, 26].

10.2 PET: Ionizing Radiation

10.2.1 Detrimental Health Effects Induced by Ionizing Radiation

Low-level exposure of patients undergoing a PET or CT examination may lead to stochastic radiation effects, the most significant being induction of cancer. Cancers caused by ionizing radiation occur several years to decades after the exposure has taken place (latency time). They do not differ in their clinical appearance from cancers that are caused by other factors. A radiation-induced cancer cannot be recognized as such, and it is only by means of epidemiological studies that increases in the spontaneous cancer incidence rates of irradiated groups can be detected. Ionizing radiation is the carcinogen that has been studied most intensely.

Increased cancer rates have been demonstrated in humans through various radio-epidemiological studies at moderate or high doses, i.e., organ or whole-body doses exceeding 50–100 mSv, delivered acutely or over a prolonged period. The so-called Life Span Study (LSS) of the survivors of the atomic bombings in Hiroshima and Nagasaki is the most important of these studies [41]. The follow-up of the atomic bomb survivors has provided detailed knowledge of the relationships between radiation risk and a variety of factors, such as the absorbed dose, the age at exposure, the

age at diagnosis, and other parameters. The LSS provides data with good radio-epidemiological evidence due to the large size of the study population (about 86,600 individuals with individual dose estimates), the broad age and dose distribution, the long follow-up period (about half a century), and an internal control group (individuals exposed only at a minute level or not at all). The LSS is, therefore, the major source for predicting radiation-induced risks for the general population. However, radiation risk estimates are not merely based on the follow-up of the atomic bomb survivors. They are also largely supported by a multitude of smaller studies, mostly on groups of persons exposed for medical reasons, both in diagnostics and in therapy [1].

There is considerable controversy regarding the risk of low levels of radiation, typical for diagnostic radiation exposures, since radiation risks evaluated at low dose levels are not based on experimental and epidemiological evidence. Given this lack of evidence, estimates on risk, derived from high doses, have been extrapolated down to low dose levels by various scientific bodies, including the "International Commission on Radiological Protection" [30], the "United Nations Scientific Committee on the Effects of Atomic Radiation" [50], and the "Biological Effects on Ionizing Radiation" committee [1]. Estimates on risk per unit of dose have been derived using the so-called linear, non-threshold (LNT) hypothesis, which is based on the assumptions that (a) any radiation dose – no matter how small – may cause an increase in risk and (b) the probability of this increase is proportional to the dose absorbed in the tissue. Although the risk evaluated at low dose levels is thus hypothetical, it is prudent to assume that it exists and that the LNT model represents an upper bound for it. It is for this reason that current radiation protection standards as well as risk assessments are based on the LNT hypothesis [30].

10.2.2 Principles of Radiation Protection

In line with the LNT philosophy, the ICRP emphasizes that proper justification and optimization of medical procedures are indispensable principles of radiation protection in medicine [31]:

There are two different levels of *justification* (§§ 60, 67): At the *generic* level, a specified radiological procedure with a specified objective is defined and justified. The aim is to judge whether the procedure will improve the diagnosis or treatment or will provide necessary information about the exposed individuals. At the next level, the application of the procedure to an *individual patient* should be justified (i.e., the particular application should be judged to do more good than harm to the individual patient). Hence all individual medical exposures should be justified in advance, taking into account all available information including the details of the proposed procedure and of alternative procedures, the characteristics of the individual patient, the expected dose to the patient, and the availability of information on previous or expected examinations or treatment.

Optimization of radiological protection (§ 70) means the same as keeping the doses "as low as reasonably achievable, economic and societal factors being taken into account" (ALARA), and is best described as management of the radiation dose to the patient to be commensurate with the medical purpose (§ 71). Although dose constraints for patients are inappropriate, management of patient dose is important. This often can be facilitated for diagnostic and interventional procedures by use of a diagnostic reference level, which is a method for evaluating whether the patient dose is unusually high or low for a particular medical imaging procedure.

The ethical and procedural aspects related to the *exposure of volunteers in biomedical research* have also been addressed (§ 121). The key aspects include the need to guarantee a free and informed choice by the volunteers, the adoption of dose constraints linked to the societal worth of the studies, and the use of an ethics committee that can influence the design and conduct of the studies. It is important that the ethics committee should have easy access to radiological protection advice.

10.2.3 Dosimetry

10.2.3.1 Fundamental Dose Quantities

It is generally assumed that the probability of detrimental radiation effects is directly proportional to the energy deposited by ionizing radiation in a specified organ or tissue, *T*. Therefore, the fundamental dosimetric quantity is the *absorbed dose*, which is defined as the radiation energy absorbed in a small volume element of matter divided by its mass. In the SI system the absorbed dose, *D*, is given in the unit *Gray* (1 Gy = 1 J/kg). For radiological protection purposes, the absorbed dose is averaged over an organ or tissue and weighted by a dimensionless *radiation weighting factor*, w_R, to reflect the higher biological effectiveness of high-LET as compared to low-LET radiations. The resulting weighted dose is designated as the *organ or equivalent dose*, H_T, and given in the unit *Sievert* (1 Sv = 1 J/kg). For γ-radiation used in PET, w_R is equal to 1.

Tissues and organs are not equally sensitive to the effects of ionizing radiation. Due to this reason, *tissue weighting factors*, w_T, are provided by the ICRP for a reference population of equal numbers of both sexes and a wide range of ages [30]. These factors indicate the relative proportion of each organ or tissue to the total health detriment resulting from a uniform irradiation of the whole body. Detriment is a multidimensional concept: Its principal components are the stochastic quantities probability of the attributable fatal cancer, the weighted probability of attributable nonfatal cancer, the weighted probability of severe heritable effects, and the length of life lost if the harm occurs [30]. If the body is exposed in a nonuniform manner, as, for example, in a patient undergoing a PET examination, the sum of the products of the organ doses and the corresponding tissue weighting factors determined for each of the various organ or tissue exposed has to be computed:

$$E = \sum_T w_T \cdot H_T \text{ with } \sum_T w_T = 1. \quad (10.1)$$

The resulting quantity is denoted as *effective dose E* (in Sv). Based on this dose quantity, it is possible to assess and to compare the probability of stochastic radiation effects resulting from different radiation exposures – as, for example, PET examinations using different radiopharmaceuticals yielding a different pattern of dose distribution in the body. It should be noted, however, that the concept of the effective dose facilitates only an overall, not an organ-specific assessment of stochastic radiation risks and is aimed at large, age and gender averaged collectives such as the working population or the whole population in a country. Nevertheless, this generic approach provides a rational framework for the justification and optimization of imaging procedures.

Based on the latest available scientific information, the tissue weighting factors, w_T, given in Table 10.1 have been modified in 2007 by the ICRP [30]. The most significant changes from the previous held values [28] relate to breast (0.05 → 0.12), gonads (0.2 → 0.08), and the remainder tissues (0.05 → 0.12 using a simplified additive system). Moreover, in the new concept sex-averaged tissue doses are used for the calculation of the effective dose.

10.2.3.2 Estimation of Organ and Effective Doses

Doses from the intake of radiolabeled compounds, such as PET radiopharmaceuticals, cannot be measured; they can only be estimated on the basis of biokinetic and dosimetric models.

Table 10.1 Tissue weighting factors, w_T, given in ICRP-103 [30]. They characterize the relative susceptibility of various tissues and organs, *T*, to ionizing radiation

Tissue or organ	w_T
Bone marrow (red), colon, lung, stomach, breast, remainder tissues[a]	0.12
Gonads	0.08
Bladder, esophagus, liver, thyroid	0.04
Bone surface, brain, salivary glands, skin	0.01

[a]The "remainder tissues" consist of the following group of additional organs and tissues with a lower sensitivity for radiation-induced effects for which the arithmetic average of organ doses must be used: adrenals, extrathoracic region, gall bladder, heart, kidneys, lymphatic nodes, muscle, oral mucosa, pancreas, prostate, small intestine, spleen, thymus, and uterus/cervix

Biokinetic models describe the uptake and retention of incorporated radionuclides in source regions of the body where they accumulate as well as their excretion from the body. They are used to calculate the numbers of nuclear transformations in the source regions which are needed to calculate the dose to target tissues by dosimetric models. In general, biokinetic models are formulated as compartment models. If the tracer is intravenously injected, the starting compartment represents the blood pool from where the material is transported to other tissue compartments representing the source regions where it accumulates and to (mainly urinary and fecal) excretion. In general, the retention in a compartment can be described by biological half-life, i.e., by a period of time within which half of the material is removed from the compartment.

Dosimetric models are used to calculate the dose to a target tissue due to a nuclear transformation in the considered source regions. For this, absorbed fractions $AF(r_T \leftarrow r_S)$ are determined, i.e., the fraction of the energy emitted in a source region r_S which is absorbed in a target tissue r_T. In case of non-penetrating radiation (α and β radiation), the simplifying assumption $AF(r_T \leftarrow r_S) = 1$ for $S = T$ and $= 0$ for $S \neq T$ is used for most pairs of source regions and target tissues. For penetrating radiation (γ radiation), absorbed fractions are calculated by Monte Carlo methods based on anthropomorphic phantoms which describe the position and the form of the source regions and target tissues. These phantoms were for a long time mathematical phantoms describing both source regions and target tissues by simple geometric objects. They are now being replaced by much more realistic voxel phantoms derived from MRI or CT images of real persons. For purposes of radiation protection, voxel phantoms are adjusted to the dimensions of the reference persons as defined by the ICRP [29]. Reference voxel phantoms for an adult male and female are published in ICRP Publication 110 [33]. However, *AF* values computed on the basis of the new models are not yet available.

Combining the results from both biokinetic and dosimetric models, dose coefficients $h(r_T)$ (in mSv/MBq) are computed that give the dose H_T to an organ T per unit activity intake. The effective dose resulting from the activity A of a radiopharmaceutical administered to a patient can thus be estimated by

$$E = \sum_T w_T \cdot H_T = A \cdot \sum_T w_T \cdot h(r_T) = A \cdot d_E \quad (10.2)$$

with d_E being the dose coefficient for the effective dose. For PET tracers more frequently used in clinical routine [6], values for d_E are listed in Table 10.2.

Table 10.2 Dose coefficients to estimate the effective dose related to the administration of PET radiopharmaceuticals frequently administered in clinical routine. The given values were calculated for the adult mathematical reference phantom using the new tissue weighting factors of ICRP-103 (2007). The biodistribution of the PET tracers was described by the biokinetic models given in ICRP-53 (2001) and ICRP-106 (2008) assuming that the bladder is emptied at 3.5 h after tracer administration

Nuclide	Radiolabeled compound	Function	Dose coefficient d_E (μSv/MBq)
^{11}C	L-Methionine	Amino acid transport and protein synthesis	7.6
	Acetate	Myocardial oxidative metabolism	2.8
^{13}N	Ammonia	Myocardial blood flow	2.2
^{15}O	Water	Regional blood flow	1.1
18F	2-Fluoro-2-deoxy-D-glucose	Glucose transport and phosphorylation	18
	L-Dopa	Presynaptic dopaminergic function	22
	Fluoride	Bone metabolism	21
^{82}Rb	Rubidium chloride	Myocardial blood flow	3.8

The given values were calculated for voxel phantoms using the biokinetic models given in ICRP-53 [27] and ICRP-106 [32] under the assumption that the bladder is emptied at 3.5 h after tracer administration and the new tissue weighting factors given in ICRP-103 [30]. They hold for a standard patient with a body weight of about 70 kg

In case of *pregnant patients* undergoing a PET examination – either based on a stringent clinical indication or due to the unawareness of pregnancy – the effective dose to the offspring as well as the resulting radiation risks have to be carefully assessed. In the early stage of pregnancy, the uterine dose is often used as surrogate for the embryonic dose. For [^{18}F]FDG, the dose coefficient for the uterine dose is 29 μSv/MBq.

10.2.4 Estimation of Radiation Risks

The effective dose is not recommended for epidemiological evaluations, nor should it be used for detailed specific retrospective investigations of individual exposure and risk ([30], § 157). For the estimation of the potential consequences of a radiation exposure to *individual patients*, it is necessary to use specific data characterizing the exposed individual.

The standard approaches to generate age, gender, and organ-specific risk estimates are based on the so-called excess absolute risk, *ear*. It denotes the *additional* risk of a person of gender *S*, after an exposure to organ dose D_T at the age *e*, to be clinically diseased with a specific radiation-induced cancer at the age *a* or, more specifically, in the interval [*a*, *a* + 1). It is commonly calculated from

$$ar_T(e,a,D_T,S) = r_T(a,S) + ear_T(e,a,D_T,S) \quad (10.3)$$

where ar_T denotes the absolute risk and r_T the normal or baseline risk of a person of gender *S* to be diseased with a specific cancer in the interval [*a*, *a* + *1*). If a *relative* risk model is used, Eq. (3) can be written as

$$ar_T(e,a,D_T,S) = r_T(a,S) \cdot \left[1 + err_T(e,a,D_T,S)\right] \quad (10.4)$$

with $err_T(e,a,D_T,S)$ representing the excess relative risk. For example, an $err_T(e,a,D_T,S) = 1$ means that the additional, radiation-induced cancer risk for a person of gender *S* who was exposed at age *e* to an organ dose D_T and attained age *a* is as high as his normal cancer risk. Estimates of the excess (relative) risk for specific organs are usually derived from cancer incidence data of the *LSS*, where a linear dose dependence is commonly assumed for solid tumors, while a linear-quadratic approach provides better results for leukemia. The most recent models are summarized in the BEIR-VII report [1].

The site-specific *excess absolute lifetime risk* or *lifetime attributable risk*, LAR_T, for a person of gender *S* who was exposed at age *e* to an organ dose D_T is calculated by summing up all $ear_T(e,a,D_T,S)$ values between $e + \Delta t$ (with Δt being the minimum latency period) and the age of, e.g., 85 years, commonly used for lifetime risk estimates. The *ear* should be corrected for competing risks by the conditional probability $P(e,a)$, i.e., the probability that a person of age *e* survives beyond the age *a:*

$$LAR_T(e,D_T,S) = \int_{a=e+\Delta t}^{85} ear_T(e,a,D_T,S) \cdot P(e,a)\, da \quad (10.5)$$

The minimum latency period Δt is the time during which the radiation-induced cancer typically does not show clinical symptoms. A Δt of about 5 years for carcinoma and of about 2 years for leukemia is widely applied for incidence data. To determine the total *LAR* for a PET examination, all site-specific LAR_T estimates (i.e., for sites with appreciable organ doses) have to be summed up.

Based on this approach as well as German disease and life table data [12, 13, 15], Fig. 10.1 gives *LAR* estimates for both cancer incidence and mortality for female and male individuals attributed to the administration of 370 MBq [^{18}F] FDG at different ages. The plots reveal that the *LAR* decreases markedly with increasing age at exposure and is always somewhat higher for females as compared to males. But even for young adults, the estimated radiation-induced risks are at least two orders of magnitude lower than the corresponding baseline lifetime risks, i.e., the "normal" risk to incur cancer during the remaining lifetime. In Germany, for example, the lifetime baseline risk for cancer incidence (mortality) is about 47 % (26 %) for men and about 39 % (21 %) for women (all cancers excluding skin cancer).

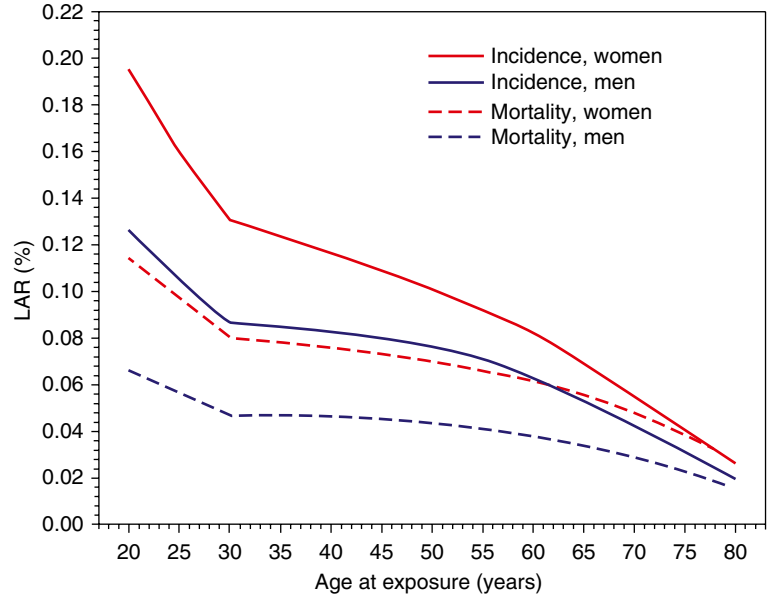

Fig. 10.1 Lifetime attributable risk for both cancer incidence and mortality for a female and male person resulting from the administration of 370 MBq [^{18}F] FDG at different ages. Risks were estimated from organ doses (computed for the adult reference phantom) using the BEIR-VII models as well as German life tables and cancer incidence rates

10.2.5 Diagnostic Reference Levels

In its publication on "Radiological Protection in Medicine" [31] the ICRP recommends the use of diagnostic reference levels (*DRLs*) for patient examinations as a measure of optimization of protection and gives the following guidance (§§ 78–84): As a form of *investigation level*, *DRL*s apply to easily measurable quantities, in nuclear medicine to the activity of administered radiopharmaceutical, and are intended for use as a simple test for evaluating whether the patient dose (with regard to stochastic effects) is unusually high for a particular imaging procedure. It should be noted that they do not apply to individual patients but rather to the mean activity value determined in practice for a suitable reference group (comprising at least 10 patients). If patient activities related to a specific diagnostic nuclear medicine procedure are consistently exceeding the corresponding *DRL*, there should be a local review (clinical audit) of the procedures and equipment. Actions aimed at the reduction of activity levels should be taken, if necessary.

DRLs are set by professional medical bodies in conjunction with national health or radiological protection authorities and reviewed at intervals that represent a compromise between the necessary stability of the protection system and the changes in the observed dose distributions. The fraction of the amount of a PET radiopharmaceutical to an adult to be administered in *pediatrics* can be calculated from the child's body weight either according to the dosage card published by the European Association of Nuclear Medicine [36] or the North American consensus guidelines [16].

10.3 MR: Nonionizing Radiation

10.3.1 Interaction Mechanisms and Biological Effects of (Electro) Magnetic Fields

In MR imaging and spatially localized MR spectroscopy, three variants of magnetic fields are employed to form cross-sectional images of the human body: (1) a high static magnetic field, B_0, generating a macroscopic nuclear magnetization,

(2) rapidly alternating magnetic gradient fields for spatial encoding of the MR signal, and (3) radiofrequency (RF) electromagnetic fields for excitation and preparation of the spin system. The biophysical interaction mechanisms and biological effects of these fields are shortly summarized in the following; a more comprehensive review can be found in [4].

10.3.1.1 Static Magnetic Fields

There are several established biophysical mechanisms through which static magnetic fields can interact with biological tissues and organisms [44]. The two most relevant mechanisms are:

Magneto-mechanical interactions. Even in a uniform magnetic field, molecules, structurally ordered molecule assemblies, or cells with a magnetic moment (e.g., outer segments of retinal rod cells, muscle fibers, filamentous virus particles, and erythrocytes) experience a mechanical torque that tends to align their magnetic moment (anti) parallel to the external magnetic field and thus to minimize the potential energy. *Orientation effects*, however, can only occur when molecular or cellular objects have a nonspherical structure and/or when the magnetic properties are anisotropically distributed. At higher temperatures, as, for example, in the human body, the alignment of structures with small magnetic moments is prevented by their thermal movement (Brownian movement). Additionally, paramagnetic and ferromagnetic objects are attracted in a nonuniform magnetic field, as, for example, in the periphery of an MR system, and thus can quickly become dangerous projectiles (*missile effect*).

Magneto-hydromechanical interactions. Static magnetic fields also exert (Lorentz) forces on moving electrolytes (ionic charge carriers), giving rise to induced electric fields and currents. Since electrolytes with a positive or negative charge moving, for example, through a cylindrical blood vessel orientated perpendicular to a magnetic field are accelerated into opposite directions, this mechanism gives rise to an electrical voltage across the vessel, which is commonly referred to as a *blood flow potential*. In humans, the largest potentials occur across the aorta after ventricular contraction and appear superimposed on the T-wave amplitude of the ECG at fields in excess of 100 mT.

A large number of studies have been conducted to detect biological responses to static magnetic fields with flux densities ranging from milliteslas to several teslas (T). These studies have been reviewed comprehensively – among others – by ICNIRP [22] and the World Health Organization [53]. Overall there is little convincing evidence from cellular, animal, human, and epidemiological studies for biologically harmful effects of short-term exposure resulting from static magnetic fields with a strength up to several teslas. Until now, most MR examinations have been performed using static magnetic fields up to 3 T, although whole-body MR systems with static magnetic fields up to 9 T are already used in clinical tests. The literature does not indicate any serious adverse health effects from the exposure of healthy human beings up to 8 T. However, sensations of nausea, vertigo, and metallic taste may occur in magnetic fields above 2 T [23]. The greatest potential health hazard comes from metallic, in particular, ferromagnetic materials (such as scissors, coins, pins, oxygen cylinders) that are accelerated in the inhomogeneous magnetic field in the periphery of an MR system and quickly become dangerous projectiles (*missile effect*). This risk can only be minimized by a strict and careful management of both patients and staff.

10.3.1.2 Alternating Magnetic Gradient Fields

Due to their low magnetic flux density, magnetic gradient fields used in MRI for spatial encoding of the MR signal can be neglected compared to the strong static magnetic field B_0 as far as interactions of *magnetic* fields with biological tissues and organisms are concerned. In contrary, however, biophysical effects related to the *electric* fields and currents induced by their temporal variation have to be considered carefully. Rapidly switched magnetic fields induce electric fields in

the human body, the strength of which is proportional to the time rate of change of the magnetic field, *dB/dt*. In conductive media, such as biological tissues, the electric fields result in *circulating eddy currents*. In general, rise times of magnetic gradients in MR are longer than 100 µs, resulting in time-varying electric fields and currents with frequencies below 100 kHz. In this frequency range, the conductivity of cell membranes is several orders of magnitude lower than that of the extra- and intracellular fluid [14]. As a consequence, the current flow is restricted to the extracellular fluid and voltages are induced across the membrane of cells. When these voltages are above a tissue-specific threshold level, they can stimulate nerve and muscle cells [42].

The primary concern with regard to time-varying magnetic gradient fields is *cardiac fibrillation*, because it is a life-threatening condition. In contrast, *peripheral nerve stimulation* (PNS) is of practical concern because uncomfortable or intolerable stimulations would interfere with the examination (e.g., due to patient movements) or would even result in a termination of the examination [51]. Bourland et al. [3] analyzed stimulation data in the form of cumulative frequency distributions that relate a *dB/dt* level to the number of healthy volunteers that had already reported on perceptible, uncomfortable, or even intolerable sensations. Their results indicate that the lowest percentile for intolerable stimulation is approximately 20 % above the median threshold for the perception of peripheral nerve stimulation. The threshold for cardiac stimulation is well above the median perception threshold for peripheral nerve stimulation, except at very long pulse durations which are, however, not relevant for clinical MR examinations (see Fig. 10.2, [42]).

10.3.1.3 RF Electromagnetic Fields

Time-varying magnetic fields used for the excitation and preparation of the spin system in MR have typically frequencies above 10 MHz. In this RF range, the conductivity of cell membranes is comparable to that of the extra- and intracellular fluid which means that no substantial voltages are induced across the membranes [14]. Due to this reason, stimulation of nerve and muscle cells is no longer a matter of concern. Instead, *thermal effects* due to tissue heating are of importance. The increase in tissue temperature is dependent not only on localized power absorption and the duration of RF exposure but also on heat transfer and the activation of thermoregulatory mechanisms leading to thermal equalization within the body. It

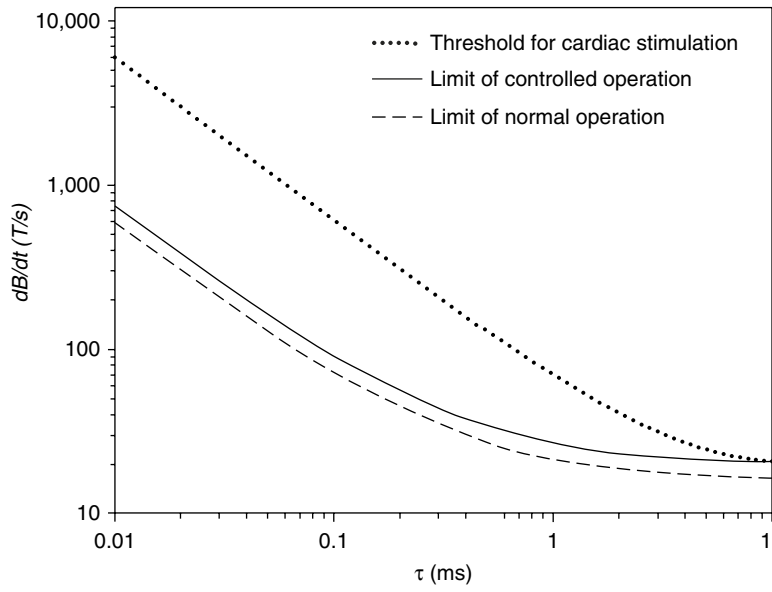

Fig. 10.2 Limits for the normal and controlled operating mode of an MR gradient system expressed as *dB/dt* as a function of the effective stimulus duration τ. The limit for the controlled operating mode is given by the median perception threshold for peripheral nerve stimulation. For comparison, the threshold for cardiac stimulation is also plotted [42]

is important to note that energy absorption is proportional to the square of the static magnetic field, B_0, which means it is markedly higher at high-field as compared to low-field MR systems.

Established biological effects of RF fields used for MR examinations are primarily caused by tissue heating. In contrast, nonthermal (or athermal) effects are not well understood but seem – as far as this can be assessed at the moment – to have no relevance with respect to the assessment of adverse effects associated with MR examinations. According to published studies, no adverse health effects are expected if the RF-induced increase in body-core temperature of healthy persons does not exceed 1 °C [23]. However, some organs of the human body are particularly vulnerable to raised temperatures. The most sensitive organs are the testes and brain as well as portions of the eye. Since temperature changes in the various organs and tissues of the body during an MR procedure are difficult to measure in clinical routine, RF exposure is usually characterized by means of the *specific absorption rate* (*SAR* in W/kg), which is defined as the average energy dissipated in the body per unit of mass and time.

10.3.2 Operating Modes and Safety Regulations

To minimize health hazards and risks to patients undergoing MR procedures, exposure limits for the three different magnetic fields used in MR are specified in:

- The safety recommendation issued by ICNRIP [23] that has been updated by an amendment concerning the exposure of patients to static magnetic fields [25]
- The product standard IEC 60601-2-33 provided by the International Electrotechnical Commission [34] for manufacturers of MR equipment to follow

In order to reflect the still existing uncertainty about deleterious effects of (electro)magnetic fields and to offer the necessary flexibility for the development and clinical evaluation of new MR technologies, both safety guidelines give exposure limits for three different modes of operation:

- *Normal mode (IEC: normal operating mode)*: Routine MR examinations that do not cause any field-induced physiological stress to patients.
- *Controlled mode (IEC: first level controlled operating mode)*: Specific MR examinations outside the normal operating range where discomfort and/or physiological stress to some patients may occur. Therefore, a clinical decision must be taken to balance such effects against expected benefits and exposure must be carried out under medical supervision.
- *Experimental mode (IEC: second level controlled operating mode)*: Experimental MR procedures with exposure levels beyond the controlled operating range. In view of the potential risks for patients and volunteers, special ethical approval and adequate medical supervision is required.

All manufacturers of MR equipment have adopted the regulations of the IEC product standard for magnetic gradient and RF fields and ensure compliance with the specified exposure limits by integrated *monitor systems*. With respect to the examination of patients in clinical routine, both the IEC standard and the ICNIRP guidelines recommended the following exposure limits:

- *Static magnetic field:* The upper limit for the normal and controlled operating mode recommended by the IEC is 3 and 4 T, respectively. In its recent amendment to static magnetic fields, ICNIRP recommends 4 and 8 T, respectively.
- *Alternating magnetic gradient fields:* The maximum recommended exposure level is set equal to a *dB/dt* value of 80 % of the PNS perception threshold for normal operation and 100 % of the PNS for controlled operation. To this end, perception threshold levels have to be determined by the manufacturers for a given type of gradient system by means of experimental studies on human volunteers. As an alternative, the generic hyperbolic strength-duration expression shown in Fig. 10.2 can be used.
- *RF electromagnetic fields:* The increase in body-core temperature is limited to 0.5 and 1.0 °C in the normal and controlled operating mode, respectively. The relatively

low-temperature threshold of the normal operating mode takes into account that heat tolerance or thermoregulation may be compromised in some individuals, such as the elderly, infants, and patients with certain medical conditions and/or taking certain medications. Additionally, local temperatures under exposure to the head, trunk, and extremities are limited to 38, 39, and 40 °C, respectively. For MR practice, the *SAR* limits summarized in Table 10.3 have been derived on the basis of experimental and theoretical studies. They should not be exceeded in order to limit the temperature rise to the stated values. But even then, severe burns can occur under unfavorable conditions at small focal skin-to-skin contact zones (e.g., between the calves). Therefore, patients should always be positioned in such a way that focal skin-to-skin contacts are avoided.

10.3.3 Contraindications

MR examinations of patients with *passive implants* (e.g., vascular clips and clamps, intravascular stents and filters, vascular access ports and catheters, heart valve prostheses, orthopedic prostheses, sheets and screws, intrauterine contraceptive devices), *active implants* (e.g., cardiac pacemakers and defibrillators, cochlear implants, electronic drug infusion pumps), or other objects of ferromagnetic or unknown material (pellets, bullets) are always associated with a serious risk, even if all procedures are performed within the established exposure limits summarized in the previous section. This risk can only be minimized by a careful interview of the patient, evaluation of the patient's file, and contacting the implanting clinician and/or the manufacturer for advice on MR safety and compatibility of the implant. MR examinations of patients with active implants are strictly contraindicated, provided that the patient implant card does not explicitly state their safety in the MR environment. Comprehensive information on the MR-compatibility of implants and other metallic objects is available in a reference manual published by Shellock [46] and online at www.MRIsafety.com. In contrast, side effects associated with the use of iron oxide or other metal-based pigments in tattoos occur extremely seldom and should not prevent patients – after informed consent – from undergoing a clinically indicated MR procedure [48].

Pregnant patients undergoing MR examinations are exposed to the combined (electro)magnetic fields discussed above. The few studies on pregnancy outcome in humans following MR examinations have not revealed any adverse effects but are very limited because of the small

Table 10.3 SAR limits for patients (and volunteers) undergoing MR procedures [22, 33] in clinical routine. They hold at environmental temperatures below 24 °C

	Averaging time: 6 min					
	Whole-body SAR (W/kg)	Partial-body SAR (W/kg)		Local SAR (averaged over 10 g tissue) (W/kg)		
Body region → Operating mode ↓	Whole-body	Any region, except the head	Head[c]	Head	Trunk	Extremities
Normal	2	2–10[a]	3.2	10[b]	10	20
Controlled	4	4–10[a]	3.2	10[b]	10	20
Experimental	>4	> (4–10)[a]	>3.2	10[b]	>10	>20
Short-term SAR	The SAR limit over any 10 s period shall not exceed 3 times the corresponding average SAR limit					

[a]Partial-body *SARs* scale dynamically with the ratio r between the patient mass exposed and the total patient mass
Normal operating mode: $SAR = (10 - 8 \cdot r)$ W/kg
Controlled operating mode: $SAR = (10 - 6 \cdot r)$ W/kg

[b]In cases where the eye is in the field of a small local coil used for RF transmission, care should be taken to ensure that the temperature rise is limited to 1 °C

[c]Partial volume *SAR*s given by IEC; ICNIRP limits *SAR* exposure to the head to 3 W/kg

numbers of patients involved and difficulties in the interpretation of the results [23]. It is thus advisable that MR procedures may be performed in pregnant patients, in particular in the first trimester, only after critical risk/benefit assessment and with informed consent of the expectant mother [10].

10.4 MR-PET: Synergistic Effects of Ionizing and Nonionizing Radiation?

The data and considerations presented in this chapter provide an appropriate foundation for the initial assessment of possible health risks for patients undergoing combined MR-PET examinations. It has to be noted, however, that they are based solely on established biophysical and biological effects related to the exposure of either ionizing radiation or (electro)magnetic fields, whereas *synergistic or antagonistic effects* are not taken into account. There are a few studies indicating that static [37] and low-frequency [17, 35, 38, 52] magnetic fields might enhance the genotoxic potential of ionizing radiation. Moreover, it is well recognized that mild hyperthermia, as, for example, caused by RF fields, has a radiosensitizing effect in tumors [18, 47]. In the light of the developing MR-PET technology, further biological studies are thus urgently required to investigate – for exposure levels and examination scenarios that will occur at MR-PET systems – whether there are synergistic effects in normal tissues and, if so, to clarify their relevance for risk assessment of patients that will be examined with this innovative imaging modality.

10.5 Justification and Optimization of MR-PET Examinations

Indications for MR-PET have not yet been established on the basis of clinical studies. Accordingly, there is at present no *generic justification* of MR-PET procedures by professional bodies in conjunction with health and radiological protection authorities as required by ICRP-105 ([31]; cf. Sect. 10.2.2). In this context, not only the improvement in diagnostic accuracy achieved by this new imaging modality will be of relevance but also its practicability, availability, and cost-effectiveness. From a radiation hygienic point of view, an MR-PET examination should be performed instead of a PET-CT examination wherever practicable as long as it provides the same or even superior diagnostic information. Nevertheless, there will be a whole string of clinical situations in which PET-CT will remain the method of choice, as, for example, when CT data are required for radiation treatment planning, when CT is indicated instead of MR for morphological imaging, or when an MR examination is contraindicated in patients due to implants or metallic objects. It goes without saying that an MR-PET examination can only be justified clinically, when there is an *individual justification* for a PET scan.

In case of combined MR-PET examinations, optimization of the entire procedure with respect to the exposure of patients to ionizing radiation reduces to the question: What *activity* of the radiopharmaceutical has to be administered for the emission scan? [^{18}F]FDG activities administered for PET-CT examinations vary between about 300 and 450 MBq [19] depending on the detector material and count rate behavior of the PET scanner, the acquisition mode used (2D vs. 3D), and, of course, the body region to be investigated. They will presumably also be adequate for MR-PET examinations.

From a clinical point of view, lower activities will eventually result in longer emission *scan times*, and thus longer overall examination times. However, excessive examination times should be avoided in multimodality imaging as they may result in patient discomfort and, thus, in motion-induced misregistrations of the complementary images. Due to this reason, diagnostic reference levels for [^{18}F]FDG studies performed at conventional PET scanners – that have meanwhile been established by many states – may not be appropriate for combined MR-PET examinations. To balance the potentially higher activities that are injected into patients in an attempt to reduce emission scan time, *voiding of the bladder* should be forced, e.g., by oral hydration with water or

the administration of a diuretic. This is a very effective measure, because FDG in the bladder is the major source of internal exposure to the bladder itself as well as to neighboring organs.

In contrast to CT, the acquisition of whole-body MR images for *transmission correction* of emission data and morpho-functional image correlation is much more challenging [2]. To realize short examination times, the measurement has to be performed with fast MR sequences relying on the use of high-performance gradient and RF systems. At least at high-field MR systems, it will therefore be necessary to carefully optimize the imaging sequences, as, for example, by utilizing SAR reduction techniques like parallel imaging or hyperechos. In this context it has to be noted that – contrary to a common opinion held among MR users – the SAR limits given in Table 10.3 do not relate to an individual MR sequence but rather to *running SAR average*s computed over each 6 min period, which is assumed to be a typical thermal equilibration time (Brix [7]). This means that sequences can be employed for which SAR levels exceed the defined values, if the acquisition time is short in relation to the averaging period and energy deposition has been low previous to the applied high-power sequence.

References

1. BEIR-VII. Committee to Assess Health Risks from Exposure to Low Levels of Ionizing Radiation. National Research Council. Health risks from exposure to low levels of ionizing radiation: BEIR VII phase 2. Washington: The National Academies Press; 2006.
2. Beyer T, Weigert M, Quick HH, Pietrzyk U, Vogt F, Palm C, Antoch G, Müller SP, Bockisch A. MR-based attenuation correction for torso-PET/MR imaging: pitfalls in mapping MR to CT data. Eur J Nucl Med Mol Imaging. 2008;35:1142–6.
3. Bourland JD, Nyenhuis JA, Schaefer DJ. Physiologic effects of intense MR imaging gradient fields. Neuroimaging Clin N Am. 1999;9: 363–77.
4. Brix G. Risks and safety issues related to MR examinations. In: Reiser M, Semmler W, Hricak H, editors. Magnetic resonance tomography. Berlin/Heidelberg/New York: Springer; 2007.
5. Brix G, Beyer T. PET/CT: dose-escalated image fusion? Nuklearmedizin. 2005;44:S51–7.
6. Brix G, Noßke D, Glatting G, Minkov V, Reske SN. A survey of PET activity in Germany during 1999. Eur J Nucl Med Mol Imaging. 2002;29:1091–7.
7. Brix G, Seebass M, Hellwig G, Griebel J. Estimation of heat transfer and temperature rise in partial-body regions during MR procedures: an analytical approach with respect to safety considerations. Magn Reson Imaging. 2002;20:65–76.
8. Brix G, Lechel U, Glatting G, Ziegler SI, Munzing W, Muller SP, Beyer T. Radiation exposure of patients undergoing whole-body dual-modality 18F-FDG PET/CT examinations. J Nucl Med. 2005;46:608–13.
9. Brix G, Nekolla EA, Noßke D, Griebel J (2009). Risks and safety aspects related to PET/MR examinations. Eur J Nucl Med Mol Imag. 36(S):132–138.
10. Colletti PM. Magnetic resonance procedures and pregnancy. In: Shellock FG, editor. Magnetic resonance procedures: health effects and safety. Boca Raton: CRC Press; 2001.
11. Collins CD. PET/CT in oncology: for which tumours is it the reference standard? Cancer Imaging. 2007;7(Spec No A):S77–87.
12. DeStatis. Gesundheitswesen, Todesursachen in Deutschland [Causes of death in Germany] Fachserie 12/Reihe 4. Editors. Wiesbaden: Statistisches Bundesamt (Federal office for statistics); 2004.
13. DeStatis. Statistisches Jahrbuch 2010 für die Bundesrepublik Deutschland (Statistical yearbook 2010 for the Federal Republic of Germany). Stuttgart: Metzler-Poeschel; 2010.
14. Foster KR, Schwan HP. Dielectrical properties of tissues. In: Polk C, Postow E, editors. Handbook of biological effects of electromagnetic fields. Boca Raton: CRC Press; 1996.
15. GEKID (Association of Population-Based Cancer Registries in Germany and Robert-Koch Institute). Cancer in Germany. Incidence and trends. 7th revised, updated ed. Saarbrücken: Association of Population-Based Cancer Registries in Germany and Robert-Koch Institute; 2010.
16. Gelfand MJ, Parisi MT, Treves ST. Pediatric radiopharmaceutical administered doses: 2010 North American consensus guidelines. J Nucl Med. 2011;52: 318–22.
17. Hintenlang DE. Synergistic effects of ionizing radiation and 60 Hz magnetic fields. Bioelectromagnetics. 1993;14:545–51.
18. Horsman MR, Overgaard J. Hyperthermia: a potent enhancer of radiotherapy. Clin Oncol (R Coll Radiol). 2007;19:418–26.
19. IAEA. Radiation protection aspects in newer imaging techniques: PET/CT: safety reprints series, no 58, vol. 1. Vienna: IAEA; 2008.
20. ICNIRP. Guidelines for limiting exposure to time-varying electric, magnetic, and electromagnetic fields (up to 300 GHz). Health Phys. 1998;74: 494–522.
21. ICNIRP. General approach to protection against non-ionizing radiation. Health Phys. 2002; 82:540–8.

22. ICNIRP. Publication ICNIRP 13/2003. Exposure to static and low frequency electromagnetic fields, biological effects and health consequences (0–100 kHz). Oberschleissheim: ICNIRP; 2003.
23. ICNIRP. Medical magnetic resonance (MR) procedures: protection of patients. Health Phys. 2004;87: 197–216.
24. ICNIRP. Guidelines on limits of exposure to static magnetic fields. Health Phys. 2009;96:504–14.
25. ICNIRP. Amendment to the ICNIRP 'Statement on medical magnetic resonance (MR) procedure: Protection of patients'. Health Phys. 2009;97: 259–61.
26. ICNIRP. Guidelines for limiting exposure to time-varying electric and magnetic fields (1 Hz to 100 lHz). Health Phys. 2010;99:818–36.
27. ICRP-53. Addendum 4 to ICRP Publication 53, http://www.icrp.org/docs/P053_addendum_4_(28interim_2002-10-15)29.pdf; 2001. Accessed 18 Oct 2011.
28. ICRP-60. Publication 60. 1990 Recommendations of the International Commission on Radiological Protection. Ann ICRP. 1991;21(1–3).
29. ICRP-89. Publication 89. International Commission on Radiological Protection. Basic anatomical and physiological data for use in radiological protection: reference values. Ann ICRP. 2002; 32(3/4).
30. ICRP-103. Publication 103. The 2007 recommendations of the International Commission on Radiological Protection. ICRP Publication 103. Ann ICRP. 2007; 37(2–4).
31. ICRP-105. Publication 105. Radiological protection in medicine. Ann ICRP. 2007;37(6).
32. ICRP-106. Publication 106. Radiation dose to patients from radiopharmaceuticals. Addendum 3 to ICRP Publication 53. Ann ICRP. 2008;38(1–2).
33. ICRP-110. Publication 110. Adult reference computational phantoms. Ann ICRP. 2009;39(2).
34. IEC (2010) IEC 60601-2-33, third edition. Particular requirements for the safety of magnetic resonance equipment for medical diagnosis. IEC, Geneva.
35. Koyama S, Nakahara T, Sakurai T, Komatsubara Y, Isozumi Y, Miyakoshi J. Combined exposure of ELF magnetic fields and X-rays increased mutant yields compared with X-rays alone in pTN89 plasmids. J Radiat Res. 2005;46:257–64.
36. Lassmann M, Biassoni L, Monsieurs M, Franzius C, Jacobs F. The new EANM paediatric dosage card. Eur J Nucl Med Mol Imaging. 2007;34:796–8.
37. Miyakoshi J. Effects of static magnetic fields at the cellular level. Prog Biophys Mol Biol. 2005; 87:213–23.
38. Miyakoshi J, Yoshida M, Shibuya K, Hiraoka M. Exposure to strong magnetic fields at power frequency potentiates X-ray-induced DNA strand breaks. J Radiat Res. 2000;41:293–302.
39. Patel CN, Goldstone AR, Chowdhury FU, Scarsbrook AF. FDG PET/CT in oncology: 'raising the bar'. Clin Radiol. 2010;65:522–35.
40. Poeppel TD, Krause BJ, Heusner TA, Boy C, Bockisch A, Antoch G. PET/CT for the staging and follow-up of patients with malignancies. Eur J Radiol. 2009;70:382–92.
41. Preston DL, Ron E, Tokuoka S, Funamoto S, Nishi N, Soda M, Mabuchi K, Kodama K. Solid cancer incidence in atomic bomb survivors: 1958–1998. Radiat Res. 2007;168:1–164.
42. Reilly JP. Applied bioelectricity: From electrical stimulation to electro-pathology. Berlin/Heidelberg/New York: Springer; 1998.
43. Saif MW, Tzannou I, Makrilia N, Syrigos K. Role and cost effectiveness of PET/CT in management of patients with cancer. Yale J Biol Med. 2010;83: 53–65.
44. Schenck JF. Physical interactions of static magnetic fields with living tissues. Prog Biophys Mol Biol. 2005;87:185–204.
45. Shellock FG. Magnetic resonance procedures: health effects and safety. Boca Raton: CRC Press; 2001.
46. Shellock FG. Reference manual for magnetic resonance safety, implants, and devices: 2011 edition. Los Angeles: Biomedical Research Publishing Company; 2011.
47. Song CW, Park H, Griffin RJ. Improvement of tumor oxygenation by mild hyperthermia. Radiat Res. 2001;155:515–28.
48. Tope WD, Shellock FG. Magnetic resonance imaging and permanent cosmetics (tattoos): survey of complications and adverse events. J Magn Reson Imaging. 2002;15:180–4.
49. Townsend DWJ. Dual-modality imaging: combining anatomy and function. Nucl Med. 2008;49:938–55.
50. United Nations Scientific Committee on the Effects of Atomic Radiation. Sources and effects of ionizing radiation. UNSCEAR 2008 report, vol. 1: sources, annex A: medical radiation exposures. New York: United Nations; 2010.
51. Vogt FM, Ladd ME, Hunold P, Mateiescu S, Hebrank FX, Zhang A, Debatin JF, Göhde SC. Increased time rate of change of gradient fields: effect on peripheral nerve stimulation at clinical MR imaging. Radiology. 2004;233:548–54.
52. Walleczek J, Shiu EC, Hahn GM. Increase in radiation-induced HPRT gene mutation frequency after nonthermal exposure to nonionizing 60 Hz electromagnetic fields. Radiat Res. 1999;151: 489–97.
53. WHO. Static fields, Environmental Health Criteria, vol. 232. Geneva: World Health Organization; 2006.

Health-Care Costs and Impacts

11

Mathias Goyen

Contents

Abstract

Continuous aging of the population, growing health consciousness, and continuous technological advances have fueled the rapid rise in health-care costs in the United States and Europe for the past several decades. The exact impact of new medical technology on long-term spending growth remains subject to some controversy. By all measures, it is apparent that new medical technology is the dominant driver of increases in health-care costs and hence insurance premiums. This chapter addresses the impact of medical technology such as MRI-PET on health-care delivery systems with regard to medical practice and cost. Factors addressing the growth of medical technology will be explored before attempting to provide a means for assessing the effectiveness of medical technology. Finally, avoidable health-care cost drivers will be identified, and relating policy issues will be discussed.

11.1 Introduction

Continuous aging of the population, growing health consciousness, and continuous technological advances have fueled the rapid rise in health-care costs in the United States and Europe for the past several decades. The increases amount to 3.5 % annually, thereby vastly exceeding the average increase in spending power. Thus, in the United States, annual spending on health care increased from $75 billion in 1970 to

M. Goyen, UCM
University Medical Center, Hamburg-Eppendorf, Martinistrasse 52, 20251 Hamburg, Germany
e-mail: mathias@goyen.de

I. Carrio, P. Ros (eds.), *PET/MRI*,
DOI 10.1007/978-3-642-40692-8_11,

$2.0 trillion in 2005 and is estimated to reach $4.2 trillion in 2015. It is projected that health expenditures, which already constitute 16 % of the US economy, will rise to 30 % of GDP (gross domestic product) by 2030 [1]. Health insurance premiums have developed accordingly, leaving a growing number of people unable to maintain coverage.

Aiming at health insurance affordability, health policymakers have over the past years focused on cost containment. All kinds of measures have been introduced in all kinds of health-care systems. Virtually all of them have one thing in common—they failed to achieve cost containment. When trying to explain failure, health policy experts point to the development and diffusion of medical technology. The same pharmacological and technical innovations which have saved so many individual lives seem to be responsible for making our health-care systems financially sick. The exact impact of new medical technology on long-term spending growth remains subject to some controversy. Most experts believe medical technology advances to account for one-half to two-thirds of annual spending increases [2]. By all measures, it is apparent that new medical technology is the dominant driver of increases in health-care costs and hence insurance premiums.

This article addresses the impact of medical technology on health-care delivery systems with regard to medical practice and cost. Factors addressing the growth of medical technology will be explored before attempting to provide a means for assessing the effectiveness of medical technology. Finally, avoidable health-care cost drivers will be identified, and relating policy issues will be discussed.

11.2 Medical Technology Impact on Health Care

The term "medical technology" refers to procedures, equipment, and processes by which medical care is delivered. Hence, medical technology innovations can relate to new medical and surgical procedures (e.g., angioplasty, joint replacements), the discovery of new drugs (e.g., biologic agents), the implementation of health-care IT systems (e.g., electronic medical records and transmission of information, telemedicine), or the development of new medical devices as discussed in this book (MRI-PET technology). All of medicine is affected by the continuous advances in medical technology.

While some new technologies—vaccines, for example—do result in lower short-term spending, research has shown that, on balance, technology advances in medicine result in increased spending [2]. The adverse cost effects of truly new medical technologies are being supplanted only by the widening of applications of established technologies (e.g., magnetic resonance imaging).

Benefits to patients and associated financial burdens caused by new medical technology are well illustrated in the case of ischemic heart disease or more specifically the treatment and prevention of heart attacks, the leading cause of death in the United States and the western world. In the 1970s, cardiac care units were introduced, lidocaine was used to manage irregular heartbeat, beta-blockers were used to lower blood pressure in the first 3 h after a heart attack, "clot buster" drugs began to be widely used, and coronary artery bypass surgery became prevalent. In the 1980s, blood-thinning agents were used following a heart attack to prevent reoccurrences, beta-blocker therapy evolved from short-term therapy immediately following a heart attack to maintenance therapy, and angioplasty (minimally invasive surgery) was used after heart attack patients were stable. In the 1990s, more effective drugs were introduced to inhibit clot formation, angioplasty was used along with stents to keep blood vessels open, cardiac rehabilitation programs were implemented sooner, and implantable cardiac defibrillators were used in certain patients with irregular heartbeats. In the 2000s, better tests became available to diagnose heart attack, drug-eluting stents were introduced, and new drug strategies were developed (aspirin, ACE inhibitors, beta-blockers, statins) for long-term management of heart attack and potential heart attack patients. Based on these measures

implemented over the past 30 years, the overall mortality rate from heart attack in the United States was reduced by almost half, from 345.2 to 186.0 per 100,000 persons [3].

11.3 How Does New Medical Technology Affect Health-Care Costs?

While a particular new technology may either increase or decrease short-term health-care spending, experts agree that, taken together, advances in medical technology are the major contributors to health-care expenditure increases. Rettig describes the mechanisms by which new medical technology affects health-care costs as follows [4]:

- Development of new treatments for previously untreatable terminal conditions, including long-term maintenance therapy for treatment of such diseases as diabetes, end-stage renal disease, and AIDS
- Major advances in clinical ability to treat previously untreatable acute conditions, such as coronary artery bypass graft
- Development of new procedures for discovering and treating secondary diseases within a disease, such as erythropoietin to treat anemia in dialysis patients
- Expansion of the indications for a treatment over time, increasing the patient population to which the treatment is applied
- Ongoing, incremental improvements in existing capabilities, which may improve quality
- Clinical progress, through major advances or by the cumulative effect of incremental improvements, that extends the scope of medicine to conditions once regarded as beyond its boundaries, such as mental illness and substance abuse

The effect of a particular new technology onto health-care expenditures depends on a variety of factors. Central to any calculation is the impact on the treatment cost of the individual patient. Does the new technology supplement existing treatment, or is it a full or partial substitute for current approaches? In looking at the impact on cost per patient, consideration needs to be given to whether the direct costs of the new technology include any effect on the use or cost of other health-care services such as hospital days or physician office visits.

A second factor relates to the level of use that a new technology achieves (i.e., how many times is the new technology used?). Does the new technology extend treatment to a broader population? Greater availability of such technologies such as magnetic resonance imaging, computed tomography, coronary artery bypass grafting, angioplasty, cardiac and neonatal intensive care units, as well as positron emission tomography is associated with greater per capita use and higher spending on these services. The impact of this effect is dependent on the kind of health-care delivery system in place. In non-budgeted "open" health-care systems, as are in place in the United States as well as some European countries, the unrestrained use of technologies result in their broad application, thereby incurring high health-care costs. Nations with a greater degree of health system integration and regulation have relied on expenditure controls and global budgets to control costs. Although diffusion of technology takes place more slowly in more tightly budgeted systems, the use of innovative technologies in those systems tends to catch up over time.

In Japan, the number of external radiation therapies undertaken per month increased from 200,366 in 2002 to 251,298 in 2005, while the number of Gamma Knife therapies per month increased from 1,262 in 2002 to 3,226 in 2005 (Survey of Medical Institutions 2005 by the Ministry of Health, Labour and Welfare, Japan). OECD health data 2008 show that MRI units per million populations are 5.6 in the United Kingdom, 5.3 in France, 7.7 in Germany, 26.5 in the United States, and 40.1 in Japan. CT scanners per million populations are 7.6 in the United Kingdom, 10.0 in France, 16.7 in Germany, 33.1 in the United States, and 92.6 in Japan. The reason behind these Japanese figures may be an increased public awareness of new medical technologies and the increasing number of consumers

who purchase more health-care services hoping to get better health and reassurance.

The effect of health-care delivery systems onto the diffusion of medical technology is well illustrated in the case of PET/CT. The rapid growth in the United States with regard to PET/CT can be attributed to the highly competitive nature of the health-care business. More than 40 % of the approx. 2,400 PET/CT scanners worldwide are installed in the United States. The culture of health-care provision in Europe is very different, with central governments controlling expenditure rather than competing independent hospitals. This led to significant discrepancies in the availability of PET and PET/CT imaging throughout Western Europe.

The applicability and recognition of PET/CT as an imaging modality in diagnostic oncology is affected by several factors in Germany. Reimbursement seems to be a major obstacle for the diffusion of PET/CT in Germany. Despite the studies by Dietlein et al. showing the cost-effectiveness for several PET indications [5, 6], the Federal Joint Committee of Physicians and Health Insurance Funds in Germany issued a statement in 2002 refusing reimbursement for outpatient PET studies. This decision dramatically reduced the funding of PET and PET/CT studies, effectively limiting reimbursement for inpatients and self-financing private patients. Additionally, excessive requirements for regulatory approval of radiopharmaceuticals and fear of radiation level are serious problems influencing the development of PET and PET/CT scanners. In Germany, approx. 60 PET/CT systems are in clinical use (Dec. 2011) in university medical centers, community hospitals, as well as private practices. Approximately 20 % of the university medical centers still do not have access to PET/CT imaging 7 years after introduction of this technique into clinical routine [personal communication with different vendors].

Comparative clinical benefits for existing PET-MRI or PET/CT approaches need to be established, as well as the caseload and case mix required for effective utilization of a hybrid MRI-PET scanner. MRI-PET has developed and matured over the last decade. Clinical systems are available for the whole body and for specific areas as illustrated in this book. The technology's cost remains a significant obstacle. Integrated MRI-PET scanners—available in Europe but not yet approved in the United States—carry a price tag of approximately US $7 million. Similar to PET/CT scanners which were very expensive when they first came out and dropped in price as the technology became more available, also MRI-PET scanners will decline in price. More research is needed to determine the cost-effectiveness of MRI-PET technology.

In general, there also are temporal aspects to evaluating the impact of new technologies on costs. Some innovations, such as a new vaccine, may cost more immediately but may lead to savings down the road if the vaccine results in fewer people seeking more expensive treatment. New technologies such as whole-body MRI-screening examinations also can extend life expectancy, which affects both the type and amount of health care that people use in their lifetime.

It is not possible to directly measure the impact of new medical technology on total health-care spending; rather, innovation in the health-care sector occurs continuously, and the impacts of different changes interrelate. The size of the health sector (16 % of gross domestic product in 2005) and its diversity (thousands of procedures, products, and interventions) also render direct measurement impractical.

Thus, economists have used indirect approaches to estimate the impact of new technology onto health-care cost [7]. In a landmark paper, Newhouse determines the impact of medical technology on health-care spending by first estimating the impact of factors that can reasonably be accounted for (e.g., spread of insurance, increasing per capita income, aging of the population, supplier-induced demand, low medical sector productivity gains). He concludes that the factors listed above account for well under half of the growth in real medical spending, and that the bulk of the unexplained residual increase is to be attributed to technological change—what he calls "the enhanced capabilities of medicine" [8].

11.4 Factors Affecting the Growth of New Medical Technology

Many factors influence innovation in medical care. Consumer demand for better health is a prime factor. Research shows that the use of medical care rises with income: as a nation and its population become wealthier, they provide a fertile market for new medical innovations. Consumers want medical care that will help them achieve and maintain good health. Advances in medical technology are perceived as means to promote those goals. Consumer demand is affected by the increased public awareness of medical technology through the media, the Internet, and direct-to-consumer advertising.

Health insurance systems that provide payment for new innovations also encourage medical advances. Medical treatments can be very expensive, and their cost would be beyond the reach of most people unless their risk of needing health care could be pooled though insurance (either public or private). The presence of health insurance provides some assurance to researchers and medical suppliers that patients will have the resources to pay for new medical products, thus encouraging research and development. At the same time, the promise of better health through improvements in medicine increases the demand for health insurance as consumers look for ways to assure access to the highest level of medical care.

Other factors driving the continuing flow of new medical technology include the desire by professionals to find better ways to treat their patients. Like most other professionals, health-care workers are also motivated by professional goals (e.g., peer recognition, tenure, prestige) to find ways to improve practice. Furthermore, direct providers of care may incorporate new technology because they feel the need to offer the "latest and best" as they compete with other providers for patients. Commercial interests such as those inherent to pharmaceutical companies and medical device makers represent the dominant force driving medical innovation. Its profound impact is easily visualized when taking a look at a medical innovation over a 40 year period in Germany. The difference is vast—commercially motivated innovations made in Germany saved many lives, while at the same time making health care considerably more expensive. Commercial companies are willing to invest large amounts in research and development as long as they are convinced of the underlying medical needs and the possibility of financial reimbursement. Finally, public and private investments in basic science research lead directly and indirectly to improvements in medical practice. Generally motivated by the desire to increase human understanding, these government-sponsored investments in basic science are increasingly regarded as programs to assure economic prosperity [7].

An estimated $111 billion was spent on US health research in 2005. The largest share was spent by the industry ($61 billion, or 55 %), including the pharmaceutical industry ($35 billion, or 31 %), the biotechnology industry ($16 billion, or 15 %), and the medical technology industry ($10 billion, or 9 %). Government spending amounted to $40 billion (36 %), most of which was spent by the National Institutes of Health ($29 billion, or 26 %), followed by other federal government agencies ($9 billion, or 8 %), and state and local government ($3 billion, or 2 %). Other organizations including universities, independent research institutes, and philanthropic foundations spent $10 billion (9 %). About 5.5 cents of every health dollar was spent on health research in 2005, a decrease from 5.8 cents in 2004 [9].

11.5 Policy Issues

The real issue is: Are we getting our money's worth in health care? Studies suggest that, on average, increases in medical spending as a result of advances in medical care have provided reasonable value. Thus, Cutler et al. found that from 1960 to 2000, average life expectancy increased by 7 years. They attributed half of this increase, i.e., 3.5 years, directly to improvements in medical technology. The cost for each year of life expectancy increase was calculated to amount to $19,900. In view of the worth of a year

of life, ranging anywhere between $50,000 and $200,000, the study concludes that the increased spending, on average, has been worth it [9].

No matter the value of advances in medical care, as the rapid growth in health-care costs increasingly strains personal, corporate, and government budgets, policymakers and the public must consider the question of how much health care we can afford.

11.6 Medical Technology Assessment/Avoidable Cost Drivers

Medical Technology Assessment is a multidisciplinary field of policy analysis that evaluates the medical, social, ethical, and economic implications of the introduction, development, and diffusion of a technology. Currently, most suggestions to slow the growth in new medical technology focus on cost-effectiveness analysis. Cost-effectiveness analysis involves non-biased, well-controlled studies of a technology's benefits and costs, followed by dissemination of the findings so they can be applied in clinical practice. The method to control the use of inappropriate technology could be through coverage and reimbursement decisions, by using financial incentives for physician and patients to use cost-effective treatments.

There are three main reasons why medical technology is not being used cost-effectively. First, patients do not pay directly for the health care they receive, so they sometimes make unreasonable demands on physicians regarding their diagnostic workup or subsequent treatment. Second, a new technology may be adopted because of its clinical superiority to existing technologies, but there is no market mechanism to ensure that it will be used where it is clinically most appropriate or where it offers highest value for a patient compared with other diagnostic or treatment options. Third, because there is no market mechanism for determining the value of medical technology, there is currently no generally accepted screening process to assess its value. In the diagnostic imaging technology category, increases are driven to a large extent by the growth in the number of machines installed. This has led in turn to overcapacities in many areas and has created incentives for doctors to prescribe unnecessary procedures. In addition, direct-to-consumer marketing fuels blind demand among consumers for advances in devices and drugs.

Duplication of procedures (i.e., a patient receives an MRI, then a PET scan, even though doing both procedures does not help doctors get closer to a diagnosis) and overuse of high-end procedures in situations where they add little value has also driven up technology spending unnecessarily.

References

1. Centers for Medicare and Medicaid Services, Office of the Actuary, National Health Statistics Group. http://www.cms.hhs.gov/NationalHealthExpendData/. Accessed Sept 28, 2013.
2. Nichols LM. Can defined contribution health insurance reduce cost growth? EBRI issue brief, vol. 246. Washington, DC: Employee Benefit Research Institute; 2002.
3. Medtap International Inc.: The value of investment in health care: better care, better lives; 2004:14–21.
4. Rettig RA. Medical innovation duels cost containment. Health Aff. 1994;13(3):7–27.
5. Dietlein M, Weber K, Gandjour A, et al. Cost-effectiveness of FDG-PET for the management of solitary pulmonary nodules: a decision analysis based on cost reimbursement in Germany. Eur J Nucl Med. 2000;10:1441–56.
6. Dietlein M, Weber K, Gandjour A, et al. Cost-effectiveness of FDG-PET for the management of potentially operable non-small cell lung cancer: priority for a PET-based strategy after nodal-negative CT results. Eur J Nucl Med. 2000;11:1598–609.
7. Anderson GF, Frogner BK, Johns RA, Reinhardt UE. Health care spending and use of information technology in OECD countries. Health Aff. 2006;25(3):819–31.
8. Newhouse JP. Medical care costs: how much welfare loss? J Econ Perspect. 1992;6(3):3–21. For a thorough discussion of the components of health care spending growth and medical technology's significant role, see the report of the Technical Review Panel on the Medicare Trustees Reports, *Review of Assumptions and Methods of the Medicare Trustees' Financial Projections* (December 2000).
9. Cutler DM, Rosen AB, Vijan S. The value of medical spending in the United States, 1960–2000. N Engl J Med. 2006;355(9):920–7.

Index

I. Carrio, P. Ros (eds.), *PET/MRI*,
DOI 10.1007/978-3-642-40692-8, © Springer-Verlag Berlin Heidelberg 2014